**POLITECNICO DI MILANO**

School of Industrial and Information Engineering

Energy department

Master of Science in Energy Engineering

# Study of temperature-related aging of lithium-ion battery through an innovative methodology for the determination of physical-model parameters

Supervisor:

Prof. Andrea Casalegno

Co-Supervisors:

Dr. Claudio Rabissi

Ing. Gabriele Sordi

Master Thesis by:

**Melissa Sedzik**

ID 913232

**Academic Year 2019 – 2020**

**Study of temperature-related aging of lithium-ion battery through an innovative methodology for the determination of physical-model parameters**

Master of Science in Energy Engineering
April, 2021

By Melissa Sedzik

Published by: Politecnico di Milano, School of Industrial and Information Engineering, Department of Energy
www.energia.polimi.it/en/energy-department/

# Extended abstract

## Introduction

Lithium ion batteries (LIBs) are the leading technology both in the electric vehicles (EVs) field and in the stationary energy storage applications, thanks to their advantageous properties with respect to other electrochemical storage systems, like high power and energy density, low self-discharge rate and long cycle life [1], [2].
Since the EVs market is already growing and it is expected to expand further in the next future [3], an increasing number of spent LIBs will have to be managed. This increase in LIBs usage makes it urgent to rethink the battery economy in a "circular way", including repurposing (second life applications) and recycling of the batteries at the end of life in order to reduce waste and environmental impact to the minimum. In fact, LIBs adopted for electric vehicles (EV) are usually considered at the end of their useful life when their capacity reaches the 80% of the nominal value [4]. Possible second life applications for batteries are to be used for stationary applications [5], [6], to provide power support to fast EVs charge stations, to be coupled with renewable energies to offer reliability in the electricity generation or to provide grid-oriented services. In a view of battery second life usage, it is fundamental to understand the degradation phenomena and their relation with the battery operating condition, to understand which are the stressors of these mechanisms and what are the consequences on the battery, in terms of state of health, of certain load conditions in its life.

This work aims to develop a non-destructive innovative method, that allows to investigate the aging phenomena related to lithium-ion batteries, detecting their presence through the interpretation of key parameters, obtained from a limited set of easily acquired experimental data. Moreover, two specific aging mechanisms will be studied. The steps that will be followed to achieve this result are the following:

1. **literature research** related to degradation mechanisms' stressors and diagnostic techniques, and data fitting algorithms;

2. adaptation and improvement of a pre-existent data-fitting algorithm (Particle Swarm Optimization) that allows the calibration of the physical model for a pristine cell, and an experimental protocol that provide the data on which the fitting is based;

3. development of a new **methodology** to calibrate the physical model is developed to account for degradation (Thesis Chapter 3);

4. investigation of two **degradation mechanisms** stressors, namely SEI growth and lithium plating. The aim would be to better understand these phenomena, their impact on the battery performance and the relation with operating conditions (Thesis Chapter 4);

5. application and validation of the implemented methodology, using the data collected along the experimental aging campaign (Thesis Chapter 5).

## 1. State of the art

### 1.1 Li-ion battery components and operation

A lithium-ion battery (LIB) is an electrochemical device that can store electric energy as chemical energy and allows the conversion from one another exploiting the reduction – oxidation reactions of lithium ions, that occur at both the battery electrodes. It is a closed system, as all the reactants and products of the reactions remain inside the battery itself.
A cell, the basic unit of a battery, is composed by essentially three components: two porous electrodes, separated by a polymeric membrane, the electrolyte (see Figure 1. Each electrode has a certain potential, depending on its composition, its thermodynamic condition and the lithium concentration presents in its active sites. An external electric circuit, linked to an electrical source or load, connects the two battery terminals and allows the flows of the electrons $e^-$ produced by the reactions and gathered in current collectors. In fact, when electrochemical reactions occur, lithium ions $Li^+$ are released on one electrode (lithium deintercalation), flows through the electrolyte and then are inserted into the other electrode (lithium intercalation); this $Li^+$ movement causes a change in the lithium concentration in the electrodes, resulting in a change of the electrodes potential. The electrode with the highest potential is the positive one, usually name cathode, while the lowest potential one is the negative electrode, usually named anode. The operating cell voltage $V$ can be obtained as the difference between these two potential values. $Q$ is the actual amount of available charge, that the LIB can store or release, and $Q_{nom}$, namely the nominal capacity, is a measure of the maximum amount of available capacity. $Q$ can be expressed with a dimensionless number, the state of charge (SOC), as the ratio between the charge that is stored in the battery $Q$ and its nominal capacity $Q_{nom}$. To define the operating current $I$ at which the battery is charged/discharged, it is commonly used the current rate or C-rate, given by the ratio between the $I$ and $Q_{nom}$.

### 1.2 Degradation phenomena and diagnostics

Lithium-ion batteries are subjected to degradation and two main types of aging can be distinguished: calendar aging, namely the aging not related to operation but just on thermodynamic conditions i.e temperature and SOC at which the battery is stored, and cycle aging, hence the one linked to the conditions at which the battery operates [8]. In both the

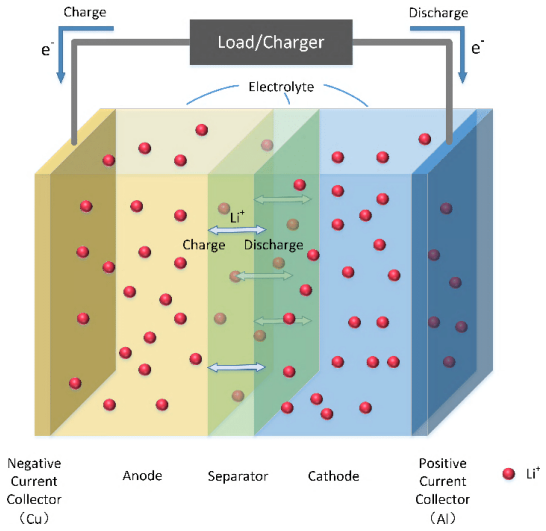


**Figure 1.** Schematic of a LIB (taken from [7])

cases the electrodes and electrolyte properties vary from their begin of life (BOL) state, due to unwanted side reactions that cause a degradation of these components. This degradation can be the result of different phenomena, such as solid electrolyte interphase (SEI) growth, particle cracking, graphite exfoliation, electrolyte decomposition, lithium deposition and current collector corrosion (see Thesis Chapter 1). Three main degradation modes can be distinguished [8], [9], [10]:

- loss of lithium inventory (*LLI*): it consists in a loss of the quantity of lithium available to be cycled between the anode and the cathode, that translates in a reduction of capacity without affecting the electrodes characteristics;
- loss of active material (*LAM*): it corresponds to a decrease in the number of active material sites, namely the sites available for lithium intercalation. This results in both power and capacity fade, as this kind of degradation leads to a reduction of the surface available for the electrochemical reactions. Two types of *LAM* can be distinguished, as it can occur both at the negative electrode ($LAM_n$) and at the positive electrode ($LAM_p$);
- conductivity loss (*CL*): it is related to the loss of electric contact and, hence, to the decrease of the specific active area for the electrochemical reactions, at which corresponds a resistance increase and therefore, a power loss.

Each of the degradation mode is the result of different physical and chemical phenomena, that are governed by many stressors. At present, there are three main diagnosis methods to detect the aging phenomena [11]: disassembly-based post-mortem analysis (destructive method), curve-based analysis (incremental capacity (IC), and differential voltage (DV) analysis) and model-based analysis (equivalent electric circuit model or the electrochemical model).

In this work, a non-intrusive methodology to detect and understand the degradation phenomena will be implemented by merging a curve-based analysis approach with a model-based method.

## 2. Methodology

### 2.1 Test bench

The test bench used for the experimental campaign was designed and assembled in a previous thesis work on the same project. Four independent channels are equipped with a Chroma UM63640-80-80 electronic load, allowing the simultaneous testing of up to four battery samples. The power supply NI RMX-4124 is used to charge the batteries. Both the voltage during operation and the voltage oscillation during EIS tests are read by the electronic loads; a NI DAQ USB 6218 acquisition board is used to measure and check these values as well. There are two climatic chambers where the batteries can be tested: one is a Binder KT 53, that can operate in the range 5°C-100°C and can only control the temperature, and the other one is a Binder MKF 720 Eucar 6, operating in a range of -40°C, 170°C and allowing the control of both temperature and relative humidity. The battery surface temperature is measured through four RS PRO type K thermocouples, and registered with a NI CDAQ 9211 acquisition board. The software LabView® is used to control the whole setup. Uncertainty's measurement on the experimental outputs i.e. exchanged charge during cycles, current, impedance and surface temperature has been evaluated (see Thesis Chapter 2).

### 2.2 Battery samples

The LIBs samples used in this work are commercially available batteries. The cathode material is NMC and the anode material is graphite and the nominal capacity is 2250 mAh. Other datasheet information provided by manufacturer are reported in Thesis chapter 2. A total of 44 cylindrical Sony US18650V3 batteries have been tested in this work: half of them was new samples and the other half was spent batteries, previously used in e-bikes.

### 2.3 Experimental techniques

The experimental techniques used during this activity are described extensively in Thesis Chapter 2. Four main types can be distinguished:

- the **charge and discharge process** can be represented with a curve that relates the battery voltage and the state of charge. The voltage profile is affected by temperature and C-rate, as it depends on the battery available capacity. To avoid excessive degradation, to fully charge a battery, after a constant current (CC) phase until the upper voltage limit is reached, a constant voltage (CV) phase, where current decreases almost exponentially, is performed;

- the **incremental capacity (IC) and differential voltage (DV)** curves are defined as the partial derivative of capacity with respect to voltage and vice versa, respectively, where the voltage and the capacity data refer to a discharge at very low current. These curves are often used in the literature, interpreting the peaks characteristics (position, movement, intensity) to describe degradation as loss of cyclable ions and reduction of active material in the electrodes;

- the **relaxation test** allows to observe the voltage trend at open circuit condition after a charge or discharge. It is usually used to study the transient behaviour of the battery to reach equilibrium after a charge step (or charge pulse) or after a discharge and provides information on the lithium concentration in the electrolyte and in the solid, on the transport properties and on the electrodes' structure and chemistry [12]

- the **electrochemical impedance spectroscopy (EIS) test** are conducted superimposing a sinusoidal current with a certain frequency on a steady state condition and recording the voltage response. It is a helful measurement to get information of the battery behaviour: as each phenomenon inside the battery has a specific characteristic time, the different frequency ranges of the EIS test allow to solicit and distinguish those phenomena singularly.

### 2.4 Physical model description

The model used in this work is the Doyle-Fuller-Newman pseudo-two dimensional electrochemical model (P2D) [13], with the addition of a 2D thermal model for cylindrical battery, implemented on the commercial software COMSOL® (see Thesis chapter 2). It was adapted from the model developed in a previous thesis on the same research topic, where a different type of batteries was employed [14].
The battery is modeled with three main components: the negative electrode, the separator and the positive electrode. Each component contains a number of nodes, placed along the dimension $x$, forming a 1D mesh, in which the model computes the partial differential equations (PDEs). The nodes belonging to the electrodes domain represent the solid particles of the electrodes and they are modeled as spheres, thanks to the introduction of an additional radial dimension $r$: in additional nodes along this radius, the solid diffusion PDEs are computed. Hence, the model is named "pseudo-two-dimensional" because, even if two dimensions ($x$, $r$) are present, most of the PDEs of the model are solved only along $x$.
These PDEs are the material balance in the electrolyte and in the electrodes, the Bulter-Volmer electrochemical kinetics, the charge conservation in the electrolyte and in the electrode, and the double layer charge or discharge. For what concerns the thermal model, the heat conduction equation are solved numerically in the nodes of a 2D mesh, where the two coordinates are along the radius and the axis of the battery cylinder; each timestep, the temperature distribution is averaged and given as an input to the electrochemical model. Similarly, the volumetric heat generation, given by the sum of the ohmic, the reaction and the reversible heat generations, is computed in each node of the 1D electrochemical model, and it is averaged along the $x$ domain, as the thermal model only accepts a single volumetric heat generation term. The thermodynamic description of the model have been improved, working directly on the electrodes intercalation curve. To allow the simulation of aged batteries, three new parameters were introduced in the model, to account for the capacity reduction due to loss of lithium inventory with respect to the nominal capacity ($LLI$) and the percentage reduction of the amount of lithium active sites in the positive ($LAM_p$) and in the negative electrode ($LAM_n$). At BOL condition all these three parameters are equal to zero. A sensitivity analysis has been performed and discussed to understand the effects of these parameters' variation and to recognize these characteristics on the aged samples' curves (see thesis Chapter 3).

## 3. Parameters estimation methods

### 3.1 Kinetic parameters estimation

In a previous thesis on the same project, a PSO to calibrate some of the main battery parameters in the physical model was developed. In that context, a sensitivity analysis of the model parameters was carried out, to identify some operating conditions and measurements where the parameters showed the highest sensitivity value. That work resulted in the selection of 22 parameters of the P2D model and the identification of an experimental protocol, that consists in a set of five measurements performed at the operating conditions that guarantees the best compromise for the proper identification of the parameters. Therefore, the PSO algorithm has the aim to find the parameters that optimize a cost function, fitting the said experimental dataset. The solution space is given by the number of model parameters involved in the optimization and by the ranges in which these parameters are defined. As the simulation time of the standard PSO was really high, an adaptive version of the standard PSO algorithm has been implemented in order to improve the convergence process [15] (see Thesis Chapter 3). The cost function has been modified to favour the convergence and to account for each of the five experimental test properly. The experimental dataset for the fitting has been properly adapted, taking into account the differences between the batteries that are tested in this work with respect to the one used in the previous work. The proposed experimental procedure (see Figure 2) is the following:

1. the climate chamber is taken at 10°C and an EIS test is performed on the battery at 100% SOC, in the 4000-1 Hz range with 20 logarithmically spaced frequencies and two sinusoids per frequency (time employed: around 2 minutes);

2. the battery is then discharged at 2 C-rate with a depth of discharge (DOD) of 50%, registering both the cell

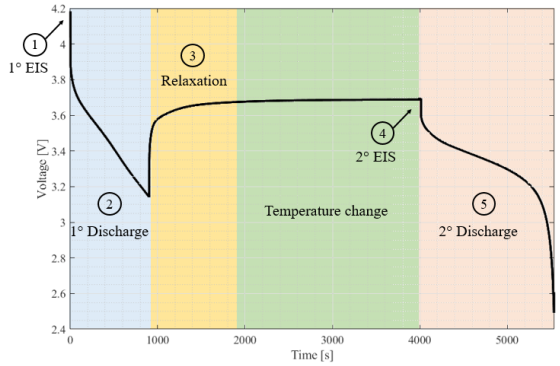


**Figure 2.** Scheme of the proposed experimental protocol, with the trend of the cell voltage in time.

voltage and the surface temperature (time employed: around 15 minutes);

3. a relaxation test of 1000s follows the discharge, measuring the voltage profile and the battery surface temperature;

4. the climate chamber temperature is set at 25°C and when the temperature is reached, after around 30 minutes, another EIS is carried out at 50% SOC and 25°C, with the same frequency range and spacing of the first one (time employed: around 2 minutes);

5. the battery is then discharged at 1 C-rate with theoretical DOD of 50%, practically until the lower voltage limit is reached (time employed: around 30 minutes).

### 3.2 Thermodynamic parameters estimation

With the methods discussed in the previous paragraph only a calibration of the pristine battery model is possible. It has already been specified that to account for degradation three thermodynamic parameters, namely $LLI$, $LAM_p$ and $LAM_n$ has been introduced in the model (see Thesis Chapter 3). For their calibration, another PSO algorithm has been developed. To distinguish between the two PSO algorithms, the one that has been previously described will be named "kinetic PSO", while the one that has just been introduced will be identified as "thermodynamic PSO". The cost function of the thermodynamic PSO is a weighted sum of the root-mean-square errors (RMSEs) between the derivative in time of the voltage profile of an experimental discharge of the aged battery at 0.1 C-rate and 25°C and the derivative of the voltage profile of the discharge simulated by the model at same condition, changing the three parameters. The algorithm has been validated, using four fictitious dataset in different conditions and proving that the solution is unique and stable.

### 3.3 Formulation of parameters estimation methodology

The progressive evolution of the battery parameters caused by the degradation can be useful to understand what aging mechanisms are behind the physical changes of the samples

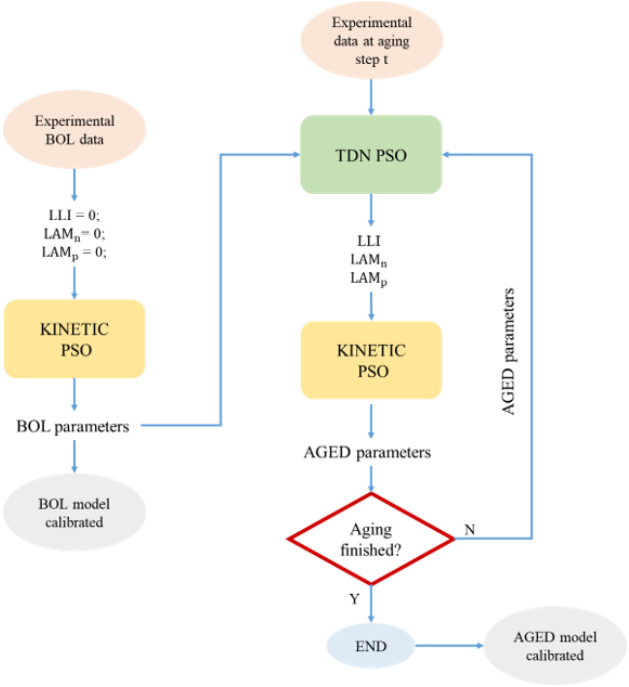


**Figure 3.** Flow chart of model calibration procedure for pristine and aged batteries.

behaviour. In this work, the batteries will be aged with controlled pathways that are expected to lead to predefined degradation phenomena: in this way, both the stressors of those phenomena and the effects on the physical parameters of the battery will be investigated and linked. In order to do so, the model parameters will be calibrated at different aging stages, throughout the aging campaign, combining together the kinetic PSO and the thermodynamic PSO for the estimation of the model parameters. The calibration involves only an already defined set of parameters (22 kinetics at BOL and 3 thermodynamic parameters), while the geometric and the remaining battery parameters are considered constants.

The proposed methodology for the calibration (see Figure 3) consists of:

- **BOL model calibration**: since the begin of life (BOL) thermodynamic parameters $LLI$, $LAM_p$ and $LAM_n$ are equal to zero, only the kinetic PSO has to calibrate the 22 physical parameters through the fitting process that compares the simulated results with the experimental dataset, that includes the five experimental tests described before;

- **model calibration at aging step t**: the 22 parameters of the electrochemical model optimized for the pristine cell are set in the model. Only 14 of them will be considered to vary with the aging (Thesis Chapter 3). Two progressive steps are needed for the calibration of the aged battery model:

  - **thermodynamic parameters calibration** : $LLI$,

$LAM_p$ and $LAM_n$ are calibrated with the thermodynamic PSO, and then, are set into the model.

– **kinetic parameters calibration**: the 14 kinetic PSO calibrates the physical parameters of the battery that may be subject to degradation.

To calibrate the model at the aging step t+1, the parameters obtained at step t are used to limit the possible variation of the parameters for the t+1 aging stage, since some parameters are expected to have a monotonic trend with the degradation. The flow diagram in Figure 3 shows the parameters calibration process. The samples will have to be tested at each aging stage, with a diagnostic procedure that provides the experimental dataset both for the fitting of the kinetic PSO (5 tests of the experimental protocol) and of the thermodynamic PSO (full discharge at 25°C and 0.1C).

## 4. Degradation phenomena analysis and aging campaign settings

### 4.1 SEI growth

The growth of SEI is a well-studied degradation mechanism in the literature. The solid electrolyte interphase (SEI) is a thin layer that is inevitably generated from the decomposition of the electrolyte, that is unstable at low potentials, and therefore, it reduces when the first charge of the first cycle is performed [16]. The SEI layer passivates on the anode surface, preventing it from further unwanted parasitic reactions with the electrolyte, that would continuously occur without the protection of the SEI [17]. However, the SEI is actually usually chemically heterogeneous and unstable, leading to continuous degradation of the electrolyte and the interphase itself during repeated cycles or long-term storage. Moreover, it is also mechanically fragile, resulting in fractures that will repair through further reactions with the electrolyte and lead to the formation of a porous and thickened SEI, that increases the battery internal resistance and extends the lithium-ion transport path [11], [18].

At high temperatures, the SEI dissolution process and the adverse electrolyte decomposition reactions, whose products may attack the SEI, leading to severe SEI decomposition reactions are accentuated [19], [20]. This leads to the alternation between breakage and regeneration phases, that causes the growth of thick and more resistive SEI layer. The SEI growth phenomenon leads to relevant capacity loss for battery cycled or stored at elevated temperatures [21]. Moreover, as SEI develops, it may reach the electrode pores, reducing the availability of active sites with time [22].
By coupling high temperatures with high SOC storage, an acceleration of the degradation is observed. In fact, as the SOC increases, parasitic reactions are promoted.

Calendar aging at 60°C has been selected to be the condition to stress the SEI growth. Four batteries have been stored for eight weeks at four different SOCs, as reported in Table 1 to investigate the storage SOC effect.

| **Calendar aging conditions** | |
|---|---|
| Temperature | SOC |
| 60°C | 100% |
| | 80% |
| | 50% |
| | 10% |

**Table 1.** Calendar aging conditions

### 4.2 Lithium plating

Lithium plating consists in the deposition of metallic lithium on the negative electrode particles surface. It may results in lithium dendrites formation, that growing across the separator could bring to short circuit. Lithium plating verifies mainly for two reasons, during charge process:

- if the rate of lithium ions transport in the electrolyte is faster than the intercalation rate in the graphite [23], as the negative electrode particles gets saturated;
- when the graphite potential is below 0V vs. $Li/Li^+$, because the lithium plating reaction is promoted, competing with the lithium intercalation reaction, resulting in a characteristic mixed potential [24], formed by the superposition of the potential of the intercalated lithium-ions and the lithium metal that has been deposited on the electrode surface [12].

Evidences have been found in the literature regarding the detection of a particular plateau in the voltage profile of the relaxation after charging at low temperatures [25], [26]: this is attributed to stripping of the deposited lithium metal, indicating that the lithium was plated during the previous charge [27]. It is possible to distinguish between [28]:

- **reversible lithium plating**: it is the deposited lithium with durable electric contact with the anode, thus, it is stripped in the discharge step, not resulting in any capacity loss;
- **irreversible lithium plating**: as this plated lithium shows only fragile electrical contact with the graphite, it may become electrically isolated from the negative electrode during the stripping process. This “dead” lithium is the cause of capacity losses due to charging at plating conditions.

Plotting the derivative of the voltage over time (dV/dt), and viceversa, the derivative of time over voltage (dt/dV), peaks can be identified: the time value that corresponds to the peak position in the dV/dt curve represents the point in time where the decay of the mixed potential merges into residual cell relaxation; the voltage related to the peak in the dt/dV plot can be attributed to the depletion of the mixed potential [12].

To investigate the stressors of the lithium plating phenomena a dedicated experimental campaign has been carried

out, analyzing the relaxation profiles after current pulses performed at the four conditions described in Table 2, at -10°C, -5°C, 0°C, 5°C. In Figure 4 are reported the voltage profile

| Current pulses | | | | |
|---|---|---|---|---|
| Type | **1** | **2** | **3** | **4** |
| $SOC_i$ | 50% | 50% | 30% | 30% |
| DOC | 30% | 30% | 30% | 50% |
| C-rate charge | 1 | 0.5 | 1 | 1 |

**Table 2.** Current pulses campaign conditions ($SOC_i$: initial state of charge, DOC: depth of charge)

during relaxation after the four type of current pulses at -10°C. On the right, the dV/dt curves are depicted, showing the characteristic peak just described. From the comparison

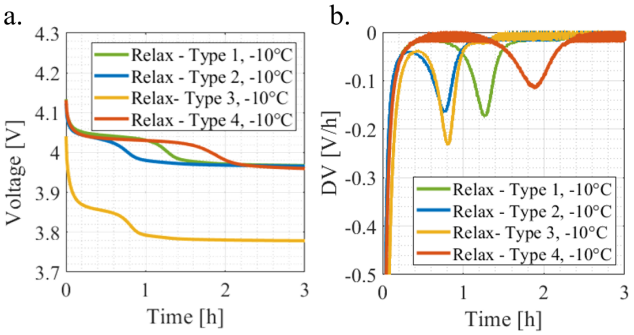


**Figure 4.** a. Voltage profile and b. dV/dt profile during relax after charge in different conditions at -10°C.

of conditions that differs only by one variable, the operative conditions effects can be assumed:

- **current effect**: a higher amount of metallic lithium is plated during charges [29] at higher current, as a longer time is needed to the depletion of the mixed potential (see green and blue curves of Figure 4);
- **$SOC_i$ effect**: starting from a lower initial SOC, with the same DOC, results to be less stressing, thanks to the fact that the graphite is less lithiated at those SOCs (see yellow and green curves of Figure 4);
- **DOC effect**: higher DOC results in an increase of the charging time and also an increase of the time for the depletion of the mixed potential (see yellow and red curves of Figure 4).

The lithium plating/stripping reactions have been implemented in the physical model to describe reversible lithium deposition during charge at plating condition. A sensitivity analysis, taking as base case the pulse type 4 of Table 2, has been simulated by varying one parameter at a time within temperature, current, $SOC_i$ and DOC has been simulated. Four values for each parameters has been investigated (for the complete description, see Thesis Chapter 4). The results showed that the model is able to reproduce the main features of the experimental tests, confirming the trends just listed, and it is helpful to understand the mechanisms inside the battery, providing information on the lithium concentration during the charge and relaxation processes at the electrode-separator interface (see Thesis chapter 4). For brevity, only the sensitivity on temperature is reported: the lithium concentration profile at the electrode close to the separator, during both charge and relaxation can be seen in Figure 5. The pulses are simulated at current pulse type 1 conditions, for temperature values equal to -10°C, -5°C, 0°C, 10°C.

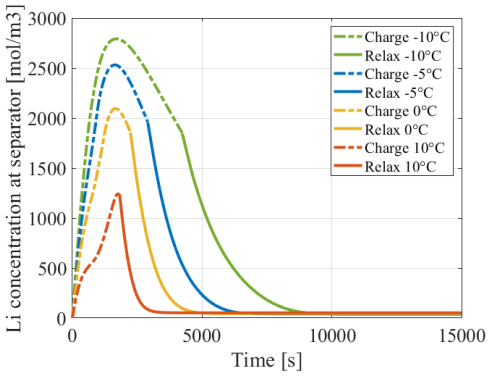


**Figure 5.** Lithium concentration at the separator.

**Temperature effect**: the model confirms that lower temperatures promote lithium plating, as a higher lithium concentration is observed during charge at -10°C (green line in Figure 5.

On the basis of the results of the low temperature current pulses campaign, the conditions listed in Table 3 have been selected: temperature, charging current, $SOC_i$ and DOC effects will be investigated and analyzed. Cycle conditions A, B, C and D will be performed both at 0°C on four pristine samples, and at -10°C, on four other pristine samples.

| Cycles | | | | |
|---|---|---|---|---|
| Cycle | A | B | C | D |
| $SOC_i$ | 50% | 50% | 30% | 30% |
| DOC | 30% | 30% | 30% | 50% |
| C-rate charge | 1 | 0.5 | 1 | 1 |
| C-rate discharge | 0.2 | 0.2 | 0.2 | 0.2 |

**Table 3.** Cycle aging conditions

To monitor the degradation, a uniform diagnostic procedure have been performed once every two weeks for the calendar aged samples, and once every 3 equivalent full cycles (EFC) fot the cycle aged samples. It is comprehensive of the experimental protocol for the calibration of the parameters of the kinetic PSO and the discharge at 25°C and 0.1C-rate necessary for the calibration of the thermodynamic PSO parameters. The slow discharge may take about 10 hours to be completed: this is still an elaboration phase, but the final

diagnostic method, in future developments, will aim to not include such a time-consuming test.

## 5. Degradation campaign

### 5.1 Calendar aging

The samples have been stored for eight weeks. In Figure 6 the capacity losses induced by the calendar operating conditions are reported for the four tested samples. It can be noticed that the storage SOC has a strong impact on degradation: the sample that was stored at SOC 10% shows basically no degradation, as only a 1% of the initial capacity has been lost, while the storage at 80% and 100% SOC is the most detrimental condition. In Figure 7 the IC and DV curves of the sample

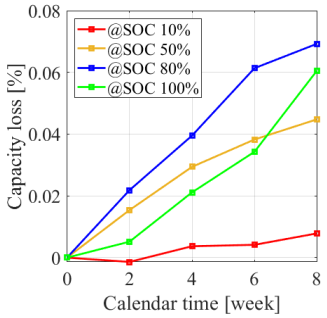


**Figure 6.** Capacity loss during calendar.

stored at 80% can be observed at different calendar time. It

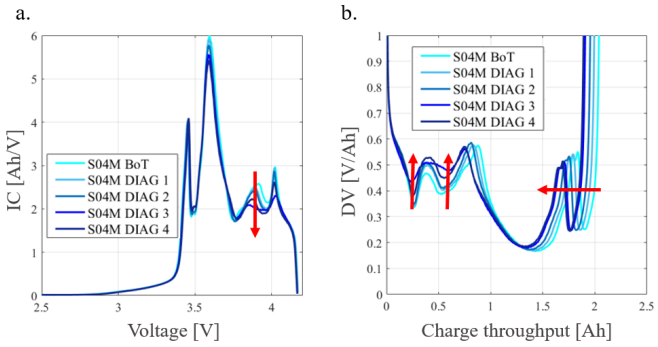


**Figure 7.** a. IC and b. DV curves of the sample stored at 80% SOC, throughout the aging campaign. (BoT: begin of test, DIAG n: 2·n weeks of calendar)

can be inferred that the main degradation modes involved in the aging are $LAM_p$ and $LLI$. The loss of lithium inventory is visible from the progressive shift of the graphite peak at high SOC, due to the electrodes' slippage that reduces the operating SOC window of the electrodes intercalation curves. The most plausible reasons for this loss of lithium inventory are SEI growth and electrolyte decomposition, that are enhanced in these operative conditions. Additionally, $LAM_p$ increase with time can be inferred by the fact that the low SOC peaks of the IC curves are basically located in the same position, seeing only a variation of their intensity, especially a decrease of the high SOC peak. Hence, the superposition of the effects of these two parameters may be able to justify the aging trend.

It is interesting to notice that a localized degradation effect is visible in the SOC range at which the battery was stored. This localized effect has been encountered in all the samples and may be ascribed to the combined effect of $LAM_p$ and $LLI$, since the electrode balancing cause a shift in the graphite peak. Calibrating the thermodynamic parameters at the end of the eight calendar weeks on the sample stored at 80% SOC, 11.7% of $LLI$ and 6.4% of $LAM$ were observed, confirm the hypothesis made in the IC-DV curves' analysis.

### 5.2 Cycle aging

The cycle aging operating conditions described in Table 3 have been applied on eight different pristine samples, four cycling at 0°C and the others at -10°C. The samples have been tested with the check-up procedure once every 3 EFCs, until 12 EFCs were reached. The capacity loss have been tracked for all the samples and it is reported on the left plot of Figure 8. Same colors are applied for samples that operated at same

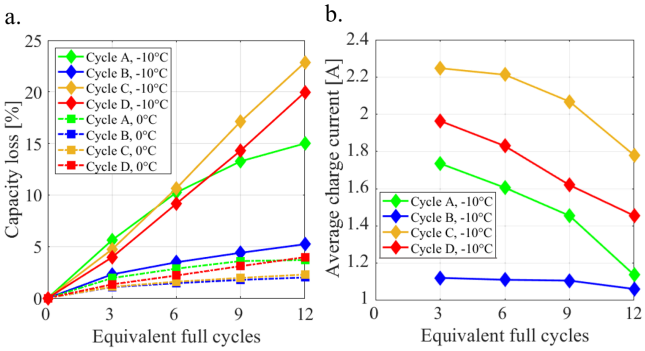


**Figure 8.** a. Capacity loss in time; b. average current

cycle conditions, except from the temperature, that is instead distinguished by a different marker shape and a different lines' style.

The results in terms of the capacity loss trend are reported:

- the batteries that cycled at -10°C show higher capacity loss with respect to the ones that operated at 0°C: this is consistent with the lithium plating stressors analysis, since at 0°C plating is not strongly promoted, but more relevant for current pulses operating in cycle A and D, that, in fact, shows the highest capacity losses between the four samples cycling at 0°C;
- the charging current affects in a relevant way the capacity loss: cycles B shows the lowest degradation compared to the other cycle conditions at the same temperatures;
- within the samples cycled at -10°C the most detrimental operating condition is the one of cycle C: this can be explained by the average charge current trend during the cycles (Figure 8b). The trend is decreasing for all the samples since, with degradation, part of the capacity gets lost and hence, the CV charge step, where the current decreases exponentially increase at each aging

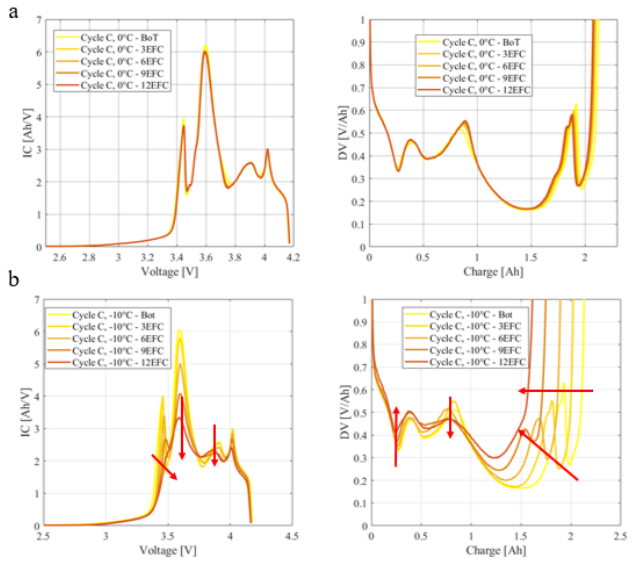


**Figure 9.** a. IC and DV curve of sample operating in Cycle C at a. 0°C and b. at -10°C.

stage. In these conditions, a slow lithium deposition occurs, with a "mossy" structure characterized by fine, fragile and more prone to electrical isolation dendrites, favouring the formation of dead lithium, and therefore, an increase of the capacity losses. On the other hand, a too long CV phase results in the so called "chemical intercalation": the plated lithium is able to intercalate into graphite, given sufficient time at high SOC [24], [30];

- low $SOC_i$ (cycle C and D) have a similar trend, but the higher DOC results in longer CV phases since the first aging step, probably resulting in chemical intercalation of lithium. Hence, the capacity losses are higher for cycle C.

The IC and DV curves' trends of the samples aged with cycle C at 0°C and -10°C are reported in Figure 9. Comparing the plots it is evident the temperature effect. From Figure 9.a it is difficult to make hypothesis on the degradation modes, while looking at 9.b, it can be inferred that *LLI* is the dominant degradation mode. On the DV curve, the low SOC peak usually attributed to the graphite shifts to the left, as a consequence of the electrode slippage caused by the reduction of lithium concentration in the electrodes. Moreover *LAM* also seems to be present, as the low SOC peaks of both the IC curve and DV curves fade away with degradation, as a probable shrinkage of the electrodes intercalation curve may exclude that portion of the graphite intercalation curve from operation. In general, *LAM* is observed as a simultaneous capacity loss in all the curve regions. The operation with high current at low temperatures may cause *LAM* due to continuous volume stresses. Persistent plating and stripping, and the surface film formation on the anode particles result in volume changes in the electrode structure which lead to contact losses due to binder breaking and particle cracking. Active material particles are likely to become electrically isolated if the electrode host material is not able to accept the volume stress created by the persistent plating (during charge) and by the dissolution of metallic lithium (during discharge).

### 5.3 BOL and AGED calibration

The methodology proposed in 3.3 was applied to calibrate the model for one of the samples, at its begin of life condition and at all the aging steps throughout the aging campaign. The sample selected was the one operating in cycle A at -10°C. The results obtained from the fitting of the discharge at 0.1C and 25°C, that is used for the optimization of the thermodynamic parameters *LLI*, $LAM_p$ and $LAM_n$ can be seen in Figure 10. The methodology applied for the calibration of

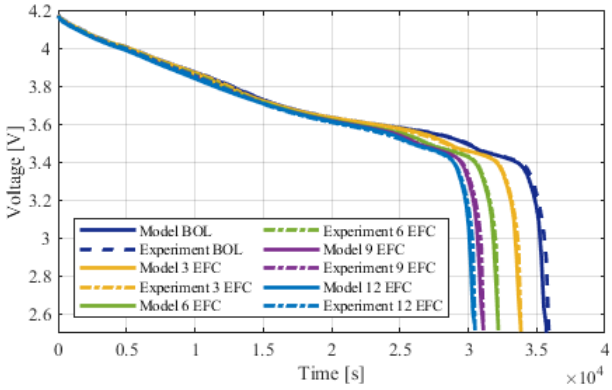


**Figure 10.** Discharges at 0.1C, 25°C at different aging stages

| Aging stage | LLI | LAMp | LAMn | RMSE |
|---|---|---|---|---|
| BOL | 0 | 0 | 0 | 41.5 mV |
| 3 EFC | 0.0503 | 0 | 0.0001 | 22.4 mV |
| 6 EFC | 0.0982 | 0.0055 | 0.0038 | 18.7 mV |
| 9 EFC | 0.1344 | 0.0109 | 0.0423 | 30.0 mV |
| 12 EFC | 0.1492 | 0.0036 | 0.0505 | 32.1mV |

**Table 4.** Thermodynamic parameters calibration

the thermodynamic parameters shows good results, as even for advanced degradation stages the curves are fitted in a satisfactory way. The *LLI*, $LAM_p$ and $LAM_n$ estimation are reported in Table 4, along with the RMSEs computed between the experimental and simulated discharges of the previous figure. The main degradation mode is the loss of lithium inventory, that reaches 14% at 12 EFC. Lithium plating, in fact causes an irreversible loss of cyclable lithium, affecting the capacity balance of the electrodes [31], [32]. Moreover, $LAM_n$ is also present: this is probably due to electrical isolation of the active particles or particle cracking that occurs as a result of volume changes during cycling [33].

The output of the fitting of the five experimental tests to obtain the calibration of the kinetic parameters, for all the aging stages, are reported in Figures 11 - 15. In Table 5 the

results in terms of RMSEs of all the fitting in the different aging stages are reported. In the literature concerning estimation

| RMSEs | Aging stages | | | | |
|---|---|---|---|---|---|
| | **BOL** | **3 EFC** | **6 EFC** | **9 EFC** | **12 EFC** |
| EIS1 [mΩ] | 2.32<br>2.28 | 2.11<br>2.48 | 2.44<br>2.52 | 3.01<br>3.04 | 2.48<br>2.60 |
| Discharge1 [mV] | 21.6 | 20.3 | 22.3 | 31.1 | 28.5 |
| Relaxation [mV] | 21.9 | 27.3 | 48.5 | 67.6 | 38.4 |
| EIS2 [mΩ] | 1.60<br>2.01 | 1.66<br>2.06 | 1.88<br>2.06 | 1.70<br>2.09 | 2.45<br>2.16 |
| Discharge2 [mV] | 8.2 | 23.6 | 30.8 | 31.6 | 35.1 |

**Table 5.** RMSEs between experimental and simulated data for the calibration throughout the aging stages.

of parameters made with a physical P2D model, the reported root-mean-square errors are mainly related to capacity tests or to driving cycles profiles. Moreover, no RMSEs calculation were found related to aged batteries. However, the results obtained in the BOL conditions, are comparable with the values present in the literature (see Thesis chapter 4).

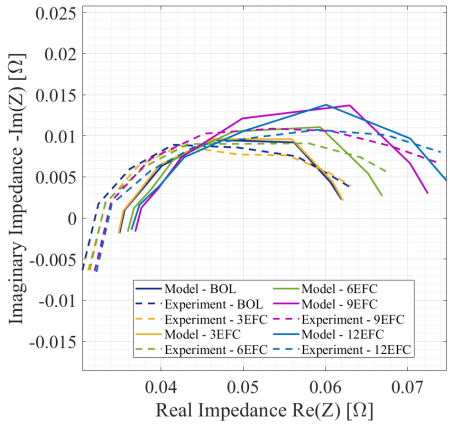


**Figure 11.** EIS1: Impedance spectrum at 10°C, 100% SOC.

- The values reported in table 5 shows similar values of RMSEs for the EIS tests: from Figure 11 and Figure 12 it is visible how the model is not able to set the right high frequency resistance (HFR) value, and as it has to optimize the error of both the tests, it finds a compromise. This aspect may be improved by selecting a ionic conductivity correlation with temperature that better reproduce the experimental behaviour.
- The discharges tests in Figure 13 and Figure 14 shows a good accordance between experimental and simulated voltage profiles. A criticality can be identified in the first section of the two discharges, as the model has a steeper slope in these parts. To improve even more the fitting, additional weight can be given to those points when computing the cost function in the data fitting algorithm. The RMSEs are quite low and comparable between the different aging stages, testifying the good quality of the fitting.

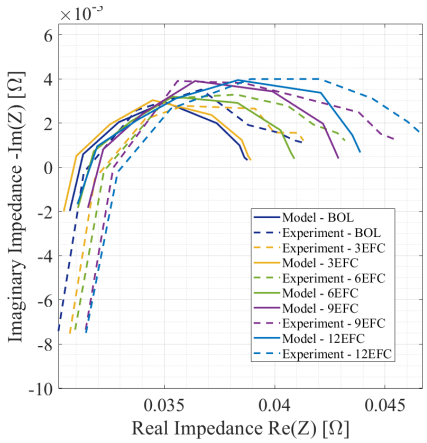


**Figure 12.** EIS2: Impedance spectrum at 25°C, 50% SOC.

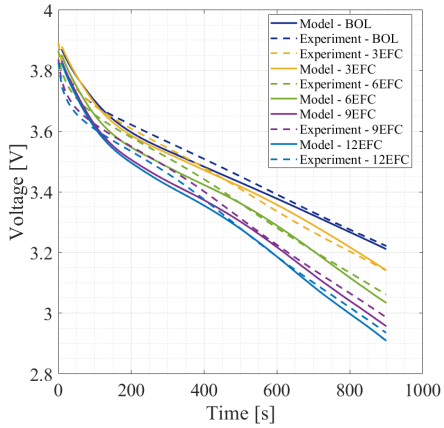


**Figure 13.** Discharge1: at 2C, 10°C, 100-50% SOC.

- The relaxation profile, in Figure 15 shows that the model presents, for all the aging stages, a quite different trend. In fact, the highest RMSEs values are related to this case. As stated in the first point, the ionic conductivity is probably not calibrated properly: since the diffusivity is related to that parameter, that could be a factor that influences negatively the relaxation fitting. To make sure that the behaviour is well reproduced, and therefore, the parameters characterizing the relaxation profile are estimated properly, their calibration could be performed dedicatedly, or an optimization on the derivative of voltage in time could be added to provide additional importance to this test.

In addition to this calibration, a validation on a larger dataset has been performed at BOL (Thesis Chapter 4) and 12 EFCs (Thesis Chapter 5).

The kinetic parameters have been tracked during the aging campaign. At each aging step, the calibration of these parameters was obtained from the kinetic PSO data fitting algorithm. Some of the parameters can be considered as “low sensitive” as also a quite relevant variation, do not affect the

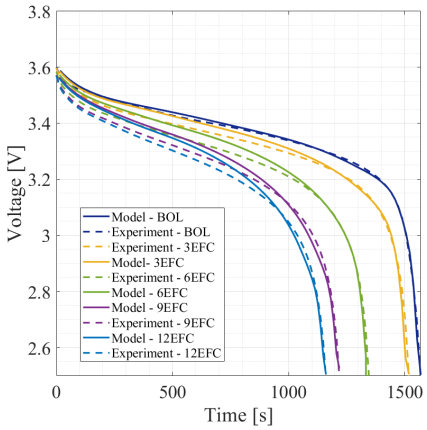


**Figure 14.** Discharge2: at 1C, 25°C, 50-0% SOC.

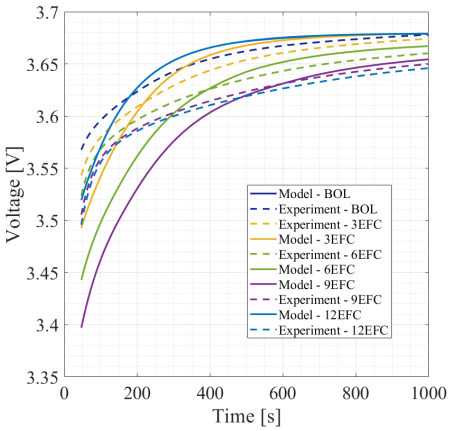


**Figure 15.** Relaxation: 2C, 10°C, 100 -50% SOC.

cell behaviour noticeably. This is the case of the diffusion coefficients, that vary in an uncontrolled manner while more sensitive parameters are calibrated. To overcome this problem, it would be useful to perform a calibration of these and the other low sensitive parameter, keeping fixed the high sensitive parameters once they have been estimated.

From the analysis of the physical parameters trend, a decrease of the negative electrode particles' radius and of its kinetic rate constant is observed, suggesting a degradation of the negative electrode properties and possible particle cracking. It can be observed that the radius of the negative electrode particles reduces significantly with the aging, while the positive electrode particles' radius remains almost constant. The kinetic rate constant of the two electrodes are both decreasing, but the one related to the anode decreases more and with a stronger trend, giving evidence of a heavier degradation related to the graphite electrode. This suggests a degradation of the properties of the graphite anode, probably linked to particle cracking that is likely to verify with cycling at low temperatures [33].

## Conclusion

Thanks to the development and the application of an innovative methodology for the estimation of the physical parameters of a LIB, the model calibration at begin of life and throughout the aging campaign has been performed. To achieve this result, the kinetic parameters and the thermodynamic parameters calibration methods, that exploit data fitting algorithms, have been combined together. To validate the proposed calibration methodology, two different degradation phenomena, namely SEI growth and lithium plating, have been investigated in an experimental aging campaign. Calendar aging at 60°C and four different SOCs has been selected as operating conditions to stress SEI growth. To investigate the stressors of lithium plating, the voltage profile during relaxation after charging at low temperatures have been studied, as it is recognized to indicate that lithium has plated in the previous charge. The lithium stripping-plating reactions have been also implemented in the physical model. Cycling at four different operating conditions and at two low temperatures (0°C and -10°C) have been selected to be the conditions stressing lithium plating. The experimental results of the aging campaign have been analyzed. Capacity losses trend and degradation modes have been assessed thanks to IC/DV analysis: *LLI* and $LAM_p$ have been observed on the more degraded samples aged through calendar, while on the samples that cycled at low temperatures *LLI* and $LAM_n$ were detected. The proposed methodology for the calibration of aged samples have been performed on one of the samples that cycled at plating conditions at -10°C, obtaining positive results in terms of RMSEs. The thermodynamic and the main kinetic parameters' trends have confirmed the presence of lithium plating and suggests particle cracking on the graphite electrode.
The proposed methodology has shown promising results, proving to be a powerful tool both for a comprehensive battery characterization and for the degradation description. The main follow up activities suggested are listed:

- due to lack of time, the complete calibration, applying the methodology, has been performed only for one sample (cycle A, -10°C). Applying the methodology to other samples would strengthen the validity of the methodology and the degradation interpretation;
- a slow discharge at 0.1C-rate (duration of about 10 hours) is necessary to calibrate the model, in the proposed methodology: this compromise have been accepted as this is still a development phase, but the final diagnostic method aims to not include such a time-consuming test;
- in the application of the methodology, 14 kinetic parameters were varied with the aging: the choice has been explained in Thesis Chapter 3, but changing the set of parameters to be optimized can be interesting, also to analyze separately the "low sensitive" parameters, once the "high sensitive" ones have been calibrated.

## References


[1] John T Warner. The handbook of lithium-ion battery pack design: Chemistry, components, types and terminology. May 2015.

[2] Ralph J. Brodd Masaki Yoshio and Akiya Kozawa, editors. *Lithium-Ion Batteries*. Springer New York, 2009.

[3] Michael Woodward Bryn Walton Jamie Hamilton. Electric vehicles, setting a course for 2030. 02/03/2021.

[4] Usabc electric vehicle battery test procedures manual. revision 2. 1 1996.

[5] Lluc Canals Casals, B. Amante García, and Camille Canal. Second life batteries lifespan: Rest of useful life and environmental analysis. *Journal of Environmental Management*, 232:354–363, 2019.

[6] Andreas Podias, Andreas Pfrang, Franco Di Persio, Akos Kriston, Silvia Bobba, Fabrice Mathieux, Maarten Messagie, and Lois Boon-Brett. Sustainability assessment of second use applications of automotive batteries: Ageing of li-ion battery cells in automotive and grid-scale applications. *World Electric Vehicle Journal*, 9(2):24, July 2018.

[7] Jianan Zhang, Lei Zhang, Fengchun Sun, and Zhenpo Wang. An overview on thermal safety issues of lithium-ion batteries for electric vehicle application. *IEEE Access*, PP:1–1, 05 2018.

[8] Christoph R. Birkl, Matthew R. Roberts, Euan McTurk, Peter G. Bruce, and David A. Howey. Degradation diagnostics for lithium ion cells. *Journal of Power Sources*, 341:373–386, 2017.

[9] She huang Wu and Po-Han Lee. Storage fading of a commercial 18650 cell comprised with nmc/lmo cathode and graphite anode. *Journal of Power Sources*, 349:27–36, 2017.

[10] Matthieu Dubarry, Cyril Truchot, and Bor Yann Liaw. Synthesize battery degradation modes via a diagnostic and prognostic model. *Journal of Power Sources*, 219:204–216, 2012.

[11] Rui Xiong, Yue Pan, Weixiang Shen, Hailong Li, and Fengchun Sun. Lithium-ion battery aging mechanisms and diagnosis method for automotive applications: Recent advances and perspectives. *Renewable and Sustainable Energy Reviews*, 131:110048, 2020.

[12] Stefan Schindler, Marius Bauer, Mathias Petzl, and Michael A. Danzer. Voltage relaxation and impedance spectroscopy as in-operando methods for the detection of lithium plating on graphitic anodes in commercial lithium-ion cells. *Journal of Power Sources*, 304:170–180, 2016.

[13] John Newman and Karen E Thomas-Alyea. Electrochemical systems. 2012.

[14] Alessandro Innocenti. An innovative methodology to estimate the parameters of a lithium battery physical model. apr 2020.

[15] Z. Zhan, J. Zhang, Y. Li, and H. S. Chung. Adaptive particle swarm optimization. *IEEE Transactions on Systems, Man, and Cybernetics, Part B (Cybernetics)*, 39(6):1362–1381, 2009.

[16] Jun-Fan Ding, Rui Xu, Chong Yan, Bo-Quan Li, Hong Yuan, and Jia-Qi Huang. A review on the failure and regulation of solid electrolyte interphase in lithium batteries. *Journal of Energy Chemistry*, 59:306–319, 2021.

[17] Satu Kristiina Heiskanen, Jongjung Kim, and Brett L. Lucht. Generation and evolution of the solid electrolyte interphase of lithium-ion batteries. *Joule*, 3(10):2322–2333, 2019.

[18] Siqi Shi, Peng Lu, Zhongyi Liu, Yue Qi, Louis G. Hector, Hong Li, and Stephen J. Harris. Direct calculation of li-ion transport in the solid electrolyte interphase. *Journal of the American Chemical Society*, 134(37):15476–15487, 2012.

[19] Christopher L. Campion, Wentao Li, and Brett L. Lucht. Thermal decomposition of LiPF[sub 6]-based electrolytes for lithium-ion batteries. *Journal of The Electrochemical Society*, 152(12):A2327, 2005.

[20] E. Peled and S. Menkin. Review SEI: Past, present and future. *Journal of The Electrochemical Society*, 164(7):A1703–A1719, 2017.

[21] D.P Abraham, J Liu, C.H Chen, Y.E Hyung, M Stoll, N Elsen, S MacLaren, R Twesten, R Haasch, E Sammann, I Petrov, K Amine, and G Henriksen. Diagnosis of power fade mechanisms in high-power lithium-ion cells. *Journal of Power Sources*, 119-121:511–516, 2003. Selected papers presented at the 11th International Meeting on Lithium Batteries.

[22] Anthony Barré, Benjamin Deguilhem, Sébastien Grolleau, Mathias Gérard, Frédéric Suard, and Delphine Riu. A review on lithium-ion battery ageing mechanisms and estimations for automotive applications. *Journal of Power Sources*, 241:680–689, 2013.

[23] JE Harlow, SL Glazier, Jing Li, and JR Dahn. Use of asymmetric average charge-and average discharge-voltages as an indicator of the onset of unwanted lithium deposition in lithium-ion cells. *Journal of The Electrochemical Society*, 165(16):A3595, 2018.

[24] Nathalie Legrand, Bernard Knosp, Philippe Desprez, François Lapicque, and Stéphane Raël. Physical characterization of the charging process of a li-ion battery and prediction of li plating by electrochemical modelling. *Journal of Power Sources*, 245:208–216, 2014.

[25] Mathias Petzl and Michael A. Danzer. Nondestructive detection, characterization, and quantification of lithium

plating in commercial lithium-ion batteries. *Journal of Power Sources*, 254:80–87, 2014.

[26] Marius Bauer, Bernhard Rieger, Stefan Schindler, Peter Keil, Mario Wachtler, Michael A. Danzer, and Andreas Jossen. Multi-phase formation induced by kinetic limitations in graphite-based lithium-ion cells: Analyzing the effects on dilation and voltage response. *Journal of Energy Storage*, 10:1–10, 2017.

[27] Johannes Wandt, Peter Jakes, Josef Granwehr, Rüdiger-A. Eichel, and Hubert A. Gasteiger. Quantitative and time-resolved detection of lithium plating on graphite anodes in lithium ion batteries. *Materials Today*, 21(3):231–240, 2018.

[28] Xiao-Guang Yang, Shanhai Ge, Teng Liu, Yongjun Leng, and Chao-Yang Wang. A look into the voltage plateau signal for detection and quantification of lithium plating in lithium-ion cells. *Journal of Power Sources*, 395:251–261, 2018.

[29] Christian von Lüders, Veronika Zinth, Simon V. Erhard, Patrick J. Osswald, Michael Hofmann, Ralph Gilles, and Andreas Jossen. Lithium plating in lithium-ion batteries investigated by voltage relaxation and in situ neutron diffraction. *Journal of Power Sources*, 342:17–23, 2017.

[30] M. C. Smart and B. V. Ratnakumar. Effects of electrolyte composition on lithium plating in lithium-ion cells. *Journal of The Electrochemical Society*, 158(4):A379, 2011.

[31] Hao Ge, Tetsuya Aoki, Nobuhisa Ikeda, Sohei Suga, Takuma Isobe, Zhe Li, Yuichiro Tabuchi, and Jianbo Zhang. Investigating lithium plating in lithium-ion batteries at low temperatures using electrochemical model with NMR assisted parameterization. *Journal of The Electrochemical Society*, 164(6):A1050–A1060, 2017.

[32] Yongjun Leng, Shanhai Ge, Dan Marple, Xiao-Guang Yang, Christoph Bauer, Peter Lamp, and Chao-Yang Wang. Electrochemical cycle-life characterization of high energy lithium-ion cells with thick li(ni0.6mn0.2co0.2)o2and graphite electrodes. *Journal of The Electrochemical Society*, 164(6):A1037–A1049, 2017.

[33] Kenji Takahashi and Venkat Srinivasan. Examination of graphite particle cracking as a failure mode in lithium-ion batteries: A model-experimental study. *Journal of The Electrochemical Society*, 162(4):A635–A645, 2015.

# Ringraziamenti

Ringrazio tutte le persone che mi hanno supportata in questi anni e che hanno contribuito a raggiungere questo traguardo.

Ci tengo a ringraziare tutto il personale del MRT Fuel Cell & Battery Lab, in particolare il professor Andrea Casalegno, il professor Claudio Rabissi e il dottorando Gabriele Sordi che hanno permesso la realizzazione di questa tesi. Grazie per avermi guidata e consigliata nell'attività.

Ringrazio tutti gli amici, quelli di Verona e quelli di Milano. Grazie a Elena, Chiara e Noemi per le serate spensierate e per il sostegno nei periodi difficili. Grazie a Perri, per i momenti di studio e di svago di questi cinque anni. Ringrazio Luca, Arianna, Vanessa e Anna che ho sempre sentito vicini, nonostante la distanza.

Ringrazio i miei nonni Sandra, Fiorbellino e Henryka e la mia famiglia, Arianna, Mariusz, Alice e Rebecca per non avermi mai fatto mancare sostegno e affetto in tutti questi anni. Grazie anche a Matteo, per rendere i miei problemi piccoli e i miei sogni grandi.

# Abstract

The electric vehicles (EVs) market is fundamental for the decarbonization of the transport sector. Since it is already growing and it is expected to expand further in the next future, an increasing number of spent lithium-ion batteries (LIBs) will have to be managed. These batteries could be repurposed and adopted in less demanding applications for the rest of their residual life. Therefore, it is fundamental to study the effects of the aging and how the degradation phenomena affect the battery performance. This work aims to develop a non-destructive innovative method, that allows to investigate the aging phenomena related to lithium-ion batteries, detecting their presence through key physical parameters, obtained from a limited set of easily acquired experimental data.

The first activity consists in the adaptation and improvement of the pre-existent tools, namely a LIB battery model, a data-fitting algorithm (Particle Swarm Optimization) that allows the calibration of the physical model for a pristine cell, and an experimental protocol that provide the data on which the fitting is based.

The second activity is the implementation of a methodology that allows the physical model calibration, also for the case of an aged battery. To account for the battery degradation, three parameters related to the degradation modes are introduced in the model, and an additional dedicated PSO algorithm is implemented for the parameters calibration. The methodology, therefore, exploits the coupling of two PSO algorithms that collaborate in the calibration of the aged battery model.

The third activity involved the investigation of the stressors governing two specific degradation mechanisms, namely solid electrolyte interphase (SEI) growth and lithium plating. Thanks to these acknowledgments, an experimental aging campaign is carried out: calendar aging at high temperature for eight weeks and cycle aging at plating conditions are performed and analyzed.

Finally, the methodology is tested and validated, calibrating the parameters of one of the samples cycled at lithium plating condition, throughout the aging campaign.

**Keywords:** lithium-ion batteries, degradation, lithium plating, physical model, methodology

# Sommario

Poiché il mercato dei veicoli elettrici è in costante aumento, un numero crescente di batterie a ioni di litio usate dovrà essere gestito. Queste batterie potrebbero trovare un secondo impiego in applicazioni meno impegnative, per il resto della loro vita utile. Perciò, lo studio degli effetti dell'invecchiamento e la comprensione di come i questi fenomeni influiscono sulle performance della batteria risultano fondamentali. Questo lavoro mira allo sviluppo di un metodo innovativo che permetta di indagare alcuni fenomeni di degradazione, rilevandone la presenza attraverso l'interpretazione di alcuni parametri fisici chiave, ottenibili da un limitato set di dati sperimentali.

La prima attività consiste nell'applicazione e nel miglioramento di metodi preesistenti, che comprendono un modello fisico della batteria, un algoritmo di data-fitting (Particle Swarm Optimization - PSO) che permette la calibrazione del modello fisico per una batteria nuova, e un protocollo sperimentale che fornisce i dati su cui viene basato il fitting.

La seconda attività riguarda l'implementazione della metodologia che permetta di calibrare i parametri del modello fisico, anche per il caso di una batteria degradata: questa viene considerata attraverso l'introduzione di tre nuovi parametri nel modello, che sono correlati a tre diverse modalità di degradazione; un PSO aggiuntivo è stato implementato per calibrare questi tre parametri. La metodologia, quindi, sfrutta la combinazione dei due PSO, che collaborano nella calibrazione del modello della batteria degradata.

La terza attività riguarda lo studio degli stressors che governano due specifici meccanismi di degradazione, ovvero la crescita del "solid electrolyte interphase" (SEI) e il "lithium plating". Grazie alle indagini svolte, sono state selezionate le condizioni operative della campagna sperimentale di invecchiamento: per stressare la crescita del SEI, le batterie vengono invecchiate tramite calendar aging ad alta temperatura, mentre, per il lithium plating, vengono scelti cicli a bassa temperatura.

Infine, la metodologia viene testata e validata, calibrando i parametri di uno dei campioni invecchiati tramite cicli in condizioni di plating, in vari stadi di degradazione.

**Keywords:** batterie a ioni di litio, degradazione, lithium plating, modello fisico, metodologia

# Introduction

In the last decade the energy generation sector has faced many changes in its mix in order to reduce greenhouse gases emissions and to mitigate climate change impacts. At the centre of these changes there is of course the growth of the renewable energy share, enabled through massive cost declines of both utility scale solar PV and onshore wind. In fact, in the ten years between 2009 and 2019 cost of onshore wind and utility scale solar PV declined by 70% and 89%, respectively [1]. Still, greater effort will be needed in the coming decades to complete the transition to a completely decarbonized energy mix and secure climate targets.

According to IEA the energy production from renewable energy could increase by 50% between 2019 and 2024 [2]. However, renewable sources are intermittent and non-programmable, creating discontinuity in the supply and grid stability issues. Battery systems are a key technology in this transition, supporting a large range of services, from providing frequency response and reserve capacity to enable electric vehicles, promoting mini-grids and rooftop solar PV for self-consumption.

Despite pumped-hydro systems are still dominating electricity storage, stationary applications battery systems are growing rapidly, offering wide deployment and huge cost-reduction potential [3].

Another fundamental sector to tackle climate change issue, is the transport one, that will see a reshaping of the existing mobility systems in the next future. The electric vehicles (EVs) market, including both full electric and hybrid vehicles, will be fundamental for the decarbonization of the transport sector and is expected to grow by 29% annually over the next ten years [4]. Moreover battery electric vehicles (BEV) are predicted to account for 81% of all new EVs sold by 2030 [4].

Lithium ion batteries (LIBs) are the leading technology both in the EV field and in the stationary energy storage applications, thanks to their advantageous properties with respect to other electrochemical storage systems: high power and energy density, low self-discharge rate and long cycle life, to give some examples [5], [6].
The increase in LIBs usage makes it urgent to rethink the battery economy in a "circular way", including repurposing and recycling of the batteries at the end of life in order to reduce waste to the minimum.
In a view of battery second life utilization, it is fundamental to study the degradation

phenomena and their relation with the battery operating condition, to understand which are the stressors that drive these mechanisms and what are the consequences of certain working conditions for the battery, in terms of state of health.

This thesis is focused on the identification of the link between the battery physical parameters and the aging mechanisms that underlie the battery degradation. Specifically, an aging campaign has been carried out to study two mechanisms, namely SEI growth and lithium plating, and to understand what are their driving stressors.

The thesis is structured as follows:

**Outline**

**Chapter 1:** describes the state of the art of lithium ion batteries technology: operating principles and materials, the degradation mechanisms and how they are studied and detected in the literature. It also introduce the research question of the thesis.

**Chapter 2:** explains the experimental techniques and the employed physical model.

**Chapter 3:** introduce the main improvements and contributions and defines the operating protocol.

**Chapter 4:** analyze the model calibration and validation on a pristine sample with the proposed operation protocol. Two degradation phenomena are selected and investigated to take decisions about the aging campaign condition.

**Chapter 5:** report the results and the analysis of the aging campaign and the calibration and validation of the model at different stages of the battery lifetime.

# Contents

# List of Figures

# List of Tables

# 1 State of the art

A lithium-ion battery (LIB) is an electrochemical device that can store electric energy as chemical energy and allows the conversion from one another exploiting the reduction – oxidation reactions of lithium ions. It is a closed system, as all the reactants and products of the reactions remain inside the battery itself.
Lithium, as an element, shows some characteristics that make it particularly beneficial when used as a reacting species: it has a low atomic number and a high electrode potential. This results in the possibility of manufacturing higher energy and power density cells, with respect to other battery chemistries, as lead acid and manganese dioxide-zinc [7]. Hence, LIBs are light, compact and allow a relatively fast charging [5].
From their introduction in the market in 1991, LIBs became the leading technology in the market of portable electronics devices [5] , as mobile phones and computers, and they are now enabling vehicle electrification and entering the utility industry, where they are used as stationary energy storage systems, even coupled with renewable energies [8].

In this chapter the basic operation and components of a battery are described. Moreover, the degradation mechanisms and the diagnostic techniques commonly adopted nowadays are outlined. Finally, the aim of the thesis is presented.

## 1.1 Introduction to Lithium-ion battery technology

A lithium ion battery is made of a number of power-generating units named cells. A cell is composed by essentially three components: two porous electrodes, separated by a polymeric membrane, the electrolyte (see Figure 1.1). Each electrode has a certain potential, depending on its composition, its thermodynamic condition and the lithium concentration presents in its active sites. The electrode with the lower electric potential is named negative electrode, while the one with the higher electric potential is called positive electrode. The operating cell voltage $V$ can be obtained as the difference between these two values. An external electric circuit connects the two battery terminals and allows the charge or discharge of the battery with a certain current $I$, namely the electrons flow rate in the circuit. The exchanged

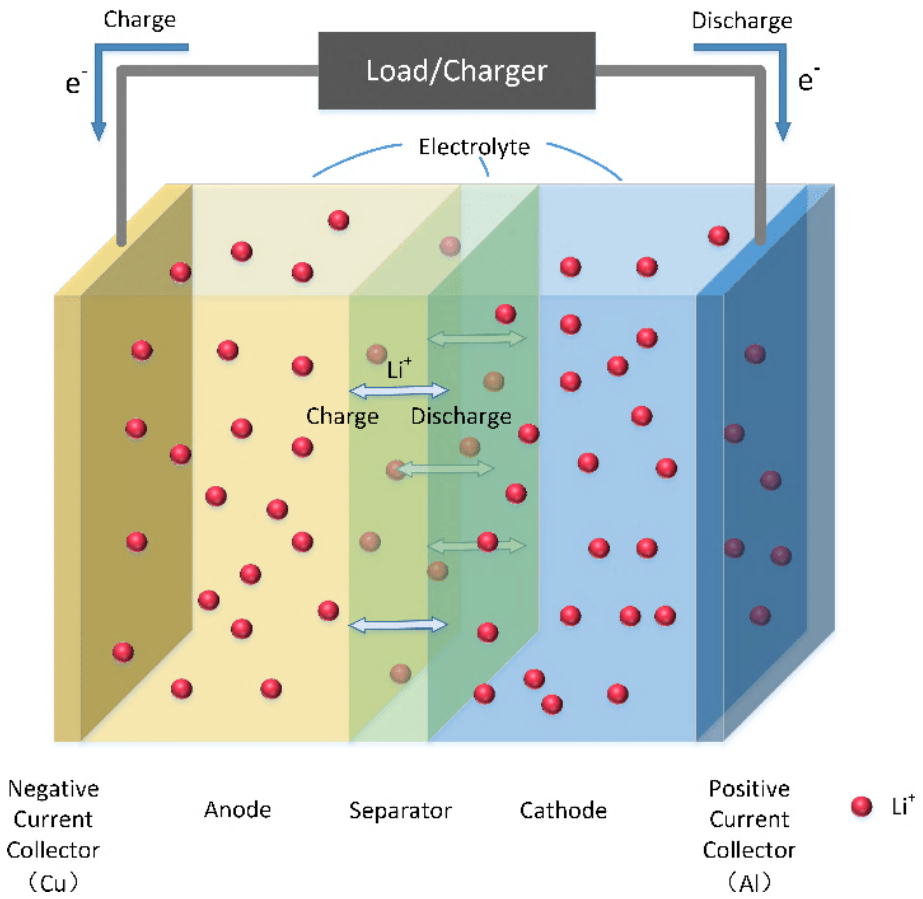


**Figure 1.1:** Schematic of the Lithium-ion cell. (Taken from [9])

charge Q can be computed as the time integral of the operating current. Hence, it represents the number of electric charges that are exchanged in a certain time

interval within the battery.

$$Q = \int_0^t I \, dt \tag{1.1}$$

The cell energy can be expressed as:

$$J = \int_0^t I \cdot V \, dt \tag{1.2}$$

where $I$ and $V$ are respectively the current and cell voltage profile in time.

Discharging a battery with a standard test procedure, one can get the nominal capacity, a value that approximately express the maximum amount of charge that a battery can discharge. This standard procedure includes specifics for thermodynamic conditions, set of highest and lowest cut-off voltages and a constant current value that allows to completely discharge the battery nominal capacity in exactly one hour. That current can be defined as 1C-rate.
The C-rate is indeed a parameter that relates a constant current value and the battery nominal capacity in the following way:

$$C - rate = \frac{I[A]\,1[h]}{Q_{nom}[C]} \tag{1.3}$$

It can also be expressed as the ratio between one hour and the time interval required to discharge the battery capacity at a certain constant current value.

$$C - rate = \frac{1[h]}{time\,interval\,from\,SOC1\,to\,SOC0\,[h]} \tag{1.4}$$

Where the state of charge (SOC) is a number between 0 and 1 that represents the ratio between the charge stored in the battery and the battery nominal capacity. The value is then 0 when the battery is at discharged state and 1 when it is fully charged.
A lithium ion battery operates in a defined range of voltage, to avoid side reactions and safety problems that may occur at too high or too low voltages. These limits vary depending on the electrodes' chemistry, and typical values can be 4.2V, as maximum value, and 2.8V, as minimum value, at 25°C. According to the SOC definition that has just been introduced, a battery that at rest and at standard temperature has a voltage equal to the upper or the lower voltage limit, is respectively at SOC 1 or SOC 0.
Cells can be connected together in modules, that can be linked to form the battery pack. The cells can be connected in series to increase the module voltage, or connected in parallel to increase its capacity.
The activity carried out in this thesis is focused on the study of a single cell, but the considerations that will be made can easily be extended to understand battery pack behaviour.

### 1.1.1 Basic operation principles

Two main processes happen simultaneously during the LIB operation:

- the movement of lithium ions: Li-ions are extracted from one electrode, move through the electrolyte to the other electrode. The Li-extraction is named deintercalation process, while the Li-insertion is the intercalation.
- the movement of electrons: electrons released from one electrode, flows through the external circuit and reach the other electrode.

To highlight the interconnection of these two processes it is necessary to go deeper into the understanding of the battery chemistry. The intercalation and de-intercalation processes are described by the following redox half-reactions:

$$Li_xC_6 \longleftrightarrow xLi^+ + xe^- + 6C \tag{1.5}$$

$$xLi^+ + xe^- + Li_{(1-x)}MO \longleftrightarrow LiMO \tag{1.6}$$

The first reaction occurs at the negative electrode that is usually made of graphite ($C_6$), while the second one takes place in the positive electrode. Conventionally, the case of the discharge is taken as the reference to name the electrodes: "anode" is referred to the negative electrode, as it undergoes electrochemical oxidation during discharge, and "cathode" is the positive electrode.
$MO$ stands for metal oxide and refers to the positive electrode host material, that consists in a blend of different metals. Both the reactions occur from left to right during discharge and in the opposite direction during charge.
When the battery is fully charged, most of the lithium is hosted in the graphite, namely one can say that the anode is fully lithiated; viceversa, the metal oxide is depleted of lithium. As the discharge starts the graphite delithiates, undergoing an oxidation, releasing electrons and lithium ions. The $Li^+$ ions flow through the electrolyte and insert in the positive electrode. Simultaneously, the generated electrons flow across the external circuit and, on the side of the positive electrode, recombines with the lithium ions and the lithium metal oxide. Hence, the cathode material reduces during the discharge, increasing its lithium concentration, while the lithium concentration in the anode decreases.

Before the introduction of the voltage profile during charge and discharge, it is important to first analyze the open circuit condition, namely the case when the battery terminals are not connected through the external circuit. The open circuit voltage ($E_{OCV}$ or simply OCV) is the voltage difference between anode and cathode that can be measured in open circuit condition, when the kinetics effects vanished and the battery can be considered as in equilibrium. This may represent the energy content of the battery: in fact, when connecting electrically the electrodes, a current is spontaneously generated, discharging the battery, until a new equilibrium condition is reached.

Hence, $E_{OCV}$ can be written as

$$E_{OCV} = E^{+} - E^{-} \tag{1.7}$$

where $E^{+}$ and $E^{-}$ are respectively the equilibrium potential of the positive and the negative electrode. Their profiles depicted against the state of charge take the name of intercalation curve (see Figure 1.2). The electrodes' potentials are conventionally measured in V vs. Li/Li+, hence taking as a reference the lithium standard electrode potential of -3.0141 V (SHE), that results then in 0 V vs. Li/Li+. This convention will always be applied, but the symbol V will be used for the sake of brevity.

As is depicted in Figure 1.2, the SOC 100% and 0% for the battery do not correspond to the extreme SOCs of the electrodes' intercalation curves. The SOC variation between the condition in which the positive electrode would contain the maximum lithium that can accept and the condition in which the negative electrode lithium concentration would be zero is called "electrode slippage", and represents the relative shift between the two curves. As can be seen in Figure 1.2, the operating window of a battery is delimited by the cut off voltages and the extreme operating states, that generally do not correspond to the upper and lower limits of lithium concentration in the electrodes. This result in an unused operating area, as the electrodes intercalation curves continue outside the operation window of the cell. Nevertheless, operating in a limited voltage window is necessary for safety reasons, but also to improve cell lifetime and consider performance worsening linked to degradation.

To obtain the OCV-SOC curve it is possible to discharge/charge a battery with an extremely low current to approximate the open circuit condition. In this way it is possible to obtain information on the thermodynamic characteristics of the battery, as the OCV is what results from the difference between the open circuit potentials of the cathode and the anode. At higher currents, in fact, voltage losses appear, as will be explained in the next section.

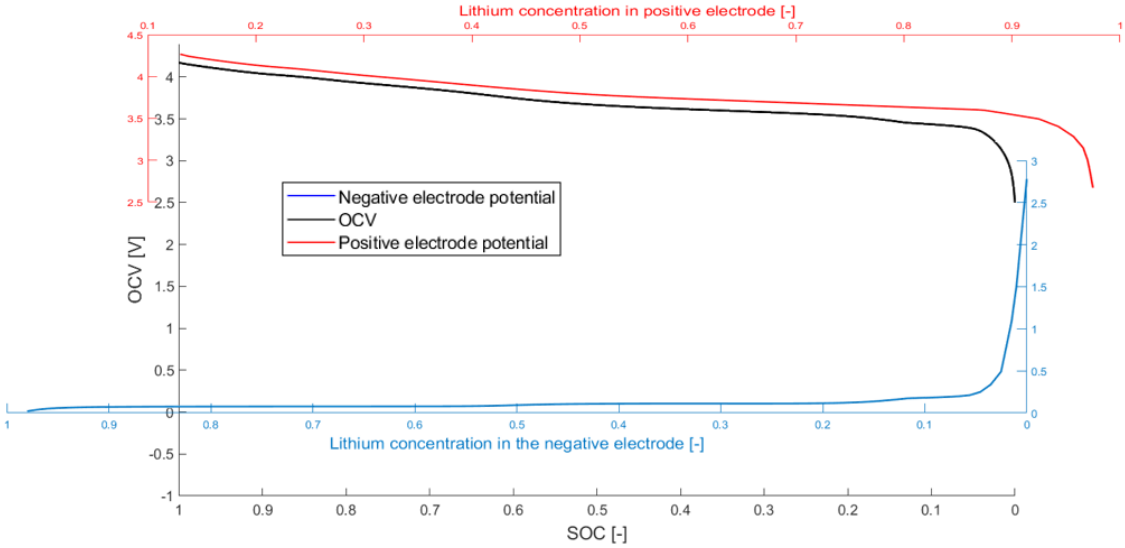


**Figure 1.2:** SOC-OCV curve and electrodes intercalation curve

### 1.1.2 Voltage losses and efficiencies

The cell voltage during operation is different from the ideal open circuit profile. This differences consists in voltage losses, also called overpotentials. They are caused by the irreversibilites introduced by the movement of a charged species in the media; hence, the higher the current, the higher the overpotentials, as can be seen in Figure 1.3. They can be classified into three main groups [10]:

- **ohmic overpotential**: it is the voltage loss caused by the cell ohmic resistances that is proportional to the operation current, following Ohm's law. It corresponds to an instantaneous voltage rise/drop as soon as the charge/discharge starts;

- **charge transfer overpotential**: it is a voltage drop caused by the charge transfer process between the different phases that requires the exceeding of an energy barrier: the higher the value of this activation energy, the higher the voltage drop. The activation energy depends on the kind of reaction and the reaction rate, on the temperature and on the operation current. This loss also takes into account the double layer formation at the solid/liquid interfaces, which basically consists in charge layers that behaves as a capacitance, smoothing the cell voltage profile at the beginning of the discharge/charge process;

- **diffusion overpotential**: the lithium diffusion processes in the liquid electrolyte and in the solid particles of the electrodes become relevant at high current rates. In fact, gradients between the surface and the bulk of the solid

particles of the electrode are generated, imposing limitation on the available lithium that can be used for the reactions.

Hence, when comparing a discharge and the OCV curve at same temperature, the first one will reach the lower voltage limit exchanging less charge with respect to the second one.

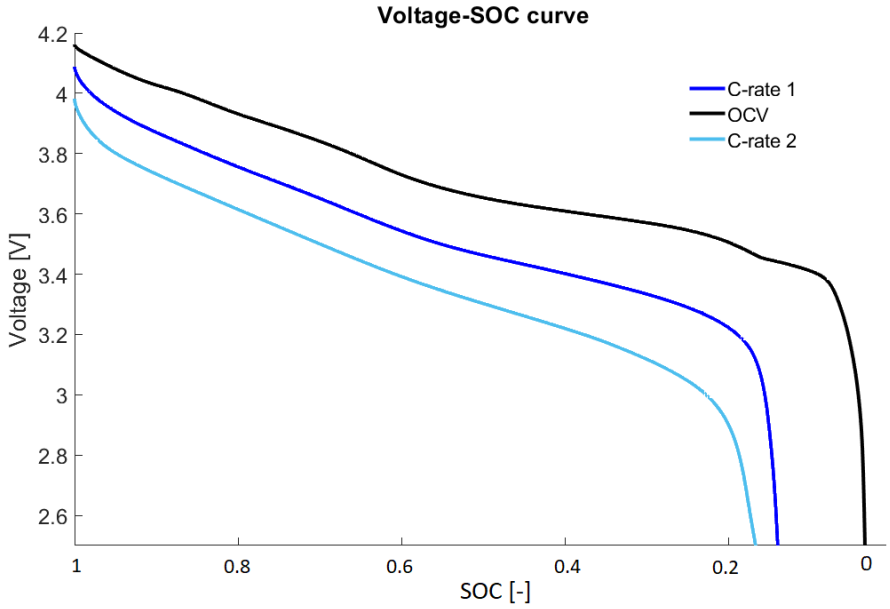


**Figure 1.3:** Comparison of OCV curve and discharges at different C-rates

After that the losses have been assessed, the battery parameters to characterize the performance can be introduced. Two main types of efficiencies can be distinguished:

- the **coulombic efficiency** $\eta_c$, defined as

$$\eta_c = \frac{\int_{dis} dC}{\int_{ch} dC} \tag{1.8}$$

where C is the exchanged charge; this parameter is defined on a closed cycle, that is composed by a discharge and a subsequent charge that allows to reach the SOC that preceded the discharge. Then, $\eta_c$ is defined as the ratio between the electric charge exchanged during the discharge step and the one exchanged during the charge step of the closed cycle [11]. An ideal battery would have $\eta_c$=100%, releasing the same moles of ions during the discharge that are received during the charge. Actually, the coulombic efficiency is a percentage value between 99.5% and 99% that accounts for the irreversible charge loss in the cycle, that is a consequence of undesired side reactions of lithium that reacts with other species in the battery to form other compounds. Repeating the cycling process, the loss of $Li^+$ increases progressively

- the **energy efficiency** $\eta_e$, defined as

$$\eta_e = \frac{\int_{dis} VQ_{nom}dSOC}{\int_{ch} VQ_{nom}dSOC} \tag{1.9}$$

It is the ratio between the amount of energy that the battery release during discharge and the energy that receives during charge in a closed cycle. Energy can be represented graphically as the area underneath the voltage curve: this area is higher for the charge than the discharge, due to the ohmic overpotentials. Since the losses increase with the current, the higher the C-rate the lower will be the energy efficiency: in the common operation condition, $\eta_e$ lays between 60% and 90% [12].

## 1.2 Components, materials, chemistries, design

The main components of a lithium ion battery cell are: the electrodes (cathode and anode), the separator and the electrolyte. The electrodes consist in metal foils (usually aluminum for the cathode and copper for the anode) coated with the electrode active material. These foils are kept apart by a separator, often made of different type of polypropylene (PP) or polyetylene (PE) plastic.
There are many possible designs for a battery as showed in Figure 1.4, [13]:

- cylindrical cell: it is the most common cell design; it is easy to manufacture and has good mechanical stability. Moreover, the tubular cylinder can withstand high internal pressures without deforming;
- button or coin cell: thanks to its compact design it was used in portable devices since the 1980s. As they are not provided a safety vent, they have to be charged with low currents to prevent overheating; due to this issue, most of the commercially available coin cells are nowadays non-rechargeable.
- pouch: it is a lightweight, flexible and cost-effective battery design; moreover, they have potential for greater nominal capacity with respect to the cylindrical cells; on the other hand, swelling can occur due to gas generation (mainly $CO_2$ and $CO$) and in extreme conditions, the pressure can crack the battery cover.
- prismatic cell: it improves space usage, allows flexible design but can be less efficient in thermal management and result in higher manufacturing costs.

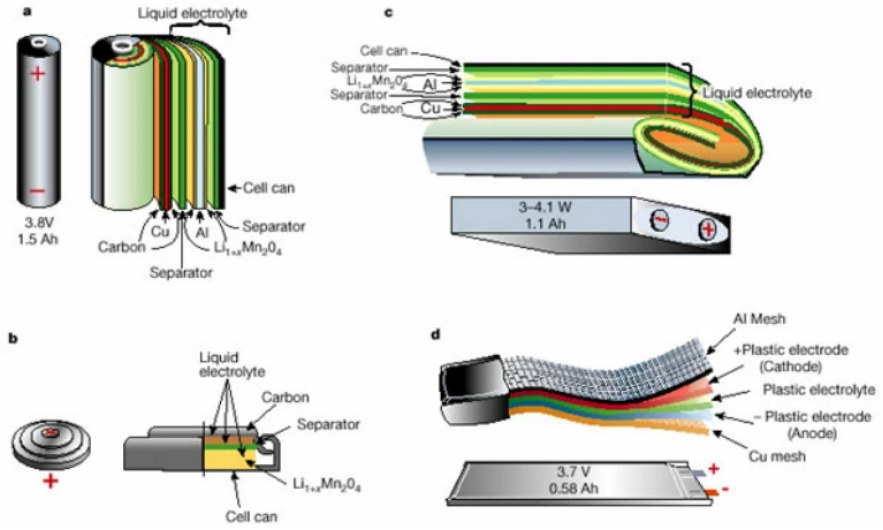


**Figure 1.4:** Typical battery configuration: a. Cylindrical cell, b. Button cell, c. Prismatic cell, d. Pouch cell. (Taken from [14])

### 1.2.1 Electrodes

Ideal electrodes' materials should have some important characteristics. As the electrodes are packed in a container with constant dimension, in order to obtain the highest energy battery, it's more important to use a material that has an high volumetric capacity ($mAh/cm^3$) than a high gravimetric capacity ($mAh/kg$) [6].
Moreover, the material should have an high electronic conductivity, namely it should favor the flow of electron, and a high lithium solid diffusion coefficient, as lithium needs to diffuse into the electrodes' structure during operation.
As the electrodes are constantly in contact with the electrolyte, side reactions that may consume cyclable lithium and the electrodes' materials have to be avoided. For the same reasons, unwanted reactions with lithium ions has to not be favoured by the electrode material.
Of course the materials has to not be toxic and flammable, to reduce safety issues, and should have high mechanical and thermal stability, to avoid volume changes during charge and discharge and decomposition at high temperatures.
Finally, a material that is also rich in resources and cheap is suitable in large-scale use of batteries.

#### Cathode materials

The positive electrode of the battery, namely the cathode, goes under reduction during discharge and oxidation during charge.
In addiction to the general electrodes' characteristics already listed, it's important that the cathode potential is high. The energy of a battery depends on the product of the cell capacity and the cell voltage (equation 1.2), that is generated by the combination of the anode and cathode potentials. Therefore, considering same anode material, the cathode material with the highest potential, is preferable as it allows to have a battery with higher energy.

The most common cathode materials are:

- **LCO**: lithium cobalt oxide, $LiCoO_2$, was the first form of layered transition metal oxide cathodes [15]. The main advantages are the high theoretical specific (274 mAh/g) and volumetric capacity (1363 mAh/$cm^3$), high discharge voltage, low self discharge and good cycling performance. Its major drawbacks are the high cost of cobalt, the low thermal stability, and the low performances at high current rates or during deep cycling. Different types of dopants has been studied to overcome LCO limitations, but with limited results. Coatings, instead, showed more effective results, increasing LCO mechanical and chemical stability and reducing the risk of side reactions with the electrolyte

[16]. Another issue that deserves special attention is that cobalt is mined in exploitative conditions in Congo; nevertheless, Benchmark Minerals' forecasts suggest that the global demand for cobalt in 2029 will be 300,000 tonnes compared with an estimated 70,000 tonnes in 2019 [17].

- **LNO**: $LiNiO_2$ was introduced, by replacing cobalt with nickel, allowing to reduce the high cost of LCO. It has a high theoretical specific capacity (275 mAh/g) and a high energy density, similarly to LCO. Nevertheless, on the side of thermal stability, it is even worse than LCO, and during delithiation $Ni^{2+}$ ions tend to substitute $Li^+$ sites, reducing the lithium diffusion [16].

- **LMO**: as mangangese is much cheaper, less toxic and has a high rate capability, compared to Co or Ni, $LiMnO_2$ lithium manganese oxide seems to be promising. The layered form tends to pass into spinel form, $LiMn_2O_4$ (LMO), that is considered even more promising, as it is a more stable structure [18]. However, it still suffers from the Mn dissolution problem that causes relevant degradation during lifecycle [19], and, it is the commercial cathode material with the lowest gravimetric capacity (148 mAh/g).

- **NCA**: nickel cobalt aluminum oxide $LiNi_{0.8}Co_{0.15}Al_{0.05}O_2$ is obtained by partially replacing some of the Ni with Co, in order to reduce the cationic disorder that was encountered in pure LMO cathode; moreover, a small quantity of aluminum is added to improve thermal stability [20]. NCA is nowadays common for electric vehicle applications due to its high theoretical volumetric (1284 mAh/$cm^3$) and gravimetric (279 mAh/g) capacity. However, especially during operations at high voltages and temperatures (higher than 40°C), the alluminum presence showed to be detrimental to the cell impedance [21]; under similar operating conditions severe capacity fade was experienced, due to solid electrolyte interphase (SEI) growth and micro-crack formation at grain boundaries.

- **NMC**: cobalt and nickel are added to form nickel cobalt manganese oxide, improving the manganese compounds structural stability. Its characteristics are similar to LCO's: it has a high theoretical gravimetric (280 mAh/g) and volumetric (1333 mAh/cm$^3$) capacity. As it contains a lower amount of cobalt, it's also cheaper than LCO. Layered $LiNi_{0.33}Co_{0.33}Mn_{0.33}O_2$, or NMC 111 is the most spread one, widely used in the battery market; the research in this material are going in the direction of increasing nickel content in NMC, as NMC 632 and NMC 811, to increase the specific capacity by reducing the relative amount of manganese and decrease the quantity of the expensive and

toxic cobalt [22].

- **LFP**: $LiFePO_4$ is the only polyanion compounds that has been commercialized. Its advantages are the high thermal stability and high electrochemical stability that allow to exploit almost all the theoretical capacity [23]. On the other hand, the theoretical capacity is quite low (170 mAh/g) and the solid diffusivity and ionic conductivity are limited. To address these criticalities, reduction in particle size combined with carbon coating and cationic doping showed effective results. Nowadays battery pack assembled with $LiFePO_4$ electrochemistry are adopted in electric buses and minibuses [24], as for this kinds of application the low energy density is not a significant problem.

**Anode materials**

In addiction to the favourable characteristics for electrodes' materials already listed, the lower the anode potential, the higher the obtainable cell voltage and so the higher the energy that the battery can provide.

The intercalation curve of graphite, namely the curve that relates the OCV and the lithium concentration, is characterized by a complex profile that has been widely studied in the literature [25], [26], [27]. It is the outcome of a complex staging process, related to the lithium intercalation process into the graphite structure of the anode (see Figure 1.5): lithium occupies at first interlayers distant to each other because of a repulsion effect, and only increasing in concentration, lithium starts to occupy the other interlayers until all the available interlayers are occupied. Hence, distinct stable Li-C solid phases (single-phase region) alternate to two-phase region (phase transition) that occur at determined voltage values, identifying two main voltage plateaus.
According to the literature, it's possible to highlight up to six different solid phases and five phase transitions [28], [29]. Stages indicated with the letter "L" have a "Liquid-like" behaviour, namely lithium is placed in the planes in a disordered manner, while in the other phases lithium is more dense and ordered.

The staging process is represented in Figure 1.5, and it is here described:

- **1L**: named as graphite solid solution regime. Lithium intercalation into graphite starts, with a disordered distribution into the graphite interlayers
- **1L-4L** phase transition is characterized by this reaction:

$$LiC_{72} + Li \longleftrightarrow 2LiC_{36} \tag{1.10}$$

- **4L**: the lithium progressively occupies active sites in every fourth available

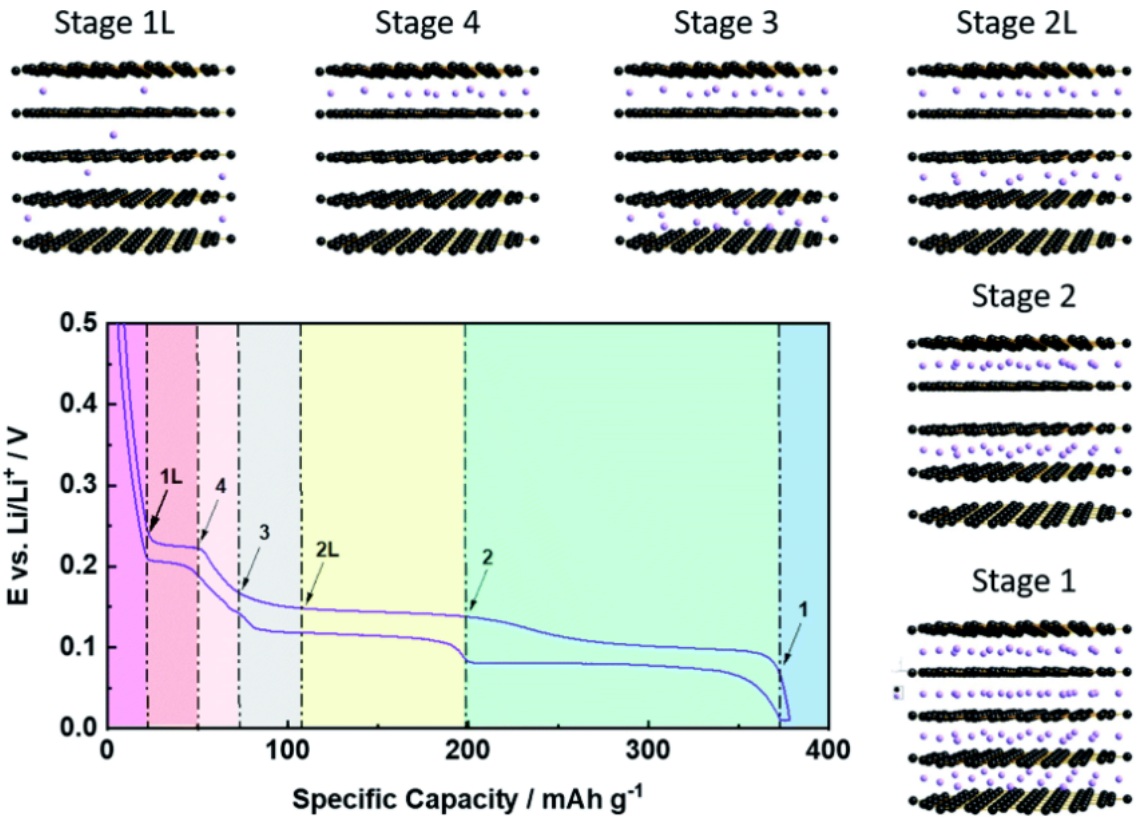


**Figure 1.5:** Staging of graphite. (Taken from [26])

interlayer;

- **4L-3L** phase transition:

$$3LiC_{36} + Li \longleftrightarrow 4LiC_{27} \tag{1.11}$$

- **3L**: the lithium progressively occupies active sites in every third available interlayer;
- **3L-2L** phase transition:

$$2LiC_{27} + Li \longleftrightarrow 3LiC_{18} \tag{1.12}$$

- **2L**: the lithium progressively occupies active sites in every second available interlayer;
- **2L-2** phase transition:

$$2LiC_{18} + Li \longleftrightarrow 3LiC_{12} \tag{1.13}$$

- **2**: the lithium occupies the same layers as the stage 2L, but the lithium density changes due to its ordered configuration;

- **2-1** phase transition:

$$LiC_6 \cdot C_6 + Li \longleftrightarrow 2LiC_6 \tag{1.14}$$

- **1**: the lithium occupies active sites in all the graphite layers.

**Graphite-Silicon** (C-Si) mixtures are used as anode material to increase the gravimetric capacity of the anode [30]. This result is reached adding even very small amount of silicon (up to 5%), as its gravimetric capacity is very high, exceeding 3000 mAh/g. The main drawback consists in an averagely higher electrode voltage.

**Lithium titanate** (LTO) is another compound employed as anode material [19]: it has a high thermal stability, good volumetric capacity ($\approx$ 600 mAh/cm$^3$) and exceptionally high coulombic efficiency. However, titanium is very expensive compared to graphite, and as the LTO's specific capacity is limited by its high electrode potential (1-2 V) [31], its use is limited to some high power application.

### 1.2.2 Electrolyte

The electrolyte is usually a liquid solution that allows the transport of lithium ions between the anode and the cathode. Then, it has to provide high ionic conductivity and high thermal and electrochemical stability. Namely, it should not decompose at high temperatures and in the operating voltage range of the electrodes (anode: 0.05-0.5 V; cathode: 3.8-4.5V).
The solutions are composed typically by carbonate solvents, lithium salts and specific additives to provide different benefits. The additives main roles are to favor the solid electrolyte interphase (SEI) layer formation and to improve the electrolyte thermal stability. The SEI formation will be discussed in detail in paragraph 1.3.2 and it basically consists in a lithium passivation film that forms on the anode surface as the first electrochemical reactions occur inside the cell, during the very first cycle. It results in a irreversible lithium loss, and then, in a capacity loss. On the other side it has the important function of protecting the anode surface from further chemical reactions that could occur with the electrolyte.
Another challenge related to the electrolytes is their behaviour during a thermal runaway event, as they are typically flammable. In fact, interest is growing for gel electrolytes, solid electrolytes and non-flammable acqueous-based electrolyte solutions [32], [33], [34].

### 1.2.3 Separator

The aim of the separator is basically to separate the anode from the cathode, in order to avoid internal short circuit, but still allowing the lithium ions movement.

It consists of a thin piece of material, that could be ceramic or plastic. The separator has to resist corrosion that could be operated by the electrolytes used in the cells, and avoid the melting at high temperatures causing internal short circuit and thereby permanent failure. This last issue is prevailing in plastic materials, and hence, to increase safety, multilayer separators are used: allowing the melting only of the internal layer, they ensure the separation of anode and cathode at high temperature. Furthermore, ceramic-layered separators are able to withstand even higher temperatures; they also tend to reduce internal resistance and hence improve the cells power rate capability [5].

## 1.3 Battery degradation

In this section concepts of battery recycling, reuse and second life applications will be reviewed. This topics are still in early stages as there are currently no regulations for LIBs recycling and the development of processes for second life usage is not always profitable.
Moreover, the degradation mechanisms will be accurately described and the diagnostics techniques known in the literature will be presented.

### 1.3.1 Second Life and circular economy of LIBs

As the battery market is expected to increase in the next years, the topic of circular economy is of the utmost importance. Circular economy is a model that involves all the phases in the lifecycle of a product, from raw materials to the production, distribution, consumption to recycling and waste management. The objective is to exploit at best existing materials and products, repurposing them in another use at the end of their life.

For what concern lithium ion batteries adopted for electric vehicles (EV), they are usually considered at the end of their useful life when their capacity is the 80% of the nominal one [35]. This may seem a strict requirement, but it is fundamental to have optimal performances throughout the EV lifetime. On the other hand, energy storage systems and light-duty EVs, as e-scooters and e-bikes, are less demanding in terms of performance and power requisites.

Possible second life applications for batteries are to be used for stationary applications [36] [37], to provide power support to fast EVs charge stations, to be coupled with renewable energies to offer reliability in the electricity generation or to provide grid-oriented services, such as area regulation and transmission deferral.

To improve battery recycling many fields have to be investigated furtherly. Of course, studies on transportation of large quantities of batteries and management of damaged battery systems have to be improved. Moreover, the implementation of an efficient logistic chain for battery disposal and extended business models to take into account recycling and reuse have to be developed.
Another fundamental asset is the research on spent lithium-ion batteries, recording life cycles and aging characteristics, in order to improve batteries and to find standard and possibly rapid diagnostics to compute the battery state of health and to predict its remaining lifetime.

### 1.3.2 Degradation mechanisms

In the view of a closer and closer future where circular economy and second-life battery are crucial aspects, the understanding of battery degradation becomes even more fundamental. However, the processes involved in the aging phenomena are complex and interconnected, so it's difficult to detect and distinguish peculiar features caused by different aging mechanisms. Moreover, even same operation condition may result in a different kind of degradation depending on the battery chemistries and materials.
Generally, two types of aging can be distinguished: calendar aging and cycle aging.

**Calendar aging** is the battery aging not correlated to the operation, but only to the thermodynamic conditions at which the battery is stored; in fact, some undesired chemical and electrochemical side-reactions may be promoted at certain thermodynamic states, resulting in lithium and active material loss and then in capacity fade [38], [39]. Assessing the calendar performance of a battery is crucial to evaluate its stability and reliability, as, for instance, a personal EV spends most of its life in parking mode.
Calendar aging has been extensively studied throughout the years, and many works on lithium-ion batteries can be found in the literature, investigating the effects of temperature and SOC on the battery aging [39], [38],[40],[41].
The extent of capacity loss strongly increases with ambient temperature and to a lesser extent with increasing the state of charge. At high temperatures dissolution processes are favoured, indeed, translating into irreversible cyclable lithium loss. In fact, high storage SoCs correspond to low anode potentials, which, aggravating electrolyte reduction, promote solid electrolyte interphase growth.
The loss of cyclable lithium caused by side reactions at the negative electrode is often reported to be the main cause of degradation at high temperatures [38] [39] [16]. Correlations between storage temperature and capacity fade in time have been found to be linear at low temperature and non linear at high temperature, [42]. The increase of cell impedance with time have been highlighted in different calendar life study [40] , [43].

Lithium ion batteries undergo **cycle aging** because of the continuous temperature, current load, mechanic stress and concentration variation that occur during operation. The main factors that are known to promote aging in the automotive sector are high temperatures, high current loads and high depth of discharges (DOD) [44]. The DOD is a parameter that indicates to what extent the battery is charged or discharged, and it can be computed as the ratio between the exchanged capacity during the charge/discharge process and the nominal battery capacity.

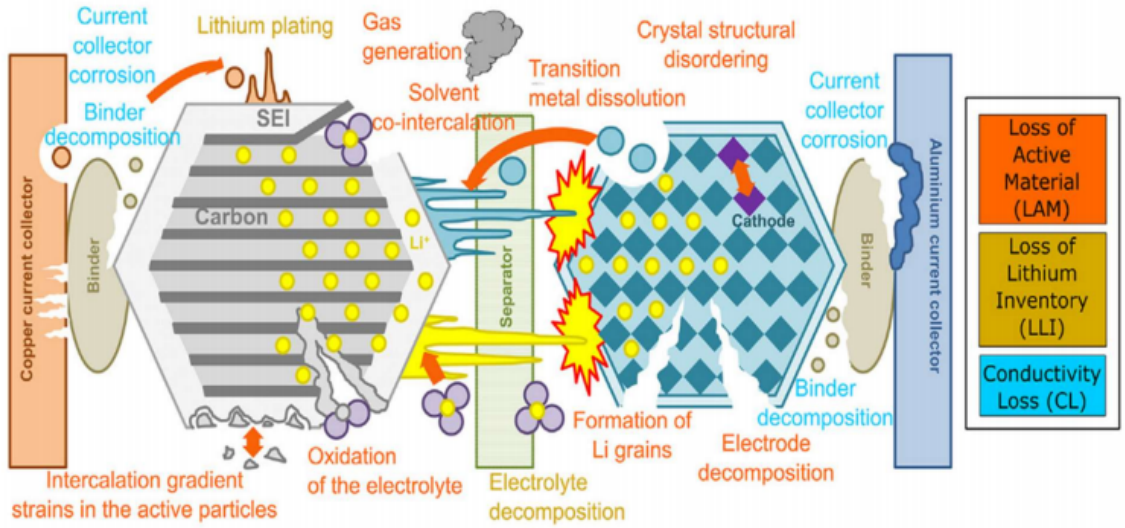


**Figure 1.6:** Schematic representation of degradation mechanisms in Li-ion cells. (Taken from [48])

The DOD effect has been investigated in the literature, and in [41] and [45] is reported how the degradation increases with DODs. The C-rate is a key factor for degradation. In [46] it is stated that the capacity fade follows a square-root dependence on time and that the current is the main parameter at low and ambient temperature, while it looses importance at higher temperatures. In [47] the capacity fade was found to be characterized by a slow linear decrease followed by a faster decrease, correlated to the rate of SEI resistance growth at the anode, on NMC cells.

A panoramic of the main degradation mechanisms can be seen in Figure 1.6. According to literature [48], [49],[50] they are often classified into three main categories:

- **Loss of lithium inventory (LLI)**
  It consists in a loss of the quantity of lithium available to be cycled between the anode and the cathode, that translates in a reduction of capacity. Some of the processes causing this kind of degradation are:
  - **SEI layer growth**
    The solid electrolyte interphase (SEI) is a thin layer that forms on the graphite anode at the first charge of the first cycle of the battery. Its formation is related to the electrolyte, that is unstable at low potentials and then, when it first experience low voltages (around 0.8V) at the anode surface, it is reduced forming this layer from its decomposition [51]. It is clear that the SEI formation consumes cyclable lithium that results in capacity face and as it consists in an additional layer to be crossed by

the ions flow, it is also an increase of the cell resistance. Nevertheless, the SEI provides many beneficial functions to the battery operation: it protects the anode from further undesired reactions with the electrolyte and it controls that the lithium is uniformly delivered to the electrode surface, where the charge-transfer reaction occurs [52]. After the first cycle, the SEI formation is hindered by the SEI itself [16], however at high temperatures a damage-reformation cycle can arise, inducing more SEI formation and further capacity and power loss.

  - **Dendrites formation**
    At high current densities metallic lithium dendrites form and deposit on the surface of the electrode, creating a dendritic interface that causes a rapid deterioration of the Li/electrolyte interface and then, a capacity derease [53]. Moreover, lithium dendrites may cause microscopic short-circuit that can easily burn out due to the generated heat [54]. Electrolytes additives, such as fluoroethylene carbonate (FEC) [55], are used to reduce dendrites formation and increase the reversibility of the anode.

  - **Lithium plating**
    The negative electrode potential can become lower than zero due to over-potentials generated by high charging currents and low temperatures [56]; in this condition, if the lithium ionic current is too high to be accepted by the anode through the intercalation reaction, the plating reaction occurs and lithium is consumed depositing in the form of metallic lithium on the anode surface. Lithium plating is promoted at low temperatures, that makes decrease the solid diffusion coefficient of lithium into graphite [57].

- **Loss of active material (LAM)**, that can occur both in the positive and the negative electrode.
  It corresponds to a decrease in the number of active material sites, namely the sites available for lithium intercalation. This results in power fade, as this kind of degradation leads to a reduction of the surface available for the electrochemical reactions [48].

  - **Metal dissolution**
    Extremely high or low voltage values may induce the irreversible dissolution of the transition metal of the cathode metal oxides [58].

  - **Pores clogging**
    The cathode reaction byproducts migrate to the anode, where they are reduced and progressively clog the anode pores, eventually hindering

lithium-ions to reach the active sites.

  - **Particle cracking**
    This phenomenon, that can occur both in cathode [59] and in anode [60], is generated by phase transitions or volume variations that induce mechanical stress, and then fractures on the electrodes particles that might loose electrical contact with the current collector.

  - **Graphite exfoliation**
    The decomposition of the electrolyte, when it interacts with the graphite structure of the anode, cause the cointercalation of the carbonate solvents with lithium in the interlayers, producing gases that can exfoliates the carbonaceous anode structure. As a consequence, active electrode particles are isolated, causing a loss of active material.

- **Conductivity loss (CL)** that is related to the loss of electric contact and, hence, to the decrease of the specific active area for the electrochemical reactions, at which corresponds a resistance increase [61].

  - **Current collectors corrosion**
    The current collectors are made of copper and aluminum for the anode and the cathode side, respectively. Corrosion may occur in case of very high potentials for the aluminum and for very low potentials for copper [62]. This mechanisms result in an increase of the cell impedance, due to the reduction in the quantity of conductive material.

  - **Binder decomposition**
    High temperatures can promote the binder decomposition reactions, resulting in a loss of electric contact and the isolation of active particles from the whole electrode [61].

### 1.3.3 Degradation phenomena characterization and diagnostics

It is clear that there are several possible reasons for degradation and that the same stressors can lead to very different aging phenomena, as they are often interconnected. The intricacy of the connection between the stressors and the aging mechanisms is highlighted in Figure 1.7.

A parameter called state of health (SOH) is commonly used to characterize a degraded battery. There are many possible definitions [63], and the simplest one is computed as the ratio between the actual maximum dischargeable capacity $Q_{max}$ of

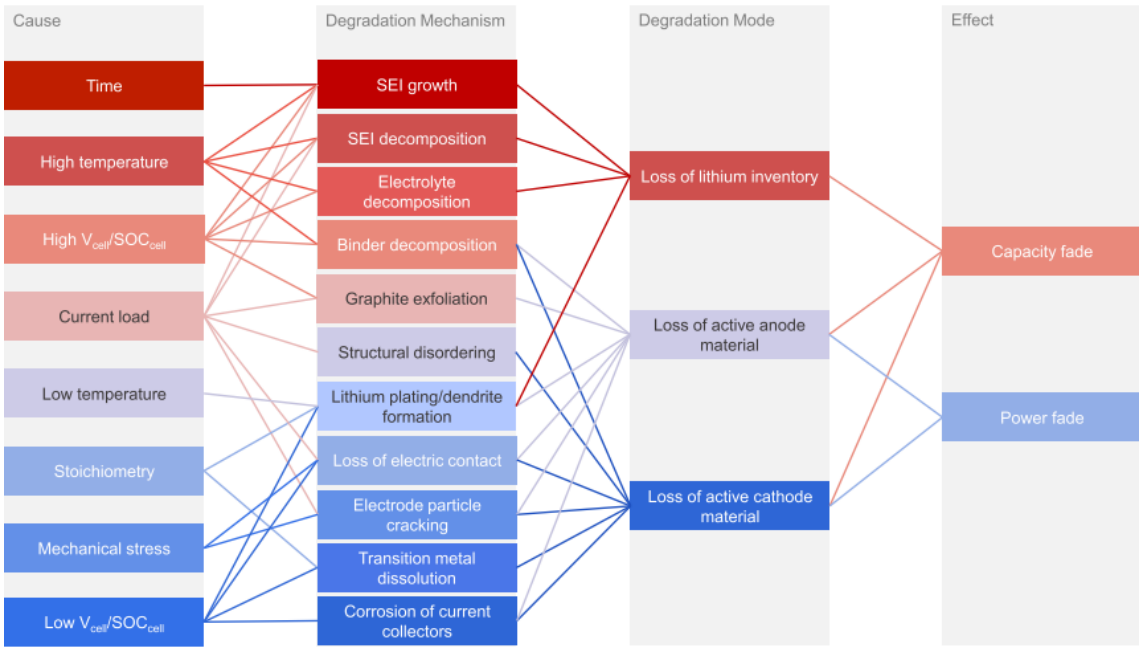


**Figure 1.7:** Summary of degradation mechanisms with the related causes and effects in lithium-ion batteries. (Taken from [48])

the aged battery and the nominal capacity $Q_{nom}$:

$$SOH = \frac{Q_{max}}{Q_{nom}} \tag{1.15}$$

More complex definitions are related to the cell internal resistance, to the achievable peak power or to the overall state of the cell.
To give a truthful representation of the battery state of health and to predict the remaining useful life a more articulated definition should be adopted, taking into account even more than the listed parameters, as the different aging mechanisms that caused the degradation have non-linear and hidden effects. For instance two batteries that have reached the same actual maximum dischargeable capacity through different aging pathways, will most likely not have the same residual life, as different mechanisms results in different rates of the aging.

At present, there are three main diagnosis methods to detect the aging phenomena [64]: disassembly-based post-mortem analysis, curve-based analysis and model-based analysis.

- The **disassembly-based post-mortem analysis** consists in a direct observation by disassembling the aged batteries in a special environment. It is possible to observe the different components and determine the aging mechanisms through material analysis [65], [66], [67]. To analyze the electrode surface morphology, transmission electron microscopy (TEM), optical microscopy

and scanning electron microscopy (SEM) are extensively deployed in the diagnostic of different mechanisms according to the different resolutions.
TEM, having the highest resolution, allows the display of particle morphology during degradation, cristallinity and stress, but has stricter requirements (cleanliness, sample size, etc.) that limits its utilization [68].
SEM generates high resolution 3D images of the samples' surface: SEI film growth, particle cracking and lithium plating at the anode can be identified [69], [70].
The optical microscopy, having the lowest resolution, is mainly used in the diagnostic of the aging reactions on the electrode surface visible at a microscale, such as deformation and electrode surface cracks [71].
To determine the composition and the concentration distribution of the sample elements, energy dispersive X-ray spectroscopy (EDX) [72], inductively coupled plasma (ICP) atomic (or optical) emission spectrometry (ICP-AES or ICP-OES) [73] and X-ray photoelectron spectroscopy (XPS) [71] are frequently used.
To study the surface crystal structure of active materials, the X-ray diffraction (XRD) is used, allowing to understand the electrode degradation [74].

- The **curve-based analysis** is a largely embraced non–destructive method that adopts incremental capacity (IC) analysis and differential voltage (DV) analysis based on OCV curves. This analysis is based on mathematical transformations of the OCV curve that allows to enhance aging mechanisms that would not be visible by looking at the OCV curve only [75]. A qualitative diagnosis of the aging mechanisms is given through the interpretation of magnitude, width and position of the IC and DV peaks. To simplify the analysis, three modes of degradation are considered to summarize all the internal aging reactions: loss of lithium inventory (LLI), loss of active material (LAM) and ohmic resistance increase (ORI). DV analysis and IC analysis will be further discussed in section 2.3.2.

- The **model-based analysis** methods consist in the implementation of a model that describes the battery operation, and hence it is clearly another non-destructive diagnostic method.
  Different types of battery models can be used, as the equivalent electric circuit model (EECM) or the electrochemical model (EM).
  The EECM is a very simple and easy to implement model, that is structured as an electric circuit that connects in series an ohmic resistor and one or more RC circuits [76]; SEI, charge transfer and double layer are modeled as resistances

and constant phases elements in the electric circuit [77]. By identifying the EECM parameters it is possible to observe the changes of different resistances during battery aging and analyze the corresponding aging reactions.
The EM model describes the battery through all the electrochemical reactions, the lithium diffusion and migration processes that occurs inside the battery. Thanks to the identification and comparison of the EM parameters it is feasible to distinguish the specific aging mechanisms and to highlight the link to the corresponding aging modes [78].

After this general review of the most common diagnostic techniques, a focus on the detection of two particular degradation phenomena is presented as they are under investigation in this thesis work.

### SEI growth

Solid electrolyte interphase can be identified through different techniques. For what concerns the adoption of post-mortem analysis, as XPS allows the observation of changes in elemental composition at different depths, is used to observe the SEI film, detecting the SEI formation and decomposition products inside the battery [79]. Complementary to XPS, the time-of-flight secondary ion mass spectrometry (TOF-SIMS) [80] is used to study the chemical structure of SEI. ICP-AES detect the growth of SEI film [81] by showing fluctuations in the cathode and anode lithium content. SEM can also be used to identify the SEI film.
In the XRD spectrum, changes in SEI film are indicated by the intensity and quantity of the peaks. As for the curve-based analysis, SEI formation and growth can be considered as a part of the LLI, and it can be detected through the interpretation of IC peaks [50].
Moreover, EMs [78] and EECMs [76] are used to compute the SEI film resistance during the battery aging.

### Lithium plating

The main methods used nowadays for lithium plating detection can be summarized as follows:

- measurement of anode potential vs $Li/Li^+$ with a reference electrode, as generally lithium plating occurs when the anode potential is lower than 0 V [82], [83], [84];
- post-mortem imaging of anode morphology [85], [86];

- nuclear magnetic resonance [87], [88] and electron paramagnetic resonance [55], [89]: through the use of these techniques it is possible to detect the range of resonance frequency that corresponds to metallic lithium;
- high precision measurement of coulombic efficiency [90], [91]: in these works, lithium plating is indicated by the deviation of the curve representing the coulombic inefficiency per hour versus time when the cell aging is dominated by SEI growth;
- cell thickness measurement [92], [93], [94]: metallic lithium deposition induces larger volume change (estimated to be 0.37 $cm^3$/Ah [92]) than the lithium ion intercalation into graphite. Moreover, the thickness change caused by lithium plating is irreversible;
- graphite lithiation degree measurement via in-situ neutron diffraction [95], [96]: in fact, according to [95], in the relaxation after a 0.2 C-rate discharge at -20°C, the lithiation degree of graphite increased by 17%. This indicates that at least 17% of lithium was plated while charging;
- detection of a particular voltage plateau after charging [97], evidenced both in the beginning of a subsequent discharge [98], [99], or of relaxation [100], [89], [101]. This voltage plateau is attributed to the stripping of deposited metallic lithium, indicating that lithium is plated during charging.

## 1.4 Aim of the thesis

This thesis work has been carried out at the MRT Fuel Cell & Battery Lab of Politecnico di Milano and it is the third part of a research track that investigates lithium ion batteries aging, started in 2018. It collocates in the framework of a European project that aims to assess circular economy of EV lithium ion batteries, developing a complete cycle from its development and packaging until final disposal. In particular, the laboratory is involved in the development of a diagnostic protocol for the electrochemical analysis and state of health characterization of spent automotive samples.

This work aims to develop a non-destructive innovative method, that allows to investigate the aging phenomena related to lithium-ion batteries, detecting their presence through the interpretation of key parameters, obtained from a limited set of easily acquired experimental data.

The steps that will be followed to achieve this result are the following:

1. adaptation and improvement of the pre-existent tools and methods, with respect to the activities of this thesis: a LIB physical model, a data-fitting algorithm (Particle Swarm Optimization) that allows the calibration of the physical model for a pristine cell, and an experimental protocol that provide the data on which the fitting is based;
2. implementation of a methodology to calibrate the physical model thanks to the improved data fitting algorithm, that also allows to account for degradation;
3. investigation of two degradation mechanisms stressors, namely SEI growth and lithium plating. The aim would be to identify the condition to stress these phenomena singularly, in an experimental aging campaign, in order to highlight their related specific features.
4. testing and validation of the implemented methodology, using the data of the aging campaign. Since the methodology will be adopted in a case where lithium plating occurs, it can be a useful tool for the understanding of this phenomena and on the effects that it would have on LIBs performance.

# 2 Methodology

In this chapter a general overview of the main tools used in this thesis, related both to the experimental asset and the physical model, is presented.
The detailed utilization of these methods in the context of the activity carried out, their implementation and adaptation will be described instead in Chapter 3.

## 2.1 Battery samples

The LIBs samples used in this work are commercially available batteries, as the scope of the thesis project is to investigate degradation mechanisms to explore second life commercial battery characteristics and behaviour. The basic data provided by manufacturer are reported in Table 2.1. A total of 44 Sony US18650V3 batteries have been tested in this work: half of them was new samples and the other half was spent batteries, previously used in e-bikes.

These batteries can be classified as **high-energy batteries**. The main character-

| **Samples' characteristics** | |
|---|---|
| Manufacturer | Sony |
| Model | US18650V3 |
| Design | Cylindrical |
| Nominal Capacity | 2250 mAh |
| Anode chemistry | Graphite |
| Cathode chemistry | NMC |
| Maximum voltage | 4.2 V |
| Minimum voltage | 2.5 V |
| Nominal voltage | 3.7 V |
| Maximum charge current | 2.25A |
| Maximum discharge current | 10A |
| Temperature range (charge) | [0 ; 45°C] |
| Temperature range (discharge) | [-20 °C ; +60°C] |
| Weight | 44 g |
| Dimensions (D x H) | 18 mm x 65 mm |

**Table 2.1:** Characteristics of battery samples

istic of this kind of batteries is their high specific capacity, that is obtained thanks

to thicker and less porous electrodes [6]: in this way, the amount of active material increases and more lithium can be stored in the electrodes. On the other hand, the cell resistance grows with the electrodes' thickness, making this type of batteries not suitable for high current rates applications. They are preferred instead, when high autonomy is required.

In Figure 2.1 it is possible to see the samples mounted inside the test stations, where power cables and sensing cables are connected to the positive and the negative terminals of the battery.

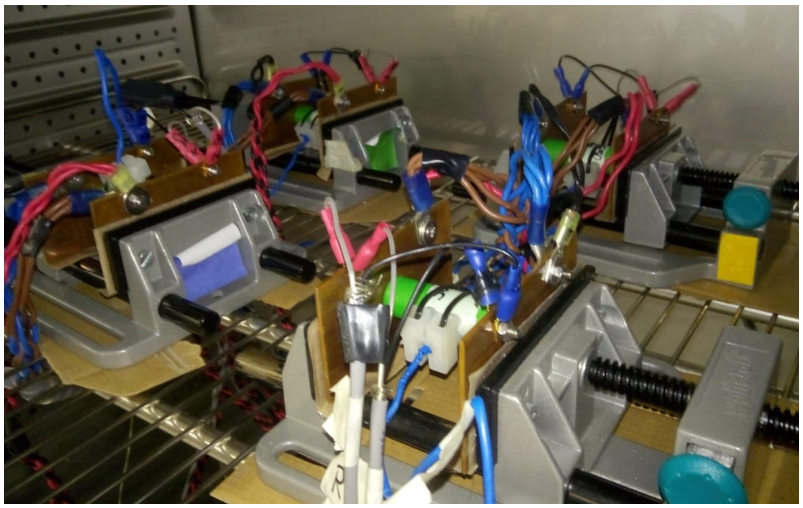

**Figure 2.1:** Photograph of battery samples mounted in the experimental setup.

## 2.2 Experimental bench

The test bench used during this work was designed and developed in the context of a previous thesis on the same project [102] and hereby improved in some aspects to increase the accuracy and reliability.

The experimental station (see Figure 2.2) allows the testing in four different chan-

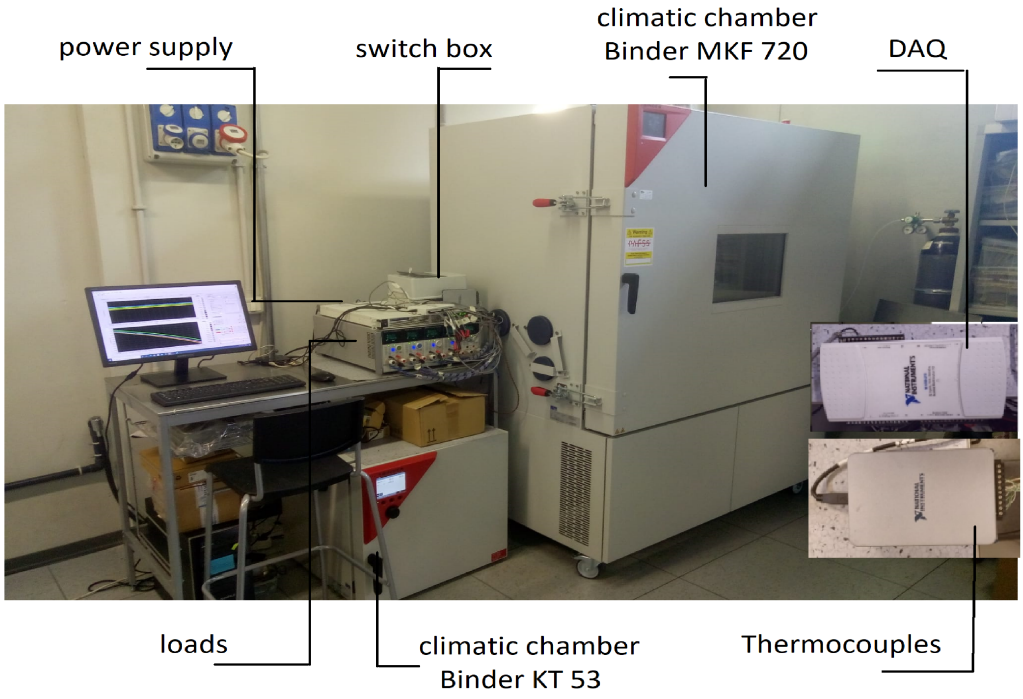


**Figure 2.2:** Picture of the laboratory test bench, highlighting the main components

nels in a flexible and independent way: each channel is equipped with a Chroma UM 63640-80-80 electronic load. A fifth electronic load is used to impose the current in the main circuit. The power supply NI RMX-4124 is used to charge the batteries. Both the voltage during operation and the voltage oscillation during EIS tests are read by the electronic loads; a NI DAQ USB 6218 acquisition board is used to measure and check these values as well. The testing systems constitute a multichannels cycler with a multirange EIS tester.

There are two climatic chambers where the batteries can be tested: one is a Binder KT 53, that can adjust and control only the temperature in the range 4°C-100°C, and the other one is a Binder MKF 720 Eucar 6, operating in a range of -40°C, 170°C and allows the control of both temperature and relative humidity and has proper safety systems to protect from fires. The battery surface temperature is measured individually for each battery through four RS PRO type K thermocouples, and registered with a NI CDAQ 9211 acquisition board.

| Instrument | Scope | Measured quantity | Uncertainty |
|---|---|---|---|
| NI RMX-4124 | Power supply | Current | ±0.5% ± 0.1%f.s |
| Chroma UM 63640-80-80 | Electronic load | Voltage<br>Current<br>Impedance | ±0.025% ± 0.01%f.s<br>±0.1% ± 0.1%f.s<br>variable |
| NI DAQ USB 6128 | Voltage acquisition | Voltage | ±0.0085% ± 0.002%f.s |
| Binder KT 53 | Temperature control | Temperature | ±0.3 K |
| Binder MKF 720 | Temperature control | Temperature | ±1 K |
| NI CDAQ 9211 w/ K-TC | Temperature measurement | Temperature | ±3 K |
| Autolab PGSTAT30+FRA2 | Impedance measurement | Impedance | variable |

**Table 2.2:** Instruments of the testing station

To perform high-precision measurements of both current, voltage and electrochemical impedance spectroscopy on the batteries, an Autolab PGSTAT30 with a FRA2 module has been occasionally employed. The list of all the test bench components is reported in Table 2.2.

The electrical scheme (see Figure 2.3) is composed by a main loop that connects the power supply and the batteries in series. Each battery has a dedicated switch that allow to put the battery in or out of the circuit:

- when the switch is open - position *a*, the battery is disconnected from the circuit and can only be discharged by the electronic load, that can drain the desired current from the battery;
- when the switch is closed - position *b*, the battery is series connected to the power supply, that can apply a fixed current, according to its range; each electronic load regulates the current that charges its respective battery, subtracting from the current applied by the power supply the amount of current that allows to reach the desired charging C-rate on the battery.

Thanks to this configuration, each battery is able to operate independently from one another, and a single power supply is needed to charge all of them.
The Autolab potentiostat, used for high precision measurements, can be connected in series to the battery to measure its current, or can be parallel connected for voltage and electrochemical impedance spectroscopy measurements, by plugging its power cables into the load corresponding to the tested battery and its sensing cables to the corresponding channel in the voltage acquisition board.

A computer is connected to the test bench, and the software LabView© is used to control the whole setup and monitor the voltage, current and temperature data. The

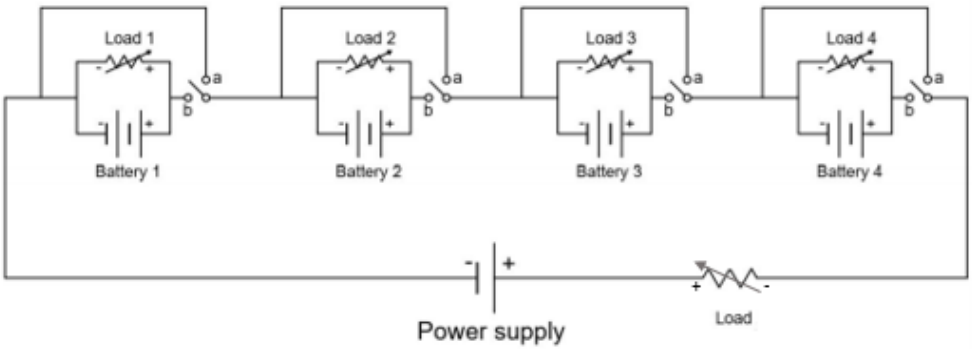


**Figure 2.3:** Electric circuit scheme

control system check that the operative conditions comply with the safety limits, to avoid that overcharge, overdischarge and overheating of the batteries do not occur, to prevent damage to the battery and the test bench itself.

These safety limits are:

The battery voltage upper and lower limits can be adjusted according to the

| | |
|---|---|
| Maximum current of the switches | **I <20A (C-rate≈8)** |
| Maximum battery voltage | **V < Vmax** |
| Minimum battery voltage | **V > Vmin** |
| Maximum battery surface temperature | **T < 65°C** |

datasheet specifications of the battery that is being tested. For the samples tested during this work, they were set to 4.2V and 2.5V, respectively 2.1.

### 2.2.1 Uncertainty analysis

**Uncertainty on voltage**

The uncertainty on the voltage value, considering that the full-scale value of the electronic load is 6V, can be computed according to the accuracy band reported by the manufacturer.

$$\sigma_V = (0.025\% + 0.01\% \cdot 6\,V) = 0.085\% \tag{2.1}$$

**Uncertainty on temperature**

The battery operative temperature is set by the climatic chamber. According to the battery manufacturer, the two chambers set the temperature with an absolute error $u_T$ of

$$\begin{aligned} &\text{Binder KT 53: } u_T = \pm 0.3K \\ &\text{Binder MKF 720: } u_T = \pm 1K \end{aligned} \tag{2.2}$$

respectively.

**Uncertainty on current measurement**

The accuracy band of the current measurement instruments, declared by manufacturers, are:

- power supply (PS) accuracy in current setting:

$$\sigma_{I,PS} = 0.5\% + 0.1\% \cdot rtg \tag{2.3}$$

  where the $rtg$ value of the power supply is equal to 150A.

- load accuracy for current setting:

$$\sigma_{I,load} = 0.1\% + 0.01\% \cdot FS \tag{2.4}$$

  where the $FS$ value is 8A, corresponding to the Constant Current Medium (CCM) Mode of the load.

During the cycling operation, the power supply provides continuously a constant current value of 6 A, while each load absorbs a portion of current, such that the batteries are reached by the desired current value. Therefore, the current that reaches the battery $I_{batt}$ can be computed as:

$$I_{batt} = I_{PS} - I_{load} \tag{2.5}$$

The uncertainty in the current setting suffers from the combination of the errors of both the instruments; applying the propagation of the uncertainties, the uncertainty on the battery current $\sigma_{I,batt}$ can be expressed as

$$\sigma_{I,batt} = \sqrt{\left(\frac{\partial I_{batt}}{\partial I_{PS}}\right)^2 \cdot \sigma_{I,PS}^2 + \left(\frac{\partial I_{batt}}{\partial I_{load}}\right)^2 \cdot \sigma_{I,load}^2} = \sqrt{\sigma_{I,PS}^2 + \sigma_{I,load}^2} \tag{2.6}$$

**Uncertainties in cycling conditions**

The cycles selected for the experimental campaign will include different operative conditions, namely charging at 1C and 0.5C and discharging at 0.2C. The current uncertainties have been computed computing Equation 2.6 for all the conditions and the results are reported in Table 2.3.

Ideally, the charge variation after a charge-discharge full cycle would be zero and computed as:

$$Q_{cycle} = (\Delta t_{charge} I_{batt,charge} - \Delta t_{discharge} I_{batt,discharge}) \tag{2.7}$$

Applying the propagation of uncertainties, a dependence on the $\Delta t$ and on $u_{I,batt}$ of both charge and discharge, is highlighted. The cycles that will be performed present

| | Charge: C-rate 1 | | Charge: C-rate 0.5 | | Discharge: C-rate 0.2 | |
|---|---|---|---|---|---|---|
| | **Current [A]** | **Uncertaninty [± A]** | **Current [A]** | **Uncertaninty [± A]** | **Current [A]** | **Uncertaninty [± A]** |
| **Load** | 3.75 | 0.01175 | 4.88 | 0.01288 | 5.55 | 0.01355 |
| **PS** | 6.00 | 0.18000 | 6.00 | 0.18000 | 6.00 | 0.18000 |
| **Battery** | 2.25 | 0.18038 | 1.13 | 0.18046 | 0.45 | 0.18051 |

**Table 2.3:** Current and uncertainties values for cycling conditions.

a CCCV charge, namely a constant current and a constant voltage step. During the CV step, the current is decreasing and therefore, the charge process will be slower in that part. Nevertheless, as the uncertainties values are almost constant, the same $u_{I,batt}$ will be considered for the whole charge duration. Moreover, as the discharges lasts much longer, since the C-rate is lower, they will constitute the main source of error. The uncertainties on the exchanged charge are estimated for the cycle conditions and reported in Table 2.4. The cycle conditions nomenclature is the following:

- A: charge 1C, discharge 0.2C, 50%-80% SOC;
- B: charge 0.5C, discharge 0.2C, 50%-80% SOC;
- C: charge 1C, discharge 0.2C, 30%-60% SOC;
- D: charge 1C, discharge 0.2C, 30%-80% SOC.

| **Cycle A** | **Cycle B** | **Cycle C** | **Cycle D** |
|---|---|---|---|
| 0.2809 | 0.2747 | 0.2913 | 0.452 |

**Table 2.4:** Uncertainties on exchanged charge. Values are reported in mAh/cycle

### Uncertainties of experimental discharges

Other experimental tests that will be performed in the experimental campaign are full discharges. The uncertainty on the cell voltage $V$ during these discharges can be expressed as:

$$u_V = \sqrt{(\sigma_V \cdot V)^2 + \left(\frac{\Delta V}{\Delta Q} \cdot u_Q\right)^2 + \left(\frac{\Delta V}{\Delta T} \cdot u_T\right)^2 + u_{OCV}^2} \tag{2.8}$$

where $\Delta V/\Delta Q$ is the voltage variation caused by a variation of exchanged charge, $\Delta V/\Delta T$ is the voltage variation related to a temperature variation and $u_{OCV}$ is the uncertainty on the initial OCV, at 100% SOC. Since these terms depend on

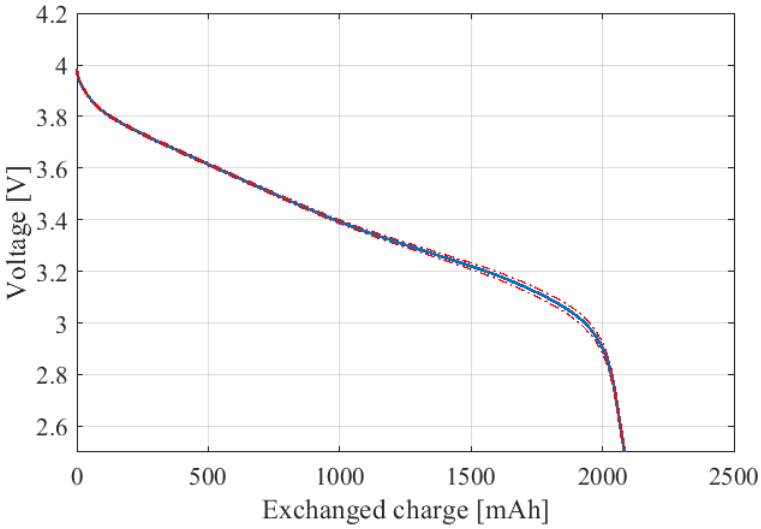


**Figure 2.4:** Error bands (in red) on the measured voltage during a full discharge from 100% SOC, at 25°C, 2C.

the C-rate, on the SOC and on the operative temperature, these values have to be computed in each specific operative conditions. The uncertainties on the cell voltages are dependent on the operating conditions and here an example is provided, for discharges at 25°C ans 2C-rate. For this case, $\Delta V/\Delta T$ is computed to be equal to 7mV/K while a single value can not be provided for $\Delta V/\Delta Q$ without introducing a relevant error. The uncertainty on the exchanged charge is computed similarly to the cycle case, considering the uncertainty on the current. $u_{OCV}$ considers the error on the starting SOC that can be present for charging at different C-rates and for the relaxation before the discharge process; it has been computed in the context of the previous thesis work analysing the experimental data, calculating the mean and the double of the standard deviation of the voltage value of the initial points of the discharge curves, assuming a normal distribution of the errors. A value of $\pm 0.0045V$ was obtained.

The results on the uncertainty on the cell voltage is depicted in Figure 2.4: the voltage error is mostly around ±7 mV and it raises up to ±15 mV in the last section of the discharge curve, where the voltage slope is higher and the uncertainty on the charge is more relevant.

### Uncertainties on impedance measurement

The employed instrument for the measurement of the cell impedance, is the electronic load, combined with the power supply. It was not possible to compute the uncertainty as the combination of the impedance, voltage and current uncertainties,

| | High frequency | Mid frequency | Low frequency |
|---|---|---|---|
| $u_{Z_R}$ $[m\Omega]$ | 5.40 | 13.1 | 13.9 |
| $u_{Z_I}$ $[m\Omega]$ | 24.5 | 2.24 | 11.6 |

**Table 2.5:** Results of the uncertainty analysis on the battery impedance

since the relationship between these quantities is very complex. Therefore, the accuracy is computed as a type A uncertainty, thanks to repeated measurements. 20 impedance measurement are performed in succession in the frequency range 10000-0.01 Hz, with 30 logarithmically spaced points, for one of the sample at 75%SOC and 25°C. Then, the uncertainty is computed as the double of the standard deviation of the measurements in every frequency point ($2\sigma$ confidence interval assuming a normal distribution of the errors), for the real part ($u_{Z_R}$) and for the imaginary part ($u_{Z_I}$):

$$\begin{aligned} u_{Z_R} &= 2 \cdot \sqrt{\frac{1}{20} \sum_{n=1}^{20} \left(\overline{Z_R} - Z_{R,n}\right)^2} \\ u_{Z_I} &= 2 \cdot \sqrt{\frac{1}{20} \sum_{n=1}^{20} \left(\overline{Z_I} - Z_{I,n}\right)^2} \end{aligned} \tag{2.9}$$

An average of the uncertainties is computed according to three frequency range: high frequency identifies the points between 10000 Hz and 100 Hz, mid frequency stands for the points between 100 Hz and 1 Hz and low frequency includes the points from 1 Hz to 0.01 Hz. The results obtained for each range are reported in Table 2.5.

## 2.3 Experimental techniques: overview

### 2.3.1 Charge and discharge curves

The charge/discharge process can be represented with a curve that relates the battery voltage and the state of charge. During a charge procedure, $Li$ ions move from the positive to the negative electrode (Chapter 1.1.1) and the cell voltage increase; the opposite happens during a discharge.
Charges and discharges can be performed at different temperatures and C-rates. Different operating conditions stress different mechanisms inside the battery and allow to study and understand different aspects of the battery behaviour. In fact, these two parameters have a strong influence on the voltage-SOC curves profile:

- the test temperature influences the lithium ion mobility: higher temperatures improve ion mobility and solid-state diffusion, reducing the cell internal impedance and overpotentials; at colder temperatures the opposite is true and the reduced ion mobility results in lower available capacity.
- the operating C-rate influences the kinetic properties of the battery, affecting voltage losses: the overpotentials increases with increasing the C-rate and this results in a lower accessible capacity and power.

In accordance with these considerations, nominal capacity of the battery is commonly measured at C-rate ranging from C/3 to 1C and at 25°C, discharging the battery from 100% SOC to the lower voltage limit [103].
To fully charge a battery up to 100% SOC two charge steps have to be performed (see Figure 2.5):

- a **constant current (CC) step**, where the current is kept at a constant value until the upper voltage limit is reached.
- a **constant voltage (CV) step**, where the upper voltage limit, reached at the end of the CC step, is kept constant while the current reduces gradually and continues to charge the battery. This charge step is done to avoid excessive degradation and extend the battery life. In fact the charge exchanged during the CV step could be provided at constant current; this would imply high voltages, higher than the upper voltage limit. This step ends when the current reaches a "termination current" that is usually around C/20. This is of course an approximation to contain the charge time that would increase extremely, selecting an even lower termination current, necessary to remove the residual voltage drop related to concentration disequilibrium.

Once 100% SOC is reached the battery can be discharged at a certain constant

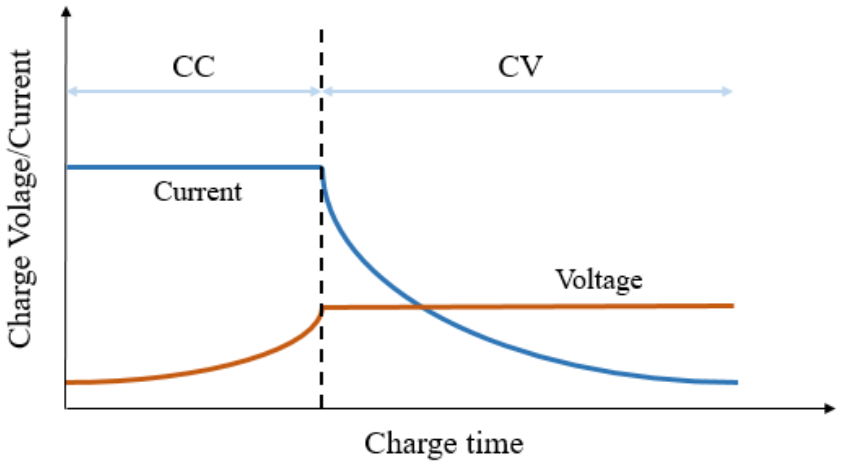


**Figure 2.5:** Examples of voltage and current profile during a CC+CV charge

current value down to the lower voltage limit; a CV step is not included in the discharge.

The voltage, the battery surface temperature, the current and the simulation time are registered during the charge/discharge test and exported as outputs. The coulomb-counting method is used to compute the exchanged capacity during the process, that basically consists of the integration of the current over time discretized according to data acquisition timesteps, as described in Equation 1.1.

### 2.3.2 IC / DV curves

Incremental capacity (IC) and differential voltage (DV) are two diagnostic tools widely used in the scientific literature works to analyze the battery OCV curve, approximated by a discharge at very low current [104]-[105], [75], [50]. They are defined as the partial derivative of capacity with respect to voltage and its opposite, respectively:

$$IC = \frac{\partial Q}{\partial V} \tag{2.10}$$

$$DV = \frac{\partial V}{\partial Q} \tag{2.11}$$

The cell voltage depends on the electrodes potentials, that are linked to lithium concentration with a complex and material-dependent relation. The battery electrodes are solid mixtures, composed by lithium and the host material; the interaction between the constituents of the electrodes and the lithium defines the mixtures' behavior, resulting in regions where phase separation occurs. The main mixture' behaviours are showed in Figure 2.6. Both the two electrodes has this behavior: as it was explained in chapter 1.5, the graphite undergoes a staging process composed

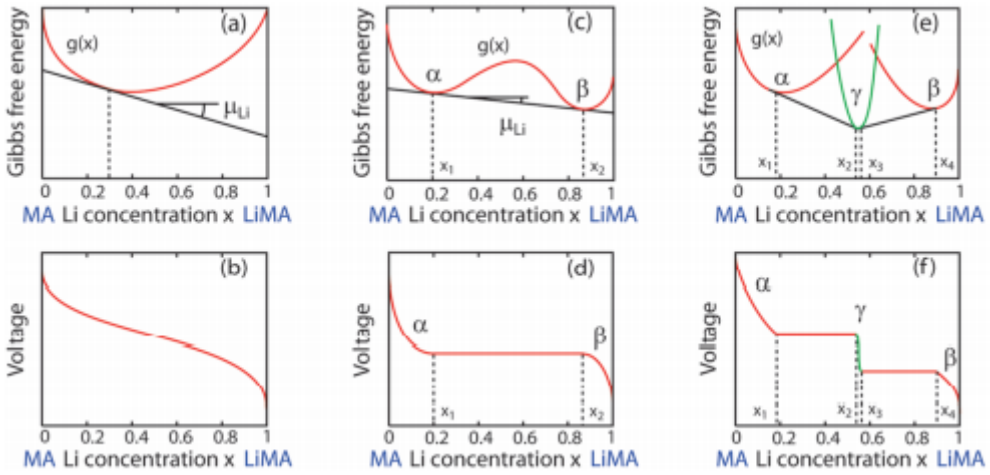


**Figure 2.6:** Examples of different open circuit potential curves, showing their correlation with the Gibbs free energy of the Li-host compound. (a) and (b): single phase solid solution; (c) and (d): two phase solid solution; (e) and (f): two phase solid solution with intermediate single phase (Taken from [106])

by the alternation of single phase regions and phase transitions, and a similar behaviour can be identified for the NMC. Therefore, the battery voltage depends on the electrodes potentials, on the maximum concentration that the their materials can accept, the number of active sites and the electrode slippage, that may cause the phase transitions of the electrodes to overlap or not. These considerations are relevant to understand the meaning of the voltage derivatives.

The IC and DV plots, that can be seen in Figure 2.7, contain similar information expressed in different ways:

- a plateau on the voltage profile is present where one or both the electrodes are going through a phase transition (Figure 2.7 (c) and (d)): this corresponds in a valley in the DV curve and a peak in the IC curve;
- during phase equilibria between phase changes the electrodes behave as solid solutions (Figure 2.7 (e) and (f)): this translates in peaks in DV and valleys in IC;
- the area underneath the DV curve corresponds to the cell voltage, while the one under the IC curve is the exchanged charge.

Incremental capacity analysis is often used to characterize state of health in aged batteries: the study of the position, the translation and the intensity variation of the peaks during the degradation is used to analyze the active material phase transformations [105], [104].

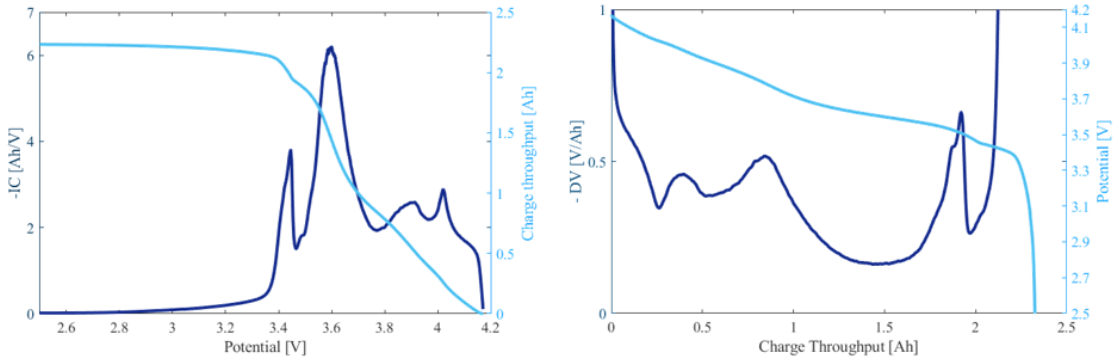


**Figure 2.7:** Examples of IC and DV curves (dark blue lines) of a discharge (light blue lines) at 0.1C and 25°C.

DV analysis enables to get information on the thermodynamic states of the battery. In fact, the profile of the curve depends on the relative position of the electrodes intercalation curves. As it changes with aging, similarly to the IC curve, the DV is used to estimate the state of health of the battery [107], assessing the degradation as loss of cyclable ions and reduction of active material in the electrodes.
For both IC and DV to be reliable, they have to be performed at small current rates (lower than C/6 [108]) to reduce diffusion effects and resistance that would drop out of the quasi-steady sate assumption.

### 2.3.3 Relaxation curves

The relaxation test is an experiment performed at open circuit condition, after the battery state has been perturbed. In this way, the trend of the voltage allows to study the transient behaviour of the battery to reach equilibrium. What can be observed is that the voltage increases after the end of a discharge and decreases after the end of a charge, with a trend similar to a decaying exponential. The voltage profile during relaxation can be analyzed, also by looking at its derivative in time. It can provide useful information as the voltage profile is linked to the lithium concentration gradient.
An example of the voltage profile during a discharge and the subsequent relaxation is reported in Figure 2.8.
In fact, the relaxation process is driven by an electrochemical re-equilibration process, that is related to the battery geometry, its composition, the concentration of lithium in the electrolyte and to the chemistry and the size of the electrodes.
One of the main phenomena that plays a role in the re-equilibration process is the lithium diffusion process. Indeed, lithium concentration gradients generates in the electrolyte and in the electrodes solid particles as a consequence of a sufficiently

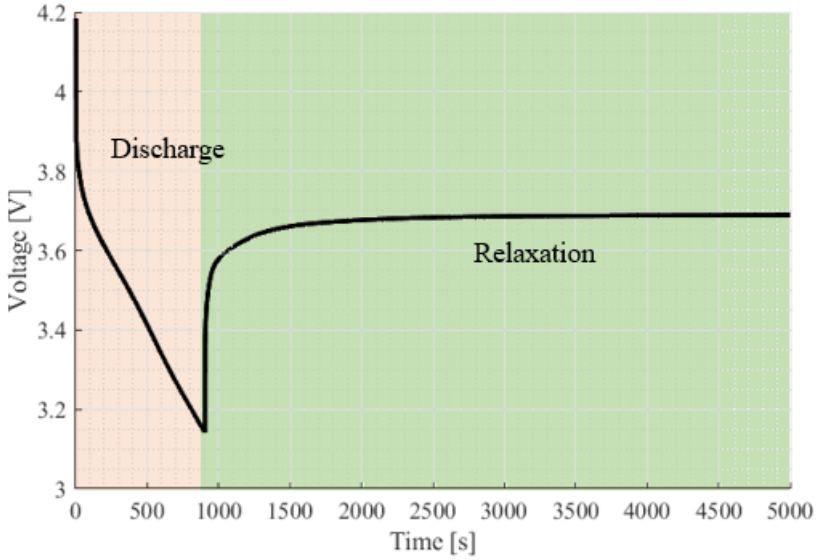


**Figure 2.8:** Examples of voltage profile during relaxation after a discharge 100%-50% at 2C and 10°C.

intense and extended current pulse, and the significance of these gradients increases with the pulse duration, the current magnitude and low temperatures. The characteristic time of the diffusion process is computed as:

$$\tau_D = \frac{L_c^2}{D} \tag{2.12}$$

where $D$ is the diffusion coefficient and $L_c$ is the diffusion characteristic length, namely it is the electrode length for the diffusion in the electrolyte and the radius of the solid particle for the solid diffusion. Generally, the diffusion in the electrode ($\tau_{D,s} \in [10^2 s - 10^3 s]$) is roughly one order of magnitude slower that the diffusion in the electrolyte ($\tau_{D,e} \in [10^1 s - 10^2 s]$) [109]. Then, concentration gradients can require a long time to flatten completely, as the diffusion driving force decreases gradually.

Therefore, the study of relaxation can be very helpful for the degradation detection, as it provides information on the lithium concentration in the electrolyte and in the solid, on the transport properties (bulk and in the electrolyte) and on the electrodes' structure and chemistry [110].

### 2.3.4 Electrochemical Impedance Spectroscopy

The Electrochemical Impedance Spectroscopy (EIS) measurements are conducted to analyse the kinetic behaviour of the cell, superimposing a sinusoidal current $I$ with frequency $f$ on a steady state condition and recording the voltage response $V$.
The measured impedance is the composition of a real and an imaginary part, and

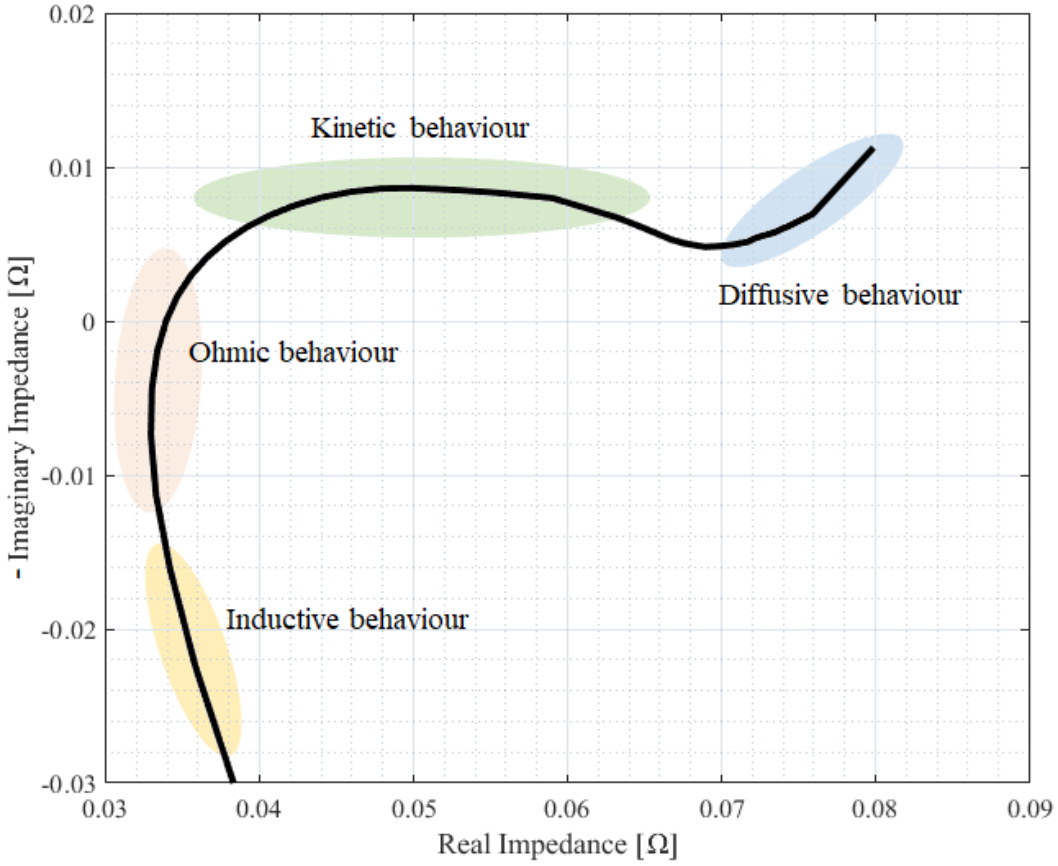


**Figure 2.9:** Example of Nyquist plot obtained with the EIS at 100% SOC and 25°C

can be computed as:

$$Z(w) = \frac{V(w)}{I(w)} = \frac{V_0 e^{i\phi_1(w)}}{I_0 e^{i\phi_2(w)}} = Z_0 e^{i(\phi_1(w)-\phi_2(w))} = Z_0(cos(\phi(w)) + isin(\phi(w)) \quad (2.13)$$

In the equation, $w$ is the angular frequency, that is computed as the frequency $f$ multiplied by $2\pi$; $Z_0$ is the impedance module, namely the ratio between the voltage and current amplitude and $\phi$ is the phase shift between the sinusoids of voltage (that has a phase $\phi_1$) and current ($\phi_2$). The impedance $Z$ is usually represented graphically on the Nyquist plot, where the real part and the imaginary part of the impedance are the axis $x$ and $y$, respectively. As a battery is a typically capacitive device, the imaginary contribution of the impedance is mostly negative and conventionally, the y-axis is reversed. To maintain the information about the frequency, the Bode plots are usually coupled with the Nyquist plot, where the imaginary and real parts of the impedance are depicted against the frequency.

The EIS relies on three main hypothesis: causality, namely the response is caused by the imposed input only, stability, meaning that the response of a certain system does

not change when repeating the input perturbation several times, and linearity. This third assumption is verified if the superposition principles holds true. Generally, electrochemical systems are non linear, but they can be approximated as pseudo-linear if the output voltage oscillation has a small amplitude (indicatively under 10mV), therefore, the battery is responding in a linear way to the current perturbation. To verify these assumptions, the experimental data are typically controlled by employing the Kramers-Kronig analysis [111].

The EIS test is very useful to characterize the battery behaviour. In fact, as each phenomenon inside the battery has a specific characteristic time, the different frequency ranges of the EIS test allow to solicit and distinguish those phenomena singularly. According to these frequency ranges, four regions that describe a distinctive battery behaviour can be identified (see Figure 2.9):

- **Inductive behavior** (f>2000 Hz) In this frequency range what prevails is the battery wires induction [112]. This contribution is theoretically purely imaginary and can be computed as:

$$Z(w) = i(2\pi w L_w) \tag{2.14}$$

  where $L_w$ indicates the cables inductance.

- **Ohmic behavior** (2000 Hz<f<500 Hz) The impedance value of the crossing point with the x-axis of the curve in the Nyquist plot, namely the point where the imaginary part is zero, is named high frequency resistance (HFR) [112]. This value accounts for the purely ohmic battery behaviour and characterize the instantaneous voltage drop that is visible when discharging/charging the battery.

- **Kinetic behavior** ($R_{ct}$) (500 Hz<f<0.5 Hz) This frequency range is related to the charge transfer resistance ($R_{ct}$) that characterize the kinetics of the intercalation reactions and the double layer behaviour of the solid-liquid (electrode/-electrolyte) interface [113], [114]. Hence, the impedance of each electrode can be written as:

$$Z_{ct} = -\frac{1}{\frac{1}{R_{ct}} + i\, w C_{dl}} \tag{2.15}$$

  where $C_{dl}$ is the double layer capacitance and the charge transfer resistance $R_{ct}$ can be modeled as:

$$R_{ct} = \frac{RT}{i_0 F} \tag{2.16}$$

  where $i_0$ is the exchange current density (it will be defined as in Equation (4) in Table 2.7) that describes the intercalation/deintercalation reactions in the

Butler-Volmer equation (Equation (3) in Table 2.7).
In the battery impedance spectrum one or more semicircle-like shapes can be observed, with the real part monotonously increases and the imaginary part shows a maximum and a minimum. The higher the value of $C_{dl}$, the lower the frequency at which the semicircle is manifested.

- **Diffusive behavior** (f<1 Hz) At these low frequencies, the lithium diffusion is the more solicited phenomenon [114]; the impedance is therefore influenced by the electrodes porosity, the lithium diffusion coefficients in the electrodes and in the electrolyte and the particle radii distribution.

Temperature has a strong impact on the shape of the impedance spectrum. As a general trend, the phenomena are promoted at high temperature, reducing the characteristic times. Consequently, the frequencies at which the spectrum can be identified are usually higher, while the impedance module is smaller, especially at mid-low frequencies [115].
The SOC instead has minor impact, that becomes more relevant at extreme SOC condition [10], where the electrodes are fully lithiated or near depletion and the interfacial reaction have limited kinetics.

## 2.4 Lithium-ion battery model

The electrochemical model (EM) used in this work was selected, developed and improved in the previous thesis works [102], [109]. It is a commercial model that exploits the "Battery & Fuel cells Module" of COMSOL Multiphysics.
It is a mechanistic model, namely it consists of a number of correlations, usually partial differential equations (PDEs), that combine the geometrical, electrochemical and thermal properties of the lithium ion battery in order to reproduce its physical behaviour. This kind of model brings some advantages: it is possible to replicate many complex phenomena in an accurate way, such as heat transfer, lithium plating and some other degradation mechanisms. Moreover, the parameters used in the correlations are often directly measurable, hence it is possible to find information on the range in which they should lie in the literature. The main disadvantage of a mechanistic model is that it requires a high computational time to provide accurate results. In fact, the partial differential equations have to be solved numerically and they involve a large number of parameters in complex models. Furthermore, those parameters will depend on the size and the chemistry of the battery modeled and they should be tailored properly. In particular, it is based on the Doyle-Fuller-Newman pseudo-two dimensional electrochemical model (P2D) [11] and it was adapted and developed in the previous theses on the same topic.

### 2.4.1 Model description

The battery electrochemical domain is composed by three main components: the negative electrode, the separator and the positive electrode. The current collectors are not modeled. Each component contains a number of nodes, placed along the dimension $x$, forming a 1D mesh, in which the model computes the PDEs. The nodes belonging to the electrodes domain represent the solid particles of the electrodes and they are modeled as spheres, thanks to the introduction of an additional radial dimension $r$: in additional nodes along this radius, the solid diffusion PDEs are computed. Hence, the model is named "pseudo-two-dimensional" because, even if two dimensions ($x$, $r$) are present, most of the PDEs of the model are solved only along $x$. A real battery electrode is composed by solid particles characterized by a complex distribution of particle radii; for sake of simplicity, the model consider the solid particles of each electrodes as equal spheres with radius $R_p$, the average value of that distribution. A schematic representation of the Fuller-Doyle-Newman P2D model domain can be seen in Figure 2.10.

Moreover, a 2D thermal model is coupled to the electrochemical one, to account both for the ambient temperature dependency of the physical parameters and the

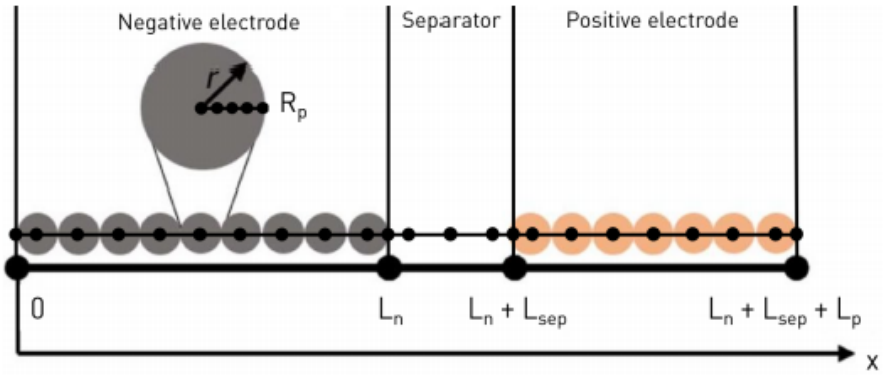


**Figure 2.10:** Representation of the Fuller-Doyle-Newman P2D model domain. (Taken from [109])

battery heating that occurs during operation at high C-rates. Therefore, the thermal model provides the electrochemical model with the value of the surface temperature of the battery, while the electrochemical model compute the heat generated by the electrochemical reactions and hand it to the thermal model, as depicted in Figure 2.11.

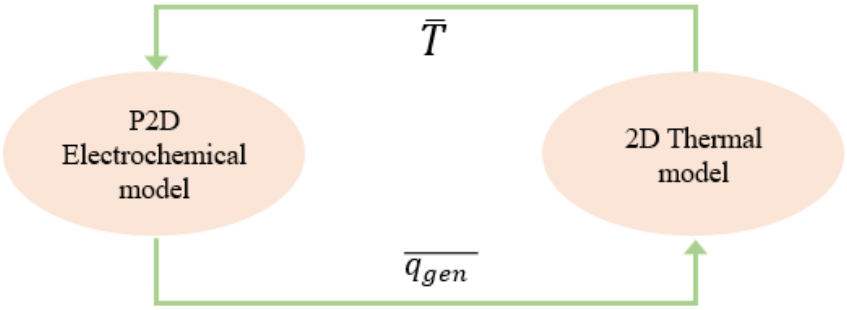


**Figure 2.11:** Scheme of the connection between electrochemical and thermal models.

All the quantities used in the model's equations are reported in Table 2.6.

### 2.4.2 Model Equations

The main governing equations of the P2D electrochemical model are listed in Table 2.7. They describes the physical and chemical processes, such as ion diffusion, migration, transport and electrochemical kinetics and also the thermal phenomena, related to energy conservation, heat generation and exchange, also occur during charge or discharge.

Equation (1) in Table 2.7 represents the **electrolyte material balance**: the accumulation term of lithium in the electrolyte is equal to the sum of the diffusion, the

| Symbol | Description |
|---|---|
| ***Latin*** | |
| $a\,[m^{-1}]$ | Specific active area |
| $A_{el}\,[m^2]$ | Electrode area |
| $c\,[mol\,m^{-3}]$ | Lithium concentration |
| $C\,[J\,kg^{-1}K^{-1}]$ | Specific heat |
| $C_{dl}\,[Fm^{-2}]$ | Double layer capacitance |
| $D\,[m^2s^{-1}]$ | Lithium diffusion coefficient |
| $EA_k\,[J\,mol^{-1}]$ | Rate constant activation energy |
| $EA_{D_s}\,[J\,mol^{-1}]$ | Solid diffusion activation energy |
| $E_{ocv}\,[V]$ | Electrode open circuit potential |
| $F\,[A\,s\,mol^{-1}]$ | Faraday constant |
| $FCE\,[-]$ | Ionic conductivity factor |
| $h\,[W\,m^{-2}\,K^{-1}]$ | Heat transfer coefficient |
| $i\,[A\,m^{-2}]$ | Current density |
| $i_0\,[A\,m^{-2}]$ | Exchange current density |
| $I\,[A]$ | Current |
| $j\,[mol\,m^{-2}]$ | Lithium molar flux |
| $k\,[m\,s^{-1}]$ | Rate constant |
| $k_T\,[W\,m^{-1}\,K^{-1}]$ | Thermal conductivity |
| $L\,[m]$ | Cell component length |
| $n[-]$ | Number of charges |
| $q\,[W\,m^{-3}]$ | Volumetric heat flux |
| $Q\,[A\,s]$ | Capacity |
| $r\,[m]$ | Battery component radius |
| $R\,[J\,mol^{-1}K^{-1}]$ | Gas constant |
| $R_b\,[m]$ | Battery total radius |
| $R_{ext}\,[\Omega m^2]$ | External resistance |
| $R_{film}\,[\Omega m^2]$ | Film resistance |
| $R_p\,[m]$ | Particle radius |
| $SOC\,[-]$ | State of charge |
| $t_0^+\,[-]$ | Lithium transference number |
| $T\,[K]$ | Battery temperature |
| $\Delta V\,[V]$ | Cell voltage |
| | |
| ***Greek*** | |
| $\alpha\,[-]$ | Transfer coefficient |
| $\varepsilon\,[-]$ | Battery material fraction |
| $\eta\,[V]$ | Overpotential |
| $\kappa_e\,[S\,m^{-1}]$ | Electrolyte ionic conductivity |
| $\kappa_D\,[A\,m^{-1}]$ | Electrolyte diffusion conductivity |
| $\phi\,[V]$ | Electric potential |
| $\rho\,[kg\,m^{-3}]$ | Density |

| Symbol | Description |
|---|---|
| ***Subscript*** | |
| $a$ | anodic |
| $am$ | active material |
| $ax$ | axial |
| $c$ | cathodic |
| $conv$ | convective |
| $e$ | electrolyte |
| $gen$ | generated |
| $i$ | inactive material |
| $man$ | mandrel |
| $max$ | maximum |
| $min$ | minimum |
| $n$ | negative |
| $nom$ | nominal |
| $ohm$ | ohmic |
| $p$ | positive |
| $r$ | reaction |
| $rad$ | radial |
| $rev$ | reversible |
| $s$ | solid |
| $sep$ | separator |
| | |
| ***Superscript*** | |
| $eff$ | effective |
| | |
| ***Coordinate*** | |
| $r$ | radial coordinate |
| $x$ | linear coordinate |
| $z$ | axial coordinate |
| $\theta$ | angular coordinate |
| $t$ | time |

**Table 2.6:** List of symbols, subscripts and superscripts used in the model description.

**(1) Electrolyte material balance**

Equation: $\varepsilon_e \frac{\partial c_e}{\partial t} = \frac{\partial}{\partial x}\left(\varepsilon_l D_e^{eff} \frac{\partial c_e}{\partial x}\right) - \frac{i_e \frac{\partial t_+^0}{\partial x}}{nF} + a j_r \left(1 - t_+^0\right)$

Boundary conditions:
$$\begin{cases} \frac{\partial c_e}{\partial x}\Big|_{x=0} = \frac{\partial c_e}{\partial x}\Big|_{x=L_n+L_{sep}+L_p} = 0 \\ -D_e^{eff} \frac{\partial c_e}{\partial x}\Big|_{x=L_n^-} = -D_e^{eff} \frac{\partial c_e}{\partial x}\Big|_{x=L_n^+} \\ -D_e^{eff} \frac{\partial c_e}{\partial x}\Big|_{x=L_n+L_{sep}^-} = -D_e^{eff} \frac{\partial c_e}{\partial x}\Big|_{x=L_n+L_{sep}^+} \end{cases}$$

**(2) Solid phase diffusion**

Equation: $\frac{\partial c_s}{\partial t} = \frac{1}{r^2}\frac{\partial}{\partial r}\left(D_s r^2 \frac{\partial c_s}{\partial r}\right)$

Boundary conditions:
$$\begin{cases} \frac{\partial c_s}{\partial r}\Big|_{r=R_p} = -\frac{j_{loc}}{D_s} \\ \frac{\partial c_s}{\partial r}\Big|_{r=0} = 0 \end{cases}$$

**(3) Electrochemical kinetics (Butler-Volmer equation)**

$$i_r = nF j_r = i_0 \left(e^{\frac{\alpha_a F}{RT}\eta} - e^{\frac{-\alpha_c F}{RT}\eta}\right)$$

**(4) Exchange current density**

$$i_o = F\left(k_c\right)^{\alpha_a}\left(k_a\right)^{\alpha_c}\left(c_{s,max} - c_s\right)^{\alpha_a}\left(c_s\right)^{\alpha_c}\left(\frac{c_e}{c_{e,0}}\right)^{\alpha_a}$$

**(5) Reaction overpotential**

$$\eta = \varphi_s - \varphi_e - E_{ocp} - i_r R_{film}$$

**(6) Solid phase charge balance**

Equation: $i_s = -\sigma_s^{eff} \frac{\partial \varphi_s}{\partial x}$

Boundary conditions:
$$\begin{cases} \varphi_s|_{x=0} = 0 \ \frac{\partial \varphi_s}{\partial x}\Big|_{x=L_n^-} = \frac{\partial \varphi_s}{\partial x}\Big|_{x=L_n+L_{sep}^+} = 0 \\ \frac{\partial \varphi_s}{\partial x}\Big|_{x=L_n+L_{sep}+L_p} = -\frac{i_s}{\sigma_s^{eff}} \end{cases}$$

**(7) Electrolyte potential**

Equation: $i_e = -\kappa_e^{eff} \frac{\partial \varphi_e}{\partial x} + \frac{2\kappa_e^{eff} RT}{F}\left(1 + \frac{\partial \ln f_\pm}{\partial \ln c_e}\right)\left(1 - t_+^0\right)\frac{\partial \ln c_e}{\partial \ln x}$

Boundary conditions:
$$\begin{cases} \frac{\partial \varphi_e}{\partial x}\Big|_{x=0} = \frac{\partial \varphi_e}{\partial x}\Big|_{x=L_n+L_{sep}+L_p} = 0 \\ \varphi_e|_{x=L_n^-} = \varphi_e|_{x=L_n^+} \\ \varphi_e|_{x=L_n+L_{sep}^-} = \varphi_e|_{x=L_n+L_{sep}^+} \end{cases}$$

**(8) Charge conservation**

$$\frac{\partial i_e}{\partial x} = -\frac{\partial i_s}{\partial x} = nF a j_r + a C_{dl} \frac{\partial(\Phi_e - \Phi_s)}{\partial t}$$

**(9) Terminal voltage**

$$\Delta V = \varphi_s|_{x=L_n+L_{sep}+L_p} - \varphi_s|_{x=0} - \frac{R_{ext} I}{A_e l}$$

**Table 2.7:** Governing equations and boundary conditions of the pseudo two-dimensional (P2D) model.

migration and the source terms, namely the reactions. In the separator the source term is equal to zero, as no reactions occur in the separator. For what concerns the boundary conditions, the lithium-ion transport is continuous at the interfaces between the two electrodes, and the walls that contain the battery are impermeable. The solid particles are modeled as spheres, and the diffusion Fick's law is solved in the additional nodes along their radial dimension, as described by equation (2); lithium flux is considered zero in the symmetrical condition and equal to the local reaction lithium flux at the particle surface.

The **local reaction current density** $i_r$ can be computed by way of the Butler-Volmer equation (3), as a function of the overpotential of the electrochemical reactions $\eta$, that is expressed as in equation (5): $R_{film}$ is the resistance of the passive films on the surface of the active electrode particles, that is modeled as a film without thickness, and the open circuit potential $E_{ocp}$ is computed from lookup tables of the two electrodes (Figure 3.5).

The **exchange current density** $i_o$ is computed as in equation (4), and since the transfer coefficient $\alpha_a$ and $\alpha_c$ are considered equal to 0.5, and the anodic and cathodic reaction rates $k_a$ and $k_c$ are assumed to be a generic electrode reaction constant k, simplifies into:

$$i_o = Fk\sqrt{(c_{s,max} - c_s)\,(c_s)}\sqrt{\frac{c_e}{c_{e,0}}} \tag{2.17}$$

The role of the concentration-related terms is to vary the exchange current density according to the lithium availability in the electrode and in the electrolyte. The **current density in the solid** $i_s$ is computed with Ohm's law as can be seen in equation 6. The potential in the solid $\phi_s$ is set to 0 on the negative electrode left boundary, to be taken as a reference point; moreover, both the current density in the solid and the potential gradient are equal to 0 at the interfaces between the separator and electrodes, as only the electrolyte is present in the separator.

The **current density in the electrolyte** $i_e$, as can be seen in equation (7), is formed by a part related to Ohm's law and another part that consider the ions' transport by the concentration gradients.

The **total current density** $i$ can be computed as the sum of the electrolyte and the solid current densities:

$$i = i_e + i_s \tag{2.18}$$

The derivative of the current density in the solid and in the electrolyte are related by the equation (8), that is composed by the sum of the reaction current density, named faradaic current, and the current density in the double layer, called non faradaic current. In equation (8), $a$ is the active surface-to-volume ratio, that is

computed as

$$a = 3\frac{\varepsilon_{s,am}}{R_p} \tag{2.19}$$

since the particles are spherical. $\varepsilon_{s,am}$ is the active solid fraction, that is equal to zero in the separator, due to the lack of active material.
A mass balance of the constituents can be written in each electrodes and in the separator:

$$\varepsilon_e + \varepsilon_s = \varepsilon_e + \varepsilon_{s,am} + \varepsilon_{s,i} = 1 \tag{2.20}$$

where $\varepsilon_{s,i}$ is the inactive solid material fraction, namely the binder, the conductive additives and the electrode part that lost electric contact.

In equation (1) the effective lithium diffusion coefficient in the electrolyte $D_e^{eff}$ also consider the tortuosity effect of the porous electrode through the Bruggeman correlation:

$$D_e^{eff} = D_e \varepsilon_l^{1.5} \tag{2.21}$$

Similarly, in equations (6) and (7), Bruggeman correlation is used to account for the effect of tortuosity, respectively, on the electrode electric conductivity $\sigma_s^{eff}$:

$$\sigma_s^{eff} = -\sigma_s \varepsilon_s^{1.5} \tag{2.22}$$

and on the ionic conductivity of the electrolyte $\kappa_e^{eff}$:

$$\kappa_e^{eff} = \kappa_e \varepsilon_l^{1.5} \tag{2.23}$$

The **overall current** $I$ is given by the product of the total current density and the electrode area:

$$I = A_{el} \cdot i \tag{2.24}$$

The model measures the **cell voltage** $\Delta V$ as the sum between the OCP, the overpotential and the voltage drop related to an external resistance that accounts for current collectors and cables resistances (see equation (9)).

The equations through which the model computes the battery capacity will be discussed in Chapter 3.2.2.

### 2.4.3 Thermal model Equations

The cylindrical battery is modeled in the thermal model as a 2D geometry with radial symmetry, composed by three layers which represent the steel can, the active material and the central mandrel, as can be seen in Figure 2.12. In all these three regions, the model solves the heat transfer equation and at the boundaries between them, the heat flux continuity holds true.

The main equations governing the thermal model are reported in Table 2.8.

**(10) Energy balance**

Equation: $\frac{1}{r}\frac{\partial}{\partial r}\left(rk_T\frac{\partial T}{\partial r}\right)+\frac{\partial}{\partial z}\left(k_T\frac{\partial T}{\partial z}\right)+\overline{q_{gen}}=\rho C\frac{\partial T}{\partial t}$

Boundary conditions:

$$\begin{cases}\frac{\partial T}{\partial r}\big|_{r=0,\,z\in[0,H]}=0\\ -k_T\,\frac{\partial T}{\partial r}\big|_{r=r_{md}^-,\,z\in[0,H]}=k_T\,\frac{\partial T}{\partial r}\big|_{r=r_{md}^+,\,z\in[0,H]}\\ -k_T\,\frac{\partial T}{\partial r}\big|_{r=r_{md}+r_{am}^-,\,z\in[0,H]}=k_T\,\frac{\partial T}{\partial r}\big|_{r=r_{md}+r_{am}^-,\,z\in[0,H]}\\ -k_T\,\frac{\partial T}{\partial r}\big|_{r=R_b^-,\,z\in[0,H]}=h_{conv}\left(T-T_{amb}\right)\big|_{r=R_b^+,\,z\in[0,H]}\\ -k_T\,\frac{\partial T}{\partial z}\big|_{r\in[0,R_b],\,z=(0,H)^-}=h'_{conv}\left(T-T_{amb}\right)\big|_{r\in[0,R_b],\,z=(0,H)^+}\end{cases}$$

**(11) Ohmic heat**

$$q_{ohm}=\sigma_s^{eff}\left(\frac{\partial\varphi_s}{\partial x}\right)^2+\kappa_e^{eff}\left(\frac{\partial\varphi_e}{\partial x}\right)^2+\kappa_e^{eff}\frac{\partial\ln c_e}{\partial x}\frac{\partial\varphi_e}{\partial x}$$

**(12) Reaction heat generation**

$$q_r=ai_r\eta$$

**(13) Reversible (entropic) heat**

$$q_{rev}=ai_rT\frac{\partial E_{ocp}}{\partial T}$$

**(14) Arrhenius' law**

$$k=k_0\,e^{\frac{EA_k}{R}\left(\frac{1}{T_0}-\frac{1}{T}\right)}\quad D_s=D_{s,0}\,e^{\frac{EA_D}{R}\left(\frac{1}{T_0}-\frac{1}{T}\right)}$$

**(15) Open circuit potential**

$$E_{ocv}=E_{ocv,0}+T\frac{\partial E_{ocv}}{\partial T}$$

**Table 2.8:** 2D Thermal model equations

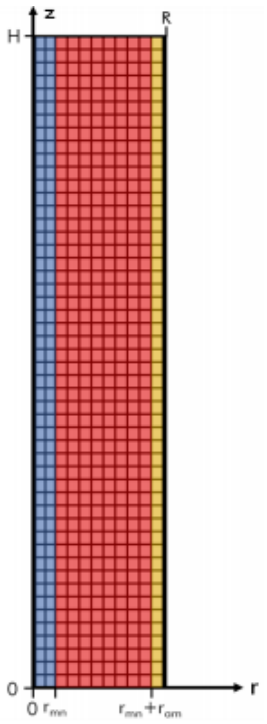


**Figure 2.12:** Geometry of the 2D cylindrical LIB thermal model. Blue area: mandrel; Red area: active material; Yellow area: steel casing. (Taken from [109])

Equation (10) describes the 2D heat conduction and is solved numerically by COMSOL in the nodes of a 2D mesh. Convective heat transfer equations describes the boundary conditions for the external surfaces, where two different convective heat transfer coefficient are employed, for the top and bottom surfaces and for the lateral surface, respectively. The internal heat generation term $\overline{q_{gen}}$ is present only where the electrochemical reactions occur, hence, only in the active material layer. Moreover, $\overline{q_{gen}}$ is the only unknown parameter of the thermal model, and has to be computed by the electrochemical model as

$$q_{gen} = q_{ohm} + q_r + q_{rev} \tag{2.25}$$

where:

- $q_{ohm}$ is the **ohmic heat** generated in the battery because of the Joule effect; it accounts for the heat generated by the passage of current in the electrodes' solid particles, in the electrolyte and the heat generated by ionic migration (see equation (11) in Table 2.8);
- $q_r$ is the **reaction heat** that is generated by the irreversibilities of the electrochemical reactions, computed as written in equation (12);
- $q_{rev}$ is the **reversible heat** generated by the electrodes' entropy change (equation (13)).

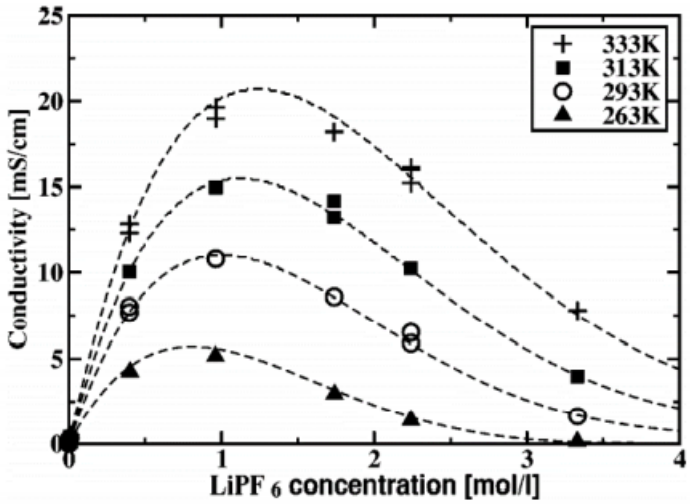


**Figure 2.13:** Trend of the electrolyte ionic conductivity with concentration and temperature given by the correlation of equation 2.26 (taken from [116])

The volumetric heat generation computed by the P2D model is computed in each node of the 1D mesh, and is averaged on the length of the battery $L$ at each timestep, in order to get a single volumetric heat generation term $\overline{q}_{gen}$ to give to the thermal model.
On the other hand, the P2D model accepts only one temperature value, while the thermal model compute a 2D temperature distribution in the active material. The said distribution has to be averaged on the area of the active material.

Temperature dependency is also implemented for the parameters that are more sensible to its variation.

An empirical correlation of temperature and lithium concentration in the electrolyte is adopted for the computation of the **electrolyte ionic conductivity** [116].

$$\begin{aligned}\kappa_e = FCE(10.5 + 0.0740\,T - 6.96 \cdot 10^{-5} + 0.668 c_e - 0.0178 c_e T + \\ + 2.8 \cdot 10^{-5} c_e T^2 + 0.494 c_e^2 - 8.86 \cdot 10^{-4} c_e^2 T)^2\end{aligned} \tag{2.26}$$

The trend of the ionic conductivity imposed by the correlation is showed in Figure 2.13. FCE is a constant that allows to scale the ionic conductivity obtained from the correlation in order to adapt it to the specific battery.
The **lithium diffusion coefficient in the electrolyte** is directly linked to the ionic conductivity through the Nernst-Planck equation [117]:

$$D_e = \frac{\kappa_e R T}{F^2 c_e} \tag{2.27}$$

Another empirical correlation [116] is used to express the **activity coefficient** re-

lation with the temperature and the lithium concentration in the electrolyte:

$$\left(1+\frac{\partial \ln f_{pm}}{\partial \ln c_e}\right) = 1+\frac{c_e}{c_{e,ref}}\left[\frac{-1.0189}{21+0.9831\sqrt{c_e}}\left(\frac{1}{\sqrt{c_e}}-\frac{0.9831}{1+0.9831\sqrt{c_e}}\right)+1.5842\right] \tag{2.28}$$

The electrodes **rate constant** $k$ and **lithium diffusion in the solid material** $D_s$ have both an Arrhenius-type relation with temperature (see equation (14) in Table 2.8).

Each electrode **open circuit potential** has an additional term for the reversible heat generation (equation (15)).

## 2.5 PSO algorithm

Particle Swarm Optimization (PSO) is a population-based stochastic optimization algorithm. It was developed by Kennedy and Eberhart in 1995 [118] and it attracted increasing attention for researches in the subfield of Artificial Intelligence, known as "Swarm intelligence" [119].
The general idea behind this optimization technique is inspired by social behaviour of animals, as the movement in a bird flock or fish school. What has been observed is that, thanks to the sharing of information among the members of a group, the individuals can profit from the other members discoveries and previous experience. The algorithm is simple to implement and it is quite robust. On the other hand, it is important that the solutions' space is explored in a proper way, to guarantee the convergence. In the literature, some works implementing this algorithm for the parameter calibration of lithium-ion batteries can be found [120], [121].

The system is initialized generating a population of particles, each one consisted of a set of solutions, randomly generated within pre-established ranges. These set of values define a determined position in the solutions' space, namely the position of the particles. This particle "swarm" will have the role of exploring the solution space by updating generations to find the optimal position, i.e. the position that optimizes the cost value. In fact, a cost function is computed to evaluate the quality of each set of solutions. Every particle tracks the information on its own personal best position, $P_i$, and on the global best solution found by the whole swarm, $P_g$. These data are used by the algorithm to determine the particles velocity and, hence, the the particles position in the next iteration.

The way in which the swarm can evolve is described by the following equation:

$$P_i^{k+1} = P_i^k + V_i^{k+1} \tag{2.29}$$

Namely, the position of particle $i$ in the subsequent iteration $P_i^{k+1}$ is equal to the sum of its current position and the velocity. The velocity is computed for each iteration as:

$$V_i^{k+1} = V_i^k w + c_1 rand_1 \left[P_i - P_i^k\right] + c_2 rand_2 \left[P_g^k - P_i^k\right] \tag{2.30}$$

where:

- $V_i^k$ is the velocity of particle $i$ at iteration $k$, and thus $V_i^{k+1}$ is the velocity of that same particle at the following iteration;
- $P_i$ is the best position of particle $i$, namely the position that obtained the best cost, of all the iteration so far and $P_g^k$ is the best global solution in the swarm;

- $w$ is the inertia coefficient: it multiplies to the velocity of the previous iteration to keep track of the information of the previous iteration;
- $c_1$ is the self-confidence factor or competitive velocity coefficient, that multiplies a velocity term that makes the particles stay close to their personal minimum;
- $c_2$ is the swarm-confidence factor or collaborative velocity factor, that multiplies a velocity term that makes the particles move towards the global optimum;
- $rand_1$ and $rand_2$ are random values in the range [0,1] to ensure that the space is better covered and to reduce the possibility of stopping in local optima.

Particles' velocity and position are limited to avoid that the particles get out of the solution space:

$$\begin{cases} if P_i < P_{min}, P_i = P_{min} \\ if P_i < P_{max}, P_i = P_{max} \end{cases} \qquad \begin{cases} if V_i < V_{min}^k, V_i^k = V_{min}^k \\ if V_i^k < V_{max}^k, V_i^k = V_{max}^k \end{cases} \tag{2.31}$$

The number of particles that explore the solution space is a free variable; of course, the higher this value, the better the way that the space is explored, but the higher the time required for the simulation of one iteration. When the maximum number of iteration $I_{max}$ is reached, or the cost value crosses a certain threshold, the optimization stops.

In the previous thesis on the same project, a PSO like the one just described was developed, to calibrate some of the main battery parameter in the physical model, finding the optimal parameters according to the comparison with a certain set of experimental data.
In that context, a sensitivity analysis of the model parameters was carried out in order to understand the effect of the variation of the model parameters when simulating tests performed also experimentally, and to finally identify some operating conditions and measurements where the parameters showed the highest sensitivity value. That work resulted in the selection of 22 parameters of the P2D model and the identification of an experimental protocol, that consists in a set of measurements performed at the operating conditions that guarantees the best compromise for the good identification of the parameters.

**Parameters**
The parameters of the battery model that are subjected to the optimization are listed in Table 2.9. Parameters dedicated to the thermal aspect of the battery

operation are also present.

The values assumed to limit the range of variation of the parameters are reasonable

| Parameter | Name in the model | Range |
|---|---|---|
| Rate constant of the cathode** | $k_{pos}[-]$ | $[2.5 \cdot 10^{-11}; 1 \cdot 10^{-8}]$ |
| Rate constant of the anode** | $k_{neg}[-]$ | $[2.5 \cdot 10^{-11}; 1 \cdot 10^{-8}]$ |
| Ionic conductivity factor | $FCE[-]$ | $[0.02; 0.7]$ |
| Radius of the cathode* | $R_{p,pos}[m]$ | $[2 \cdot 10^{-6}; 12.5 \cdot 10^{-6}]$ |
| Radius of the anode | $R_{p,neg}[m]$ | $[2 \cdot 10^{-6}; 12.5 \cdot 10^{-6}]$ |
| Double layer conductivity of the cathode$^{+}$ | $C_{dl,pos}[F\,m^{-2}]$ | $[0.05; 25]$ |
| Double layer conductivity of the anode$^{+}$ | $C_{dl,neg}[F\,m^{-2}]$ | $[0.05; 25]$ |
| Negative electrode film resistance$^{++}$ | $R_{film,neg}[\Omega\,m^2]$ | $[0.001; 0.05]$ |
| Positive solid conductivity* | $\sigma_{s,pos}[S\,m^{-1}]$ | $[1; 10]$ |
| Rate constant activation energy of the cathode | $EA_{k,pos}[J\,mol^{-1}]$ | $[2 \cdot 10^4; 8 \cdot 10^4]$ |
| Rate constant activation energy of the anode | $EA_{k,neg}[J\,mol^{-1}]$ | $[2 \cdot 10^4; 8 \cdot 10^4]$ |
| Solid diffusivity of the cathode* | $D_{s,pos}[m^2\,s^{-1}]$ | $[1 \cdot 10^{-16}; 1 \cdot 10^{-12}]$ |
| Solid diffusivity of the anode$^{++}$ | $D_{s,neg}[m^2\,s^{-1}]]$ | $[5 \cdot 10^{-16}; 5 \cdot 10^{-12}]$ |
| Solid diffusivity activation energy of the cathode | $EA_{D_{s,pos}}[J\,mol^{-1}]$ | $[2 \cdot 10^4; 8 \cdot 10^4]$ |
| Solid diffusivity activation energy of the anode | $EA_{D_{s,neg}}[J\,mol^{-1}]$ | $[2 \cdot 10^4; 8 \cdot 10^4]$ |
| Electrolyte fraction in the cathode | $\varepsilon_{l,pos}[-]$ | $[0.3; 0.45]$ |
| Electrolyte fraction in the anode | $\varepsilon_{l,neg}[-]$ | $[0.3; 0.45]$ |
| Electrolyte concentration | $C_e0[mol\,m^{-3}]$ | $[1000; 1500]$ |
| Battery specific heat | $C_{p,batt}[J\,kg^{-1}\,K^{-1}]$ | $[800; 1200]$ |
| Battery radial thermal conductivity | $k_{Tr,batt}[W\,m^{-1}\,K^{-1}]$ | $[0.1; 1]$ |
| Transference number | $t_0^+[-]$ | $[0.3; 0.4]$ |
| Convective heat transfer coefficient | $h_{conv}[W\,m^{-2}\,K^{-1}]$ | $[10; 50]$ |

**Table 2.9:** Model parameters involved in the optimization. * assumed from [122];** [123]; $^{+}$ [124]; $^{++}$ [117]

and taken from literature and restrict the solution space in which the particles move.

**Experimental procedure for parameter estimation**

The experimental protocol combined three different experimental techniques i.e. discharge, relaxation and electrochemical impedance spectroscopy, investigating a variety of operative conditions.

The following procedure was proposed:

- the climate chamber is taken at 10°C and an EIS test is performed on the battery at 100% SOC, in the 4000-1 Hz range with 20 logarithmically spaced frequencies and two sinusoids per frequency (time employed: around 2 minutes);

- the battery is then discharged at 3 C-rate with a depth of discharge (DOD) of 75%, registering both the cell voltage and the surface temperature (time employed: around 15 minutes);
- a relaxation test of 1000s follows the discharge, measuring the voltage profile and the battery surface temperature;
- the climate chamber temperature is set at 25°C and when the temperature is reached, after around 30 minutes, another EIS is carried out at 25% SOC and 25°C, with the same frequency range and spacing of the first one (time employed: around 2 minutes);
- the battery is discharged at 1 C-rate with theoretical DOD of 25%, practically until the lower voltage limit is reached (time employed: around 15 minutes).

The proposed methodology showed promising results, as using that experimental dataset only, it was possible find a set of parameters that reproduced the battery behaviour.

**Cost function**

In the previous thesis work, the cost function of the PSO algorithm was computed as the sum of seven subcostfunctions, one for each experimental output, composed by the root-mean-square error (RMSE) between the experimental data an the data simulated by the model.
It was expressed as:

$$CF = \sum_{j=1}^{N_f} \left( f_j \cdot \sqrt{\frac{1}{N_{d,j}} \cdot \sum_{i=1}^{N_{d,j}} \frac{(x_{i,j}^{exp} - x_{i,j}^{mod})^2}{\overline{x_j}^{exp}}} \right) \tag{2.32}$$

where $N_f$ and $N_{d,j}$ are the number of subcostfunctions (subCFs) and the number of points in which the dataset are simulated, respectively, and compared to the experimental ones; $x_{i,j}^{exp}$ is the value at point $i$ of the test $j$ obtained experimentally, while $x_{i,j}^{mod}$ is the value obtained in the same condition, but simulated by the model. $\overline{x_j}^{exp}$ is the average value of the experimental output $j$ and $f_j$ is an arbitrary parameter introduced to take into account the different types of quantity of each subCF.
The subCFs considered for the computation of the $CF$ are seven:

- each EIS test is associated to two subcostfunctions: one related to the real part and the other to the imaginary part;
- each discharge is linked to a subCF related to the voltage;
- another subCF accounts for the voltage data during the relaxation test.

Summarizing, in the context of the previous thesis work, the PSO had to solve a complex problem, characterized by a cost function with the shape described in equation 2.32, to find a solution that minimizes that cost function. The solution consists in the 22 electrochemical model parameters and hence, the algorithm has to generate particles that explores a 22-dimensional solution space, according to the logic described in this chapter.

# 3 Methods for parameters estimation

This chapter analyzes the methods developed in this thesis to characterize the model parameters estimation, in order to calibrate the model. The thermodynamic description of the model was examined and improved. Two PSO algorithm have been developed, and they will be called in different ways to distinguish them: the "kinetic PSO" and the "thermodynamic PSO". The first one has the same role of the PSO algorithm introduced in chapter 2.5, namely it allows the calibration of the electrochemical model parameters, but was adapted and improved. The second one, the thermodynamic PSO, is used to calibrate three new thermodynamic parameters that account for the description of the battery degradation.

## 3.1 Method for kinetic parameters estimation

The PSO algorithm described in section 2.5 and developed in the previous work thesis for the calibration of the model parameters has been improved in three main aspects during this thesis:

- the **"Adaptive PSO"**, namely an adaptive version of the standard PSO algorithm has been implemented in order to improve the convergence process;
- the **experimental protocol** has been generalized, extending its validity to the battery type adopted in this work;
- the **cost function** has been modified to favour the convergence and to account for each experimental test properly.

### 3.1.1 Adaptive PSO

The optimization problem that the said PSO has to solve is very complex: the solution space is in 22 dimensions, as the number of parameters to be optimized, and the cost function shape is unknown; this would make necessary to initialize a high number of particles to ensure a wide enough exploration, and a lot of generations are needed to achieve convergence. Therefore, a relevant computational effort is needed for the fitting procedure.

A more efficient algorithm, named Adaptive PSO (APSO) and introduced by Zahn Z. H. et al. has been applied [125]. The main improvement is that the inertial term

$w$ and the velocity coefficients $c_1$ and $c_2$ are progressively redefined, adjusting the collective behaviour to the different state of the fit. For instance, the exploration of the solution space will be favoured in a case where the particles are randomly distributed, while the convergence will be promoted in the case where a possible solution is found.

To obtain this adaptive behaviour, the particles collect information about their position and the distance between the particles in the 22-dimensional space. The particles' distribution is estimated as the mean between the lengths of the diagonals that connect a particle to all the others and a new parameter, the **evolutionary factor** $f$, is calculated at each iteration:

$$f = \frac{d_g - d_{min}}{d_{max} - d_{min}} \tag{3.1}$$

where $d_{min}$ and $d_{max}$ are respectively the minimum and the maximum of the said mean distances and $d_g$ is the one of the particle with the lowest cost function. This means that the particle related to $d_{min}$ is the closest particle to the swarm barycentre, while the one assigned to $d_{max}$ is the most distant. If the best particle is also located close to the swarm barycentre, $f$ will tend to 0; if instead the best solution is found far from the swarm barycentre, $d_g$ will approach $d_{max}$ and $f$ will tend to 1.

The evolutionary factor is used to compute the inertial coefficient $w$, as

$$w = w(f) = \frac{1}{1 + 1.5e^{-2.6f}} \tag{3.2}$$

and to select the evolution of the self-confidence and swarm-confidence factors, $c_1$ and $c_2$, that are both initialized equal to 2 and has to lie in the [1.5;2.5] range. The authors suggested that the variation of the acceleration coefficients is randomly generated in the interval [0.05, 0.1], but, these values were considered to be too high for the problem solved by the PSO used in this work, resulting in a rapid saturation of the $c_1$ and $c_2$ values. Smaller increments and decrements were then adopted in order to promote a wider exploration. The boundary condition for the acceleration coefficients is that the sum of the two has to be lower than 4, and if that value is exceeded they are re-scaled as:

$$c_i = 4\frac{c_i}{c_1 + c_2},\ i = 1, 2. \tag{3.3}$$

Four stages can be defined, as showed in Figure 3.1, according to the value of $f$:

- **S1 - Exploration**: this stage applies for newly generated swarm that are distributed in a random way in the solution space; $f$ will be closer to 1, $c_1$ will be increased by 0.1 and $c_2$ decreased by the same amount, so that each particle trusts more its personal experience and the exploration is favoured;

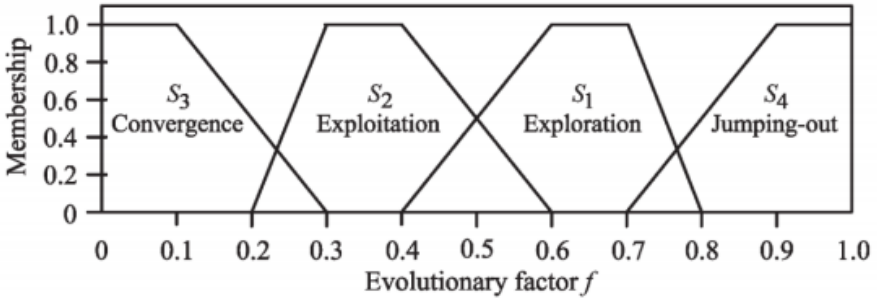


**Figure 3.1:** Stages of the APSO algorithm defined by the evolutionary factor $f$. (Taken from [125])

- **S2 - Exploitation**: the particles starts to group around a candidate optimal solution, $f$ is lowered and $c_2$ is increased by 0.05 at the expenses of $c_1$, that is decreased by the same quantity;
- **S3 - Convergence**: the process started in the previous stage continue progressively to seek convergence; both the trust in their personal experience and in the group increase slightly, by 0.02.
- **S4 - Jumping out**: this stage applies for the particular case in which the actual best solution is found by a particle located away from the swarm barycentre; $c_1$ is decreased by 0.2, while the trust in the global best grows by 0.2. Thus, the inertia of the swarm is increased: in this way, the particles that were converging close to the swarm barycentre will spread in the solution space, and switch from the jumping out state to the exploration state.

The extra computation needed to run the APSO algorithm add only a few $ms$ to the duration of one simulation, with respect to the basic PSO algorithm. The improvement in the exploration and the convergence mechanisms, instead, allow for a drastic reduction of the population size and, thus, in an overall decrease of the total computation time.

Finally, the PSO algorithm parameters are initialized with these values:

- $N_p$ - number of particles: $\geqslant 22$;
- $c_1$ and $c_2$ - personal and social velocity coefficients: 2;
- $I_{max}$ - maximum number of iterations: $\geqslant 35$;
- $V_{max}$: $0.05 \cdot (P_{max} - P_{min})$
- $V_{min}$: $-0.05 \cdot (P_{max} - P_{min})$

The particles number may seem low, but several attempts performed with different

combination of $N_p$ and $I_{max}$ proved, for the case of this particular problem, a stronger influence of the iteration number with respect to the particles' number, on the quality of the solution.

### 3.1.2 Adapted experimental protocol

The experimental protocol introduced in section 2.5 was developed studying the behaviour of different samples from the ones adopted in this work (described in section 2.1). Namely, the batteries used were Sony US26650VT, that are high power batteries, designed for high current drain applications; moreover the cathode chemistry, the size and the nominal capacity are also different. Therefore, changes in the protocol were expected.

Discharging at 3 C-rate and 10°C resulted to be a too stressing condition for these samples: the voltage outputs from the tests were not repeatable nor comparable within samples. Moreover at such current rate the cells generated a lot of heat, and also the local cooling management of the climatic chamber is affected, having effects on the experimental test. As the purpose of the protocol is the calibration of parameters, what is needed is a more reliable, predictable test. Hence, a 2 C-rate was selected instead of the 3 C-rate for the first discharge. In addition, as can also be seen in Figure 3.2.a, the 3C-rate discharge from 100% to 25% SOC reaches the lower voltage limit before the 25% SOC is achieved. With a view of applying this procedure to calibrate physical parameters also in aged batteries, where the available capacity will be much lower than the nominal one, the DOD of the first discharge was reduced to 50%. Therefore, what was selected as more suitable discharge condition for the samples used in this work is represented in Figure 3.2.b, namely a discharge from 100% to 50% SOC at 2C-rate and 10°C. This implies that the second electrochemical impedance spectroscopy test will be carried out at 50% SOC and 25°C. Accordingly, the second discharge will have a theoretical 50% DOD for batteries tested at begin of life (BOL) condition, that will be lower for aged batteries, as the discharge will start from the nominal 50% SOC down to the lower voltage limit.

In summary, the adapted experimental procedure is the following (see Figure 3.3):

1. the climate chamber is taken at 10°C and an EIS test is performed on the battery at 100% SOC, in the 4000-1 Hz range with 20 logarithmically spaced frequencies and two sinusoids per frequency (time employed: around 2 minutes);

2. the battery is then discharged at 2 C-rate with a depth of discharge (DOD) of 50%, registering both the cell voltage and the surface temperature (time employed: around 15 minutes);

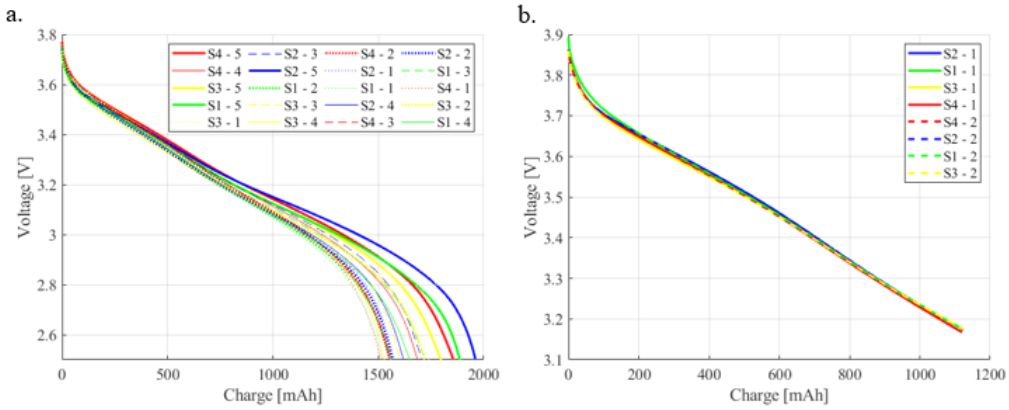


**Figure 3.2:** First discharge of the experimental protocol; a. Discharge at 10°C, 3C, 100%-75% SOC; b. Discharge at 10°C, 2C, 100%-50% SOC. The presented results refers to four pristine samples (S1, S2, S3, S4) and the number after the dash indicates the repetition of the test.

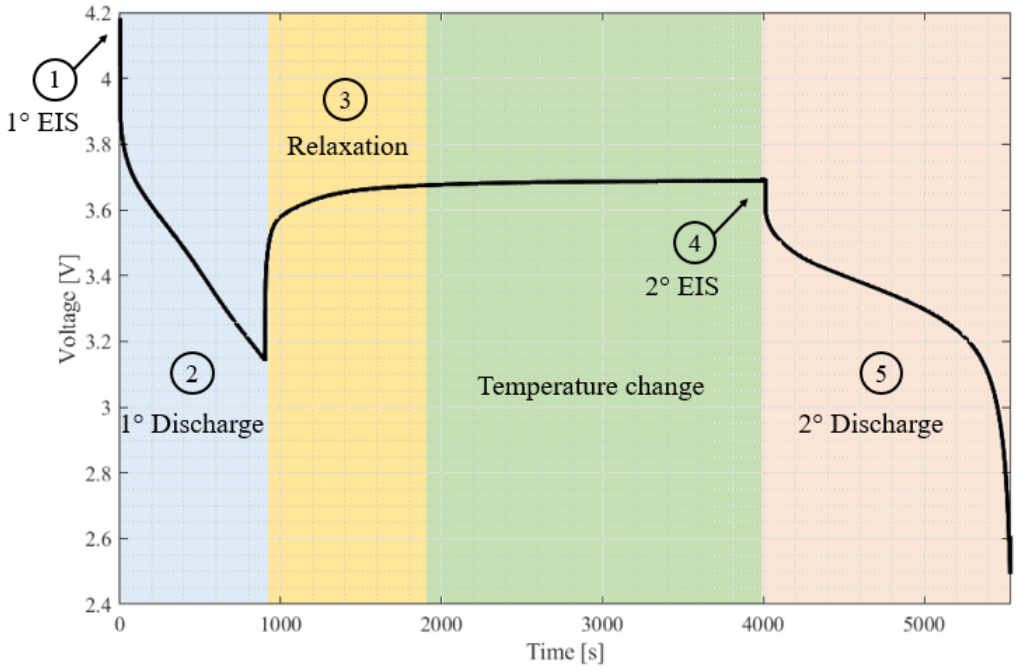


**Figure 3.3:** Explanation of the proposed experimental protocol, with the trend of the cell voltage in time.

3. a relaxation test of 1000s follows the discharge, measuring the voltage profile and the battery surface temperature;

4. the climate chamber temperature is set at 25°C and when the temperature is reached, after around 30 minutes, another EIS is carried out at 50% SOC and 25°C, with the same frequency range and spacing of the first one (time employed: around 2 minutes);

5. the battery is then discharged at 1 C-rate with theoretical DOD of 50%, practically until the lower voltage limit is reached (time employed: around 30 minutes).

### 3.1.3 Cost function

As previously specified, the optimization is based on the comparison of a set of experimental tests with the same set of tests simulated by the model, with the parameters corresponding to a certain position of the particle.

The choice of an adequate objective function is important for an optimal convergence of the algorithm. In this case a set of five different experimental curves have to be fitted. Some changes have been made to the objective functions developed in the previous thesis work, in order to balance the weight of each test. In fact, the total cost function was expressed as the sum of the subcostfunctions (subCFs) related to the experimental outputs (Equation 2.32). In place of that formulation, the total cost function has been modified to be the norm of a vector that has those subCFs as components. In this way, a case where the subCFs have all intermediate values is favored with respect to the case where some of the subCFs are zero and the others have higher values. The cost function is then computed as:

$$CF_{TOT} = \|CF\| \tag{3.4}$$

where CF is a vector whose components are the subCFs related to the experimental and simulated outputs. A total of nine subcostfunctions is present (instead of the seven of the pre-existing version):

- each EIS test is associated to two subCFs: one related to the real part and the other to the imaginary part;

- each discharge is linked to a subfunction related to the voltage and one related to its derivative over time. The introduction of the optimization on the derivative has shown relevant result, improving the quality of the simulated curves. In this way, in fact, also the voltage trend during the discharge becomes an object of the optimization and the model avoids to find a set of parameters that

give as output a voltage profile that is close enough to the experimental one in terms of voltage values, but with a wrong slope, alternating overestimations and underestimations of the voltage to minimize the error.

- another subCF accounts for the voltage data during the relaxation test.

All the subCFs are computed as the norm of the difference between the experimental data vector $x^e$ and the model data vector $x^m$, divided by the norm of $x^e$:

$$sub\,CF = f_i \frac{\|x^e - x^m\|}{\|x^e\|} \tag{3.5}$$

In the equation, $f_i$ keeps the meaning it had in the previous cost function formulation (see Chapter 2.5).

## 3.2 Improvements of the thermodynamic description

Further work, with respect to the previous thesis, has been performed, working on the thermodynamic description. The main improvement was to make some adjustments in the materials' intercalation curves.

### 3.2.1 Electrodes material intercalation curves

The samples used in this are the one described in Chapter 2.1. The negative electrode is made of graphite, while the positive electrode's material is pure NMC. No specific information were provided on the percentages of Ni, Co, and Mn present in the material. The characteristics of these materials can be found in chapter 1.2.1. The intercalation curves of graphite and NMC used in the P2D model initially, were the ones provided by the COMSOL materials' database.

The geometrical parameters of the battery were updated to consider the different cells' type adopted in this thesis work, with respect to the previous one. The volume fractions of solid active material in the electrodes and the maximum lithium concentrations that can be hosted in the electrodes were taken from literature. The electrodes' thickness and surface area were calibrated, assuming reasonable ranges of variations for these parameters from literature, to get a consistent value of the capacity of the two electrodes and of the full cell itself. The limit concentration of the anode were properly assumed both comparing with literature [46] and by aligning the peaks of the DV of its intercalation curve, provided by COMSOL, with the ones of an experimental discharge of a pristine sample. The cathode limit concentrations were taken from literature [126], after modifications of the COMSOL NMC lookup table were operated to add details to the shape of the intercalation curve.
The fixed parameters are summarized in Table 3.1.

| **Parameter** | **Anode** | **Separator/Electrolyte/Battery** | **Cathode** |
|---|---|---|---|
| $L[m]$ | $5.41 \cdot 10^{-5}$ | $2.25 \cdot 10^{-5}$ | $5.2 \cdot 10^{-5}$ |
| $SOC_{min}[-]$ | 0.015 | - | 0.13 |
| $SOC_{max}[-]$ | 0.8 | - | 0.89 |
| $c_{s,max}[mol\, m^{-3}]$ | 31000 | - | 37105 |
| $\epsilon_s[-]$ | 0.5 | - | 0.45 |
| $A_c[m^2]$ | - | 0.1275 | - |

**Table 3.1:** Model fixed parameters.

Analyzing the DV curve (introduced in Chapter 2.3.2) of positive and negative

electrodes and comparing the profiles with the literature [47] where the same type of batteries was employed, room for improvement was encountered. This kind of measurements, that directly describe the potentials of the two electrodes singularly are done with a reference electrode, but are not feasible on a full cell, as only the total voltage difference between the electrodes can be measured. In fact, as can be seen in Figure 3.4 in the dV/dQ curves of the cell some characteristics can be attributed to the electrodes: the peak at low SOC and the one close to 50% SOC are commonly assigned to the graphite, while the peak at high SOC is assigned to the NMC.

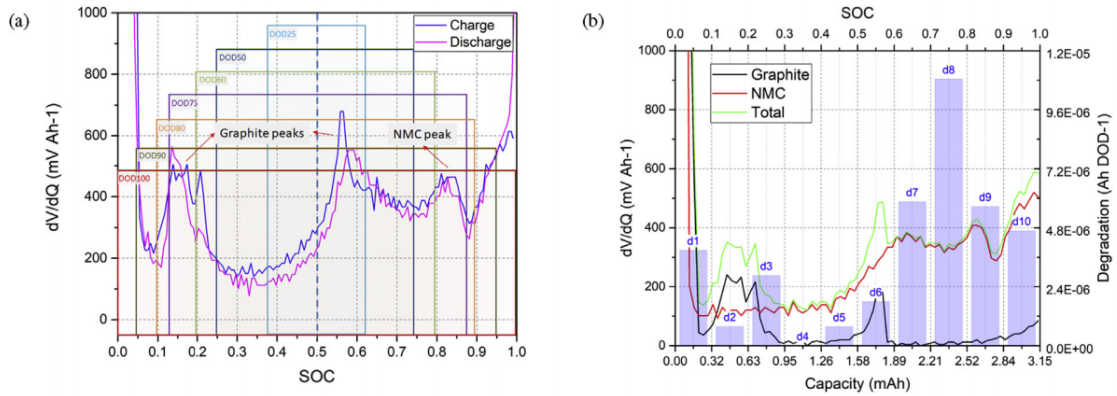


**Figure 3.4:** (a) dV/dQ curve for the full cell for slow rate charge and discharge conditions with individual peaks recognized and DOD regions highlighted. (b) dV/dQ curves of negative, positive electrodes and their sum from coin cell characterization during charging. (Taken from [47]).

According to these insights, the intercalation curves have been modified following these steps:

- the experimental discharge at 25°C and 0.1 C-rate was considered as the OCV curve: 12 mV were summed to the whole profile to account for the ohmic losses, as this number is the overpotential value expressed as a voltage shift, that model simulate to accounts for the fact that the discharge at 25°C and 0.1C-rate is not the OCV;
- the NMC was modified to be linearly decreasing from 0% to around 50% SOC; moreover its DV profile was manually modified in the range between 50% and 60% in order not to account for the graphite peak that falls in that range. Then, the graphite intercalation curve was computed as the difference between the NMC and the OCV: in this way the peaks of the graphite are adjusted;

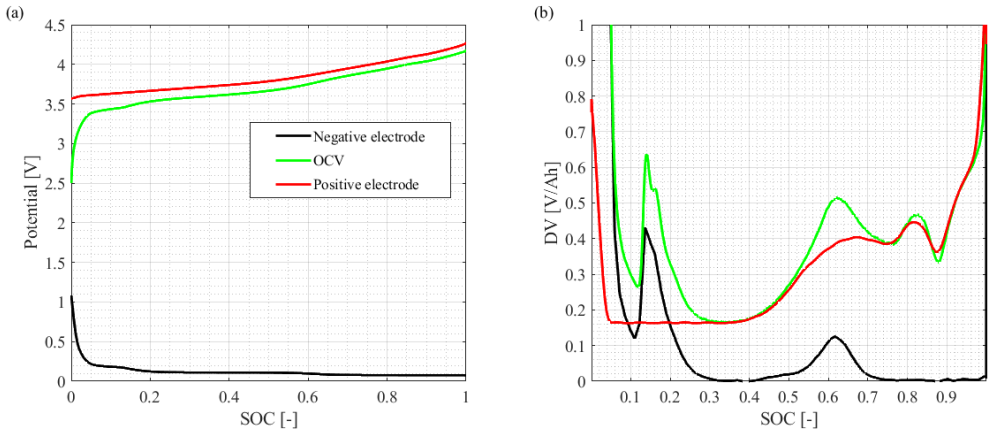


**Figure 3.5:** (a) OCV-SOC and electrodes potentials curves; (b) corresponding dV/dQ curve of negative and positive electrodes and full cell

- the NMC is then obtained as the sum between this new graphite curve and the OCV.

### 3.2.2 Introduction of thermodynamic parameters for degradation

Three parameters, $LLI$, $LAM_p$ and $LAM_n$ representing the three degradation modes presented in Chapter 1.3.3, were introduced in the model in order to account for the battery degradation.

The first parameter, loss of lithium inventory $LLI$, accounts for the capacity loss. It represents the permanent loss of lithium that causes a decrease in the available battery capacity. The other two parameters, $LAM_p$ and $LAM_n$ account for the loss of active material respectively in the positive and in the negative electrodes, that occurs with the degradation. In fact, the volume fraction of solid active material is computed as

$$\varepsilon_{s,n} = \varepsilon_{s,n}^{BOL}\,(1 - LAM_n) \tag{3.6}$$

for the case of the negative electrode, and as

$$\varepsilon_{s,p} = \varepsilon_{s,p}^{BOL}\,(1 - LAM_p) \tag{3.7}$$

for the positive one, where $\varepsilon_{s,n}^{BOL}$ and $\varepsilon_{s,p}^{BOL}$ are the volume fractions of solid active material in the positive and negative electrodes of a pristine cell. Therefore, a $LAM$ values increment corresponds to a growth in the percentage of inactive material. It should be noted that, in the literature [127], the $LAM$ is usually represented as the sum of two components: the active electrode material particle that is lost in lithiated states, and the one that is lost in delithiated states. Therefore, the $LAM_p$ can be divided into loss of lithiated positive electrode material ($LAM_{p,li}$) and loss of

delithiated material ($LAM_{p,de}$), and, similarly, for the loss of active material of the negative electrode ($LAM_{n,li}$ and $LAM_{n,de}$). In this work, $LAM_p$ and $LAM_n$ refers only to the delithiated portion of active material loss.

The battery capacity is related to these three parameters as follows:

$$Q = Q^{BOL}(1 - LLI) - A_c F(LAM_n L_n \varepsilon_{s,n}^{BOL} cs_{max,n} SOC_{min,n}^{ref} + \\ + LAM_p L_p \varepsilon_{s,p}^{BOL} cs_{max,p} SOC_{min,p}^{ref}) \tag{3.8}$$

In the equation, $A_c$ is the cell cross sectional area, $F$ is the Faraday constant, $L_n$ and $L_p$ are the thickness of the negative and positive electrode, respectively, and $\varepsilon_{s,n}^{BOL}$ and $\varepsilon_{s,p}^{BOL}$ are the volume fractions just introduced. $cs_{max,p}$ and $cs_{max,n}$ are the maximum lithium concentrations that the positive and the negative electrodes can accept. $SOC_{min,n}^{ref}$ and $SOC_{min,p}^{ref}$ are the minimum SOC at which of the two electrodes. Note that the capacity $Q$ is the actual battery capacity value, meaning that it is the capacity that is actually available for cycling.
For a pristine cell, $LLI$, $LAM_n$ and $LAM_p$ are all equal to zero, and therefore $Q = Q^{BOL}$.

**Sensitivity analysis**
To better understand the influence of these parameters on the OCV curve, a sensitivity analysis has been performed, changing one parameter at a time and simulating a slow discharge at 0.1C-rate and 25°C, that can be considered a good approximation of the OCV. Moreover, this sensitivity analysis will be useful to recognize the degradation modes' characteristics on the experimental data of aged samples. In real conditions, the starting OCV value may vary slightly, while for this case the discharges are simulated by imposing the same starting OCV of 4.18V in the model. The DV and IC curves are also reported to enhance the differences in the voltage profile caused by the parameters variation. In the DV and IC plots the sign of the negative electrode curve is changed to exploit the property of the sum of the electrodes that provide the full cell.

- Figures 3.6, 3.7 and 3.8 represents the discharge at 0.1C-rate and 25°C, its DV and IC obtained by varying the $LLI$ in the range [0;0.9] with a 0.1 step. Of course, such high $LLI$ values are unlikely to happen, but still useful to understand how the battery behavior could be affected.
  As $LLI$ increases, the overall amount of lithium available for cycling decreases, but there are no changes in the electrodes' physical properties. This translates into a lower lithium concentration in the electrodes, with respect to the begin of life case. Graphically, it can be seen as a relative shift of the electrodes' intercalation curves, named electrode slippage. In fact, since what it is imposed

in the discharges is the starting OCV value, as $LLI$ grows, the lithium has to be redistributed to guarantee this voltage value. The shift is then given by the electrode slippage, as the electrodes' intercalation curves have to realign so that, for the superposition of the effects, the discharge is obtained.
What can be observed from Figure 3.6 is a constant decrease in the exchanged capacity, proportional to $LLI$. In fact, setting $LAM_n$ and $LAM_p$ to zero in Equation 3.8, the battery capacity is exactly computed as the product between 1-$LLI$ and the begin of life capacity. From the DV curve in Figure 3.7, it is evident that the shift of the low SOC peak in the battery DV curve is a consequence of the shift of the related graphite peak (red curve), as a consequence of the reduction of the lithium content in the anode. This characteristic is observed only for the $LLI$ degradation mode, and it is pronounced and easily identifiable: following this peak evolution, both in terms of shift and intensity variation, can be an indicator of loss of lithium inventory.
For $LLI$ values up to 30%, the said peak keeps the initial magnitude, as the intercalation curve of the NMC (green line) is linear in that SOC range, while for higher values of $LLI$ the peak increases, according to the change of slope of the positive electrode that corresponds to those SOCs. The IC profiles (Figure 3.8) shows a progressive decrease in the peaks magnitude and a shift of the characteristics towards higher voltages.

- When $LAM$ occurs, the electrode involved in the degradation decreases its ability to accept intercalating ions, even if they are still available and thus, it behaves as a smaller electrode. This results in a shrinkage of the intercalation curve of the electrode affected by $LAM$. The results of the variation of the $LAM_p$ parameter on the discharge, the IC and the DV curves can be seen in Figure 3.9, 3.10 and 3.11. The positive electrode intercalation curve shrinks progressively with the increase in $LAM_p$ with respect to the graphite intercalation curve, resulting in lower exchanged capacity. On the DV plot (figure 3.10), the effect of the contraction of the NMC curve is evident at low SOCs, where the positive electrode becomes the limiting electrode. At high SOC, the characteristic peak of the graphite seems to fade. The IC curve in Figure 3.11 shows how, increasing values of $LAM_p$, for the same voltage window between 4.2V and 2.5V, corresponds to a lower amount of charge. Moreover, comparing the plot with the one obtained for the $LLI$ case, a different trend of degradation can be identified. In fact, if the IC in the $LLI$ case showed something similar to a progressive shift in the curves, that is given by the shift in the negative electrode intercalation curve, as already explained; the IC curves in the $LAM_p$ case, instead, show that the charge

reduction does not affect the characteristic peaks, especially the one at high SOC, in terms of position but only in terms of intensity.
Both the characteristics evidenced on the DV and the IC plots are a consequence of the shrinkage of the NMC intercalation curve: as it shrinks, the portion of the curve that overlaps to the negative electrode intercalation curve diminishes. For $LAM_p$ values higher than 20% the negative electrode is mostly flat and hence the main contribution to the cell voltage is the one of the positive electrode intercalation curve.

- A similar point can be made about the effect of $LAM_n$. In this case, it is the negative electrode intercalation curve that shrinks. It was not possible to simulate discharges with $LAM_n$ lower than 20%, as the graphite electrode becomes saturated. To simulate the effects of only $LAM_n$ is important to understand how this condition would affect the battery, but it is an unlikely event. Moreover this 20% value is already high enough to account for this kind of degradation from an experimental point of view and does not limit the applicability of the approach. The capacity loss related to this kind of degradation is smaller (Figure 3.12), with respect to the case of the loss of active material in the positive electrode. This effect is reasonable, since the negative electrode is usually oversized and a reduction of active sites should not affect significantly the battery operation. Considering discharges obtained with increasing $LAM_n$ and starting from the same initial voltage, as the negative electrode intercalation curve appears almost flat for those SOCs, the positive electrode will be substantially the same. Consistently, looking at the IC plot (Figure 3.14), it appears that even though the charge distributes differently in the operating voltage window, it remains fixed.

These parameters are adequate to describe the degradation at a thermodynamic level, involving well recognizable deviations from the begin of life discharge curve and they will be used in the method for the degradation detection developed in this work.

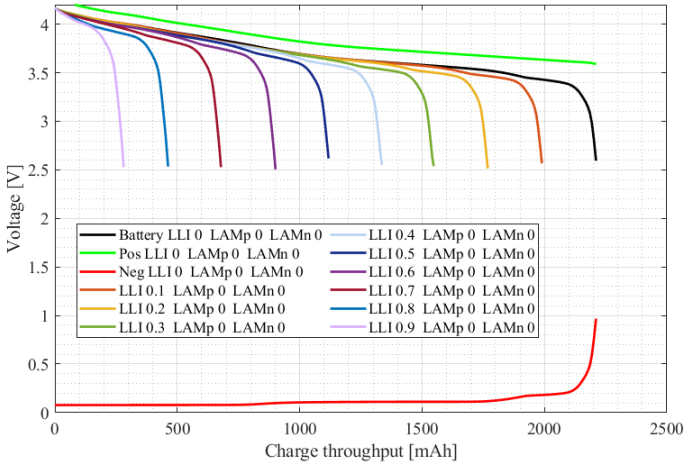


**Figure 3.6:** Discharge curves at 0.1C and 25°C with *LLI* variation in the range 0-90%. The green and red lines are the potentials of the negative and positive electrode at BOL conditions, respectively.

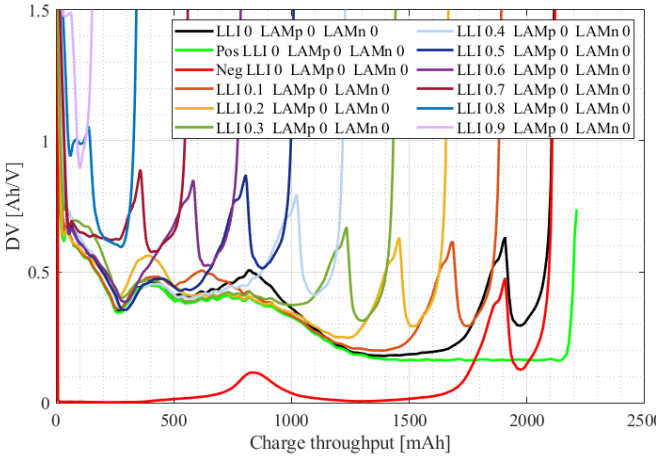


**Figure 3.7:** DV curves with *LLI* variation in the range 0-90%. The green and red lines are the DV of the negative and positive electrode at BOL conditions, respectively.

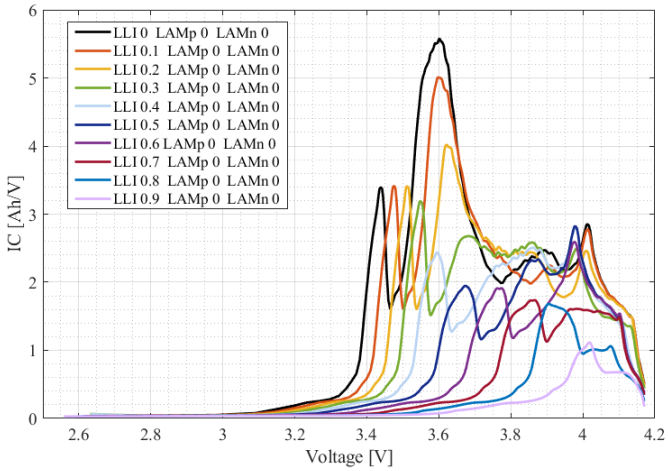


**Figure 3.8:** IC curves with *LLI* variation in the range 0-90%.

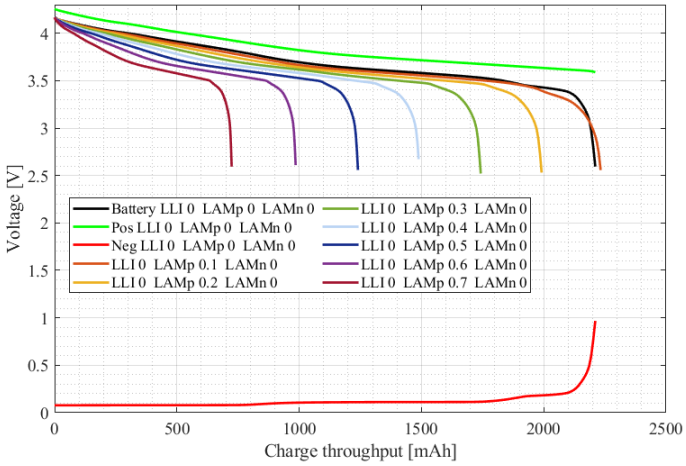


**Figure 3.9:** Discharge curves at 0.1C and 25°C with $LAM_p$ variation in the range 0-70%. The green and red lines are the potentials of the negative and positive electrode at BOL conditions, respectively.

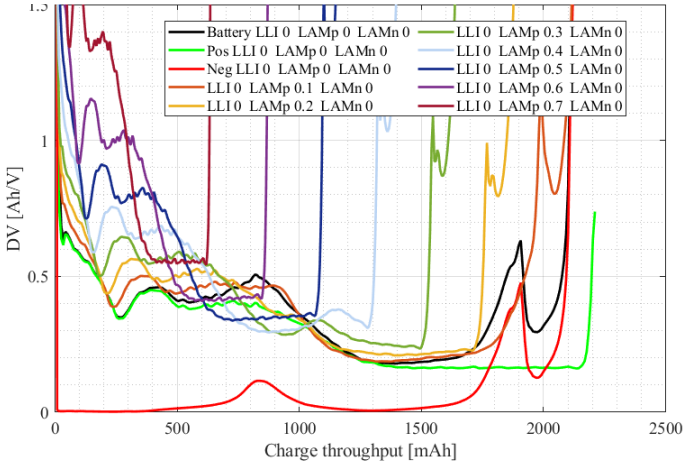


**Figure 3.10:** DV curves with $LAM_p$ variation in the range 0-70%. The green and red lines are the DV of the negative and positive electrode at BOL conditions, respectively.

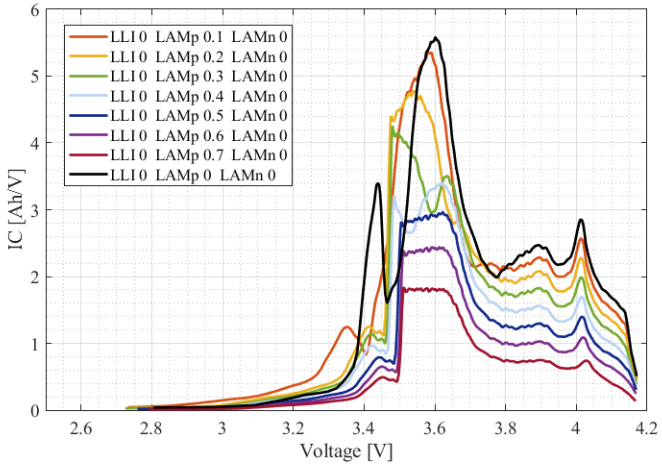


**Figure 3.11:** DV curves with $LAM_p$ variation in the range 0-70%.

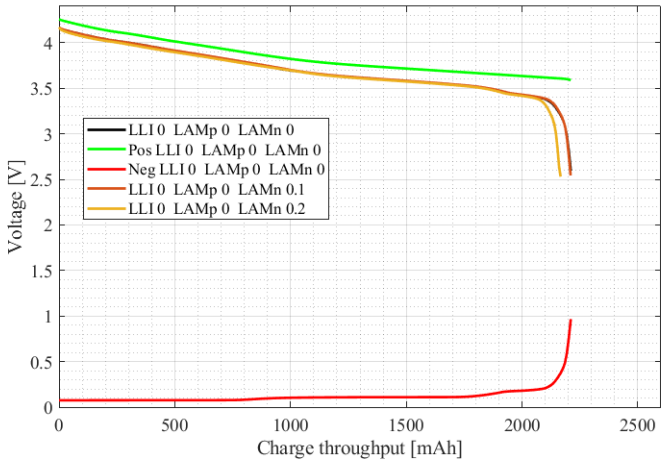


**Figure 3.12:** Discharge curves at 0.1C and 25°C with $LAM_n$ variation in the range 0-70%.The green and red lines are the potentials of the negative and positive electrode at BOL conditions, respectively.

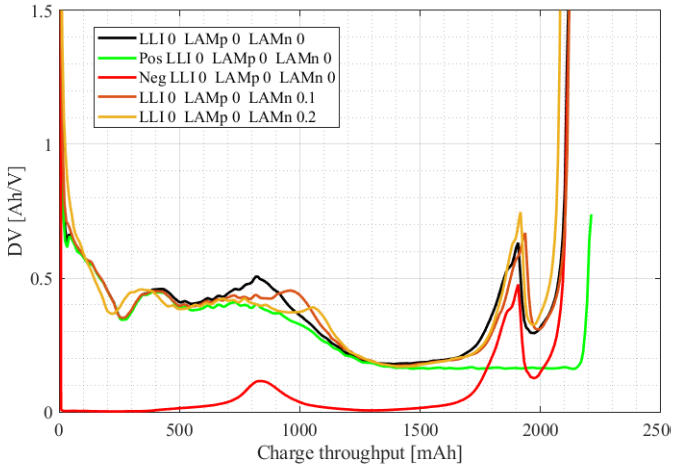


**Figure 3.13:** DV curves with $LAM_n$ variation in the range 0-70%. The green and red lines are the DV of the negative and positive electrode at BOL conditions, respectively.

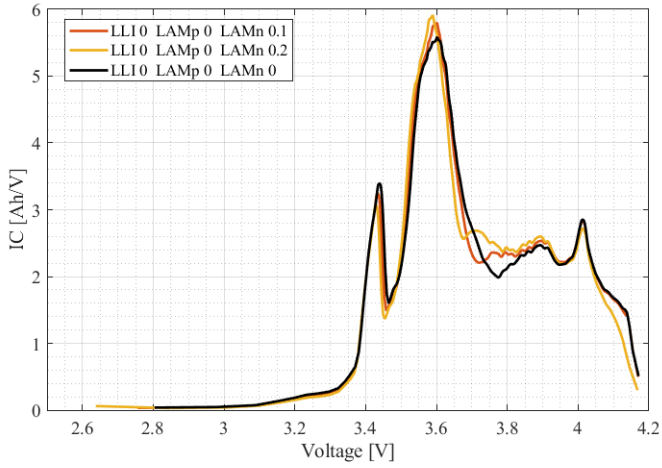


**Figure 3.14:** DV curves with $LAM_n$ variation in the range 0-70%.

## 3.3 Method for thermodynamic parameters estimation

As $LLI$, $LAM_p$ and $LAM_n$ have been introduced in the electrochemical model, a dedicated PSO, like the one described in section 2.5, have been implemented for the calibration of these three parameters. This particular PSO will be identified as "thermodynamic PSO", to be distinguished from the "kinetic PSO" (section 3.1).

The main logic behind this algorithm is the same described in section 2.5 and hence it does not make use of the adaptive behavior described in section 3.1.1, as, optimizing only three parameters, it has not to solve such a complex problem, having to generate particles that explore a 3-dimensional solution space. Moreover the time required for the simulation of one particle position is about 40 seconds and hence much lower than the one of the kinetic PSO.

The particles are not initialized randomly, but they are generated in a determined range in order to favour the conversion. Since the solution space is 3-dimensional (3D) it's useful to plot the solution space in a 3D graph (see Figure 3.15). The space in which the particles are generated is limited by two concentric quarter sphere of different radius. The $x$, $y$ and $z$ axis represents the range of variation of $LLI$, $LAM_p$ and $LAM_n$ normalized between 0 and 1. This means, for example, that $x$ equal to 1, corresponds to a $LLI$ value equal to the upper limit value of the $LLI$ variation range.

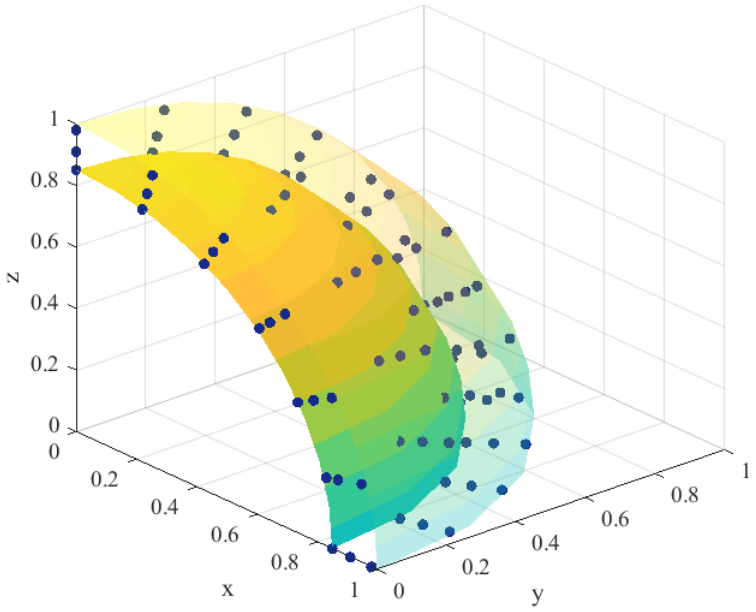


**Figure 3.15:** Particles initialization in the (x;y;z) space.

The experimental data that are used for the optimization are the one of a slow discharge at 25°C and 0.1C, in order to reduce the overpotentials and to have a curve that provides information on the thermodynamic and on the two electrodes intercalation curves. The data related to this discharge are also used to define the parameters range; as seen in the sensitivity of $LLI$, $LAM_p$ and $LAM_n$ (chapter 3.2.2, the parameters' values is close to the value of the capacity loss. Therefore, the variation of the parameters will be limited by this value plus a margin. It is clear, looking at the radii in the Figure 3.15 that the particles' generation is guided to be closer to the upper limit of the parameters.

The cost function is obtained as the root mean square error (RMSE) between the derivative of the said experimental discharge and the derivative of the voltage profile of the discharge in time simulated by the model with a certain set of $LLI$, $LAM_p$ and $LAM_n$. Therefore, it can be expressed as:

$$CF = \sqrt{\frac{1}{N_d} \cdot \sum_{i=1}^{Nd} \frac{(x_i^{exp} - x_i^{mod})^2}{\overline{x}^{exp}}} \tag{3.9}$$

where $CF$ stands for cost function, $N_d$ is the number of datapoints associated to the simulated discharge, and $x_i^{mod}$ is the i-value of the derivative of the voltage simulated by the model, and $x_i^{exp}$ and $\overline{x}^{exp}$ are the i-value of the derivative of the experimental voltage and its average value, respectively.

By performing the optimization on the voltage derivative it was possible to obtain more accurate results. In fact, optimizing on the derivative, it is possible to obtain a better alignment of the derivative peaks, namely a better coupling of the electrodes is reached. Moreover, optimizing only on the discharge voltage profile, the slope of the discharge would be of secondary importance, and discharges that alternates overestimation or underestimation of the voltage values to minimize the cost function would be considered good fit. Considering only the derivative may result in errors, as the derivative can not take into account the possibility of a vertical shifts. Nevertheless, this can not verify in this case. As the discharge is simulated in a specific number of points, to promote the convergence, an additional penalization is introduced for simulated discharges that are shorter or longer than the experimental ones.

The thermodynamic PSO algorithm parameters are initialized with these values:

- $N_p$ - number of particles: 85;
- $c_1$ and $c_2$ - personal and social velocity coefficients: 1.665;
- $I_{max}$ - maximum number of iterations: 30;

- $V_{max}$: $0.05 \cdot (P_{max} - P_{min})$
- $V_{min}$: $-0.05 \cdot (P_{max} - P_{min})$

### 3.3.1 Validation with simulated dataset

Before fitting the experimental data, the tuning of the data fitting algorithm was performed, in order to verify that the said algorithm is able to obtain a truthful result in terms of parameters' values. For this purpose, different simulated training dataset were selected and tested. The model was provided with the three parameters and the discharge at 25°C and 0.1C-rate was simulated. Then, the resulting voltage profile was used as fictitious experimental data in the Thermodynamic PSO, that finally obtains the set of $LLI$, $LAM_n$ and $LAM_p$ values that better reproduce the said dataset.

This test is very useful to understand whether it is possible that the set found by the algorithm not only reproduces in a satisfactory way the experimental dataset, but also represents the correct values of the parameters and that the solution is unique and stable.

Four set of parameters were selected to investigate how well the algorithm is able to reach the convergence in very different conditions, namely three cases when only one mechanism is present and one where all the three are different from zero. The parameters and the data about the fitting are reported in Table 3.2.

| | Dataset - $LLI$ only | | | | Dataset - $LAM_p$ only | | |
|---|---|---|---|---|---|---|---|
| | Real value | Fitted value | RMSE | | Real value | Fitted value | RMSE |
| $LLI$ | 0.25 | 0.2568 | | $LLI$ | 0 | 0.0016 | |
| $LAM_p$ | 0 | 0 | 42.9mV | $LAM_p$ | 0.58 | 0.5760 | 4.83mV |
| $LAM_n$ | 0 | 0 | | $LAM_n$ | 0 | 0.0233 | |

| | Dataset - $LAM_n$ only | | | | Dataset - Mix | | |
|---|---|---|---|---|---|---|---|
| | Real value | Fitted value | RMSE | | Real value | Fitted value | RMSE |
| $LLI$ | 0 | $4 \cdot 10^{-34}$ | | $LLI$ | 0.20 | 0.1949 | |
| $LAM_p$ | 0 | $7 \cdot 10^{-18}$ | 4.51mV | $LAM_p$ | 0.15 | 0.1305 | 7.99mV |
| $LAM_n$ | 0.11 | 0.1105 | | $LAM_n$ | 0.03 | 0.024 | |

**Table 3.2:** Simulated dataset and RMSE of the voltage during discharge.

The root mean square error (RMSE) is used as a measure of the average distance between the experimental data and the results of the model. The RMSE between

these two curves is calculated as:

$$RMSE = \sqrt{\frac{1}{N_d}\sum_{i=1}^{N_d}\left(x_i^{exp} - x_i^{mod}\right)^2} \tag{3.10}$$

The four set of parameters found by the thermodynamic PSO algorithm are very similar to the actual values of the four fictitious dataset. An higher value of RMSE, i.e. $42.9mV$, is found for the "$LLI$ only" case, even if the fitted parameters values are very close to the real ones. In fact, even such a small increment of $LLI$ make the discharge profile shrinks slightly: as the last section of the discharge curve is approximately vertical, the voltage difference in that part will have a greater impact on the RMSE, e.g. by excluding the last 1000 seconds (the complete discharge lasts more than seven hours), the RMSE value drops to $5.92mV$.

The discharge curves resulting from the fitting of the fictitious dataset can be seen in Figure 3.16.

The results obtained from the fitting of fictitious dataset show evidence to conclude that the thermodynamic PSO algorithm is able to converge on the correct values of the parameters in a satisfactory way.

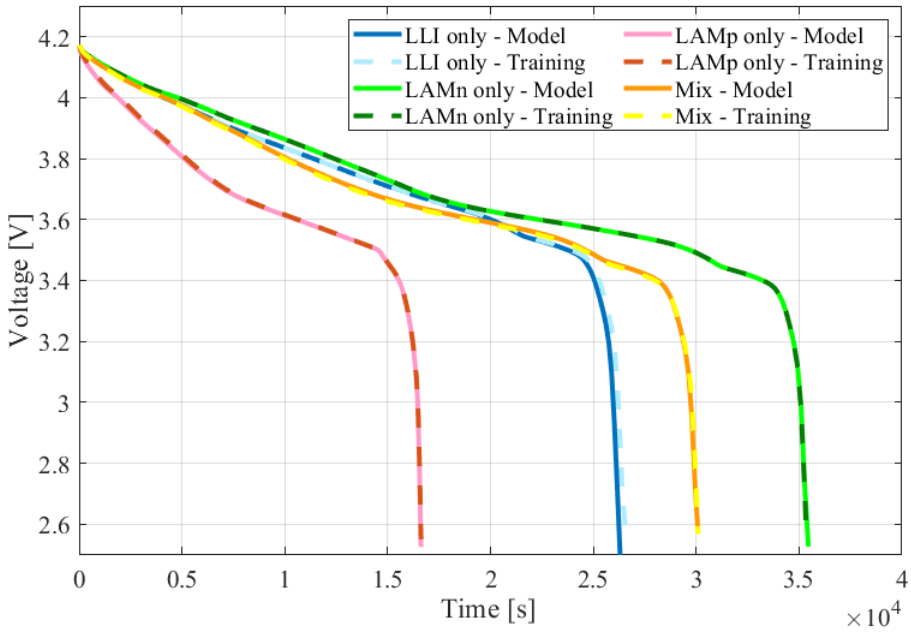


**Figure 3.16:** Discharge profiles of the fictitious training dataset and the output of the model fitting.

## 3.4 Calibration methods for pristine and degraded batteries

Since the model parameters are related to intrinsic properties of the battery, the progressive evolution of the parameters caused by the degradation can be an indicator of physical changes within the battery itself. Therefore, by tracking the parameters trend with the aging, it may be possible to deduce what aging mechanisms are behind the battery degradation.

In the case of this work, the batteries will be aged with controlled pathways that are expected to lead to predefined degradation phenomena. What will be investigated are the stressors of those phenomena and the effects on the physical parameters of the battery. In order to do so, the model parameters will have to be calibrated both for the pristine cell and in different aging step throughout the aging campaign. For this purpose, the kinetic PSO and the thermodynamic PSO are combined together for the calibration of the model parameters.

The calibration procedure can be described as follows:

- **BOL model calibration**
  As explained in section 3.2.2 the begin of life (BOL) thermodynamic parameters $LLI$, $LAM_p$ and $LAM_n$ are equal to zero. The kinetic PSO has then to calibrate the physical parameters listed in Table 2.9 through the fitting process that compares the simulated results with the experimental dataset, that includes the five experimental tests described in section 3.1.

- **model calibration at aging step t**
  The 22 parameters of the electrochemical model optimized for the pristine cell are set in the model. Some of those parameters will be considered constant during degradation, some others will be again considered the variables to be optimized by the kinetic PSO. Two progressive steps are needed for the calibration of the aged battery model:

  - **thermodynamic parameters calibration** : $LLI$, $LAM_p$ and $LAM_n$ are calibrated with the thermodynamic PSO, and then, are set into the model.

  - **kinetic parameters calibration**: the 14 kinetic PSO calibrates the physical parameters of the battery that may be subject to degradation.

It is important to note that the batteries will have to be tested at each aging stage, in order to provide the experimental dataset both for the fitting of the kinetic PSO

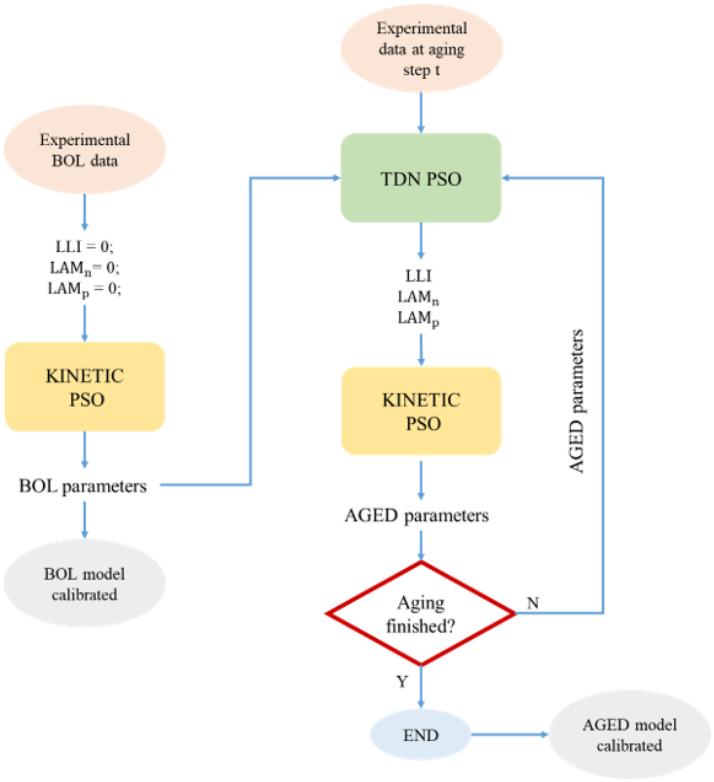


**Figure 3.17:** Flow chart of model calibration procedure for pristine and aged batteries.

and of the thermodynamic PSO. The detailed diagnostic procedure will be discussed in the next chapter (Chapter 4).

The flow diagram in figure 3.17 shows the parameters calibration process. The connector on the right indicates that the parameters of a certain aging stage are used in the calibration process of the following aging stage: in fact, as it will be explained in the next section, the parameters of the current aging stage are used to limit the variation of the parameters of the following stage, making reasonable assumption on the evolution of the said parameters.

### 3.4.1 Decisions on parameters calibration for pristine and aged batteries

For what concerns the calibration of the aged batteries, a choice on the parameters to involve in the optimization was made. In fact, some parameters are not expected to change with the battery aging, e.g. the battery thermal properties, and some others are expected to have a monotonic behaviour, only increasing or decreasing with degradation.

The selection of the parameters that will vary with cycling is relevant: if not enough parameters are variable or all the parameters necessary to describe a certain phe-

nomenon, it would not be possible to calibrate the model or the parameters may vary too much in order to try to account for a degradation that should involve other parameters; on the other hand, if too many parameters are involved in the optimization, the complexity of the problem increases, resulting in higher computational time. Moreover, the sensitivity of the parameters on the simulated output on which the optimization is based can affect the reliability of their values. In fact, "highly sensitive" parameters can be identified more easily and correctly than "low sensitive" parameters.
In the literature [128–131], there is no general rule on what parameters are expected to change, neither on the type of evolution of each parameter. The latter is often obtained through regression's analysis, fitting the trend of the values simulated during aging with linear forms, power forms or exponential forms.
K. Uddin et al. [130] considered only the variation of three parameters, i.e. the electronic conductivity, the active surface area and the maximum number of accessible active sites in the positive electrode, to study the case where the samples are cycled from 100% to 0% SOC under small currents and ambient temperature.
L. Zhang et al. [131] studied the degradation of batteries cycled at 1C from 100% to 0% SOC at 50°C. They identified nine key parameters: the diffusion coefficients in the solid for both the electrodes and the diffusion coefficient in the electrolyte, the volume fraction of active material in the anode and the cathode, the film resistance of the negative electrode, the positive and negative electrodes kinetic rate constants and the stoichiometric number of the anode when the battery is fully charged.

In this work, a total of 14 parameters of the electrochemical model have been selected (see Table 3.3). With respect to the begin of life selection of parameters, the activation energies of both the rate constant and the diffusion in the solid, in addition to the thermal parameters, are considered fixed. The other parameters should change with degradation, and will be considered variable to see how the model will account for their variation. It is necessary to specify that not all of the fourteen parameters selected are "highly sensitive", but, as they are expected to vary with aging, they will be considered as variables, at least in a first attempt to validate the developed methodology.

The batteries state will be tested step by step, through periodic diagnostics, to track performance evolution over time. Consistently, the model parameters calibration will be performed in a "chronological" way, using some of the parameters computed in the calibration of the previous aging step to limit the variation range of the current simulation. Therefore, the calibration of the pristine cell will be the first step, and then the aging stages will be calibrated one by one. The constraints on

| Parameter | Anode | Separator/Electrolyte/Battery | Cathode |
|---|---|---|---|
| $C_{dl}[F\,m^{-2}]$ | $[0.05; 25]$ | - | $[0.05; 25]$ |
| $k[m\,s^{-1}]$ | $[2.5 \cdot 10^{-11}; 2 \cdot x]$ | - | $[2.5 \cdot 10^{-11}; 2 \cdot x]$ |
| $c_{e,0}[mol\,m^{-3}]$ | - | $[1000; 1.2x]$ | - |
| $FCE[-]$ | - | $[0.02; 1.2x]$ | - |
| $t_0^+[-]$ | - | fixed | - |
| $\sigma_s[Sm^-1]$ | $[1; 1.2x]$ | - | - |
| $R_p[m]$ | $[2 \cdot 10^{-6}; 1.2x]$ | - | $[2 \cdot 10^{-6}; 1.2x]$ |
| $D_s[m]$ | $[1 \cdot 10^{-16}; 2x]$ | - | $[5 \cdot 10^{-16}; 2x]$ |
| $R_{film}[m^2]$ | - | - | $[x/1.2; 0.05]$ |
| $\varepsilon_e[-]$ | $[0.2; 1.2x]$ | - | $[0.2; 1.2x]$ |
| $EA_k[J\,mol^{-1}]$ | fixed | - | fixed |
| $EA_{D_s}[J\,mol^{-1}]$ | fixed | - | fixed |
| $C_{batt}[J\,kg^{-1}\,K^{-1}]$ | - | fixed | - |
| $k_{T,rad,am}[W\,m^{-1}\,K^{-1}]$ | - | fixed | - |
| $h_{conv}[W\,m^{-2}\,K^{-1}]$ | - | fixed | - |

**Table 3.3:** Constraints on parameters variation with aging.

the model parameters are reported in Table 3.3: the $x$ value, that is used to indicate the parameter obtained in the previous aging step, multiplies a number (1.2 or 2), suitable for the order of magnitude of the parameter and its original variation range, to consider a tolerance for the limit value of the parameter.

## 3.5 Final remarks

In this chapter, the methods for the model calibration were presented, consisting in the calibration of the thermodynamic part and the kinetic part.

The kinetic part of the model exploited a methodology developed in a previous thesis work on the same topic [109]. The PSO algorithm was improved, by implementing an adaptive behaviour for the particles' evolution in the solution space; modifications to the cost function were also made. Moreover the experimental protocol used by the algorithm for the data fitting was adapted to account for the different battery type.

For what concerns the thermodynamic description, after calibrating and improving the electrodes intercalation curves of the electrodes in a pristine cell, three parameters are introduced to account for the degradation modes: loss of lithium inventory $LLI$ and loss of active material on the positive $LAM_p$ and on the negative $LAM_n$ electrode. A sensitivity analysis has been performed and discussed to understand the effects of these parameters' variation. A thermodynamic PSO algorithm has been implemented to calibrate these parameters, through the fitting of an experimental discharge at 0.1C-rate and 25°C. Thanks to the calibration on fictitious dataset, the reliability of the model has been proven.

Finally, the procedure to combine together the two calibration methods for the complete characterization of an aging stage has been illustrated. This procedure has been applied to describe a battery behaviour in five degradation stage throughout the aging campaign. In the following chapters the results obtained applying the proposed methodology will be presented.

# 4 BOL data analysis and aging campaign settings

In this chapter, the calibration of the model parameters at the begin of life (BOL) condition is reported. Moreover, the selection of the testing condition of the aging campaign is made, aiming to stress two different phenomena: SEI growth and lithium plating.

## 4.1 BOL calibration and validation of the results

As explained in section 3.4 the procedure for the begin of life calibration is obtained through the kinetic PSO, setting the thermodynamic parameters $LLI$, $LAM_p$ and $LAM_n$ to zero. The kinetic PSO compares at each iteration the experimental protocol described in chapter 3.1 with the results simulated by the model, with the set of parameters of that iteration. Therefore, the batteries were tested following the experimental protocol at begin of life; the dataset obtained is given as an input to the kinetic PSO.

The values obtained for the begin of life parameters are reported in Table 4.1.

The comparison between the BOL experiments and the model on the measurement involved in the proposed protocol, is shown from figure 4.2 to 4.5, and it can be found at the end of this section.

At BOL condition, the batteries were also tested to provide an experimental dataset in order to understand how the validation of the results obtained by the optimization can be extended and if the set of the estimated parameters effectively represents the battery behaviour. This validation dataset includes:

- four complete discharge curves from 100% to the lower voltage limit at 1C-rate, with four different temperatures: 0°C, 10°C, 25°C, 40°C;
- four complete discharge curves from 100% to the lower voltage limit at 2C-rate, with four different temperatures: 0°C, 10°C, 25°C, 40°C;
- two complete discharge curves from 100% to the lower voltage limit at 0.5C-rate, at 25°C and 40°C;
- four impedance spectra from 10 kHz to 10 mHz with 30 logarithmically spaced points, at 50% SOC and four different temperatures: 0°C, 10°C, 25°C, 40°C;

| Parameter | Anode | Separator/Electrolyte/Battery | Cathode |
|---|---|---|---|
| $C_dl[F\,m^{-2}]$ | 0.738 | - | 0.455 |
| $k[m\,s^{-1}]$ | $1.46{\cdot}0^{-9}$ | - | $1.40{\cdot}10^{-9}$ |
| $c_{e,0}[mol\,m^{-3}]$ | - | 1497 | - |
| $FCE[-]$ | - | 0.115 | - |
| $t_0^+[-]$ | - | 0.39 | - |
| $\sigma_s[Sm^-1]$ | - | - | 7.23 |
| $R_p[m]$ | $1.12{\cdot}10^{-5}$ | - | $7.5{\cdot}10^{-6}$ |
| $D_s[m]$ | $7.55{\cdot}10^{-15}$ | - | $1.00{\cdot}10^{-13}$ |
| $R_{film}[\Omega m^2]$ | 0.014 | - | - |
| $\epsilon_e[-]$ | 0.37 | - | 0.37 |
| $EA_k[J\,mol^{-1}]$ | 49420 | - | 56836 |
| $EA_{D_s}[J\,mol^{-1}]$ | 45209 | - | 56476 |
| $C_{batt}[J\,kg^{-1}\,K^{-1}]$ | - | 871 | - |
| $k_{T,rad,am}[W\,m^{-1}\,K^{-1}]$ | - | 0.256 | - |
| $h_{conv}[W\,m^{-2}\,K^{-1}]$ | - | 29 | - |

**Table 4.1:** Model parameters optimized for BOL condition.

- four impedance spectra from 10 kHz to 10 mHz with 30 logarithmically spaced points, at 25°C and different states of charge: 100% SOC, 75% SOC, 50% SOC, 25% SOC.

These tests were chosen to show different operative conditions from the ones of the experimental protocol on which the calibration is based, and hence they can highlight strengths and limits of the obtained set of model parameters.

It is possible to see the comparison between the experiments and the model in the validation dataset from Figure 4.7 to 4.10.

The root mean square error (RMSE) is used as a measure of the average distance between the experimental data and the output simulated by the model. The results are reported in Table 4.2. In the literature, works related to the parameter identification of a P2D physical model report the RMSE calculation to qualify the results of the simulated discharge curves. Zhang et al. [132], testing $LiCoO_2$ batteries, obtained RMSEs in the range between 8 and 24 mV for discharges between 0.5C and 2C at 30°C and in the range between 20 and 37 mV for discharges in the said C-rate range but at 15°C. Park et al. [133] worked with a NCA battery and reported RMSEs of 25.5 mV and 11.8 mV, respectively for a 1C and 0.5C discharge, both at 25°C. Li et al [134] achieved RMSEs between 6.4 mV and 12.9 mV for discharge

curves with C-rate in the range 0.5C-3C and at 25°C, with a LMO battery. Yang et al. [120] obtained RMSEs of 21.6 mV and 15.6 mV for a 2C and 1C discharge curve at 25°C, respectively, working with an NMC batty. For what concerns the calculation of RMSEs between experimental EIS and EIS simulated with a phyisical model, no literature is present, except for the previous thesis work [109], that obtained values ranging between 0.3 and 2.7 mΩ for EIS at 25°C, at SOC between 20% and 100%, on NMC-LMO batteries.

Analyzing the results obtained for the calibration of the pristine cell, it is possible to observe that:

- low values of RMSE are obtained for discharges at high temperature, 40°C, even for high C-rate. In fact, in the case of the discharge at 1C it is achieved a RMSE of 9.02mV, while for the one a 2C it is equal to 18.93mV, which is comparable to the literature values.

- for the discharge curves simulated at 25°C in Figure 4.7 there is a very good accordance with the experiments, both at 0.5C, 1C and 2C. Nevertheless a consideration on the meaning of the RMSEs values has to be made. In fact, this kind of methods for the error estimation of the data, is not totally fair for two main reasons. The first one is that if a simulated discharge lasts less than the experimental one (see discharges at 10°C and 0°C in Figure 4.8), the comparison of the data using the RMSE will only be computed in the curves section where both the discharges are existing, neglecting the fact that the experimental discharge lasts longer. Therefore, this may appear as an underestimation of the error, but that it's not completely true, and the reason why is connected to the second point. The second reason is related to the "nature" of the data that are being compared, namely the shape of the voltage profile during a discharge. As in the last section of the discharge the voltage decreases rapidly, becoming almost vertical, if even a very small shift between the simulated and the experimental discharge is present in that section, the RMSE would increase dramatically, bringing to an overestimation of the error. Therefore, referring to the previous case, the error on the simulated discharge that lasts much less than the experimental one, could be adequate. The RMSEs that are obtained for the discharge at 1C, 10°C and 0°C are 68.5mV and 101.5mV, that are the highest values obtained. On the other hand, there are cases, e.g. the discharges at 25°C of Figure 4.7 where the experimental behaviors are well fitted, but their quality is underestimated by a quite high RMSE due to a small shift. In Figure 4.1 it is possible to see the residual between the experimental and the simulated discharges: the error generally ranges between

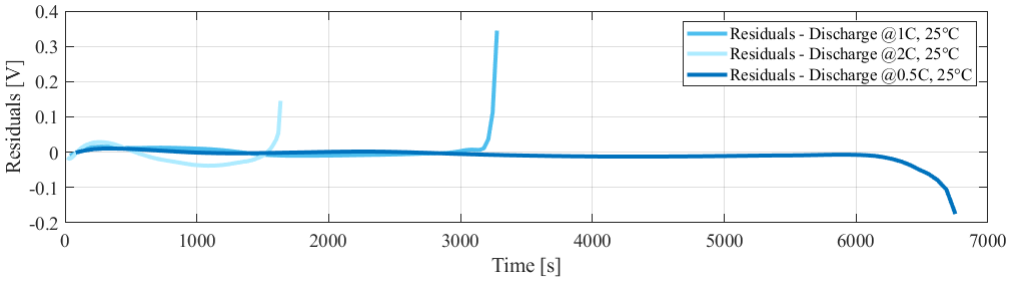


**Figure 4.1:** Residuals between experimental and simulated discharges.

±0.02V, and at the end of the discharges it is possible to see an increase or decrease, corresponding to a delay/advance of the simulated discharge with respect to the experiments.

- at low temperature the simulated discharges do not always fit well the experimental characteristics.
- in the EIS tests (Figure 4.2, Figure 4.3, Figure 4.11, Figure 4.10), higher RMSEs are obtained, compared to the ones obtained in the previous thesis work. What can be observed is a shift in the HFR value that is well-reproduced only at 25°C. At lower temperatures, the HFR of the simulated curves increases too much with respect to the one of the experimental tests. This is probably due to a non-optimal correlation between the ionic conductivity and the battery temperature. As the $FCE$ parameter is quite low, the ionic conductivity has a high impact on the HFR. The dependence of this parameter with temperature is provided by the correlation described in equation 2.26 and is not a fitted characteristic. Even if the lithium diffusion coefficient in the electrolyte is directly linked to the ionic conductivity through the Nernst-Planck equation (see chapter 2.4.3), the diffusive phenomena seems quite well described by the model, even in relation with temperatures variation as can be observed in Figure 4.9. For future developments, may be necessary to change the temperature relation of the ionic conductivity, or decoupling the ionic conductivity from the lithium diffusion coefficient.

| Technique | Operating condition | RMSE |
|---|---|---|
| Discharge curve | 0.5C, 25°C, 100 − 0% SOC | 25.1mV |
| | 1C, 0°C, 100 − 0% SOC | 101.5mV |
| | 1C, 10°C, 100 − 0% SOC | 68.5mv |
| | 1C, 25°C, 100 − 0% SOC | 37.5mV |
| | 1C, 40°C, 100 − 0% SOC | 9.02mV |
| | 2C, 0°C, 100 − 0% SOC | 45.54mV |
| | 2C, 10°C, 100 − 0% SOC | 29.45mV |
| | 2C, 25°C, 100 − 0% SOC | 29.32mV |
| | 2C, 40°C, 100 − 0% SOC | 18.93mV |
| EIS | 25°C, 100% SOC | $Z_R$: 5.66mΩ<br>$Z_I$: 5.46mΩ |
| | 25°C, 75% SOC | $Z_R$: 5.43mΩ<br>$Z_I$:5.52mΩ |
| | 25°C, 50% SOC | $Z_R$: 5.04mΩ<br>$Z_I$: 5.05mΩ |
| | 25°C, 25% SOC | $Z_R$: 3.73mΩ<br>$Z_I$:5.66mΩ |
| | 40°C, 50% SOC | $Z_R$: 5.28mΩ<br>$Z_I$:5.60mΩ |
| | 10°C, 50% SOC | $Z_R$: 9.71mΩ<br>$Z_I$:6.49mΩ |
| | 0°C, 50% SOC | $Z_R$: 16.7mΩ<br>$Z_I$:8.27mΩ |

**Table 4.2:** Summary of the RMSE between the model data and the experimental data in the validation dataset at BOL condition.

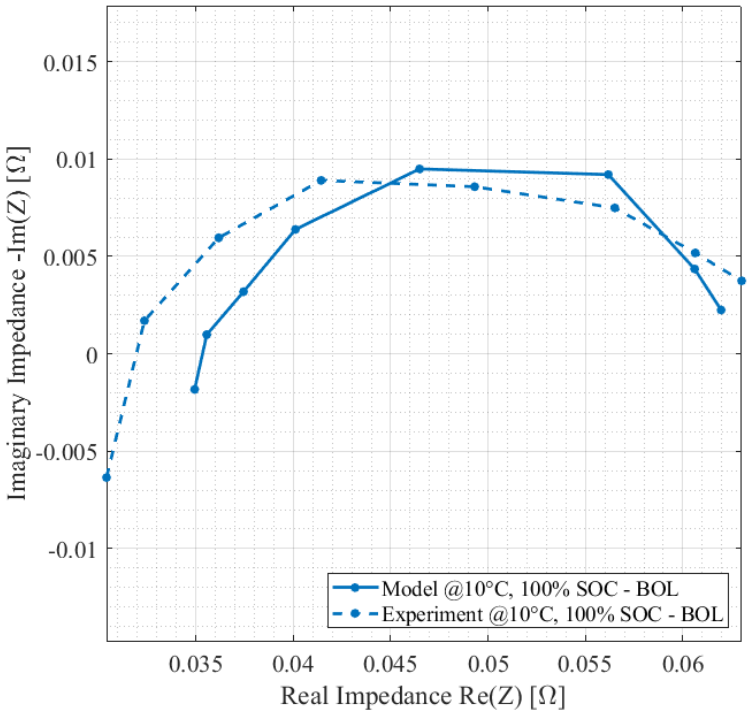


**Figure 4.2:** BOL: Impedance spectrum at 10°C, 100% SOC. RMSE real impedance: 2.32 mΩ, RMSE imaginary impedance: 2.28 mΩ

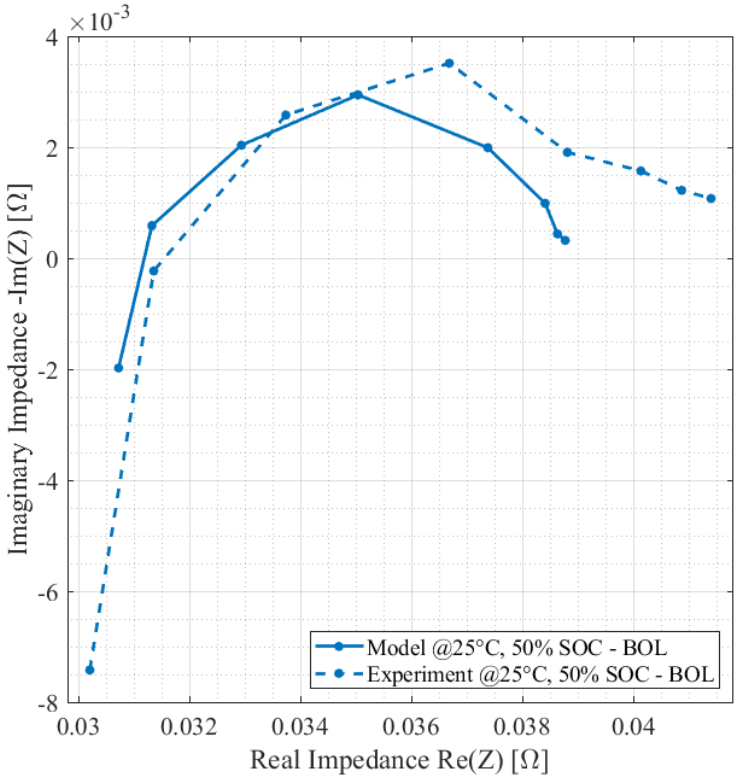


**Figure 4.3:** BOL: Impedance spectrum at 25°C, 50% SOC. RMSE real impedance: 1.60 mΩ, RMSE imaginary impedance: 2.01 mΩ

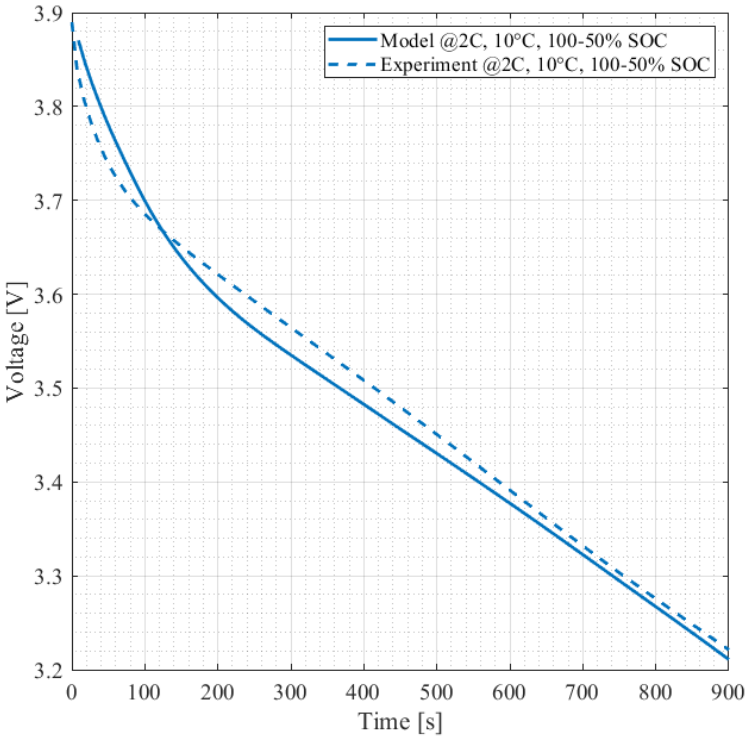


**Figure 4.4:** BOL: Discharge curve at 2C, 10°C, from 100% SOC to 50% SOC. RMSE: 25.9 mV

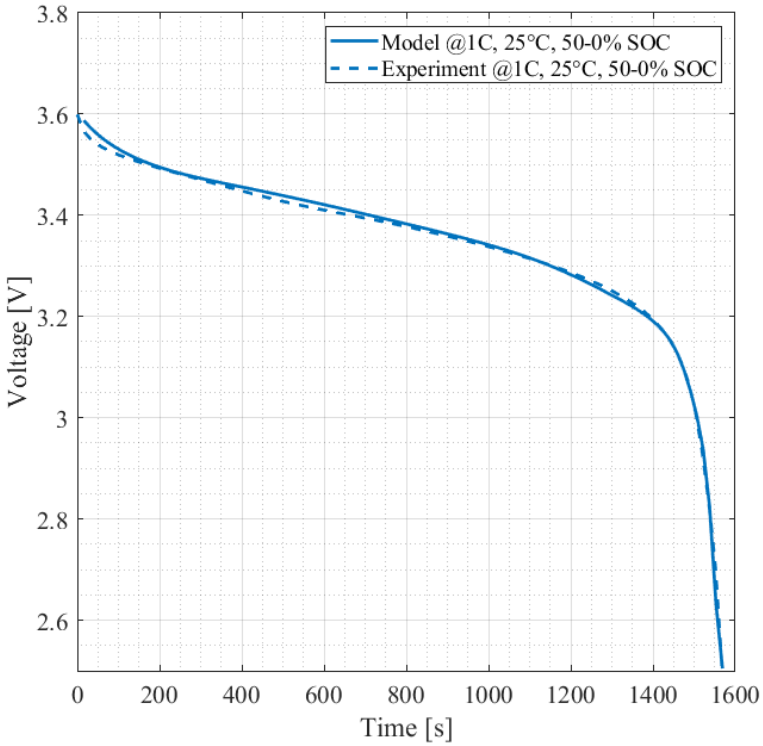


**Figure 4.5:** BOL: Discharge curve at 1C, 25°C, from 50% SOC to 0% SOC. RMSE: 9.62 mV

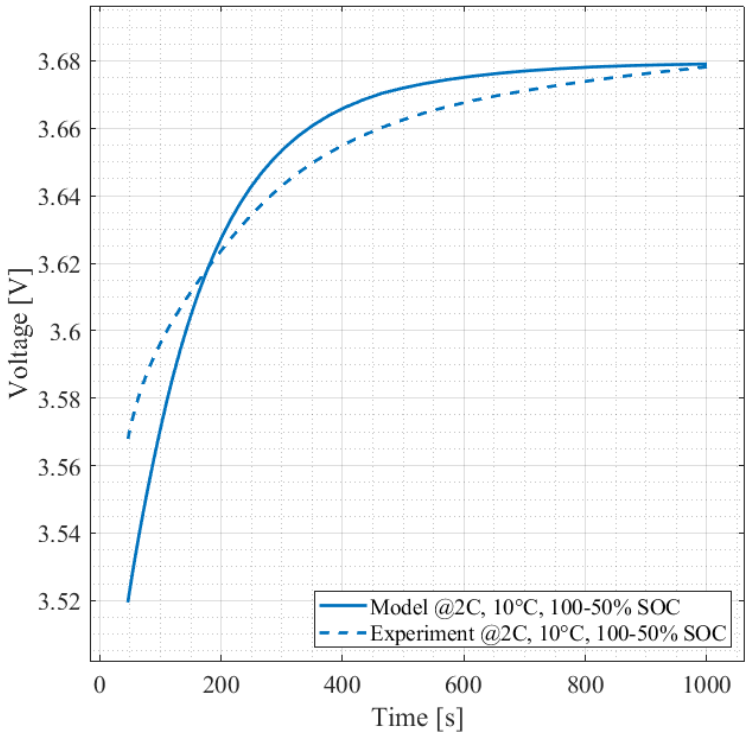


**Figure 4.6:** BOL: Relaxation curve after discharge at 2C, 10°C, from 100% SOC to 50% SOC. RMSE: 21.9 mV

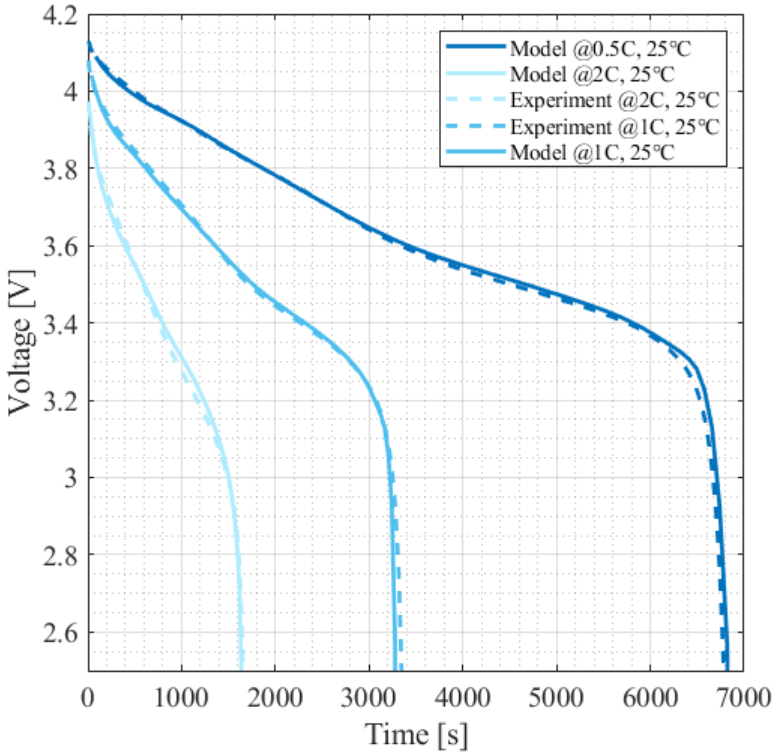


**Figure 4.7:** Validation dataset BOL: Discharge curves at 25°C, from 100% SOC to 2.5V, current rate variation.

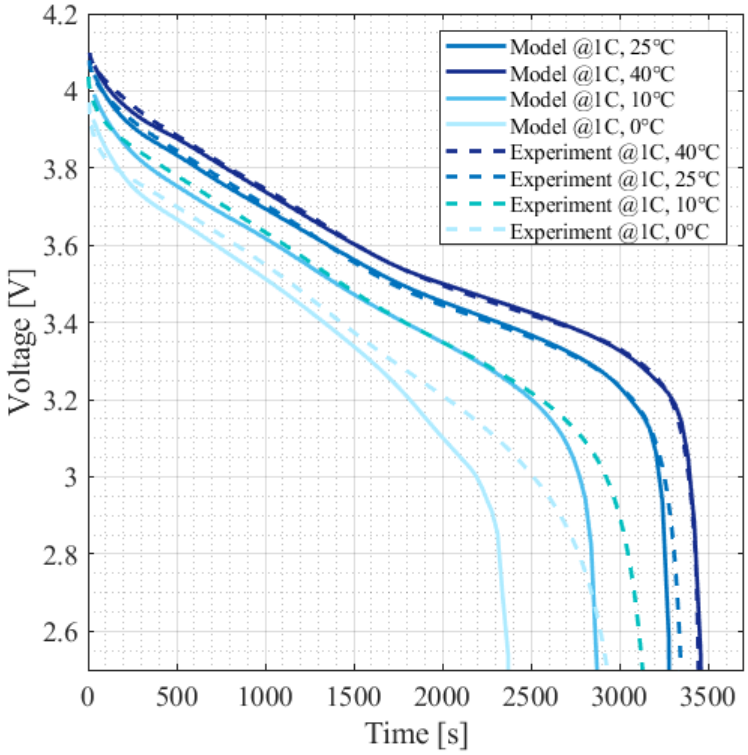


**Figure 4.8:** Validation dataset BOL: Discharge curves at 1C-rate, from 100% SOC to 2.5V, temperature variation.

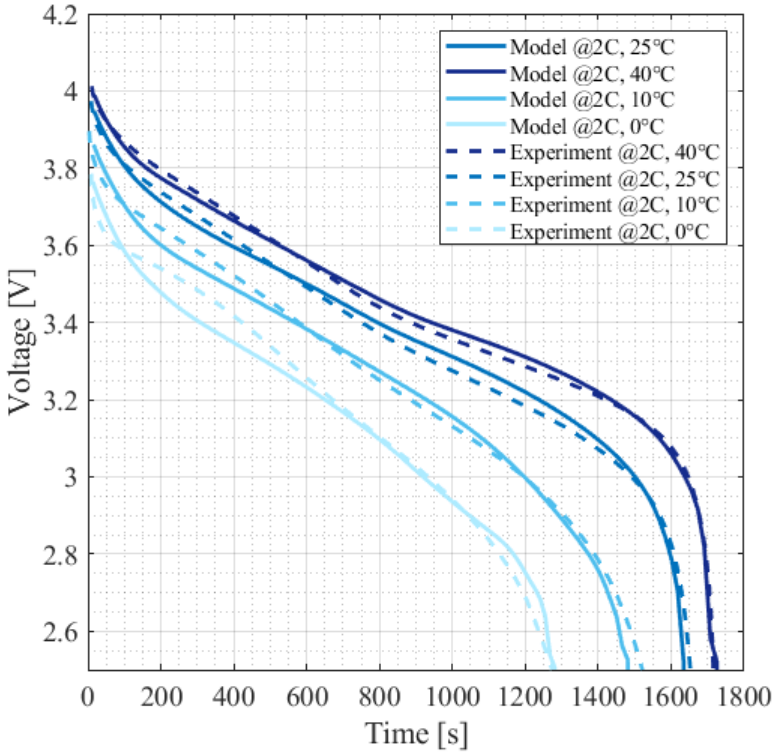


**Figure 4.9:** Validation dataset BOL: Discharge curves at 2C-rate, from 100% SOC to 2.5V, temperature variation.

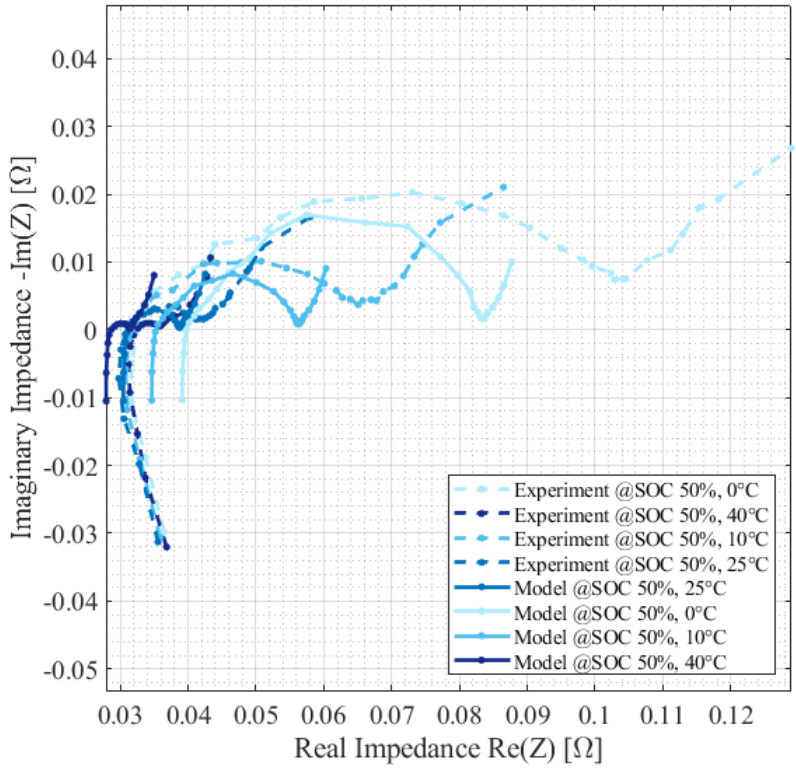


**Figure 4.10:** Validation dataset BOL: Impedance spectra at 50% SOC, temperature variation

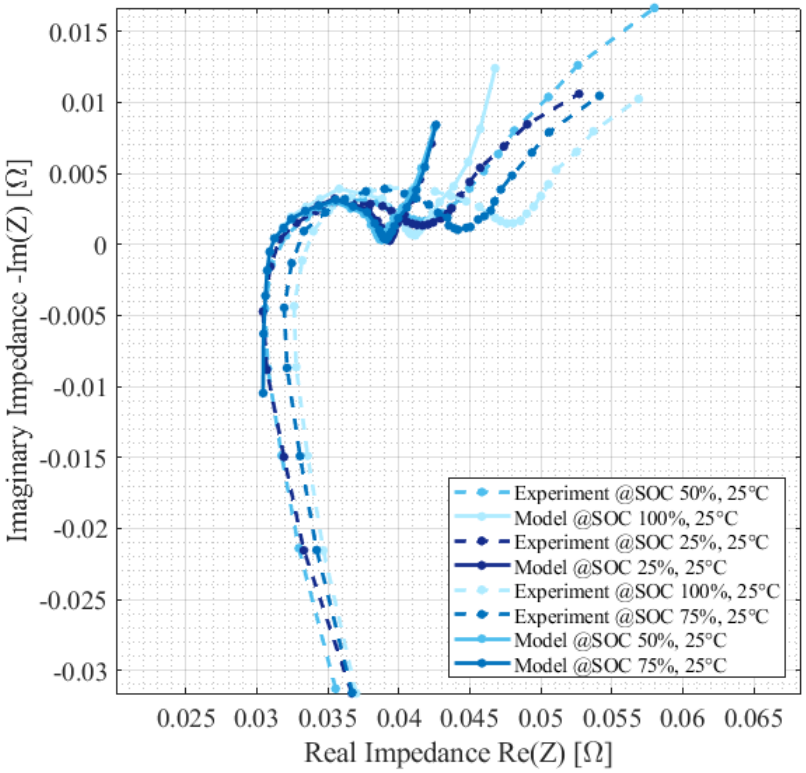


**Figure 4.11:** Validation dataset BOL: Impedance spectra at 25°C, SOC variation.

## 4.2 Understanding of SEI growth stressors

The battery degradation manifests itself as power and energy fades associated with impedance rise and capacity loss. The battery components experience different aging processes, according to their operating conditions. The aim in this work is to evaluate two degradation mechanisms separately, to better understand their aging effect on the battery behaviour singolarly: SEI growth and lithium plating. The solid electrolyte interphase (SEI) is a thin layer that is inevitably generated on the negative electrode surface at the first charge of the first cycle of the battery. It generates from the decomposition of the electrolyte, that is unstable at low potentials, and therefore, it reduces when the anode first experiences low potentials [135]. The SEI formation passivates the anode surface, preventing it from further unwanted parasitic reactions with the electrolyte, that would continuously occur without the protection of the SEI [136]. Ideally, the SEI should have a high ionic conductivity to favour the ions transport, a proper thickness and uniformity, mechanical strength, and high chemical and structural stability to enable a longer cycle life and improve the safety of the batteries [137], [138]. However, the SEI is actually usually chemically heterogeneous and unstable, leading to continuous degradation of the electrolyte and the interphase itself during repeated cycles or long-term storage, and also mechanically fragile, resulting in fractures: breakage and reconstruction phases alternates, consuming the electrolyte and leading to the formation of a porous and thickened SEI, that increases the battery internal resistance and extends the lithium-ion transport path [64], [139].

At high temperatures, the SEI dissolution process is enormously intensified. The high temperature also intensifies adverse electrolyte decomposition reactions, whose products may attack the SEI, leading to severe SEI decomposition reactions [140]. These two mechanisms lead to the breakage and regeneration phases just described, causing the growth of thick and more resistive SEI layer. The SEI growth phenomenon leads to relevant capacity loss for battery cycled or stored at elevated temperatures.

Moreover, as SEI develops, it may reach the electrode pores, reducing the availability of active sites with time [141].
By coupling high temperatures with high SOC storage, an acceleration of the degradation is observed. The effects that are expected for the operation at high temperatures are depicted in Figure 4.12.

In the literature, SEI growth on the graphite anode is highlighted to be the most relevant aging mechanism in the battery calendar aging process [141–143]. This

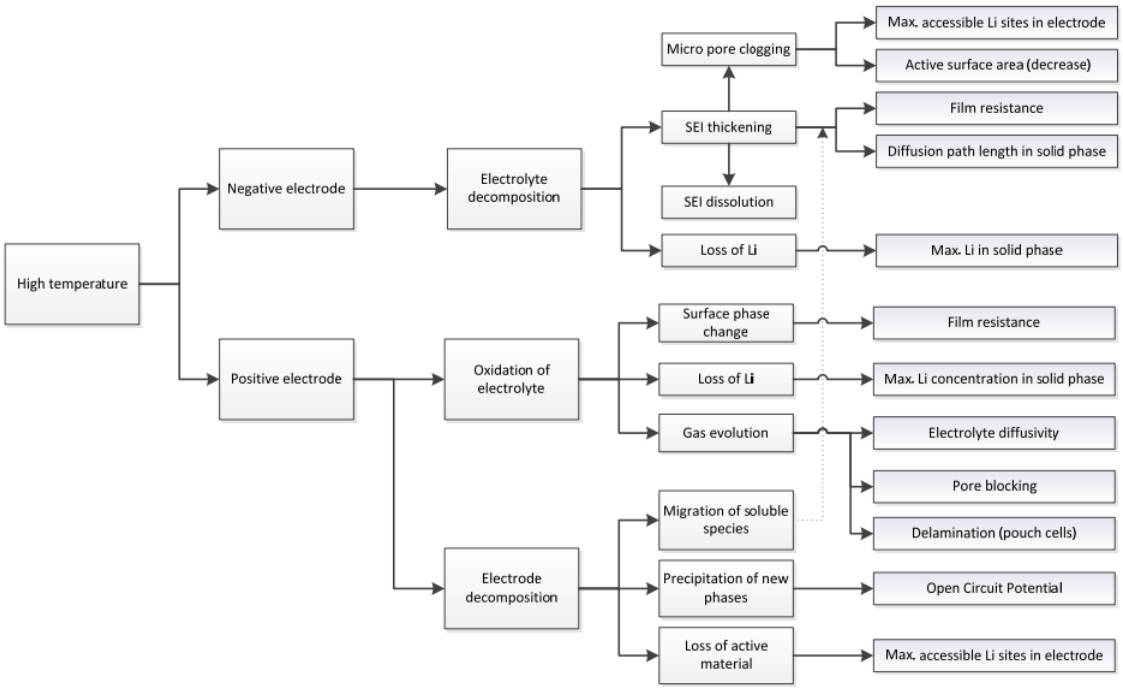


**Figure 4.12:** Expected battery degradation caused by high temperatures. (Taken from [130])

results in the irreversible loss of lithium inventory and in the increment of the cell's impedance [144]. Moreover, loss of active material also occurs on both the electrodes, leading to additional capacity fade, during the calendar time.

The capacity loss rate is highly dependent on some stress parameters, as the storage SOC and the temperature [145]. Maures et al. studied the effects of calendar aging at different temperatures on NCA batteries, and modeled the degradation mode (LAM and LLI) relation with temperature with an Arrhenius law, and proportional to the square root of the storage time [143].

On the basis of this literature review, high temperature is selected as the main stressor for the investigation of SEI formation and growth mechanism during calendar aging. Additionally, the effect of different storage SOCs will be investigated.

### 4.2.1 Selection of calendar conditions and diagnostics

To investigate the effect of SOC on calendar aging, four batteries has been stored at four different SOC and at a constant temperature of 60°C (see Table 4.3) in the climatic chamber Binder KT 53 for eight weeks. The temperature and the voltage of the four batteries were recorded once per hour. Storing the batteries at different SOCs allow to study the relation between the SEI growth formation and the state of charge at which the battery is stored.

| Calendar aging conditions | |
|---|---|
| Temperature | SOC |
| 60°C | 100% |
| | 80% |
| | 50% |
| | 10% |

**Table 4.3:** Calendar aging conditions

To monitor the degradation of the batteries and to have an understanding of the aging behaviour throughout the storage period, the checkup procedure was performed periodically, once every two weeks. The procedure is summarized in Table 4.4, and the main steps are:

1. the batteries are transferred in the climatic chamber Binder MKF 720 Eucar 6 and charged up to 100% SOC with a CC+CV charge process at 25°C an 0.1C-rate (variable required time, according to the staring SOC, <10 hours);
2. the samples are tested according to the experimental protocol described in chapter 3.1 (<2 hours);
3. the battery are charged to 100% SOC at 0.1C-rate and 25°C (<10 hours);
4. a full slow discharge at 25°C and 0.1C-rate is performed;
5. the batteries are charged to 100% SOC at 0.1C-rate and 25°C (<10 hours);
6. the samples are brought to their storage SOC with a 0.1C discharge at 25°C and are then placed again in the chamber Binder KT 53 at 60°C.

The procedure includes pauses between the subsequent steps to allow the relaxation of the samples, to guarantee that steady state is reached. The time necessary for the check-ups is quite long; the charge steps were sometimes accelerated by charging at higher C-rate (1C) up to 80% SOC and completing the remaining charge to 100% at 0.1C-rate: this allows to reduce significantly the charge time.
The choice of the tests is linked to the parameter calibration methods: the five tests of the experimental protocol provide the experimental data for the calibration of the kinetic parameters, while the discharge described in step 4 allows the calibration of the three thermodynamic parameters.

| | Steps | Parameters | Time duration |
|---|---|---|---|
| 1 | Charge CC+CV | I=C/10, until 100%SOC | <10h |
| - | Pause | - | <2h |
| 2 | Protocol | see | <2h |
| 3 | Slow charge | I=C/10, until 100%SOC | <10h |
| - | Pause | - | <2h |
| 4 | Discharge | I=C/10, until 2.5V | <10h |
| 5 | Charge CC+CV | I=C/10, until 100%SOC | <10h |
| - | Pause | - | <2h |
| 6 | Discharge | I=C/10, until SOC=$SOC_{calendar}$ | <10h |

**Table 4.4:** Diagnostic procedure

## 4.3 Understanding of Lithium plating stressors

The aim of this part of the activity is a non-destructive characterization of the aging behaviour and degradation effects of cells undergoing lithium plating. Therefore, it is fundamental to understand what are the conditions that promote the lithium plating phenomenon.

Two main mechanisms are involved in the lithium plating, and they may verify at the same time or not:

- during the charge process, *Li* ions migrate from cathode to anode, in order to intercalate into the negative electrode material [146]. When the rate of lithium ions transport in the electrolyte is faster than the intercalation rate in the graphite, lithium plating will occur [147], as the negative electrode particles gets saturated;
- when the graphite potential is below 0V vs. $Li/Li^+$, the lithium plating reaction is promoted: therefore, lithium intercalation and lithium plating are in competition, resulting in a characteristic mixed potential [148].

The plated lithium favors the lithium dendrites' growth, especially at high current densities (see chapter 1.3.3): the dendrites grow rapidly and, if they penetrate in the separator and connect the anode and the cathode, result in internal short circuit [149].

Lithium metal deposition is the most notable degradation mechanism at low temperatures. In fact, at low temperatures the intercalation and deintercalation of lithium ions are hindered, because of a more limiting grain boundary resistance at

the cathode and a slower solid state diffusion at the anode [57]. Moreover, the ionic conductivity of the electrolyte decreases, as its viscosity increases with lower temperatures [150]. Meantime, the lithium ions permeability is reduced by SEI film [151]. Therefore, as in those conditions lithium deposition is the favoured reaction with respect to intercalation, lithium plating occurs. The plated lithium may also react with the electrolyte, causing the SEI layer to grow: as a result, the SEI resistance and the cell impedance increase [57]. Lithium plating leads to severe performance degradation and safety issues.

As described in Chapter 1.3.3, in the literature many diagnostic technique to detect lithium plating can be found. Among those methods, the analysis of the voltage plateau is the most feasible method to detect lithium plating, as it does note require particular and expensive equipment and it is nondesctructive. This kind of measurement is still under investigation, and most of the literature work refer to tests on LiFePo cells, for which the evolution of the cathode during low-temperature operation can be considered negligible [152]. is rarely investigated.
The presence of this voltage plateau after charging at low temperature appears because the deposition of metallic lithium onto graphite leads to a characteristic mixed potential, which is formed by the superposition of the potential of the intercalated lithium-ions and the lithium metal that has been deposited on the electrode surface [110]. Plotting the derivative of the voltage over time, and viceversa, plotting the derivative of time over voltage, a peak/valley can be identified. In the literature, the characteristics of this peak are related to the amount of lithium plated during the charge process: Comparing the results obtained from this kind of analysis with an in-situ neutron diffraction, Luders et al. [153] demonstrates that the lithium plating amount is proportional to the increase of the time at which the dV/dt peak is identified.

Summarizing, the presence of the voltage plateau in the relax after charging at plating condition is related to the metallic lithium deposition into graphite. Nevertheless, part of the lithium plated during charge is stripped during the subsequent relax. Therefore it is possible to distinguish between:

- **reversible lithium plating**: it is the deposited lithium with durable electric contact with the anode, thus, it is stripped in the relaxation step, becoming again available for cycling and not resulting in any capacity loss;

- **irreversible lithium plating**: as this plated lithium shows only fragile electrical contact with the graphite, it may become electrically isolated from the negative electrode during the stripping process. This “dead” lithium is the

cause of capacity losses due to charging at plating conditions.

An experimental campaign of current pulses at low temperatures is carried out, to understand what conditions promote lithium plating. This will be helpful to choose the operating conditions for the aging campaign, ensuring that lithium plating is stressed.

### 4.3.1 Voltage relaxation campaign

Evidence of lithium plating, detected by looking for the presence of the voltage plateau after a charge at low temperature, has been investigated carrying out a dedicated experimental campaign, performing current pulses at different operating conditions and analyzing the voltage profiles of the subsequent relaxations.

As described in chapter 2.3.2, a plateau in the voltage translates into a valley in the DV (for the relaxation curve it corresponds to the derivative of the voltage in time dV/dt) and a peak in the IC (dt/dV) curve. Therefore the peak position and intensity that characterize the voltage during relaxation in the IC-DV plots are employed for the interpretation of the relaxation tests.

The stressors that govern these particular characteristics have been investigated. The experimental matrix with the selected operating conditions can be seen in Table 4.5. The effects of current, temperature, initial SOC ($SOC_i$) and depth of charge (DOC) on the voltage plateau characteristics will be analyzed.

The results of the experimental campaign are reported from Figure 4.13 to Figure 4.16. In each figure, three plots are present: the voltage during relaxation in time, the IC and the DV of the said voltage profile. The legend reports the charge condition and is visible in the first plot, but refers to the whole figure.

Each figure depicts the voltage behaviour during relaxation after that a charge in a particular condition has been performed. The voltage during relaxation, after a charge pulse, generally would decrease similarly to a decaying exponential, as described in chapter 2: different mechanisms are involved, each occurring with a specific characteristic time; potential gradient and lithium concentration gradient start evolves to reach an equilibrium state. Additionally, in this case lithium plating may verify during charge: therefore, in the relaxation also stripping of the reversibly plated lithium may occur.

Different curve colors in the same figure identify a test performed in same conditions but at a different temperature. What can be observed is that the local peaks in the IC plots, that characterize the plating detection, are present for each charge condition at the same voltage value, even for different temperatures. In all the IC

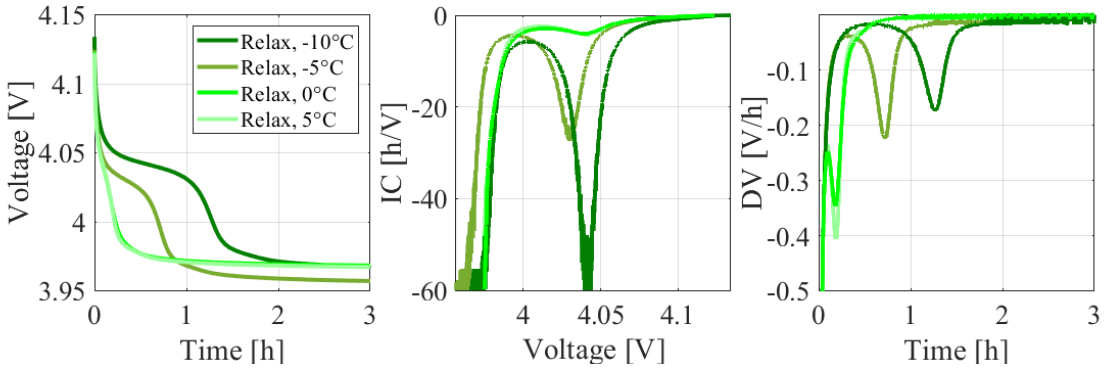


**Figure 4.13:** Voltage profile, IC and DV during relax after charge 1C, 50-80% SOC

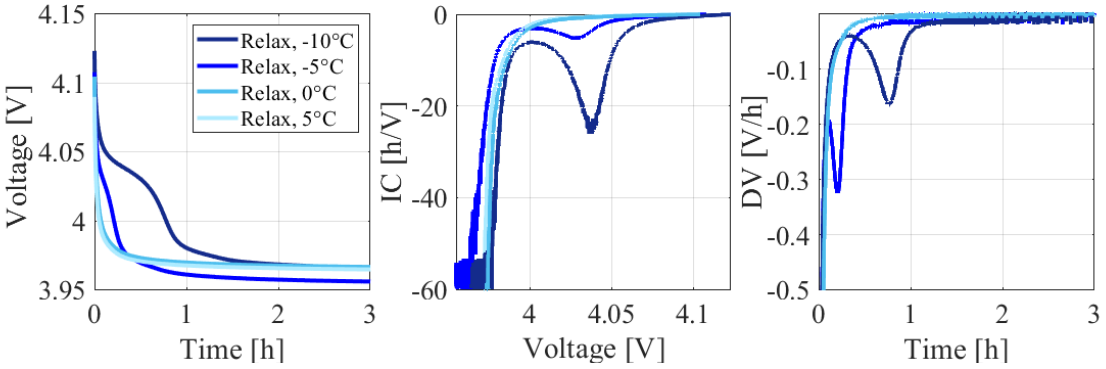


**Figure 4.14:** Voltage profile, IC and DV during relax after charge 0.5C, 50-80% SOC

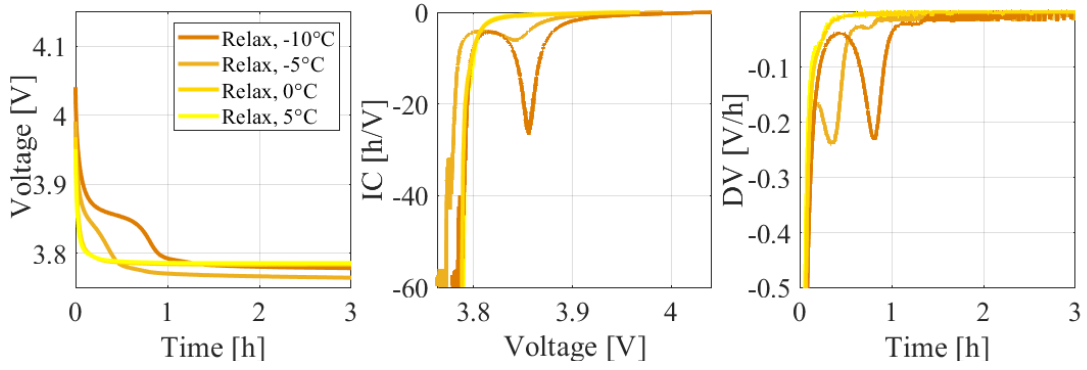


**Figure 4.15:** Voltage profile, IC and DV during relax after charge 1C, 30-60% SOC

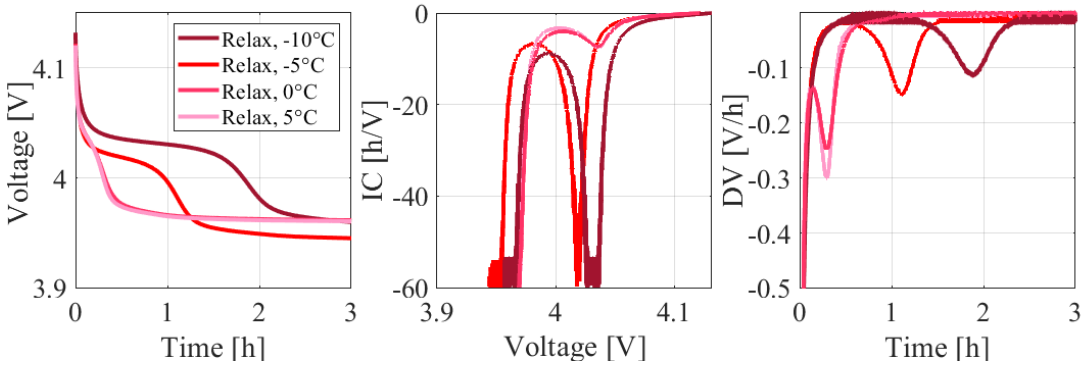


**Figure 4.16:** Voltage profile, IC and DV during relax after charge 1C, 30-80% SOC

| **Temperature** | 5°C | | | | -5°C | | | |
|---|---|---|---|---|---|---|---|---|
| **Cycle** | A | B | C | D | A | B | C | D |
| **SOC**$_i$ | 50% | 50% | 30% | 30% | 50% | 50% | 30% | 30% |
| **DOC** | 30% | 30% | 30% | 50% | 30% | 30% | 30% | 50% |
| **C-rate charge** | 1 | 0.5 | 1 | 1 | 1 | 0.5 | 1 | 1 |
| **C-rate discharge** | 0.2 | 0.2 | 0.2 | 0.2 | 0.2 | 0.2 | 0.2 | 0.2 |

| **Temperature** | 0°C | | | | -10°C | | | |
|---|---|---|---|---|---|---|---|---|
| **Cycle** | A | B | C | D | A | B | C | D |
| **SOC**$_i$ | 50% | 50% | 30% | 30% | 50% | 50% | 30% | 30% |
| **DOC** | 30% | 30% | 30% | 50% | 30% | 30% | 30% | 50% |
| **C-rate charge** | 1 | 0.5 | 1 | 1 | 1 | 0.5 | 1 | 1 |
| **C-rate discharge** | 0.2 | 0.2 | 0.2 | 0.2 | 0.2 | 0.2 | 0.2 | 0.2 |

**Table 4.5:** Experimental matrix for current pulses campaign

plots small deviation can be noted, but observing the related voltage profile that deviation can be assessed to an undesired slight difference in the starting SOC, that reflects on the whole measurement. The voltage value corresponding to the peak seems to be related to the initial and final SOC of the charge, but independent from the current values, at least for these C-rates, as the values are around 4.03V-4.04V for both C-rate 1 (Figure 4.13) and C-rate 0.5 (Figure 4.14). The said voltage value corresponds to the inflection point of the IC curve: the change in the slope can be attributed to the depletion of the mixed potential. The presence of this feature is, therefore, a clear indicator that lithium plating is occurred on the negative electrode in the previous charge step. A similar consideration can be made about the meaning of the time values related to the peaks in the DV plots: they represent the point in time where the decay of the mixed potential merges into residual cell relaxation.

- **temperature effect**: as the temperature decreases, the depletion time of the mixed potential is shifted exponentially towards higher values and the characteristic peak is stretched. At 5°C and 0°C peaks are only present for operating conditions of Figure 4.13 and Figure 4.16: these are the only conditions that reaches high SOCs (80%) with an high temperature (1C);

- **DOC effect**: higher DOC results in an increase of the charging time and also an increase of the time for the depletion of the mixed potential

- **initial SOC effect**: comparing Figure 4.13 and Figure 4.15, from the DV plots, it appears that for all the temperatures the peaks verifies after a longer time, from the begin of relaxation; this, probably happens due to the fact that the graphite is more lithiated at higher SOCs;
- **current effect**: comparing Figure 4.13 and Figure 4.14, it can be observed that a lower charging current result in less accentuated peaks in the IC and that, in the DV plot, the peaks appear earlier in time, namely the depletion time of the mixed potential related to the deposited lithium is faster.

The presence of the voltage plateau was encountered in many of the investigated conditions. This plateau is related to the presence of lithium plating during charge, and the characteristics of the peaks in the DV and IC plots suggest the stressors that govern this phenomenon:

- low temperatures;
- high DOC;
- high current;
- high initial SOC.

Therefore, after the observation of the phenomena in the experiments, a model implementation of the stripping/plating reactions would be a useful tool to understand the relation between the voltage plateau in the relaxation and the amount of deposited lithium and to confirm the hypothesis made on the stressors.

### 4.3.2 Model implementation

Lithium plating and stripping have been modeled and incorporated in the P2D electrochemical-thermal model described in chapter 2, and it has been applied to study the voltage plateau behavior after charging at low temperatures. The phenomenon, as it has been implemented, it is completely reversible; this hypothesis is reasonable, as this model is not used for the interpretation of the plating related degradation, but only for the study of the charge-relaxation dynamic.

The reversible reaction of lithium metal stripping/plating and the reaction of lithium ion intercalation/deintercalation into the graphite occur simultaneously in the negative electrode:

$$\mathrm{Li^+ + e^- \underset{\text{Stripping}}{\overset{\text{Plating}}{\rightleftharpoons}} Li\,(s)} \tag{4.1}$$

$$\mathrm{Li^+ + e^- + C_6 \underset{\text{Deintercalation}}{\overset{\text{Intercalation}}{\rightleftharpoons}} LiC_6} \tag{4.2}$$

| Parameters | |
|---|---|
| $c_{Li}^{ref}$ $[mol/m^3]$ | 1000 |
| $c_e^{ref}$ $[mol/m^3]$ | 1000 |
| $k_{Li}$ [-] | $1 \cdot 10^{-8}$ |
| $k_{gr}$ [-] | $0.5 \cdot 10^{-10}$ |
| $R_{p,a}$ $[\mu m]$ | $3 \cdot 10^{-6}$ |
| $D_{s,a}$ $[m/s^2]$ | $5 \cdot 10^{-14}$ |
| $\alpha_a$ [-] | 0.3 |
| $\alpha_c$ [-] | 0.7 |

**Table 4.6:** Negative electrode and the plating reactions parameters

The total current density in the negative electrode can be computed as the sum of the current densities of the two reactions

$$i_a = i_{gr} + i_{Li} \tag{4.3}$$

where $i_{gr}$ is the current density of negative electrode intercalation reaction and $i_{Li}$ is the current density of the lithium metal deposition reaction. The current density of the intercalation reaction can be calculated with the Butler-Volmer equation:

$$i_{gr} = a i_{0,gr} \left( e^{\frac{\alpha_{a,gr} F}{RT} \eta_{gr}} - e^{\frac{\alpha_{c,gr} F}{RT} \eta_{gr}} \right) \tag{4.4}$$

where $i_{0,gr}$ is the exchange current density of the intercalation reaction, $\alpha_{a,gr}$ and $\alpha_{c,gr}$ are the anodic and cathodic charge transfer coefficients and $\eta$ is the overpotential. The exchange current density of the intercalation reaction is computed as:

$$i_{0,gr} = k_{gr} \left( c_{s,max} - c_s \right)^{\alpha_{a,gr}} \left( c_s \right)^{\alpha_{c,gr}} \left( c_e \right)^{\alpha_{a,gr}} \tag{4.5}$$

where $k_{gr}$ is a rate constant, $c_s$ is the lithium ion concentration at the anode surface, $c_{s,max}$ is the maximum lithium ion concentration and $c_e$ is the electrolyte concentration.

To compute the current density of the lithium metal deposition reaction, a form of the Butler-Volmer equation specific for deposition reactions is used, as in [154]:

$$i_{Li} = i_{0,Li} \left( \frac{c_{Li}}{c_{Li}^{ref}} exp \left( \frac{\alpha_a F}{RT} \eta \right) - \frac{c_e}{c_e^{ref}} exp \left( -\frac{\alpha_c F}{RT} \eta \right) \right) \tag{4.6}$$

The concentration of lithium metal $c_{Li}$ is computed with the Faraday's law:

$$\frac{\partial c_{Li}}{\partial t} = -\frac{i_{Li}}{nF} \tag{4.7}$$

The terms $c_{Li}^{ref}$ and $c_e^{ref}$ are the reference concentration of lithium metal and of the electrolyte respectively, that defines the exchange current density $i_{0,Li}$ as follows:

$$i_0 = Fk_{0,Li}\left(c_{Li}^{ref}\right)^{\alpha_c}\left(c_e^{ref}\right)^{\alpha_a} \tag{4.8}$$

where $k_{0,Li}$ is a rate constant.

Both the negative electrode and the plating reactions parameters adopted for the lithium plating model simulation are reported in Table 4.6. The values of $i_{0,Li}$ that can be found in the literature vary by two orders of magnitude []. Therefore, a qualitative calibration has been performed.

To provide an example of how the plating model works, three cases of charges and following relaxation simulated by the model are reported in Figure 4.17 and compared with the experiments at same conditions.

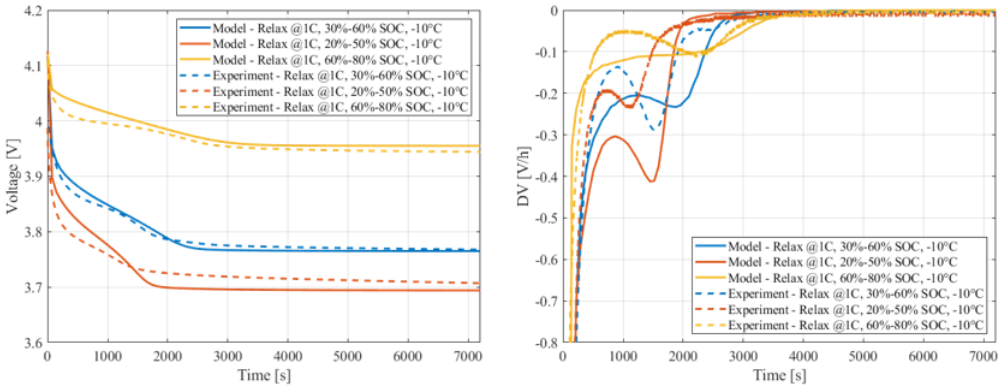


**Figure 4.17:** Comparison between experimental and simulated voltage profile during relaxation after charge.

Moreover, a sensitivity analysis on the operating conditions have been simulated to understand their effects. All the parameters, both the ones of the negative electrode, and the ones describing the electrochemical reactions are kept constant. The reference current pulse case is characterized by these operating conditions: -10°C, 1C, initial SOC 30% and final SOC 80%. Only one of them at a time is varied. Therefore, effects of temperature, current, initial and final SOC of the current pulses have been investigated.

**Temperature effect**

The current pulses and relaxation have been simulated for four different temperatures: -10°C, -5°C, 0°C and 10°C. In Figure 4.18 the lithium concentration in the negative electrode, at the separator side can be observed. The dash-dot lines stand for the charge processes, while the solid lines represents the concentration profiles

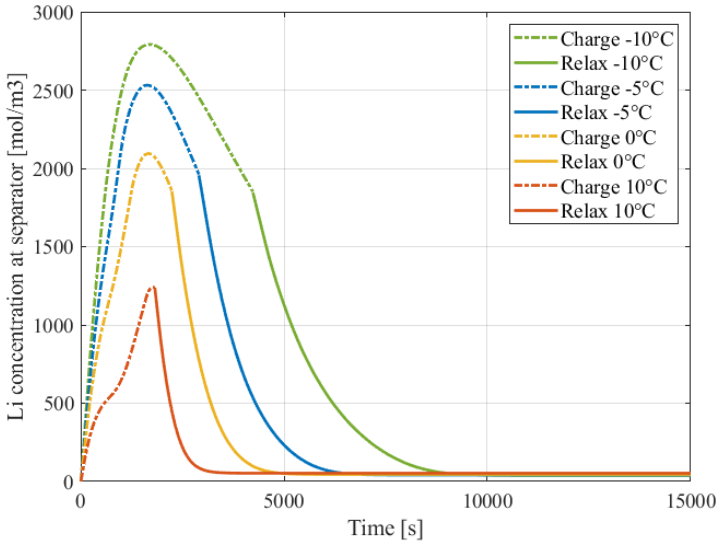


**Figure 4.18:** Lithium concentration at the separator during charge and subsequent relaxation at -10°C, -5°C, 0°C and 10°C.

during relaxation. Lower temperatures result in an increase of the lithium concentration that reaches the negative electrode during charge and therefore represents a higher possibility that the lithium is also plated. An inversion is present during charge, and is related to the fact that the battery enters the CV charge steps. As soon as the relaxation begins the lithium concentration gradient starts to deplete: this process is faster for higher temperature, while it requires longer at lower temperatures.

### Current of charge effect

Four charging C-rate have been simulated: 0.2C, 0.5C, 1C and 2C. The lithium concentrations at the separator for all the cases is reported in Figure 4.19. The lithium concentration peaks present in the charge, as mentioned before, can be related to the beginning of the CV step. What can be observed is that for higher currents, a higher lithium concentration is present on the negative electrode, near the separator. The relation with the C-rate is not linear, and the charge pulses at 1C and 2C shows basically no differences, as, charging at those C-rates at -10°C, the CV steps is reached rapidly and effects of different C-rates are not relevant.

### Initial state of charge ($SOC_i$) effect

The four conditions explored to understand the $SOC_i$ effect on the lithium concentration are: 30%, 40%, 50% and 60%. For these simulation, the DOC is kept constant and equal to 30%. In Figure 4.20, it can be noted that in the case with lower average SOC, the lithium concentration at the separator reaches higher values; this can be explained by the fact that such conditions correspond to a shorter CV

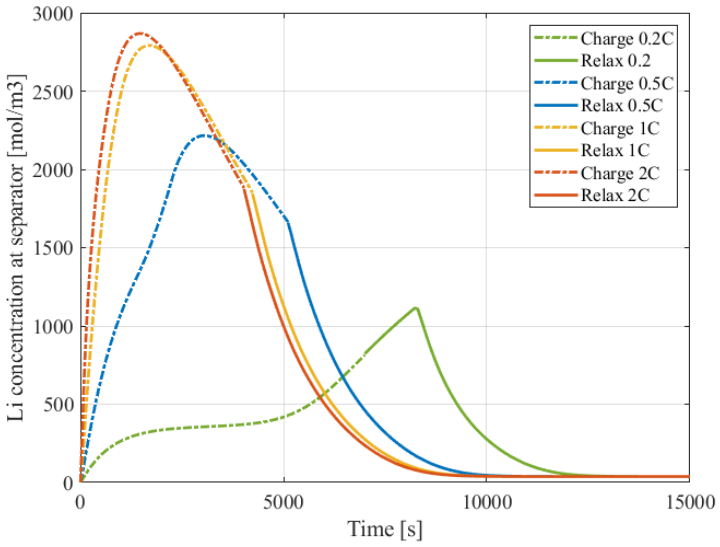


**Figure 4.19:** Lithium concentration at the separator during charge at different C-rates and subsequent relaxation.

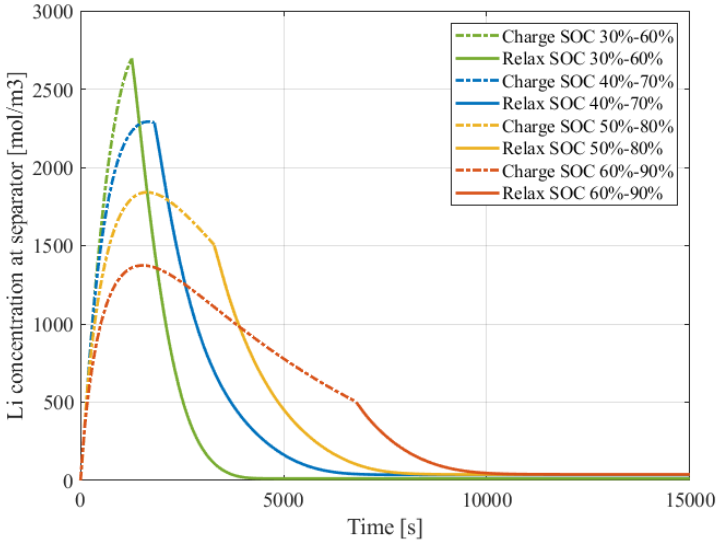


**Figure 4.20:** Lithium concentration at the separator during charge at different $SOC_i$ and subsequent relaxation.

phase, and therefore an higher average current in the current pulse, with respect to other cases. However, it can also be observed that the time required to deplete the lithium concentration is much faster for that case. On the other hand, at high SOCs the concentration of lithium does not present such a relevant increase, and, since a very long CV phase is necessary to reach 90% SOC, the current decrease causes also a reduction in lithium concentration; when relaxation starts the concentration decreases with a flatter slope. This may suggest that both the SOC and the charge duration play a role in the lithium deposition phenomenon, since a too short charge step result in a rapid and provisional concentration increase that is unlikely to be plated, and a too long charge, namely a too long CV step, hinders lithium plating as low currents do not solicit the phenomenon. Since at low temperatures to reach high SOCs long CV phases are needed, to promote lithium plating a compromise between charge duration and starting SOC may result in the most stressing condition, that for the case in Figure 4.20 is probably one among the SOC 40%-70% (blue curve) and the SOC 50%-80% (yellow curve).

**DOC effect**

To investigate the DOC effects, the final SOC is kept constant, equal to 80%, while the starting SOC varies. Four conditions have been simulated, where $SOC_i$ is equal to 30% (DOC=50%), 40% (DOC=40%), 50% (DOC=30%) and 60% (DOC=20%). In Figure 4.21 is shown the trend of the lithium concentration at the separator. Starting at lower $SOC_i$ results in higher lithium concentration during charge, as a longer charge process is needed. Therefore, for cases with same final SOC, the higher the DOC (the lower the $SOC_i$), the higher the amount of lithium that will reach the negative electrode.

### 4.3.3 Selection of cycle conditions and diagnostics

An aging campaign has been performed, with the aim to stress lithium plating and understand the effects of the operating conditions. The experimental current pulse campaign and the lithium plating implementation on the model provide useful information to select operating conditions in the aging campaign, to both stress and investigate the degradation resulting from lithium plating.

Therefore, the conditions listed in Table 4.7 have been selected.

The effect of cycling at plating condition will be investigated at two different temperatures: 0°C and -10°C. What it is expected is a more accentuated degradation in the batteries that will cycle at -10°C.

The differences in the aging from cycling at high SOCs with respect to cycling at low SOCs will be also investigated, as cycle A and C differs only for that aspect.

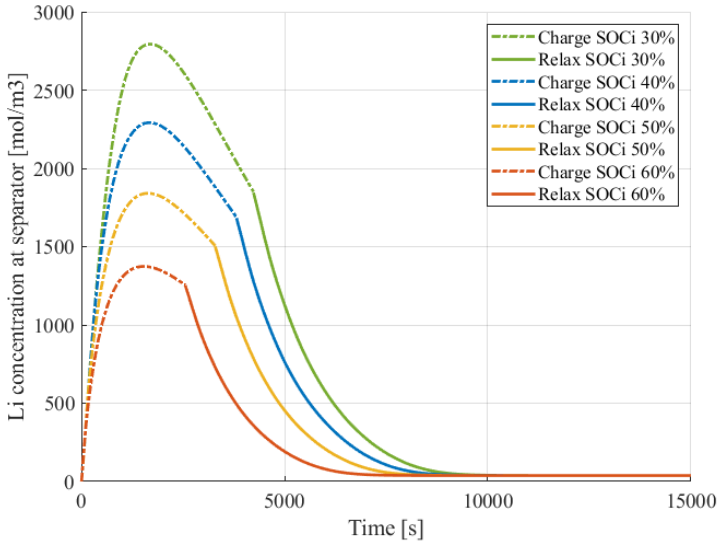


**Figure 4.21:** Lithium concentration at the separator during charge at different temperature and subsequent relaxation.

Comparing A and D, it is expected to highlight the influence of the DOC on the lithium plating formation.

Finally, the effect of the C-rate will be examined, from the comparison of the battery cycling with the A procedure and the one cycling with the B operating condition.

| **Cycles** | | | | |
|---|---|---|---|---|
| Cycle | A | B | C | D |
| $SOC_i$ | 50% | 50% | 30% | 30% |
| DOD | 30% | 30% | 30% | 50% |
| C-rate charge | 1 | 0.5 | 1 | 1 |
| C-rate discharge | 0.2 | 0.2 | 0.2 | 0.2 |

**Table 4.7:** Cycle aging conditions. Cycles A, B, C and D will be performed at 0°C and -10°C.

To track the batteries' performance evolution during aging a diagnostic procedure will be adopted. The diagnostics will be performed once every three equivalent full cycle (EFC). An EFC is completed when the exchanged charge during the discharge and charge steps are equal to the battery nominal capacity.
The diagnostic procedure is very similar to the one introduced for the batteries aged through calendar and described in Table 4.4. The only difference is that the batteries are brought to the initial SOC, $SOC_i$ (that refers always to the nominal capacity value), and that both the cycling and the diagnostics are performed inside

the same climatic chamber, Binder MKF 720 Eucar 6. Therefore, also the batteries that are cycled aged will be tested to provide the experimental data that allow the model calibration, through to the fitting of those data, operated by both the thermodynamic and the kinetic PSO.

## 4.4 Final remarks

In this chapter the methodology to calibrate the model of a pristine sample have been applied. To extend the validity of the estimated parameters, an additional dataset has been simulated and compared to the experiments with the calculation of RMSEs (section 4.1).

In section 4.2 the SEI growth phenomena and its stressors have been studied and calendar aging at 60°C and four different SOCs has been selected as the operating condition to investigate this degradation mechanism.

In section 4.3 the lithium plating phenomenon have been described. The voltage plateau detection in the relaxation subsequent to a charge pulse at low temperatures have been adopted in an experimental campaign dedicated to understand more about this feature and the link of the operating conditions with the lithium deposition on the graphite anode has been assessed thanks to the model implementation of the stripping/plating reactions. Finally, the operating conditions for cycle aging to stress lithium plating have been selected (see Table 4.7).

# 5 Aging modeling and interpretation

In this chapter, the results obtained from the experimental aging campaign have been analyzed and interpreted. Moreover, the methodology for the LIB model calibration during the degradation has been applied on one of the samples that underwent cycle aging in lithium plating condition.

## 5.1 Calendar aging analysis

Four batteries have been calendar aged, at the operating conditions specified in Table 4.3. The samples were all pristine, used only for some spot measurements; the tests performed before the aging campaign did not affect in a relevant way the batteries' performance and the slight differences between the samples, that can be observed at the "begin of test" condition, namely before the aging campaign beginning, are considered irrelevant for the scopes of this activity.

The samples have been stored for eight weeks. Since calendar aging may require long periods before showing relevant degradation, the analysis of the aging in this condition has to be considered as partial.

### 5.1.1 Capacity loss

In Figure 5.1 the capacity losses induced by the calendar operating conditions are reported for the four batteries. What can be noticed is that the storage SOC is a very influent parameter. The battery that was stored at SOC 10% shows basically no degradation, as only a 1% of the initial capacity has been lost. The sample stored at 50% SOC lost about 4.5% of the BOT capacity at the end of the eight calendar weeks. The most detrimental conditions are the ones at high SOCs: the sample stored at 80% showed a linear loss of about 40 mAh (2% of the BOT capacity) every two calendar weeks, and seems to slow down at the last recorded calendar diagnostics, where 20 mAh were lost in two weeks; the sample stored at 100% SOC instead, shows its maximum capacity loss in the last recorded degradation step, where about 60 mAh (2.5% of the BOT capacity) were lost. Observing the 6-8 weeks capacity loss trend, it is expected that more calendar time at 60°C will make the capacity loss of the sample stored at 100% SOC overtake the one of the sample stored at 80% SOC. Comparing these results with literature, the numbers obtained are reasonable. Keil et al. in NMC cells that were calendar aged for 2.4 months

at 50°C detected a capacity fade of about 7% of the nominal capacity for samples stored at 100% SOC, a slightly lower value for samples stored at 80% (6-7%), 4% capacity loss for samples stored at 50% and about 1% loss for the battery calendar aged at 10% SOC [39]. Taking into account that the calendar time is two weeks longer and the temperature is 10°C lower, with respect to the aging conditions of this work, the results are comparable.

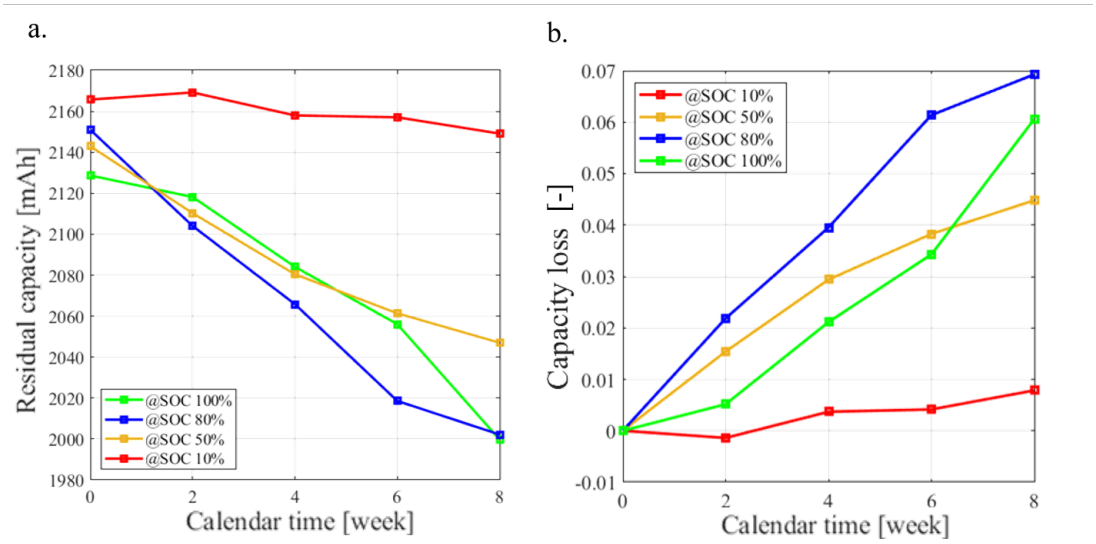


**Figure 5.1:** Calendar aging effect in terms of: a. Residual capacity; b. Percentage of capacity loss.

It can be assumed that a relevant impact on the cell capacity fade is related to the anode potential corresponding to the storage SOCs: SOC 100% and 80% corresponds to the graphite plateau with the lowest potential, while 50% SOC lays in the anode plateau with medium potential, and 10% SOC corresponds to higher anode potential values. Therefore, an increasing capacity fade is reported for lower anode potentials. The IC and DV analysis data could be useful to understand the contribution of the degradation mechanisms that originated that capacity fade.

### 5.1.2 IC and DV curve analysis

Figures from 5.3 to 5.6 show the discharge profiles, the IC and the DV curves related the four batteries that underwent calendar aging. In the legends, BOT refers to the begin of calendar aging condition, while the different diagnostics, that were carried out once every two weeks of calendar aging throughout a period of eight weeks, are indicated as "DIAG" followed by the number of the diagnostic test.

Some interesting aspects can be highlighted:

1. The battery stored at 10% SOC shows basically no degradation (see Figure

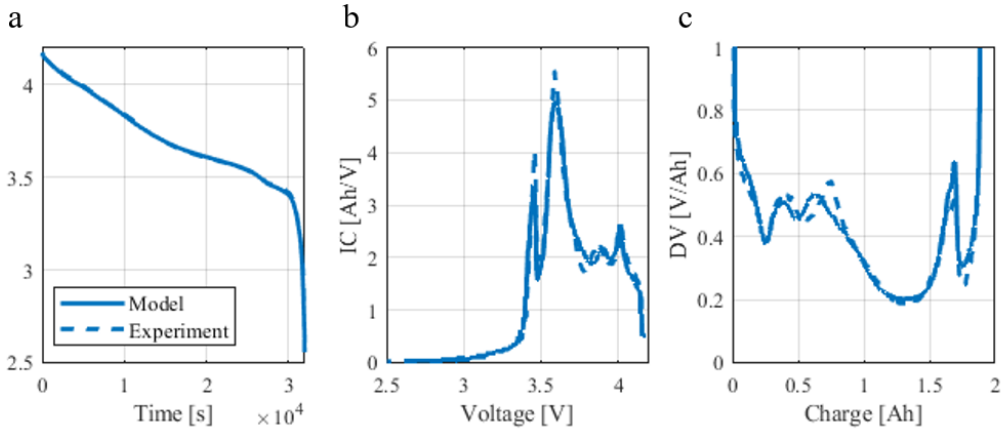


**Figure 5.2:** Experimental and simulated (a) discharge, (b) IC and (c) DV at 0.1C, 25°C after 8 weeks of calendar aging at 80% SOC.

5.6). Also looking at the IC an DV curves, that enhance the differences between the discharge profiles, no relevant differences can be identified;

2. Looking at the IC plots of the samples stored at 80% and 50% SOC (Figure 5.4 and Figure 5.5), the main deviations from the BOT condition occur in the SOC area (or voltage area) corresponding to the SOC at which they were stored. This may represent the combined effect of degradation of the positive electrode characteristics and of the electrode balancing, that may lead to a progressive displacement of the graphite peaks.

3. Keeping in mind what has been observed in the sensitivity analysis of $LLI$, $LAM_p$ and $LAM_n$ (chapter 3.2.2), it can be inferred that the main degradation modes involved in the aging are loss of lithium inventory, followed by loss of active material on the positive electrode. In the DV plots, $LLI$ is visible from the progressive shift of the graphite peak at high SOC, due to the electrodes' slippage that reduces the operating SOC window of the electrodes intercalation curves. This effect is more evident for the calendar at high SOCs, namely 100% and 80%. The $LAM_p$ increase can be inferred by the fact that the low SOC peaks of the IC curves are basically located in the same position, only seeing a variation of the intensity. If only $LLI$ was present, a shift of the IC curves towards higher SOCs would be expected, with aging. The effect of only $LAM_p$ on the IC curve, instead, would cause a decrease of the high SOC peak (as it can be seen in Figure 5.4) and a slight shift of the main peak to the left (similarly to Figure 5.5). Hence, the superposition of the effects of these two parameters may be able to justify the aging trend.

The method was applied for the calibration of the begin of life kinetic parameters and the thermodynamic parameter at the aging stage reached after eight weeks, for the sample stored at 80% SOC.

$LLI$ is estimated to be 11.7%, and $LAM_p$ is equal 6.4%. No $LAM_n$ was detected. This results confirm the hypothesis on the degradation mode, made in the IC-DV analysis. This kind of degradation can be related to SEI growth and electrolyte reduction. Moreover, the high temperature may have promoted side reactions, resulting in binder decomposition and transition metal dissolution.

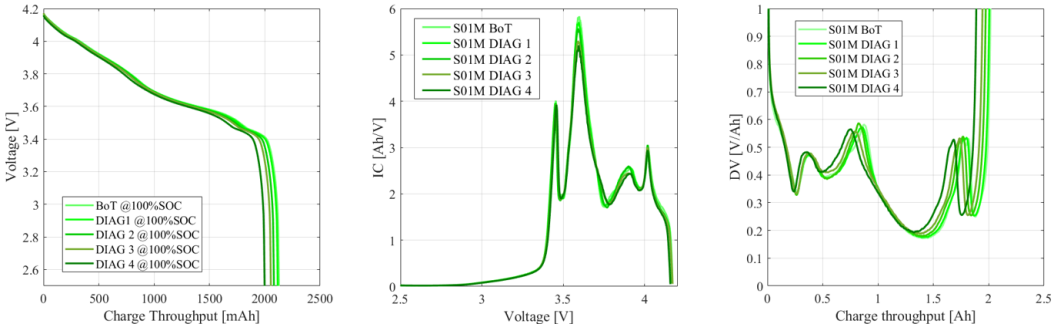


**Figure 5.3:** Discharge profiles, IC and DV curves of the sample stored at 100% SOC, throughout the aging campaign.

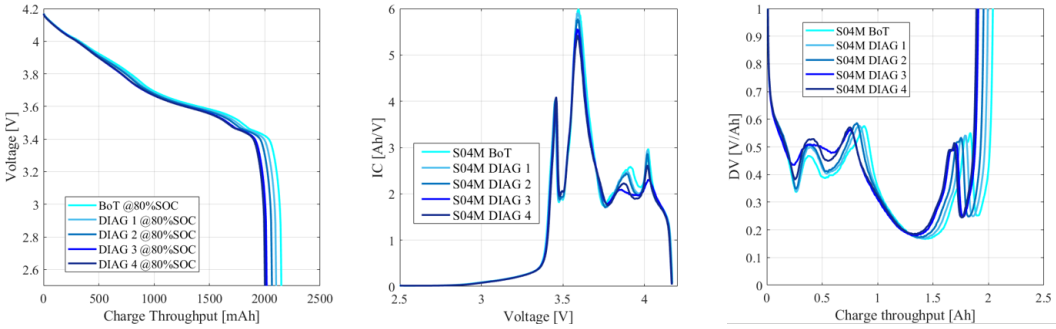


**Figure 5.4:** Discharge profiles, IC and DV curves of the sample stored at 80% SOC, throughout the aging campaign.

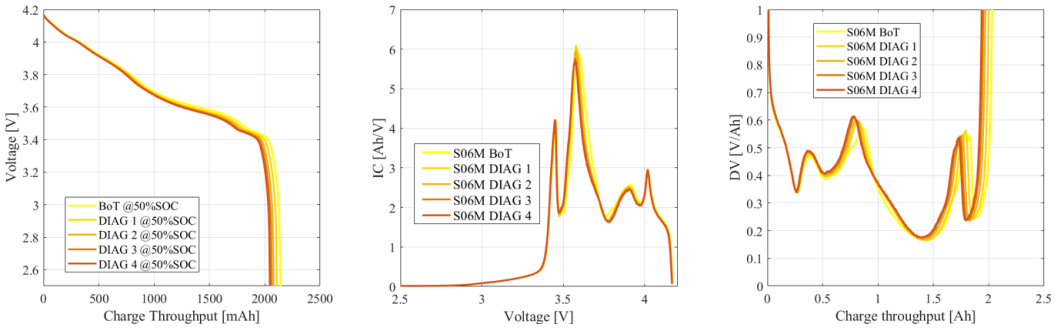


**Figure 5.5:** Discharge profiles, IC and DV curves of the sample stored at 50% SOC, throughout the aging campaign.

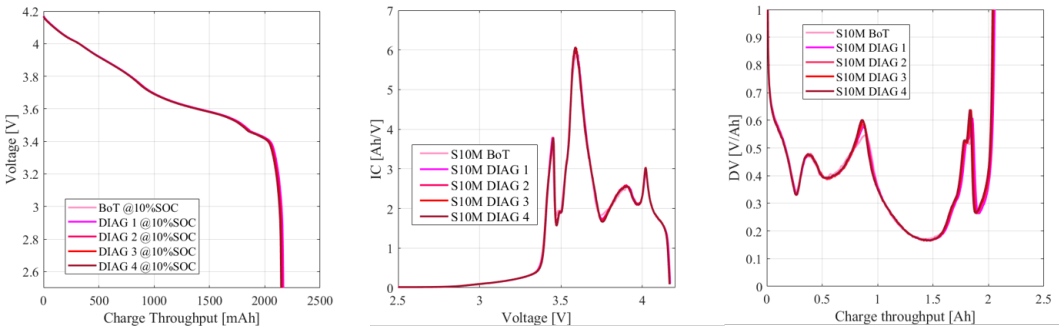


**Figure 5.6:** Discharge profiles, IC and DV curves of the sample stored at 10% SOC, throughout the aging campaign.

## 5.2 Cycle aging analysis

The cycle aging operating conditions described in Table 4.7 have been applied on eight different pristine samples, four cycling at 0°C and the others at -10°C. The samples have been tested with the check-up procedure described in Table 4.4, once every 3 EFCs, until 12 EFCs were reached. The same nomenclature introduced in chapter 4.3.3 will be used to identify the cycles conditions (A - charge 1C, 50%-80% SOC, discharge 0.2C; B - charge 0.5C, 50%-80% SOC, discharge 0.2C; C - charge 1C, 30%-60% SOC, discharge 0.2C; D - charge 1C, 30%-80% SOC, discharge 0.2C).

### 5.2.1 Capacity loss

Figure 5.7 shows the capacity loss trend during the aging campaign for all the samples that underwent cycle aging. Same colors are applied for samples that operated at same cycle conditions, except from the temperature, that is instead distinguished by a different marker shape and a different lines' style.

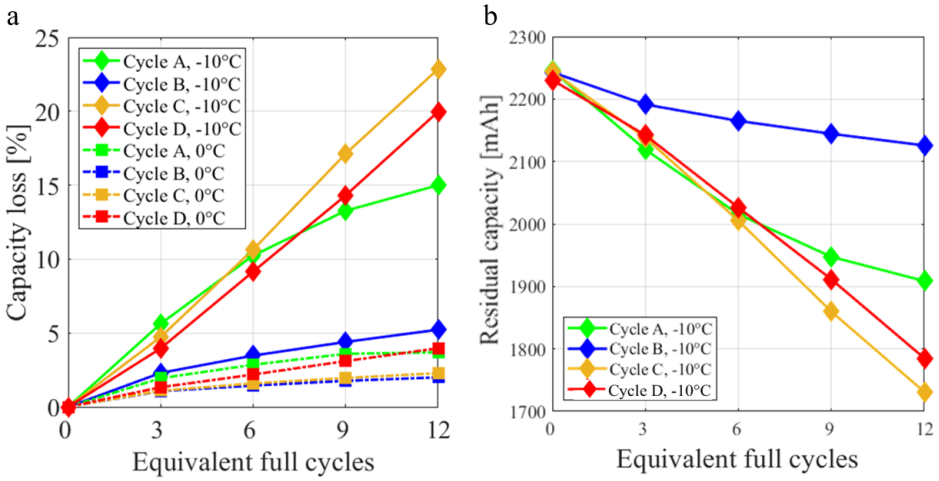


**Figure 5.7:** Cycle aging effect in terms of: a. Percentage of capacity loss; b. Residual capacity.

It can be observed that the batteries that cycled at -10°C show higher capacity loss, up to 23% for the most degraded one, with respect to the ones that operated at 0°C, as their capacity loss is in all the cases lower than 5%. This is consistent with the lithium plating stressors analysis carried out in chapter 4.3, since at 0°C the plating condition is less promoted. In fact, during low temperature charging, intercalation of lithium ions into graphite and lithium plating are in competition: lower temperatures hinder lithium ions diffusion into graphite, and therefore, lithium plating is favored.

Consistently with what has been observed in the current pulses campaign for cycles

conditions at 0°C, lithium plating has more impact for current pulse operated as in cycle A and D. In fact, within the samples cycled at 0°C, the ones operating in those conditions appear to have less residual capacity. The samples operated in cycle B, the cycle with the lower charge C-rate, are least affected by the degradation. This confirms that the charge current is definitely one of the main lithium plating stressors. The effect of the discharge C-rate was also investigated: 6 EFC cycle were performed by an additional sample operating as in cycle A at -10°C but switching the charge and the discharge C-rates; the sample showed about 1% degradation. Therefore, it can be stated that the discharge C-rate does not affect the degradation, especially for the discharge C-rate selected for the cycles operation.

The results in terms of the capacity loss trend of the samples cycled at -10°C, may seem to contrast with what was inferred during the relax analysis of chapter 4.3, that identified the condition of cycles A and D as the ones where lithium plating is more promoted, therefore the conditions with higher DOD (cycle D) and higher mean SOC (cycle A). It is important to keep in mind that the number of cycles to be performed to reach 1 EFC it is different for the various cycles' types, and therefore the comparison with the results of the current pulse campaign is not totally fair. What it is observed in Figure 5.7, is that, considering the same number of EFC, the most detrimental operating condition was the one of cycle C. This can be once again attributed to the current during the charge steps. In fact, low temperatures corresponds to a growth of the voltage polarization that leads to short CC phases. Therefore, most of the charge is achieved during the CV phases, especially for the cycle conditions that require to reach high SOCs, i.e cycle A and D.

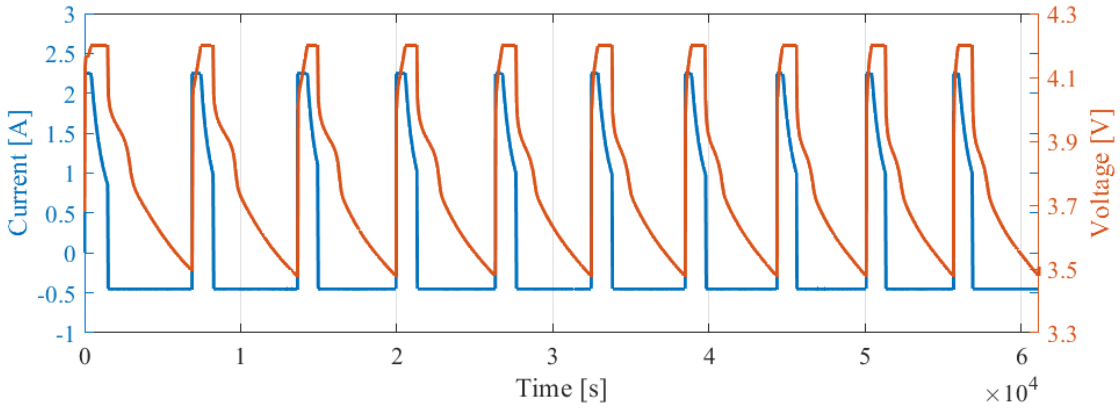


**Figure 5.8:** Current and voltage profile during 0-3 EFC for cycle A at -10°C.

In Figure 5.8, voltage and current profiles in time during cycle type A at -10°C are reported. It can be observed that, as just stated, the CV phases accounts for most

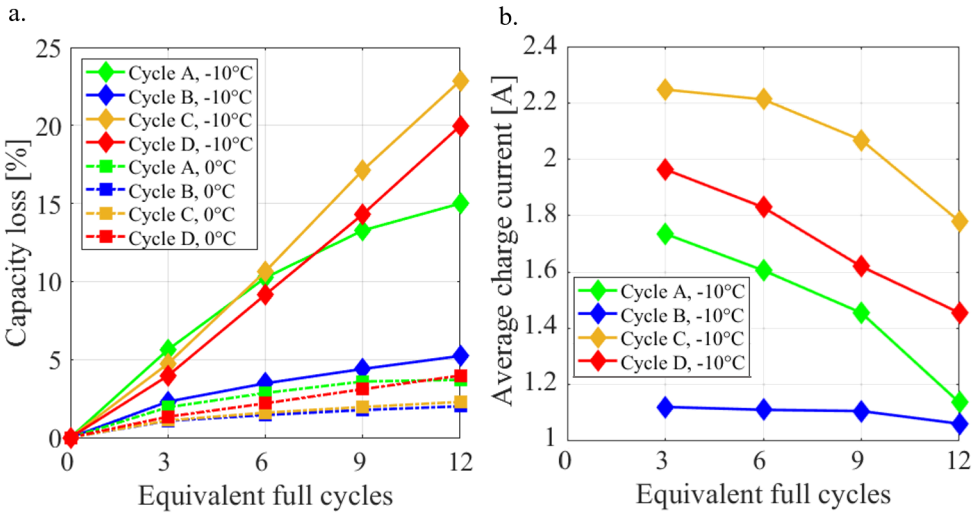


**Figure 5.9:** a. Capacity loss [%] during cycle aging; b. Average current during charge.

of the charge exchanged during the charge process.

The charge currents decrease almost exponentially during the CV phase. In Figure 5.9.b the capacity loss is plotted against the average current within the CC and CV phases of all the cycles.

Nevertheless, the trend in the capacity loss is not determined only by this aspect: looking at the capacity loss after 3 EFC, cycle A is the most detrimental. Cycle C, despite having always the highest current values, after 3 EFC does not present the highest capacity loss. Moreover, it can be noted that, even if its average current decreases over the aging steps, the capacity loss keeps the same rate. The average current is not an actual variable, but more of an indicator, that gives an idea of the current behaviour during a certain cycle condition; by making an average, current intensity variation in time and also in space (current is heterogeneous in the electrode) are not considered, and these variables are the ones that actually affect lithium plating.
Other parameters that may account for the capacity loss that is not covered by the current rate decrease are the average voltage during the cycle and the duration of the CV phase. These two parameters are clearly interconnected, as a longer CV phase corresponds to an increase of the average voltage value during the cycle.

The CV phases are crucial in the formation of dead lithium. In fact, at high voltage, i.e. during CV phases, the intercalation reaction exceeds lithium plating, because of the low charge current and the high voltage, creating a disperse and porous lithium structure close to the negative electrode surface [155]. Small currents lead

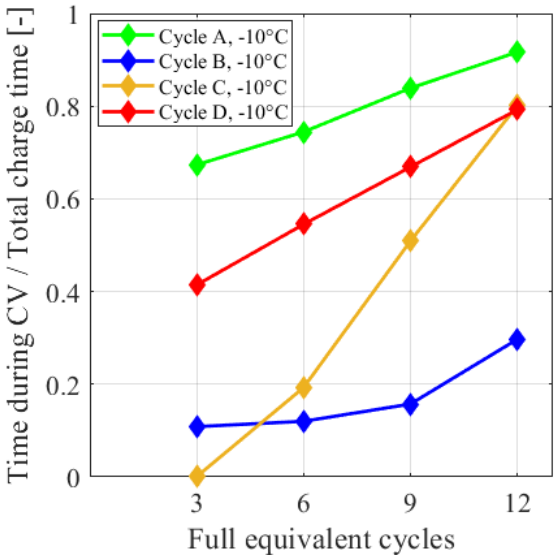


**Figure 5.10:** Ratio of charge time in CV step and total charge time, every 3 EFC, for the samples cycled at -10°C.

to a slow lithium deposition: the dendrites are fine and fragile and more prone to electrical isolation. This morphology is commonly named mossy, in the literature [156], [157]. Surface films formation is enhanced due to the high surface area of the porous structure. Since the deposits of porous lithium that are closer to the electrode surface are oxidized first, during discharge, the lithium structures located further from the graphite electrode are easily isolated, resulting in dead lithium. Nevertheless, a too long CV at high SOCs (80% - cycles A and D) results in the so called "chemical intercalation": the plated lithium, may become able to intercalate into graphite, given sufficient time at high SOC [99],[148], [158].
The CV phases duration increases throughout the aging steps, as the samples are gradually degrading in Figure 5.10 the fraction of charge time passed in the CV phase, cumulative on the 3 EFC, is reported for the four samples cycling at -10°C.

At the first aging step, namely 0-3 EFC, cycle C does not even include a CV phase (yellow line). At low SOC (30% SOC) and high current the lithium is plated fast and regionally with a dense and stable structure that ensures good electrical contact, with thick dendrites [159]. This lithium would be mostly reversible, thus stripped during discharge. However, at medium SOC this process continues and the plated lithium grows through the SEI, getting in contact with the electrolyte and forming surface films that lead to capacity loss and isolation of dead lithium during discharge [155]. It can be inferred that the increase in the time at high voltage, during the CV phase, in the case of cycle C, results in a lithium deposition with a mossy

structure, therefore, in higher amount of dead lithium, i.e. higher capacity loss, that compensate for the average current decrease.

Comparing the cycle C and cycle D capacity loss, it can be be observed that their trend are similar: with aging the $\Delta$V in which the cycles operates is basically the same, and the differences between the two can be attributed to the lower average current of cycle D, since higher SOC is reached through longer CV phases from the first aging step, probably resulting into chemical intercalation of lithium.

Looking at the cycle A capacity loss trend, the degradation seems to slow down gradually. This behaviour can be justified as the sample benefits from the decrease in current and the increase of the CV phase duration.

### 5.2.2 IC and DV curve analysis

As the battery check-up procedure included a discharge at 0.1C and 25°C, it is possible to depict changes in the IC and DV curve during the aging campaign. The voltage profile during the said discharge, its IC and DV curve are reported in Figure from 5.11 to 5.18. Each figure refers to one of the cycle type. Both the curves referring to the samples that cycled at 0°C and -10°C are reported.

The characteristics of the degradation of the samples that operated at 0°C are very similar to each other. The level of aging reached with the 12 EFC, at this temperature, may be not enough to highlight the differences between the samples. The IC and DV plots shows similar features. On the DV plot, the low SOC peak of the graphite shifts to the left, especially for cycle A and D, while the peak at 0.8 Ah becomes more evident and moves slightly to the right. These peaks are the one attributed to the graphite, meaning that the degradation is probably involving more this electrode than the other. In fact, the high SOC peak of the DV curve is the one related to the NMC curve and does not seem to modify, at least at this stage of degradation. The IC plots shows mainly a reduction of the main peak at 3.6V.

Comparing the figures of the cycles at 0°C with the ones at -10°C it is clearly visible the temperature influence on the degradation: the samples cycled at -10°C result in relevant capacity losses, much higher than the one showed by the samples at 0°C, for all of the cycles type. Within the samples that cycled at -10°C:

- cycle B is the least detrimental conditions, compared at same number of EFC. Comparing cycle A and cycle B, the effect of the current during charge can be highlighted: a higher current resulted in a decreasing of the peaks of the IC curve; on the DV plot, the high SOC part moves to the left and decreases. These degradation effects can be related to the sum of $LLI$ and $LAM_n$, as the

peak related to the NMC shows minor variations;

- cycles C and D were the ones that worked with lower starting SOC, and therefore, cycled for more time in CC phase, with respect to cycle A: this resulted in a higher average current, as described in the previous section, that resulted to be particularly detrimental for the samples. Similar features are visible on the IC and DV plots of these two cycles. The main peaks of the IC plots decrease in intensity and the one at 3.8V becomes almost completely smooth. On the DV plot, the low SOC characteristic peak moves to the left and decrease in intensity, similarly to what happened for cycle A. This kind of degradation, namely the significant capacity loss in that region, is mainly determined by $LLI$, that may be lost due to the exfoliation of plated lithium and the formation of surface films: the exfoliated lithium looses the electrical contact with the negative electrode, becoming electrochemically inactive ("dead lithium"). However, remaining chemically active, that lithium can still react with the electrolyte, leading to further degradation. $LAM_n$ is generally observed as a simultaneous capacity loss in all the curve regions, and may be present,since lithium plating cause continuous volume stresses. In fact, persistent plating and stripping, and the surface film formation on the anode particles result in volume changes in the electrode structure which lead to contact losses due to binder breaking and particle cracking. Active material particles are likely to become electrically isolated if the electrode host material is not able to accept the volume stress created by the persistent plating (during charge) and by the dissolution of metallic lithium (during discharge).

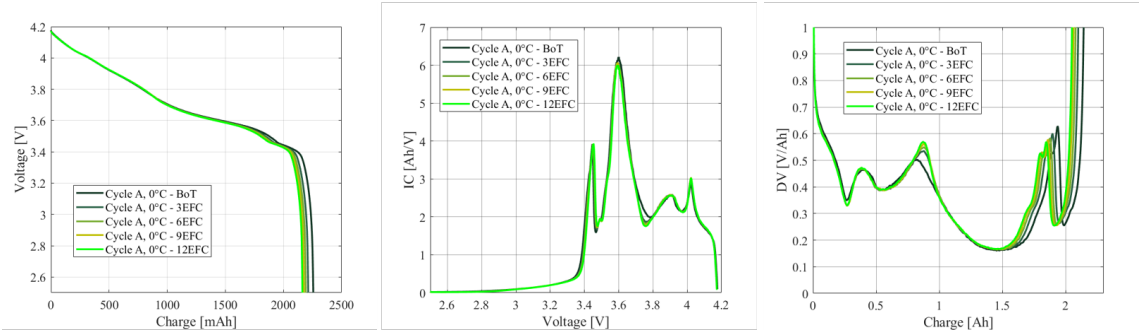


**Figure 5.11:** Discharge profiles, IC and DV curves of the sample operating at cycle A - charge 1C, 50%-80% SOC, discharge 0.2C - 0°C throughout the aging campaign.

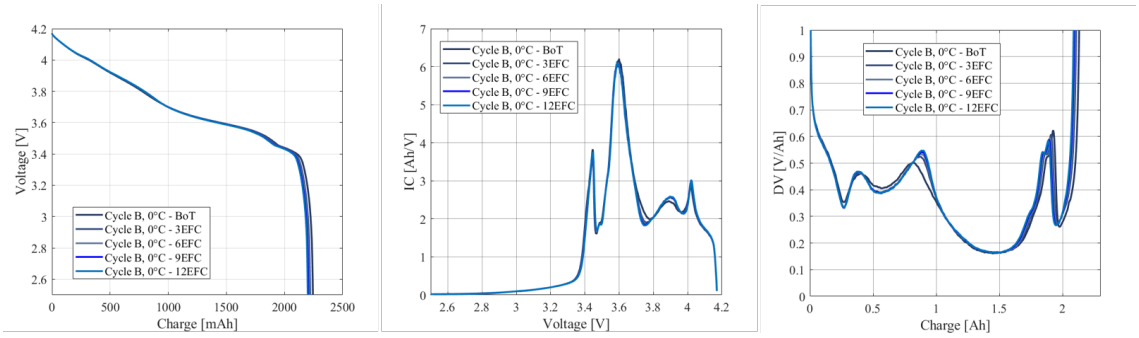


**Figure 5.12:** Discharge profiles, IC and DV curves of the sample operating at cycle B - charge 0.5C, 50%-80% SOC, discharge 0.2C - 0°C throughout the aging campaign.

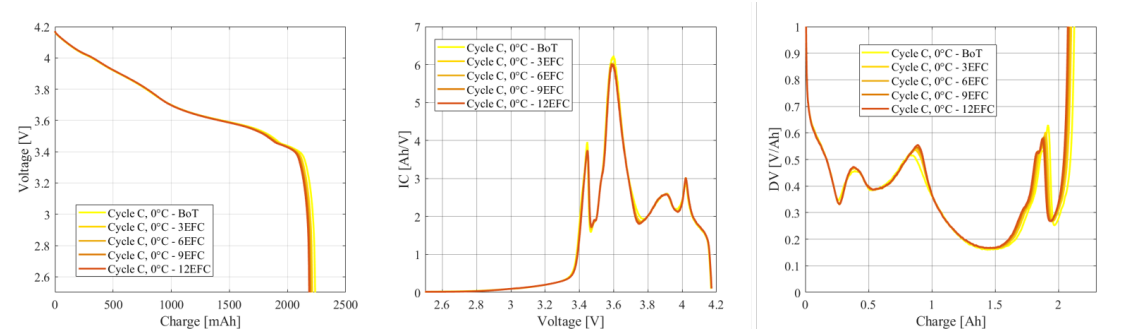


**Figure 5.13:** Discharge profiles, IC and DV curves of the sample operating at cycle C - charge 1C, 30%-86% SOC, discharge 0.2C - at 0°C throughout the aging campaign.

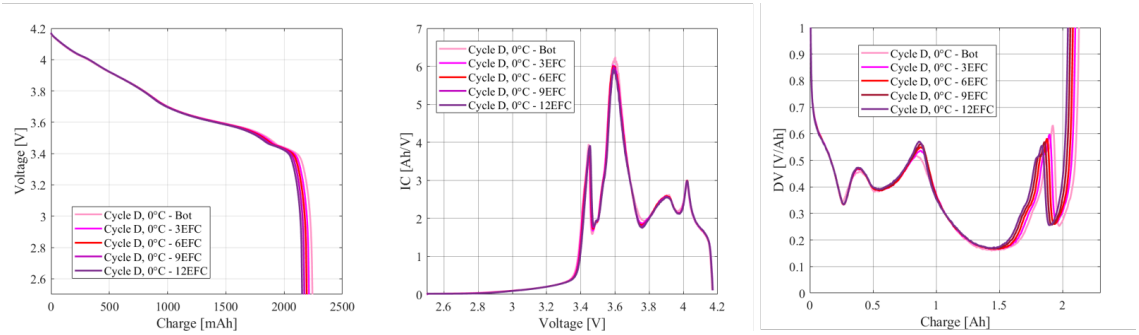


**Figure 5.14:** Discharge profiles, IC and DV curves of the sample operating at cycle D - charge 1C, 30%-80% SOC, discharge 0.2C - at 0°C throughout the aging campaign.

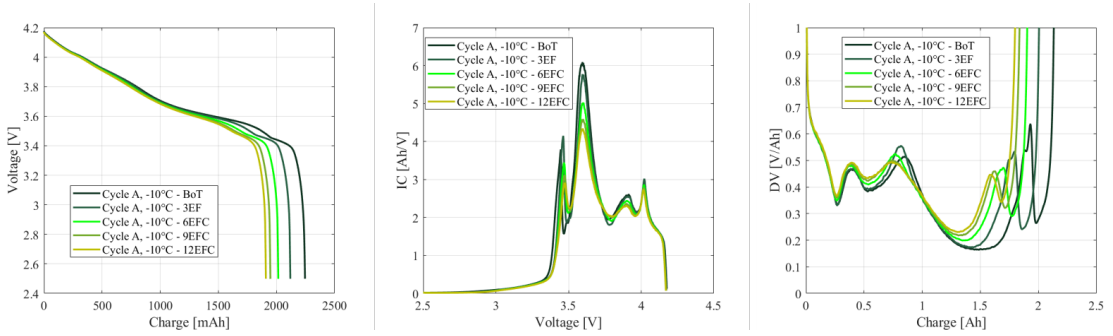


**Figure 5.15:** Discharge profiles, IC and DV curves of the sample operating at cycle A - charge 1C, 50%-80% SOC, discharge 0.2C - at -10°C throughout the aging campaign.

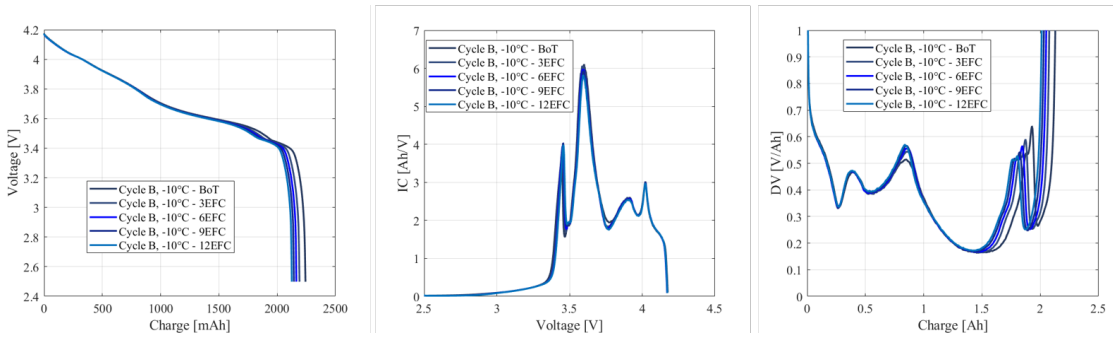


**Figure 5.16:** Discharge profiles, IC and DV curves of the sample operating at cycle B - charge 0.5C, 50%-80% SOC, discharge 0.2C - at -10°C throughout the aging campaign.

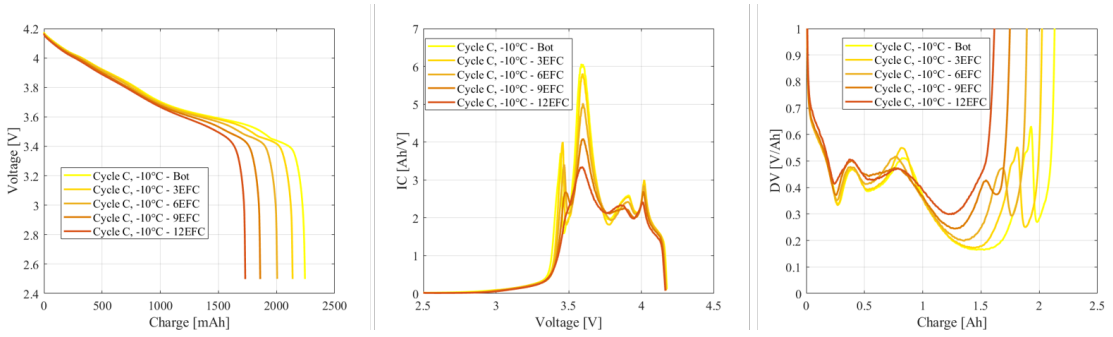


**Figure 5.17:** Discharge profiles, IC and DV curves of the sample operating at cycle C - charge 1C, 30%-60% SOC, discharge 0.2C - at -10°C throughout the aging campaign.

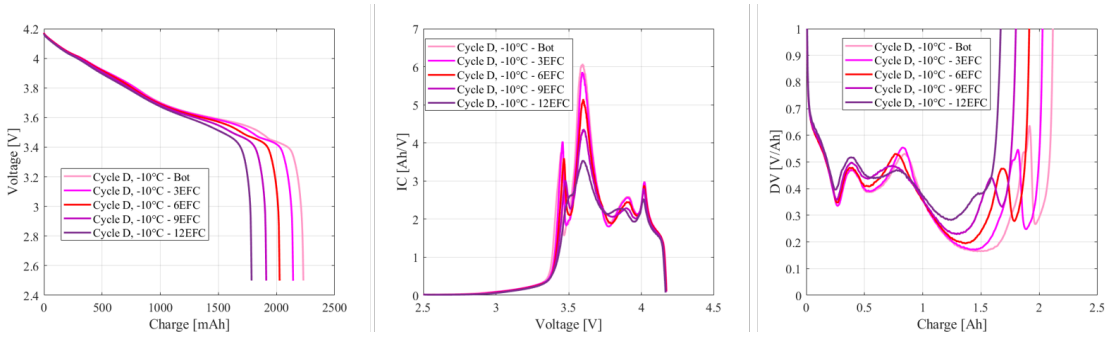


**Figure 5.18:** Discharge profiles, IC and DV curves of the sample operating at cycle D - charge 1C, 30%-80% SOC, discharge 0.2C - at -10°C throughout the aging campaign.

## 5.3 Calibration of an aged sample and validation of the results

On all the samples, the diagnostic procedure has been performed once every 3 EFC 4.3.3. One of the samples have been selected to calibrate the model parameters through the procedure described in 3.4, throughout the battery aging.
The sample analyzed is the one that operated at cycle condition A, at -10°C, namely charging at 1C and discharging at 0.2C between 50-80% SOC.

### 5.3.1 Calibration and validation of the results

Starting from BOL calibration, an iterative procedure has been carried out, putting together the parameters of the thermodynamic PSO with the ones of the kinetic PSO.

The results of the data fitting on each aging stage are reported from Figure 5.19 to 5.23. The RMSEs have been computed for all the tests and the values are reported in Table 5.1.

| RMSEs | **Aging stages** | | | | |
|---|---|---|---|---|---|
| | **BOL** | **3 EFC** | **6 EFC** | **9 EFC** | **12 EFC** |
| EIS 10°C, 100% SOC [mΩ] | 2.32 | 2.11 | 2.44 | 3.01 | 2.48 |
| | 2.28 | 2.48 | 2.52 | 3.04 | 2.60 |
| Discharge 2C, 10°C, 100-50% SOC [mV] | 21.6 | 20.3 | 22.3 | 31.1 | 28.5 |
| Relax 2C, 10°C, 100-50% SOC [mV] | 21.9 | 27.3 | 48.5 | 67.6 | 38.4 |
| EIS 25°C, 50% SOC [mΩ] | 1.60 | 1.66 | 1.88 | 1.70 | 2.45 |
| | 2.01 | 2.06 | 2.06 | 2.09 | 2.16 |
| Discharge 1C, 10°C, 50-0% SOC [mV] | 8.2 | 23.6 | 30.8 | 31.6 | 35.1 |

**Table 5.1:** RMSEs between experimental and simulated data for the calibration throughout the aging stages.

The data have been validated at the last aging stage, 12 EFC. The dataset includes:

- two discharges, 100%-0% SOC, one at 25°C and 1C and the other one at 40°C and 2C (Figure 5.25);
- two charges, 0%-100% SOC, at 25°C and 1C, and at 10°C and 0.5C (Figure 5.26);
- three EIS tests, at 100%SOC at both 25°C and 40°C and at 75% SOC at 25°C (Figure 5.24).

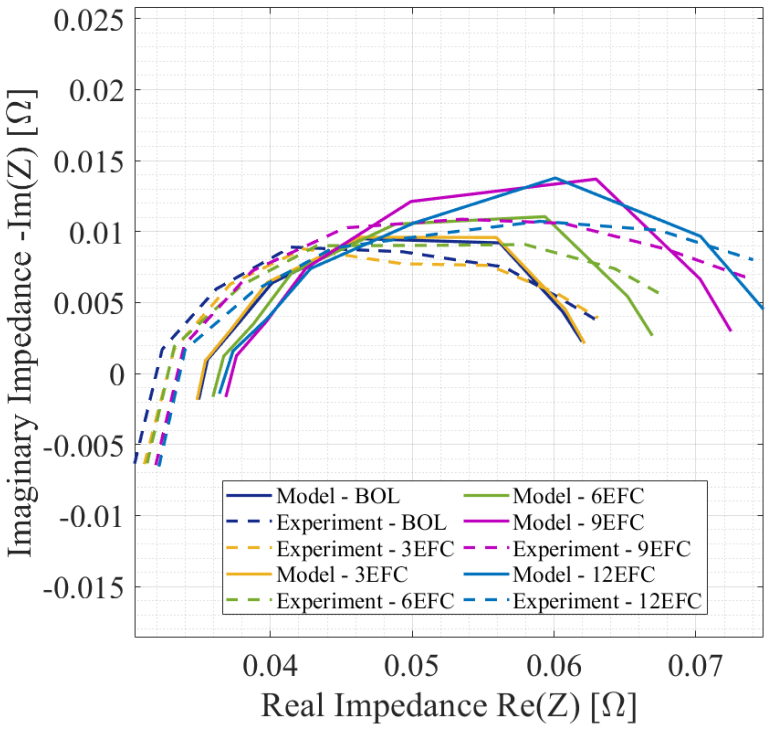


**Figure 5.19:** Impedance spectrum at 10°C, 100% SOC, for different aging stages.

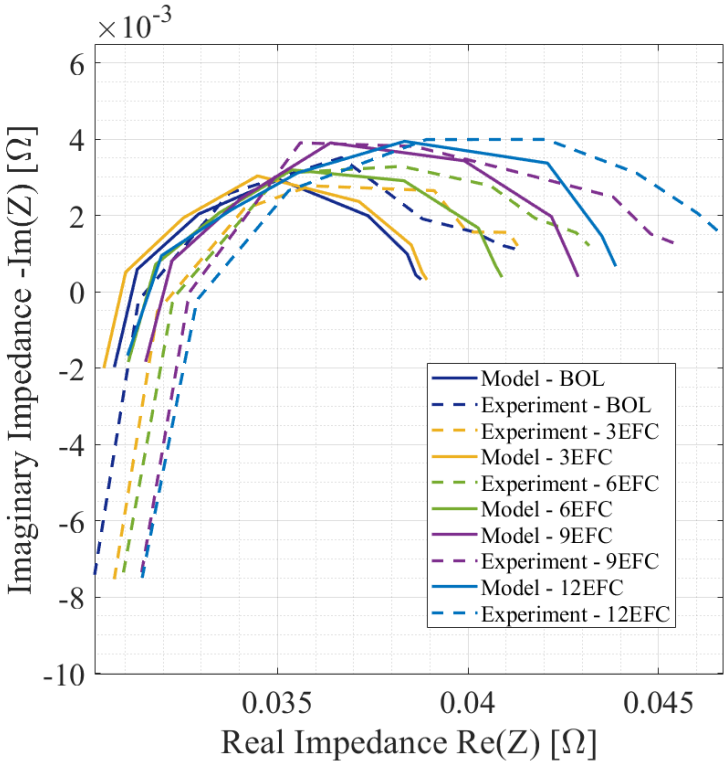


**Figure 5.20:** Impedance spectrum at 25°C, 50% SOC, for different aging stages.

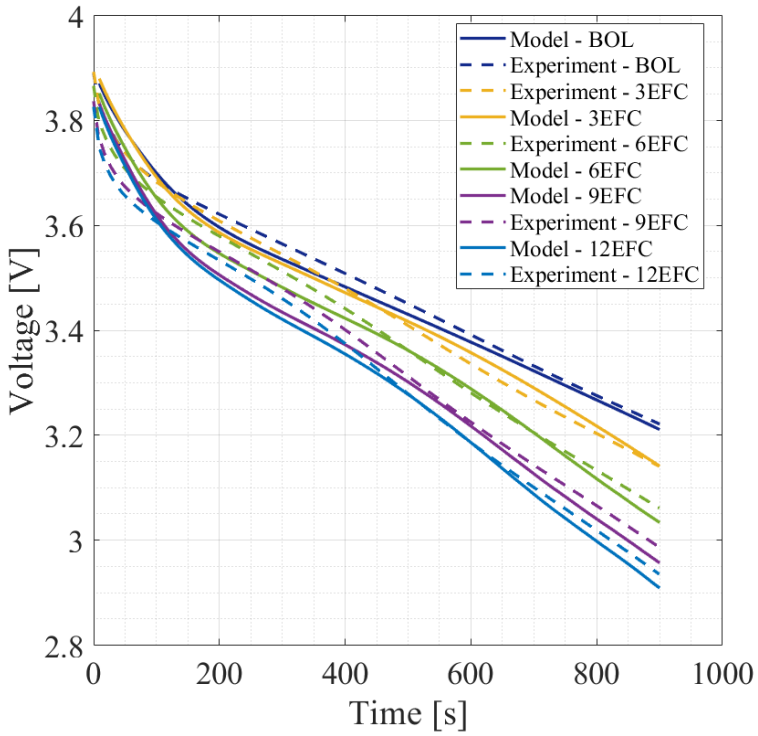


**Figure 5.21:** Discharge curve at 2C, 10°C, from 100% SOC to 50% SOC, for different aging stages.

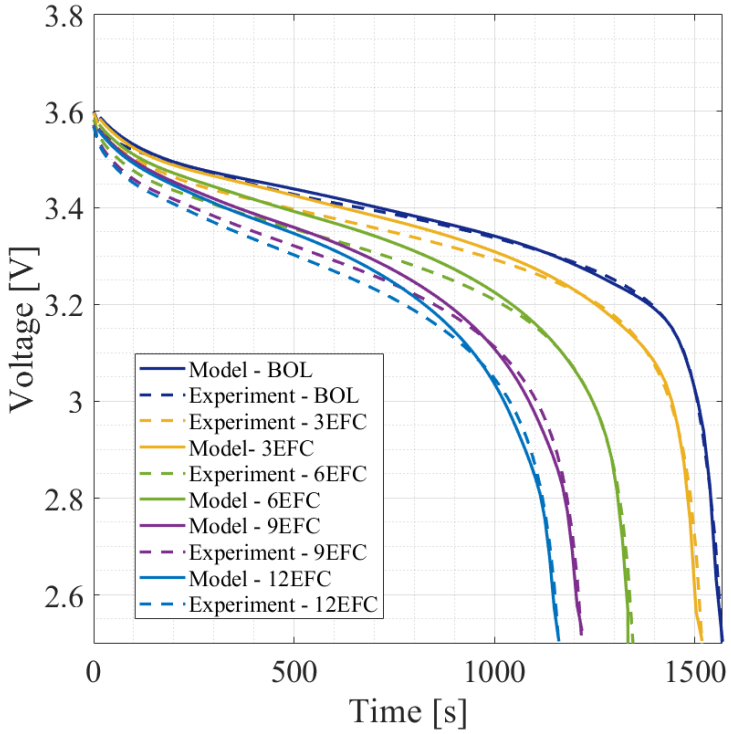


**Figure 5.22:** Discharge curve at 1C, 25°C, from 50% SOC to 0% SOC, for different aging stages.

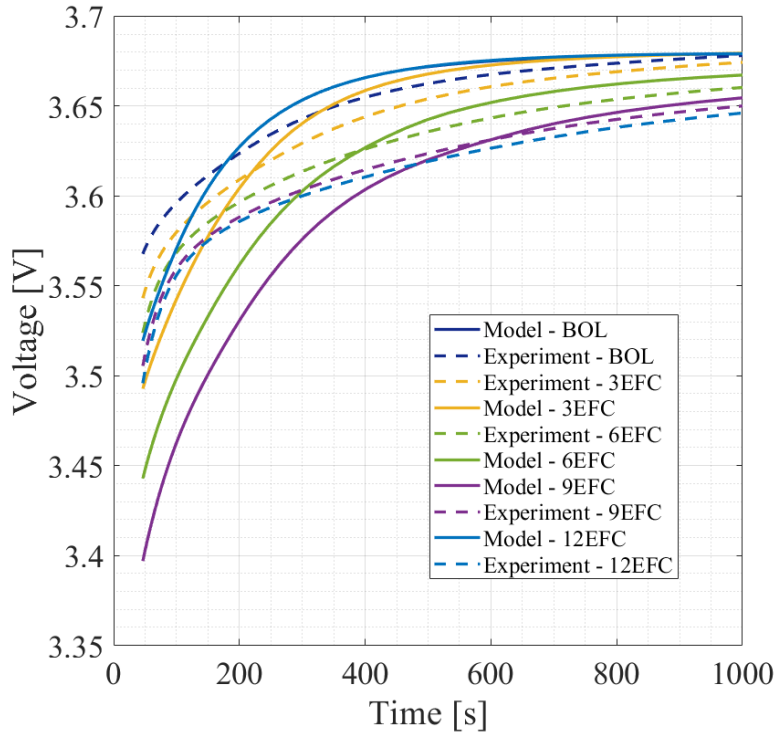


**Figure 5.23:** Relaxation curve after discharge at 2C, 10°C, from 100% SOC to 50% SOC.

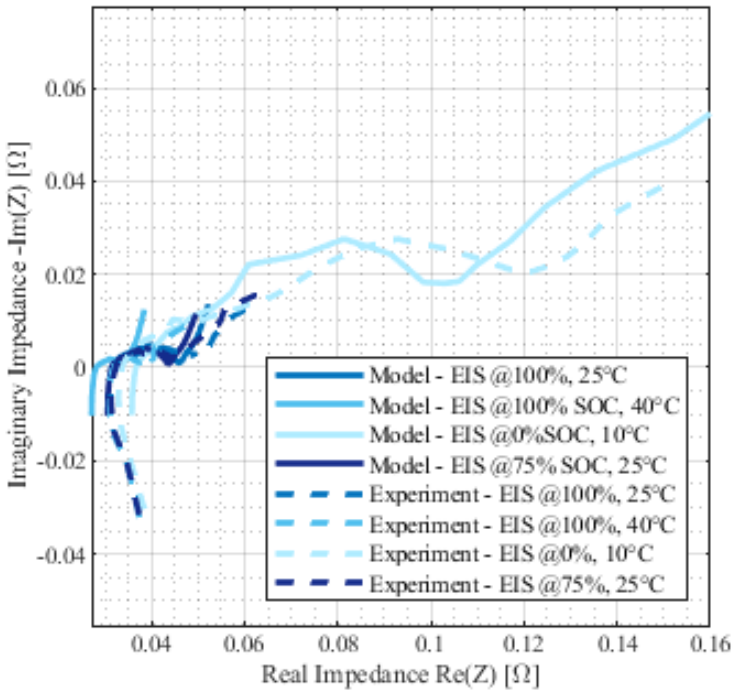


**Figure 5.24:** Validation dataset: impedance spectra, for 12 EFC.

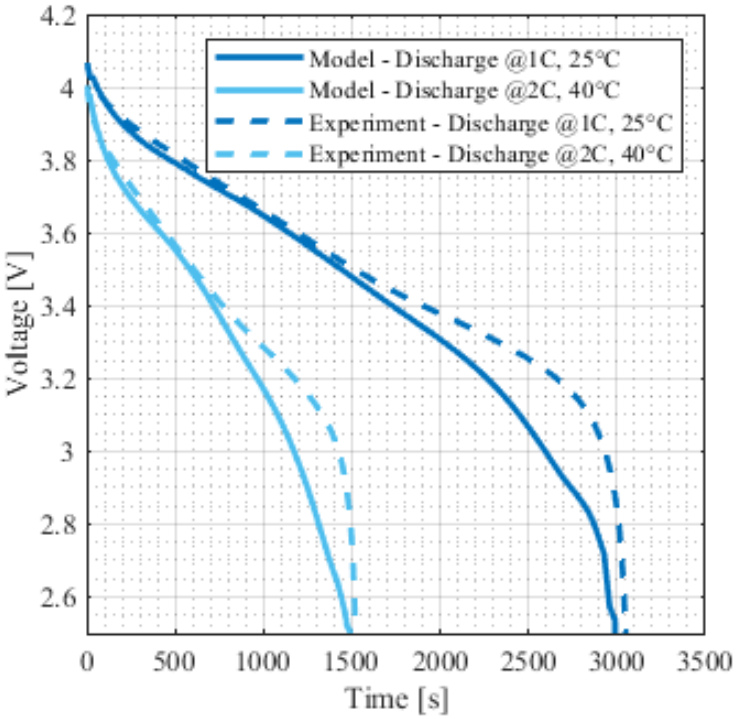


**Figure 5.25:** Validation dataset: discharges, for 12 EFC.

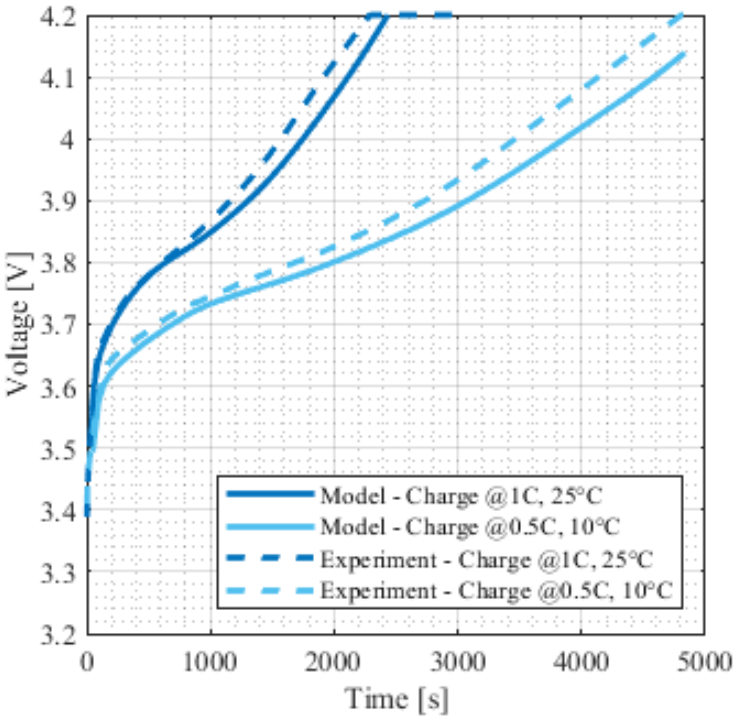


**Figure 5.26:** Validation dataset: charges, for 12 EFC.

Results in terms of RMSEs for the validation dataset are reported in Table 5.2. Some aspects on both the calibration and validation fitting can be highlighted:

- The values reported in table 5.1 shows similar values of RMSEs for the EIS tests: from Figure 5.19 and Figure 5.20 it is visible how the model is not able to set the right high frequency resistance (HFR) value, and as it has to optimize the error of both the tests, it finds a compromise. Since the HFR is dominated by the ohmic cell resistance, that mainly depends on the electrolyte conductivity, to improve this aspect the ionic conductivity correlation (equation 2.26) may be modified to reproduce the experimental behaviour.
- The discharges in Figure 5.21 and Figure 5.22 shows a good accordance between experimental and simulated voltage profiles. The RMSEs are quite low and comparable between the different aging stages, testifying the good quality of the fitting. A criticality can be identified in the first section of the two discharges, as the model has a steeper slope in these parts. To improve even more the fitting, additional weight can be given to those points when computing the cost function in the data fitting algorithm.
- The relaxation profile, in Figure 5.23 shows that the model presents, for all the aging stages, a quite different trend from the experimental ones. In fact, the highest RMSEs values are related to this case. To make sure that the behaviour is well reproduced, and therefore, the parameters characterizing the relaxation profile are estimated properly, their calibration could be performed dedicatedly, or an optimization on the derivative of voltage in time could be added to provide additional importance to this test.
- The results in terms of RMSEs on the validation dataset with respect to the BOL calibration show generally greater values for the discharge tests and comparable values for the EIS tests. Looking at the discharge profiles in Figure 5.25, a different behaviour is observed on the low SOC part of the curves. This may happen as a consequence of a wrong estimation of the parameters related to diffusion (see section 5.3.2). From the charges in Figure 5.26, it seems that the model overestimates the losses, and this effect is higher with decreasing temperature.

### 5.3.2 Parameters evolution with aging

Thanks to periodic diagnostics, it was possible to calibrate the battery physical model, throughout the aging campaign. With the methodology described in 3.4, the parameters obtained at each aging step has been tracked in time and analyzed. Their variation has been interpreted and correlated to the aging mechanisms.

| Technique | Operative condition | RMSE |
|---|---|---|
| Discharge curve | 1C, 25°C, 100 − 0% SOC | 119mV |
| | 2C, 40°C, 100 − 0% SOC | 161mV |
| Charge curve | 1C, 25°C, 0 − 100% SOC | 40mV |
| | 0.5C, 10°C, 0 − 100% SOC | 53mV |
| EIS | 25°C, 100% SOC | $Z_R$: 3.20mΩ<br>$Z_I$: 5.26 mΩ |
| | 25°C, 75% SOC | $Z_R$: 4.37mΩ<br>$Z_I$:5.69mΩ |
| | 10°C, 0% SOC | $Z_R$: 14.0mΩ<br>$Z_I$:16.9mΩ |
| | 40°C, 100% SOC | $Z_R$: 5.29mΩ<br>$Z_I$: 5.45mΩ |

**Table 5.2:** Summary of the RMSE between the model data and the experimental data in the validation dataset for 12 EFC.

**Thermodynamic parameters evolution**

The thermodynamic parameters, $LLI$, $LAM_p$ and $LAM_n$ have been calibrated through the fitting of a discharge at 0.1C and 25°C, by the data fitting algorithm, that we introduced as thermodynamic PSO. The experimental and simulated discharges are depicted in Figure 5.27. The results in terms of RMSE between experimental and simulated voltage profile are computed for all the aging step and reported in Table 5.3, in the column on the right. The $LLI$, $LAM_p$ and $LAM_n$ obtained from the thermodynamic calibration are also reported in Table 5.3.

What can be observed is that the main contribution in terms of degradation mode,

| Aging stage | LLI | LAMp | LAMn | RMSE |
|---|---|---|---|---|
| BOL | 0 | 0 | 0 | 41.5 mV |
| 3 EFC | 0.0503 | 0 | 0.0001 | 22.4 mV |
| 6 EFC | 0.0982 | 0.0055 | 0.0038 | 18.7 mV |
| 9 EFC | 0.1344 | 0.0109 | 0.0423 | 30.0 mV |
| 12 EFC | 0.1492 | 0.0036 | 0.0505 | 32.1mV |

**Table 5.3:** Thermodynamic parameters calibration at BOL, 3 EFC, 6 EFC, 9 EFC and 12 EFC.

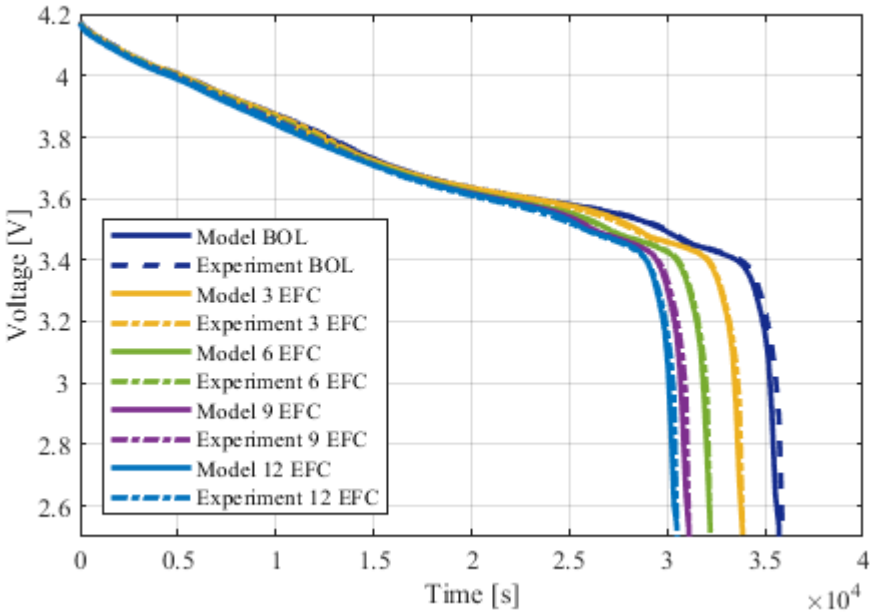


**Figure 5.27:** Discharges at 0.1C, 25°C, performed at BOL, 3 EFC, 6 EFC, 9 EFC and 12 EFC; a. Voltage profiles.

is the $LLI$. $LAM_n$ begins to unfold at 9 EFC, and it reaches 5% after 12 EFC. $LAM_p$, instead, is considered zero. Therefore, the hypothesis on the degradation mode proposed in section 5.2.1 are confirmed to be right. $LLI$ is probably related to lithium plating while $LAM_n$ can be the consequence of the volume stresses induced by lithium plating, that may lead to contact losses due to binder breaking and particle cracking.

The capacity loss during the aging was commented in section 5.2.1, attributing the performance worsening to the lithium plating formation. The capacity loss is higher in the first aging step, since the degradation of the battery makes increase the CV phase duration, that, results in a decrease of the average current. The current decrease, as well as the chemical intercalation are inferred to be the main causes of the aging slowdown that can be observed also from Figure 5.27.

The methodology for the thermodynamic parameters calibration shows interesting results: in terms of RMSEs the results are positive. The procedure was the same for the calibration of each aging stage: the same number of particles and iterations were employed for all the cases, and, retrospectively, the fitting was evaluated. The numbers obtained are not important, per se, since additional attempts of calibration with more iteration or more particles may be performed, to iron out for higher detail.
The BOL RMSE value appears even higher than the others. Keeping in mind

that the BOL thermodynamic parameters, $LLI$, $LAM_p$ and $LAM_n$, have not been calibrated for the BOL condition, but were assumed to be zero, the RMSE value for this case is a measure of the quality of the thermodynamic description of the model, that has been improved in chapter 3.2. The simulated and the experimental discharges have basically the same voltage profile, as can be seen in Figure 5.27, and the differences between the two are only due to a slightly lower exchanged capacity in the case of the simulated discharge. However, this translates in a voltage difference that becomes numerically relevant, as the discharge curve is practically vertical and that result in the RMSE increase, that is not a fair representation of the quality of the fitting. Therefore, as this capacity differences are negligible and may be caused both by measurement error or by natural differences between the samples, the thermodynamic description is considered to be accurate and detailed.

**Kinetic parameters evolution**

The kinetic parameters have been tracked during the aging campaign. At each aging step, the calibration of these parameters was obtained from the "PSO kinetic" data fitting algorithm, with the procedure described in chapter 3.4. Therefore, the evolution of fourteen parameters have been tracked during the aging campaign. As it was specified in section 3.4, some of the fourteen parameters can be considered as "low sensitive", as, also a quite relevant variation, do not affect the cell behaviour noticeably. This is the case of the diffusion coefficients, of which effects are superseded by the ones of more sensitive parameters.

It can be observed that the radius of the negative electrode particles reduces significantly with the aging, while the positive electrode particles' radius remains almost constant. This suggests a degradation of the graphite anode, probably linked to particle cracking that is likely to verify with cycling at low temperatures [60]. The kinetic rate constant of the two electrodes are both decreasing, but the one related to the anode decreases more and with a stronger trend, giving evidence of a heavier degradation related to the graphite electrode.

Another aspect that has to be mentioned, is that an increase of the film resistance at the negative electrode, due to lithium plating, was expected. This parameter influences the HFR of the impedance spectrum, that in turn is also affected by the electrolyte conductivity. By looking at the experimental EIS tests evolution with the degradation, an increase of the HFR value was encountered. This phenomenon should be described by the electrolyte degradation caused by the surface film formation on the plated lithium. Summarizing, what is attended is [152]:

- an increase of the negative film resistance;

- a decrease of the electrolyte ionic conductivity, since the lithium metal of the surface film leads to reduction of the electrolyte solvents.

The ionic conductivity is described by equation 2.26 in the model, as a function of the lithium concentration in the electrolyte and the FCE (see chapter 2.4.3). However, it has been already highlighted how the model was not able to reproduce the HFR behaviour, and how this correlation should be adapted or substituted with one that better fit the behaviour of this kind of samples. The FCE and initial electrolyte concentration showed decreasing trend with the aging. On the other hand, the estimation of the film resistance on the negative electrode probably failed, since it's not possible to identify a clear trend. Thus, this parameter should be considered as "low sensitive".

The double layer capacitance at the two electrodes values may be considered constant for this kind of degradation, as they were completely free to vary in the range [0.05, 25] $F/m^2$, but stayed close to the initial value, as it can be seen in Figure 5.28.

To overcome the problem of the estimation of the low sensitive parameters, it may be useful to perform an additional calibration of these parameters, keeping fixed the high sensitive parameters once they have been estimated.

For future developments, it would be interesting to compare the kinetic parameters, estimated with the proposed methodology, of samples aged with different pathways e.g. comparing the parameters achieved in this case with the ones that would be obtained from one of the calendar aged samples, highlighting the effects of the different aging mechanisms.

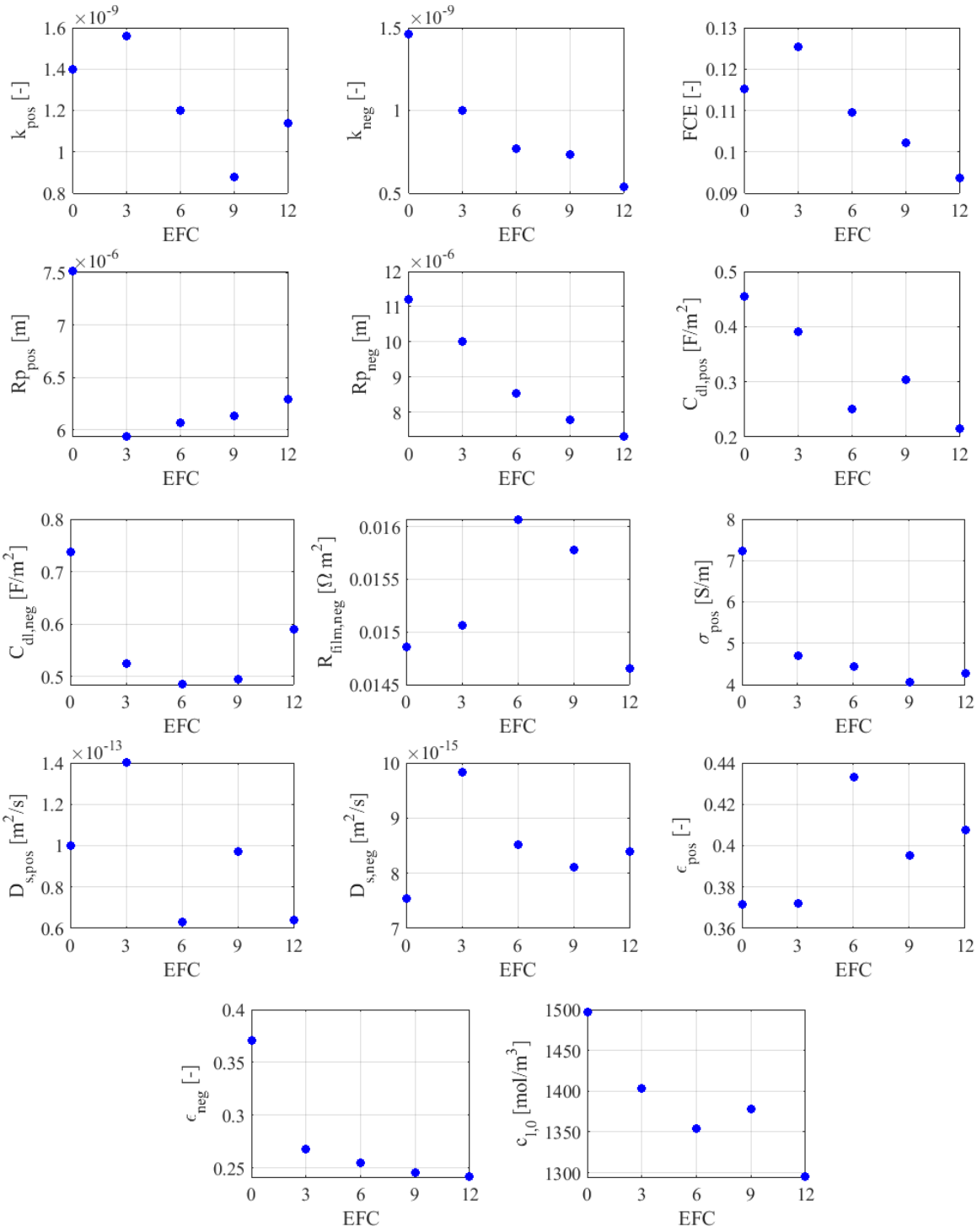


**Figure 5.28:** Dispersion graphs of the 14 estimated kinetic parameters trends with degradation. Please note the different scales of the axis.

## 5.4 Final remarks

The results obtained applying the proposed methodology suggest that, merging the calibration of thermodynamic parameters with the calibration of the kinetic battery parameters, a more detailed understanding of the degradation is provided, with respect to distinguish between model-based analysis and curve-based analysis without interaction between the two. Good results were obtained in the model calibration both for a pristine cell and especially throughout the aging stages. This novel and comprehensive approach for the battery aging characterization represents a first step in the definition of a complete diagnostic procedure to characterize the state of health of spent lithium-ion batteries.
The open issues that have to be addressed are the following:

- the diagnostic procedure necessary for the proposed calibration method needs a slow discharge at 0.1C-rate, that lasts about 10 hours for a pristine cell; this condition was selected as the methodology is still in a development phase, but the final diagnostic method aims to not include such a time-consuming test;
- despite the acceleration of the convergence thanks to the implementation of the "APSO" logic, the computational time necessary to run a simulation of the kinetic PSO is quite high. The bottleneck of the process is the model simulation via COMSOL, especially for the EIS tests. Improvements in this direction could be for instance model parallelization or change the LIB physical model software;
- the fitting of the experimental dataset can be improved: the first section of the discharge at 2C and 10°C and the relaxation fitting are not optimal; adding additional weight to these tests in the cost function may help the convergence toward more correct parameters;
- the checkup procedure has been performed on all the samples, but the methodology for the degradation calibration has been implemented only for one case, i.e. cycle A at -10°C. It is expected that adopting the methodology on samples that aged in different operating conditions, differences in the parameters may be highlighted, allowing to understand the degradation mechanisms effects even more and furthermore, providing an additional validation of the methodology;
- the choice of what kinetic parameters can vary with the aging is basically arbitrary; changing the set of parameters to be optimized can be interesting, also to analyze the parameters that were considered as "low sensitive", once the "high sensitive" ones have been calibrated.

# Conclusions

This master's thesis fits into the framework of circular economy for lithium-ion batteries, as in the next future an increasing amount of spent batteries retired from electric vehicles will need to be managed and may be employed in less demanding second life application. To enable this circular economy context, a standard and reliable methodology for the characterization of batteries' state of health and estimation of remaining useful lifetime is made necessary. This work aims at the definition of an innovative methodology that allows the calibration of a physical LIBs model both for a new sample and a degraded one.

- The pre-existing methodology, related to a previous thesis work on the same project, have been adapted and improved. The PSO was improved implementing an adaptive version, that allowed to favour the convergence.
- The thermodynamic description of the model was studied and improved, working directly on the electrodes intercalation curve. Moreover, three new thermodynamic parameters were introduced in the model to account for the main degradation modes, i.e. loss of lithium inventory, loss of active material on the positive and on the negative electrode. An additional PSO algorithm has been developed to allow the calibration of the three parameters.
- From the combination of the kinetic parameters and the thermodynamic parameters calibration methods, a novel methodology to calibrate the model for degraded batteries was developed. Providing the two PSO algorithms with the experimental dataset required for the fitting, also the model for a sample at a certain aging stage can be calibrated, calibrating the thermodynamic parameters first and subsequently the kinetic ones.
- To validate the proposed calibration methodology, two different degradation phenomena, namely SEI growth and lithium plating, have been selected to be investigated in an experimental aging campaign:
  - SEI growth: calendar aging at 60°C and four different SOCs has been selected as operating conditions to stress SEI growth. The experimental results of the aging campaign have been analyzed. Capacity losses trend have been analyzed: the samples with higher strage SOC (100% and 80%) were the most affected by degradation. Thanks to IC and DV analysis, SEI growth presence have been identified from the detection of

$LLI$ effects on the IC and DV curves; $LAM_p$ effects was also recognized. The parameter estimation on the sample stored at 80% SOC for eight weeks confirmed the results of the IC/DV analysis;

- lithium plating: to investigate the stressors of lithium plating, the voltage profile during relaxation after charging at low temperatures have been studied: lower temperatures and higher charging currents are the main parameters that promote lithium plating. The lithium stripping-plating reactions have been implemented on the physical model and was helpful to understand the effects of the different operating conditions. Four different types of cycle at two low temperatures (0°C and -10°C) have been selected to be the conditions stressing lithium plating. The capacity loss trends confirmed the temperature effect observed in the previous stressors analysis; moreover, a relation with the charging current of cycling has been highlighted. From the IC/DV analysis $LLI$ and $LAM_n$ have been identified on the samples aged at -10°C, giving evidence of lithium plating and probably particle cracking.

- Moreover the proposed methodology for the calibration of an aged samples have been performed on one of the samples that cycled at plating conditions at -10°C, obtaining positive results in terms of RMSEs. The thermodynamic parameters' trend are reported and analyzed: at the end of the cycling period (12 EFC) $LLI$ reached almost 15% and a 5% of $LAM_n$ was also detected, suggesting that lithium plating occurred and a degradation of the negative electrode structure, e.g. particles cracking and loss of electric contact. Within the kinetic parameters, the radius of the negative electrode particles' radius and the kinetic rate constant show a significant decrease with degradation, that can be interpreted as a confirmation graphite electrode degradation and particle cracking.

The proposed methodology has shown promising results, proving to be a powerful tool both for a comprehensive battery characterization and for the degradation description. Several proposals for follow up activities in the next future are suggested:

- the diagnostic procedure that provides the experimental dataset necessary for the data fitting algorithm, has been performed for all the samples at the different aging stages. Due to lack of time, the complete calibration, applying the methodology, has been performed only for one sample (cycle A, -10°C). A future activity may involve the application of the methodology to other samples, to study the parameters variation and highlight differences and similar-

ities with the case already studied. Moreover, other degradation mechanisms may be studied with this methodology;

- the calendar aging campaign to stress SEI growth may be extended for a longer period to appreciate further degradation;
- a slow discharge at 0.1C-rate (duration of about 10 hours) is necessary to calibrate the model, in the proposed methodology: this compromise have been accepted as this is still a development phase, but the final diagnostic method aims to not include such a time-consuming test;
- in the application of the methodology, 14 kinetic parameters were varying with the aging, but the choice is basically arbitrary; changing the set of parameters to be optimized can be interesting, or a two steps calibration may be performed to analyze the parameters that were considered as "low sensitive" in a second step, once the "high sensitive" ones have been calibrated in the first step;
- the methodology developed is interpretative and is a very helpful tool for the qualitative detection of degradation phenomena; SEM and in-situ investigation may be useful to confirm and quantify the presence of lithium plating and SEI growth on the samples adopted in this work.

# References


[1] "Levelized Cost of Energy and Levelized Cost of Storage 2019". In: (2/03/2021). URL: https://www.lazard.com/perspective/lcoe2019.

[2] "Market analysis and forecast from 2019 to 2024". In: (2/03/2021). URL: https://www.iea.org/reports/renewables-2019.

[3] "Electricity storage and renewables: Costs and markets to 2030". In: (2/03/2021). URL: https://www.irena.org/publications/2017/Oct/Electricity-storage-and-renewables-costs-and-markets.

[4] Michael Woodward Bryn Walton Jamie Hamilton. "Electric vehicles, Setting a course for 2030". In: (2/03/2021). URL: https://www2.deloitte.com/uk/en/insights/focus/future-of-mobility/electric-vehicle-trends-2030.html.

[5] John T Warner. "The Handbook of Lithium-Ion Battery Pack Design: Chemistry, Components, Types and Terminology". In: (May 2015).

[6] Ralph J. Brodd Masaki Yoshio and Akiya Kozawa, eds. *Lithium-Ion Batteries*. Springer New York, 2009. DOI: 10.1007/978-0-387-34445-4.

[7] B. Dunn, H. Kamath, and J.-M. Tarascon. "Electrical Energy Storage for the Grid: A Battery of Choices". In: *Science* 334.6058 (Nov. 2011), pp. 928–935.

[8] M. Bauer T. T. Nguyen A. Jossen J. Lygeros. "Evaluating frequency regulation operated on two stationary energy systems with batteries from electric vehicles". In: *Energy Procedia* 155 (2018), pp. 32–43.

[9] Jianan Zhang et al. "An Overview on Thermal Safety Issues of Lithium-ion Batteries for Electric Vehicle Application". In: *IEEE Access* PP (May 2018), pp. 1–1. DOI: 10.1109/ACCESS.2018.2824838.

[10] Xing Zhou et al. "An easy-to-implement multi-point impedance technique for monitoring aging of lithium ion batteries". In: *Journal of Power Sources* 417 (2019), pp. 188–192.

[11] John Newman and Karen E Thomas-Alyea. "Electrochemical Systems". In: (2012).

[12] K. Li and King-Jet Tseng. "Energy efficiency of lithium-ion battery used as energy storage devices in micro-grid". In: *IECON 2015 - 41st Annual Conference of the IEEE Industrial Electronics Society* (2015), pp. 005235–005240.

[13] Robert Schröder, Muhammed Aydemir, and Günther Seliger. "Comparatively Assessing different Shapes of Lithium-ion Battery Cells". In: *Procedia Manufacturing* 8 (2017). 14th Global Conference on Sustainable Manufacturing,

GCSM 3-5 October 2016, Stellenbosch, South Africa, pp. 104–111. ISSN: 2351-9789. DOI: https://doi.org/10.1016/j.promfg.2017.02.013.

[14] J.-M. Tarascon and M. Armand. "Issues and challenges facing rechargeable lithium batteries". In: *Nature* 414.6861 (Nov. 2001), pp. 359–367.

[15] K. Mizushima et al. "LixCoO2 (0<x<-1): A new cathode material for batteries of high energy density". In: *Materials Research Bulletin* 15.6 (1980), pp. 783–789.

[16] J. Vetter et al. "Ageing mechanisms in lithium-ion batteries". In: *Journal of Power Sources* 147.1-2 (Sept. 2005), pp. 269–281.

[17] "Cutting battery industry's reliance on cobalt will be an uphill task". In: (5/01/2020). URL: https://www.theguardian.com/environment/2020/jan/05/cutting-cobalt-challenge-battery-industry-electric-cars-congo.

[18] Michael M. Thackeray. "Manganese oxides for lithium batteries". In: *Progress in Solid State Chemistry* 25.1 (1997), pp. 1–71.

[19] Naoki Nitta et al. "Li-ion battery materials: present and future". In: *Materials Today* 18.5 (2015), pp. 252–264.

[20] C.H. Chen et al. "Aluminum-doped lithium nickel cobalt oxide electrodes for high-power lithium-ion batteries". In: *Journal of Power Sources* 128.2 (Apr. 2004), pp. 278–285.

[21] Ira Bloom et al. "Effect of cathode composition on capacity fade, impedance rise and power fade in high-power, lithium-ion cells". In: *Journal of power sources* 124 (Nov. 2003), pp. 538–550.

[22] Gaurav Assat and Jean-Marie Tarascon. "Fundamental understanding and practical challenges of anionic redox activity in Li-ion batteries". In: *Nature Energy* 3.5 (Apr. 2018), pp. 373–386.

[23] A. Yamada, S. C. Chung, and K. Hinokuma. "Optimized LiFePO[sub 4] for Lithium Battery Cathodes". In: *Journal of The Electrochemical Society* 148.3 (2001), A224.

[24] Adriano Alessandrini et al. "Advantages of retrofitting old electric buses and minibuses". In: *Energy Procedia* 126 (2017). ATI 2017 - 72nd Conference of the Italian Thermal Machines Engineering Association, pp. 995–1002.

[25] Hao Zhang et al. "Graphite as anode materials: Fundamental mechanism, recent progress and advances". In: *Energy Storage Materials* 36 (2021), pp. 147–170.

[26] Jakob Asenbauer et al. "The success story of graphite as a lithium-ion anode material fundamentals, remaining challenges, and recent developments including silicon (oxide) composites". In: *Sustainable Energy & Fuels* 4.11 (2020), pp. 5387–5416.

[27] A. Senyshyn et al. “Lithium Intercalation into Graphitic Carbons Revisited: Experimental Evidence for Twisted Bilayer Behavior”. In: *Journal of The Electrochemical Society* 160.5 (2013), A3198–A3205.

[28] T. OHZUKU, Y. IWAKOSHI, and K. SAWAI. “Formation of Lithium-Graphite Intercalation Compounds in Nonaqueous Electrolytes and Their Application as a Negative Electrode for a Lithium Ion (Shuttlecock) Cell.” In: *ChemInform* 24.51 (Aug. 2010), no–no.

[29] Michael Hess. “Kinetics and stage transitions of graphite for lithium-ion batteries”. In: (2013).

[30] George E. Blomgren. “The Development and Future of Lithium Ion Batteries”. In: *Journal of The Electrochemical Society* 164.1 (Dec. 2016), A5019–A5025. DOI: 10.1149/2.0251701jes.

[31] K. Zaghib et al. “Safe and fast-charging Li-ion battery with long shelf life for power applications”. In: *Journal of Power Sources* 196.8 (2011), pp. 3949–3954. ISSN: 0378-7753. DOI: https://doi.org/10.1016/j.jpowsour.2010.11.093.

[32] Jürgen Janek and Wolfgang G. Zeier. “A solid future for battery development”. In: *Nature Energy* 1.9 (Sept. 2016).

[33] Emine S Karaman et al. “Functionalized carbon nanotube doped gel electrolytes with enhanced mechanical and electrical properties for battery applications”. In: *Materials Chemistry and Physics* 264 (2021), p. 124448.

[34] Qingjiang Yu et al. “Recent progress of composite solid polymer electrolytes for all-solid-state lithium metal batteries”. In: *Chinese Chemical Letters* (2021).

[35] “USABC electric vehicle Battery Test Procedures Manual. Revision 2”. In: (Jan. 1996).

[36] Lluc Canals Casals, B. Amante García, and Camille Canal. “Second life batteries lifespan: Rest of useful life and environmental analysis”. In: *Journal of Environmental Management* 232 (2019), pp. 354–363.

[37] Andreas Podias et al. “Sustainability Assessment of Second Use Applications of Automotive Batteries: Ageing of Li-Ion Battery Cells in Automotive and Grid-Scale Applications”. In: *World Electric Vehicle Journal* 9.2 (2018), p. 24.

[38] M Broussely et al. “Aging mechanism in Li ion cells and calendar life predictions”. In: *Journal of Power Sources* 97-98 (2001). Proceedings of the 10th International Meeting on Lithium Batteries, pp. 13–21.

[39] Peter Keil et al. “Calendar Aging of Lithium-Ion Batteries”. In: *Journal of The Electrochemical Society* 163.9 (2016), A1872–A1880.

[40] I Bloom et al. “An accelerated calendar and cycle life study of Li-ion cells”. In: *Journal of Power Sources* 101.2 (2001), pp. 238–247.

[41] Madeleine Ecker et al. “Calendar and cycle life study of Li(NiMnCo)O2-based 18650 lithium-ion batteries”. In: *Journal of Power Sources* 248 (2014), pp. 839–851.

[42] Qi Zhang and Ralph E. White. “Capacity fade analysis of a lithium ion cell”. In: *Journal of Power Sources* 179.2 (2008), pp. 793–798.

[43] R.B Wright et al. “Calendar- and cycle-life studies of advanced technology development program generation 1 lithium-ion batteries”. In: *Journal of Power Sources* 110.2 (Aug. 2002), pp. 445–470.

[44] Quirin Kellner et al. “Battery cycle life test development for high-performance electric vehicle applications”. In: *Journal of Energy Storage* 15 (2018), pp. 228–244.

[45] Stefan Käbitz et al. “Cycle and calendar life study of a graphite LiNi1/3Mn1/3Co1/3O2 Li-ion high energy system. Part A: Full cell characterization”. In: *Journal of Power Sources* 239 (2013), pp. 572–583.

[46] John Wang et al. “Degradation of lithium ion batteries employing graphite negatives and nickel–cobalt–manganese oxide+spinel manganese oxide positives: Part 1, aging mechanisms and life estimation”. In: *Journal of Power Sources* 269 (2014), pp. 937–948. ISSN: 0378-7753. DOI: https://doi.org/10.1016/j.jpowsour.2014.07.030.

[47] Arpit Maheshwari, Michael Heck, and Massimo Santarelli. “Cycle aging studies of lithium nickel manganese cobalt oxide-based batteries using electrochemical impedance spectroscopy”. In: *Electrochimica Acta* 273 (May 2018), pp. 335–348.

[48] Christoph R. Birkl et al. “Degradation diagnostics for lithium ion cells”. In: *Journal of Power Sources* 341 (2017), pp. 373–386.

[49] She-huang Wu and Po-Han Lee. “Storage fading of a commercial 18650 cell comprised with NMC/LMO cathode and graphite anode”. In: *Journal of Power Sources* 349 (2017), pp. 27–36.

[50] Matthieu Dubarry, Cyril Truchot, and Bor Yann Liaw. “Synthesize battery degradation modes via a diagnostic and prognostic model”. In: *Journal of Power Sources* 219 (2012), pp. 204–216.

[51] E. Peled and S. Menkin. “Review SEI: Past, Present and Future”. In: *Journal of The Electrochemical Society* 164.7 (2017), A1703–A1719.

[52] Ajaykrishna Ramasubramanian et al. “Lithium Diffusion Mechanism through Solid–Electrolyte Interphase in Rechargeable Lithium Batteries”. In: *The Journal of Physical Chemistry C* 123.16 (Mar. 2019), pp. 10237–10245.

[53] F Orsini et al. “In situ Scanning Electron Microscopy (SEM) observation of interfaces within plastic lithium batteries”. In: *Journal of Power Sources* 76.1 (1998), pp. 19–29.

[54] Shriram Santhanagopalan, Premanand Ramadass, and John (Zhengming) Zhang. “Analysis of internal short-circuit in a lithium ion cell”. In: *Journal of Power Sources* 194.1 (2009). XIth Polish Conference on Fast Ionic Conductors 2008, pp. 550–557.

[55] Johannes Wandt et al. “Operando electron paramagnetic resonance spectroscopy formation of mossy lithium on lithium anodes during charge discharge cycling”. In: *Energy & Environmental Science* 8.4 (2015), pp. 1358–1367.

[56] Thomas Waldmann, Björn-Ingo Hogg, and Margret Wohlfahrt-Mehrens. “Li plating as unwanted side reaction in commercial Li-ion cells – A review”. In: *Journal of Power Sources* 384 (2018), pp. 107–124.

[57] Xiaosong Hu et al. “Battery warm-up methodologies at subzero temperatures for automotive applications: Recent advances and perspectives”. In: *Progress in Energy and Combustion Science* 77 (2020), p. 100806.

[58] Chun Zhan et al. “Dissolution, migration, and deposition of transition metal ions in Li-ion batteries exemplified by Mn-based cathodes a critical review”. In: *Energy & Environmental Science* 11.2 (2018), pp. 243–257.

[59] Tao Cheng et al. “Cracks Formation in Lithium-Rich Cathode Materials for Lithium-Ion Batteries during the Electrochemical Process”. In: *Energies* 11.10 (Oct. 2018), p. 2712.

[60] Kenji Takahashi and Venkat Srinivasan. “Examination of Graphite Particle Cracking as a Failure Mode in Lithium-Ion Batteries: A Model-Experimental Study”. In: *Journal of The Electrochemical Society* 162.4 (2015), A635–A645.

[61] Simon Müller et al. “Quantification and modeling of mechanical degradation in lithium-ion batteries based on nanoscale imaging”. In: *Nature Communications* 9.1 (June 2018).

[62] Agnieszka Gabryelczyk et al. “Taguchi method in experimental procedures focused on corrosion process of positive current collector in lithium-ion batteries”. In: *Electrochimica Acta* 360 (2020), p. 137011.

[63] M.S. Hossain Lipu et al. “A review of state of health and remaining useful life estimation methods for lithium-ion battery in electric vehicles: Challenges and recommendations”. In: *Journal of Cleaner Production* 205 (2018), pp. 115–133.

[64] Rui Xiong et al. “Lithium-ion battery aging mechanisms and diagnosis method for automotive applications: Recent advances and perspectives”. In: *Renewable and Sustainable Energy Reviews* 131 (2020), p. 110048.

[65] Thomas Waldmann et al. “Correlations between Electrochemical Data and Results from Post-Mortem Analysis of Aged Lithium-Ion Batteries”. In: *Journal of The Electrochemical Society* 162.8 (2015), A1500–A1505.

[66] Thomas Waldmann et al. “Review: Post-Mortem Analysis of Aged Lithium-Ion Batteries: Disassembly Methodology and Physico-Chemical Analysis Techniques”. In: *Journal of The Electrochemical Society* 163.10 (2016), A2149–A2164.

[67] Matilda Klett et al. “Non-uniform aging of cycled commercial LiFePO4//graphite cylindrical cells revealed by post-mortem analysis”. In: *Journal of Power Sources* 257 (2014), pp. 126–137.

[68] Mariyam Susana Dewi Darma et al. “The influence of cycling temperature and cycling rate on the phase specific degradation of a positive electrode in lithium ion batteries: A post mortem analysis”. In: *Journal of Power Sources* 327 (2016), pp. 714–725.

[69] PPRML Harks, FM Mulder, and PHL Notten. “In situ methods for Li-ion battery research: A review of recent developments”. In: *Journal of power sources* 288 (2015), pp. 92–105.

[70] Zhe Li et al. “A review of lithium deposition in lithium-ion and lithium metal secondary batteries”. In: *Journal of Power Sources* 254 (2014), pp. 168–182.

[71] Barbara Stiaszny et al. “Electrochemical characterization and post-mortem analysis of aged LiMn2O4–Li(Ni0.5Mn0.3Co0.2)O2/graphite lithium ion batteries. Part I: Cycle aging”. In: *Journal of Power Sources* 251 (2014), pp. 439–450.

[72] Zeyu Ma et al. “A mechanism identification model based state-of-health diagnosis of lithium-ion batteries for energy storage applications”. In: *Journal of Cleaner Production* 193 (2018), pp. 379–390.

[73] Quentin Badey et al. “Mechanisms and Modeling of Lithium-Ion Battery Aging for a Vehicle Usage”. In: *ECS Meeting Abstracts*. 15. IOP Publishing. 2011, p. 742.

[74] Kenza Maher and Rachid Yazami. “Effect of overcharge on entropy and enthalpy of lithium-ion batteries”. In: *Electrochimica Acta* 101 (2013), pp. 71–78.

[75] Matthieu Dubarry et al. “Incremental Capacity Analysis and Close-to-Equilibrium OCV Measurements to Quantify Capacity Fade in Commercial

Rechargeable Lithium Batteries". In: *Electrochemical and Solid-State Letters* 9.10 (2006), A454.

[76] T. K. Dong et al. "Dynamic Modeling of Li-Ion Batteries Using an Equivalent Electrical Circuit". In: *Journal of The Electrochemical Society* 158.3 (2011), A326.

[77] Carlos Pastor-Fernández et al. "Identification and quantification of ageing mechanisms in Lithium-ion batteries using the EIS technique". In: (2016), pp. 1–6.

[78] Rujian Fu et al. "Modeling of degradation effects considering side reactions for a pouch type Li-ion polymer battery with carbon anode". In: *Journal of Power Sources* 261 (2014), pp. 120–135.

[79] Tony Jaumann et al. "SEI-component formation on sub 5 nm sized silicon nanoparticles in Li-ion batteries: the role of electrode preparation, FEC addition and binders". In: *Physical Chemistry Chemical Physics* 17.38 (2015), pp. 24956–24967.

[80] Timo Schwieters et al. "Lithium loss in the solid electrolyte interphase: Lithium quantification of aged lithium ion battery graphite electrodes by means of laser ablation inductively coupled plasma mass spectrometry and inductively coupled plasma optical emission spectroscopy". In: *Journal of power sources* 356 (2017), pp. 47–55.

[81] Naoki Kimura et al. "Cycle deterioration analysis of 0.6 Ah-class lithium-ion cells with cell chemistry of LiNi0. 6Co0. 2Mn0. 2O2-based/graphite". In: *Journal of Power Sources* 332 (2016), pp. 187–192.

[82] Sophie Solchenbach et al. "A Gold Micro-Reference Electrode for Impedance and Potential Measurements in Lithium Ion Batteries". In: *Journal of The Electrochemical Society* 163.10 (2016), A2265–A2272.

[83] Yancheng Zhang and Chao-Yang Wang. "Cycle-Life Characterization of Automotive Lithium-Ion Batteries with LiNiO[sub 2] Cathode". In: *Journal of The Electrochemical Society* 156.7 (2009), A527.

[84] Yongjun Leng et al. "Electrochemical Cycle-Life Characterization of High Energy Lithium-Ion Cells with Thick Li(Ni0.6Mn0.2Co0.2)O2and Graphite Electrodes". In: *Journal of The Electrochemical Society* 164.6 (2017), A1037–A1049.

[85] N. Ghanbari et al. "Detection of Li Deposition by Glow Discharge Optical Emission Spectroscopy in Post-Mortem Analysis". In: *ECS Electrochemistry Letters* 4.9 (July 2015), A100–A102.

[86] Yvonne Kramer et al. “A New Method for Quantitative Marking of Deposited Lithium by Chemical Treatment on Graphite Anodes in Lithium-Ion Cells”. In: *Chemistry - A European Journal* 21.16 (Mar. 2015), pp. 6062–6065.

[87] J. Arai et al. “In Situ Solid State7Li NMR Observations of Lithium Metal Deposition during Overcharge in Lithium Ion Batteries”. In: *Journal of The Electrochemical Society* 162.6 (2015), A952–A958.

[88] Hao Ge et al. “Investigating Lithium Plating in Lithium-Ion Batteries at Low Temperatures Using Electrochemical Model with NMR Assisted Parameterization”. In: *Journal of The Electrochemical Society* 164.6 (2017), A1050–A1060.

[89] Johannes Wandt et al. “Quantitative and time-resolved detection of lithium plating on graphite anodes in lithium ion batteries”. In: *Materials Today* 21.3 (2018), pp. 231–240.

[90] J. C. Burns, D. A. Stevens, and J. R. Dahn. “In-Situ Detection of Lithium Plating Using High Precision Coulometry”. In: *Journal of The Electrochemical Society* 162.6 (2015), A959–A964.

[91] Q. Q. Liu et al. “Effects of Electrolyte Additives and Solvents on Unwanted Lithium Plating in Lithium-Ion Cells”. In: *Journal of The Electrochemical Society* 164.6 (2017), A1173–A1183.

[92] Bernhard Bitzer and Andreas Gruhle. “A new method for detecting lithium plating by measuring the cell thickness”. In: *Journal of Power Sources* 262 (2014), pp. 297–302.

[93] F. Grimsmann et al. “Determining the maximum charging currents of lithium-ion cells for small charge quantities”. In: *Journal of Power Sources* 365 (2017), pp. 12–16.

[94] Claudia Birkenmaier et al. “Lithium Plating on Graphite Negative Electrodes: Innovative Qualitative and Quantitative Investigation Methods”. In: *Journal of The Electrochemical Society* 162.14 (2015), A2646–A2650.

[95] Veronika Zinth et al. “Lithium plating in lithium-ion batteries at sub-ambient temperatures investigated by in situ neutron diffraction”. In: *Journal of Power Sources* 271 (2014), pp. 152–159.

[96] Jörn Wilhelm et al. “In Situ Neutron Diffraction Study of Lithiation Gradients in Graphite Anodes during Discharge and Relaxation”. In: *Journal of The Electrochemical Society* 165.9 (2018), A1846–A1856.

[97] Mathias Petzl and Michael A. Danzer. “Nondestructive detection, characterization, and quantification of lithium plating in commercial lithium-ion batteries”. In: *Journal of Power Sources* 254 (2014), pp. 80–87.

[98] M.C. Smart et al. “Performance characteristics of lithium ion cells at low temperatures”. In: *IEEE Aerospace and Electronic Systems Magazine* 17.12 (2002), pp. 16–20.

[99] M. C. Smart and B. V. Ratnakumar. “Effects of Electrolyte Composition on Lithium Plating in Lithium-Ion Cells”. In: *Journal of The Electrochemical Society* 158.4 (2011), A379. DOI: 10.1149/1.3544439. URL: https://doi.org/10.1149/1.3544439.

[100] C. Uhlmann et al. “In situ detection of lithium metal plating on graphite in experimental cells”. In: *Journal of Power Sources* 279 (2015). 9th International Conference on Lead-Acid Batteries – LABAT 2014, pp. 428–438.

[101] Marius Bauer et al. “Multi-phase formation induced by kinetic limitations in graphite-based lithium-ion cells: Analyzing the effects on dilation and voltage response”. In: *Journal of Energy Storage* 10 (2017), pp. 1–10.

[102] Gabriele Sordi. “Thermodynamic and kinetic analysis of commercial lithium ion battery for identification of degradation mechanisms”. In: (Apr. 2019).

[103] International Organization for Standardization (ISO). “Electrically propelled road vehicles — Test specification for lithium-ion traction battery packs and systems”. In: (2018).

[104] M. Maures et al. “Lithium-ion battery SoH estimation based on incremental capacity peak tracking at several current levels for online application”. In: *Microelectronics Reliability* 114 (2020). 31st European Symposium on Reliability of Electron Devices, Failure Physics and Analysis, ESREF 2020, p. 113798. ISSN: 0026-2714. DOI: https://doi.org/10.1016/j.microrel.2020.113798.

[105] Zhicheng Xu et al. “Estimation and prediction of state of health of electric vehicle batteries using discrete incremental capacity analysis based on real driving data”. In: *Energy* 225 (2021), p. 120160. ISSN: 0360-5442. DOI: https://doi.org/10.1016/j.energy.2021.120160.

[106] Gao Jian, Si-Qi Shi, and Hong Li. “Brief overview of electrochemical potential in lithium ion batteries”. In: *Chinese Physics B* (2016). DOI: 10.1088/1674-1056/25/1/018210.

[107] Limei Wang et al. “State of health estimation of battery modules via differential voltage analysis with local data symmetry method”. In: *Electrochimica Acta* 256 (2017), pp. 81–89.

[108] A. Fly and R. Chen. “Rate dependency of incremental capacity analysis (dQ/dV) as a diagnostic tool for lithium-ion batteries”. In: *Journal of Energy Storage* 29 (2020), p. 101329.

[109] Alessandro Innocenti. “An innovative methodology to estimate the parameters of a lithium battery physical model”. In: (Apr. 2020).

[110] Stefan Schindler et al. “Voltage relaxation and impedance spectroscopy as in-operando methods for the detection of lithium plating on graphitic anodes in commercial lithium-ion cells”. In: *Journal of Power Sources* 304 (2016), pp. 170–180.

[111] J Dambrowski. “Validation of Impedance-Data and of Impedance-Based Modeling Approach of Electrochemical Cells by Means of Mathematical System Theory”. In: *39th Annual Conference of the IEEE Industrial* 60 (2013), pp. 1–7.

[112] “Electrode contributions to the impedance of a high-energy density Li-ion cell designed for EV applications”. In: *Solid State Ionics* 237 (2013), pp. 50–55.

[113] Evgenij Barsoukov et al. “Kinetics of lithium intercalation into carbon anodes: in situ impedance investigation of thickness and potential dependence”. In: *Solid state ionics* 116.3-4 (1999), pp. 249–261.

[114] Salim Erol and Mark E Orazem. “The influence of anomalous diffusion on the impedance response of LiCoO2| C batteries”. In: *Journal of Power Sources* 293 (2015), pp. 57–64.

[115] Haifeng Dai, Bo Jiang, and Xuezhe Wei. “Impedance Characterization and Modeling of Lithium-Ion Batteries Considering the Internal Temperature Gradient”. In: *Energies* 11.1 (Jan. 2018), p. 220. DOI: 10.3390/en11010220.

[116] Lars Ole Valo and Jan N. Reimers. “Transport Properties of LiPF[sub 6]-Based Li-Ion Battery Electrolytes”. In: *Journal of The Electrochemical Society* 152.5 (2005), A882.

[117] Myounggu Park et al. “A review of conduction phenomena in Li-ion batteries”. In: *Journal of Power Sources* 195.24 (Dec. 2010), pp. 7904–7929.

[118] James Kennedy and Russell Eberhart. “Particle swarm optimization”. In: *Proceedings of ICNN’95-international conference on neural networks*. Vol. 4. IEEE. 1995, pp. 1942–1948.

[119] Mehrdad Rostami et al. “Review of swarm intelligence-based feature selection methods”. In: *Engineering Applications of Artificial Intelligence* 100 (2021), p. 104210. ISSN: 0952-1976. DOI: https://doi.org/10.1016/j.engappai.2021.104210.

[120] Xiao Yang et al. “Parameter Identification of Electrochemical Model for Vehicular Lithium-Ion Battery Based on Particle Swarm Optimization”. In: *Energies* 10.11 (Nov. 2017), p. 1811. DOI: 10.3390/en10111811.

[121] Md Ashiqur Rahman, Sohel Anwar, and Afshin Izadian. “Electrochemical model parameter identification of a lithium-ion battery using particle swarm

optimization method". In: *Journal of Power Sources* 307 (2016), pp. 86–97. ISSN: 0378-7753. DOI: https://doi.org/10.1016/j.jpowsour.2015.12.083.

[122] Hyung-Joo Noh et al. "Comparison of the structural and electrochemical properties of layered Li[NixCoyMnz]O2 (x=1/3, 0.5, 0.6, 0.7, 0.8 and 0.85) cathode material for lithium-ion batteries". In: *Journal of Power Sources* 233 (2013), pp. 121–130. ISSN: 0378-7753. DOI: https://doi.org/10.1016/j.jpowsour.2013.01.063.

[123] Sang Woo Han. "Transport and Kinetic Phenomena Linked to Power Performance of Lithium-Ion Batteries". In: (2014).

[124] I J Ong and J Newman. "Double-layer capacitance in a dual lithium ion insertion cell". In: *Journal of the Electrochemical Society* 146.12 (Dec. 1999). ISSN: 0013-4651.

[125] Z. Zhan et al. "Adaptive Particle Swarm Optimization". In: *IEEE Transactions on Systems, Man, and Cybernetics, Part B (Cybernetics)* 39.6 (2009), pp. 1362–1381. DOI: 10.1109/TSMCB.2009.2015956.

[126] Chaofeng Liu, Zachary G. Neale, and Guozhong Cao. "Understanding electrochemical potentials of cathode materials in rechargeable batteries". In: *Materials Today* 19.2 (2016), pp. 109–123. ISSN: 1369-7021. DOI: https://doi.org/10.1016/j.mattod.2015.10.009.

[127] Yang Gao et al. "The Mechanism and Characterization of Accelerated Capacity Deterioration for Lithium-Ion Battery with Li(NiMnCo) O2 Cathode". In: *Journal of The Electrochemical Society* 166.8 (2019), A1623–A1635.

[128] Alexander P. Schmidt et al. "Model-based distinction and quantification of capacity loss and rate capability fade in Li-ion batteries". In: *Journal of Power Sources* 195.22 (2010), pp. 7634–7638. ISSN: 0378-7753. DOI: https://doi.org/10.1016/j.jpowsour.2010.06.011.

[129] Venkatasailanathan Ramadesigan et al. "Parameter Estimation and Capacity Fade Analysis of Lithium-Ion Batteries Using Reformulated Models". In: *Journal of The Electrochemical Society* 158.9 (2011), A1048. DOI: 10.1149/1.3609926.

[130] Kotub Uddin et al. "Characterising Lithium-Ion Battery Degradation through the Identification and Tracking of Electrochemical Battery Model Parameters". In: *Batteries* 2.2 (Apr. 2016), p. 13.

[131] Liqiang Zhang et al. "Non-Destructive Analysis of Degradation Mechanisms in Cycle-Aged Graphite/LiCoO2 Batteries". In: *Energies* 7.10 (Sept. 2014), pp. 6282–6305. DOI: 10.3390/en7106282.

[132] Liqiang Zhang et al. "Parameter Sensitivity Analysis of Cylindrical LiFePO4Battery Performance Using Multi-Physics Modeling". In: *Journal*

*of The Electrochemical Society* 161.5 (2014), A762–A776. DOI: 10.1149/2.048405jes.

[133] Saehong Park et al. "Optimal Experimental Design for Parameterization of an Electrochemical Lithium-Ion Battery Model". In: *Journal of The Electrochemical Society* 165 (Jan. 2018), A1309–A1323. DOI: 10.1149/2.0421807jes.

[134] Jun Li et al. "Parameter Identification of Lithium-Ion Batteries Model to Predict Discharge Behaviors Using Heuristic Algorithm". In: *Journal of The Electrochemical Society* 163.8 (2016), A1646–A1652. DOI: 10.1149/2.0861608jes.

[135] Jun-Fan Ding et al. "A review on the failure and regulation of solid electrolyte interphase in lithium batteries". In: *Journal of Energy Chemistry* 59 (2021), pp. 306–319.

[136] Satu Kristiina Heiskanen, Jongjung Kim, and Brett L. Lucht. "Generation and Evolution of the Solid Electrolyte Interphase of Lithium-Ion Batteries". In: *Joule* 3.10 (2019), pp. 2322–2333.

[137] Xin-Bing Cheng et al. "A Review of Solid Electrolyte Interphases on Lithium Metal Anode". In: *Advanced Science* 3.3 (Nov. 2015), p. 1500213.

[138] Rui Xu et al. "The reduction of interfacial transfer barrier of Li ions enabled by inorganics-rich solid-electrolyte interphase". In: *Energy Storage Materials* 28 (2020), pp. 401–406.

[139] Siqi Shi et al. "Direct Calculation of Li-Ion Transport in the Solid Electrolyte Interphase". In: *Journal of the American Chemical Society* 134.37 (2012), pp. 15476–15487. DOI: 10.1021/ja305366r.

[140] Christopher L. Campion, Wentao Li, and Brett L. Lucht. "Thermal Decomposition of LiPF[sub 6]-Based Electrolytes for Lithium-Ion Batteries". In: *Journal of The Electrochemical Society* 152.12 (2005), A2327.

[141] Anthony Barré et al. "A review on lithium-ion battery ageing mechanisms and estimations for automotive applications". In: *Journal of Power Sources* 241 (2013), pp. 680–689. ISSN: 0378-7753. DOI: https://doi.org/10.1016/j.jpowsour.2013.05.040.

[142] Matthieu Dubarry, Nan Qin, and Paul Brooker. "Calendar aging of commercial Li-ion cells of different chemistries–A review". In: *Current Opinion in Electrochemistry* 9 (2018), pp. 106–113.

[143] M. Maures et al. "Impact of temperature on calendar ageing of Lithium-ion battery using incremental capacity analysis". In: *Microelectronics Reliability* 100-101 (2019). 30th European Symposium on Reliability of Electron Devices, Failure Physics and Analysis, p. 113364.

[144] Pierre Kubiak et al. “Calendar aging of a 250 kW/500 kWh Li-ion battery deployed for the grid storage application”. In: *Journal of Power Sources* 372 (2017), pp. 16–23.

[145] Akram Eddahech, Olivier Briat, and Jean-Michel Vinassa. “Performance comparison of four lithium–ion battery technologies under calendar aging”. In: *Energy* 84 (2015), pp. 542–550.

[146] Yoshio Nishi. “The development of lithium ion secondary batteries”. In: *The Chemical Record* 1.5 (2001), pp. 406–413.

[147] JE Harlow et al. “Use of asymmetric average charge-and average discharge-voltages as an indicator of the onset of unwanted lithium deposition in lithium-ion cells”. In: *Journal of The Electrochemical Society* 165.16 (2018), A3595.

[148] Nathalie Legrand et al. “Physical characterization of the charging process of a Li-ion battery and prediction of Li plating by electrochemical modelling”. In: *Journal of Power Sources* 245 (2014), pp. 208–216.

[149] Jian Duan et al. “Building safe lithium-ion batteries for electric vehicles: a review”. In: *Electrochemical Energy Reviews* 3.1 (2020), pp. 1–42.

[150] Upender Rao Koleti et al. “The development of optimal charging strategies for lithium-ion batteries to prevent the onset of lithium plating at low ambient temperatures”. In: *Journal of Energy Storage* 24 (2019), p. 100798.

[151] Marco-Tulio F Rodrigues et al. “A materials perspective on Li-ion batteries at extreme temperatures”. In: *nature energy* 2.8 (2017), pp. 1–14.

[152] Mathias Petzl, Michael Kasper, and Michael A. Danzer. “Lithium plating in a commercial lithium-ion battery – A low-temperature aging study”. In: *Journal of Power Sources* 275 (2015), pp. 799–807.

[153] Christian von Lüders et al. “Lithium plating in lithium-ion batteries investigated by voltage relaxation and in situ neutron diffraction”. In: *Journal of Power Sources* 342 (2017), pp. 17–23.

[154] Xiao-Guang Yang et al. “A look into the voltage plateau signal for detection and quantification of lithium plating in lithium-ion cells”. In: *Journal of Power Sources* 395 (2018), pp. 251–261.

[155] Jiang Fan and Steven Tan. “Studies on Charging Lithium-Ion Cells at Low Temperatures”. In: *Journal of The Electrochemical Society* 153.6 (2006), A1081.

[156] Jun-ichi Yamaki et al. “A consideration of the morphology of electrochemically deposited lithium in an organic electrolyte”. In: *Journal of Power Sources* 74.2 (1998), pp. 219–227.

[157] Jianwu Wen, Yan Yu, and Chunhua Chen. “A Review on Lithium-Ion Batteries Safety Issues: Existing Problems and Possible Solutions”. In: *Materials Express* 2.3 (Sept. 2012), pp. 197–212.

[158] S.S. Zhang, K. Xu, and T.R. Jow. “Study of the charging process of a LiCoO2-based Li-ion battery”. In: *Journal of Power Sources* 160.2 (2006). Special issue including selected papers presented at the International Workshop on Molten Carbonate Fuel Cells and Related Science and Technology 2005 together with regular papers, pp. 1349–1354.

[159] C. Brissot et al. “Dendritic growth mechanisms in lithium/polymer cells”. In: *Journal of Power Sources* 81-82 (1999), pp. 925–929.